



Universitat Autònoma de Barcelona

ADVERTIMENT. L'accés als continguts d'aquesta tesi queda condicionat a l'acceptació de les condicions d'ús establertes per la següent llicència Creative Commons:  http://cat.creativecommons.org/?page_id=184

ADVERTENCIA. El acceso a los contenidos de esta tesis queda condicionado a la aceptación de las condiciones de uso establecidas por la siguiente licencia Creative Commons:  <http://es.creativecommons.org/blog/licencias/>

WARNING. The access to the contents of this doctoral thesis it is limited to the acceptance of the use conditions set by the following Creative Commons license:  <https://creativecommons.org/licenses/?lang=en>



Universitat Autònoma
de Barcelona

Miniaturisation, automation and parallelisation of (bio)chemical analyses using novel Lab on a Chip systems

Natalia Sandez Fernandez

Tesi Doctoral
Programa de Doctorat en Química
Director: Julian Alonso Chamarro

Departament de Química
Facultat de Ciències
2018

Memòria presentada per aspirar al Grau de Doctora per

Natalia Sandez Fernandez

Vist i plau

Julian Alonso Chamarro

Catedràtic
Departament de Química

Bellaterra, 28 de Novembre de 2018

Financial support

The work presented in this dissertation was carried out with the following financial support:

- BES-2013-063843** Ayudas para contratos predoctorales para la formación de Doctores 2013. Ministerio de Economía y Competitividad, Gobierno de España. 2013.01.16 - 2017.01.15
- EEBB-I-17-11921** Ayudas a la movilidad predoctoral para la realización de estancias breves en centros de I+D 2016. Ministerio de Ciencia, Innovación y Universidades, Gobierno de España. 2017.08.21 - 2017.11.27
- CTQ2017-85011-R** Lab on a chip multiparametricos para aplicaciones aeroespaciales, medioambientales, agroalimentarias y biomédicas. Ministerio de Economía y Competitividad, Gobierno de España. Co-funded by FEDER. 2018.01.01 - 2020.12.31
- CTQ2012-36165** Miniaturización, integración y paralelización de ensayos químicos y biológicos mediante nuevas plataformas de microfluídica. Ministerio de Economía y Competitividad, Gobierno de España. Co-funded by FEDER. 2013.01.01 - 2015.12.31
- 2017 SGR 220** Convocatòria d'ajuts per donar suport a les activitats dels grups de recerca. Departament d'Universitats, Recerca i Societat de la Informació, Generalitat de Catalunya. 2017.01.01 - 2019.12.31
- 2014 SGR 837** Convocatòria d'ajuts per donar suport a les activitats dels grups de recerca. Departament d'Universitats, Recerca i Societat de la Informació, Generalitat de Catalunya. 2014.01.01 - 2016.12.31
- 2009 SGR 0323** Convocatòria d'ajuts per donar suport a les activitats dels grups de recerca. Departament d'Universitats, Recerca i Societat de la Informació, Generalitat de Catalunya. 2009.09.25 - 2014.04.30

A mi madre

Acknowledgements

Tenia tantes ganes que arribés el moment d'escriure els agraïments. Primer, perquè això vol dir que ja veig la llum al final del túnel. I segon, i quasi més important, perquè em fa una il·lusió tremenda donar les gràcies a tots els que heu posat un granet (o un cubell sencer) de sorra en tot plegat.

Primero de todo, está claro, agradecerte, Julian, esta maravillosa oportunidad de formar parte de un grupo de personitas tan bonitas, de cuidarme cuando ha hecho falta y cuando no, y de ser un director sin igual. Eres una persona magnífica. Gràcies, Mar, per la part que et pertoca en tot això.

Cinc anys (potser més) han donat per molt al grup. He vist com els compis es feien grans i passaven per on estic a punt de passar jo. La Sara, la rossa que ens unia a tots. L'Ori, el meu mentor de la centrífuga. El Pedro, que cuidava de mi des de la distància quan jo estava a Porto. I el Miki, que no només l'he vist fer-se doctor, sinó també ser pare! Alguns sortien, i altres entraven. Com la Mariona, que per culpa meva potser li tindrà una mica de mania a la centrífuga. I l'Alex, que puja fort! Sense oblidar els temporals, que són molts, tot i que guardo un especial record del Xavi i de l'Ernest, que eren l'alegria de la huerta!

I no, no m'oblido dels que encara hi sou. De fet, per això us he deixat pels últims. Perquè us estimo horrors. Eva, ets la repera. Quan algú et demana un cop de mà, tu dones el braç sencer. Ets tan especial! Has estat allà sempre i per tot, i no en puc estar més agraïda. Y Tony, mi pepito grillo, que por culpa tuya (gracias a ti) ahora me entero de qué pasa en el mundo (o lo intento). Que me has enseñado tantísimas cosas (incluyendo cómo hacer la declaración de la renta). Que siempre estás igual, y te mataría a veces. Pero te admiro. No sabes cuánto. Eres un ejemplo a seguir para mí en todos los sentidos. Y aunque no se me dé muy bien eso de la vida en general, no será porque no haya tenido un buen consejero. Gracias. Muchas, muchas gracias. Eva, Tony, os voy a echar de menos cuando ya no ronde por allí. Sois los mejores compañeros de trabajo (y, al final, de vida) que uno pueda desear.

Morar no Porto foi uma das melhores experiências da minha vida. Eu mudei. E descobri, não só que sou muito mais forte do que pensava, mas também que sou cool! Quero agradecer aos meus chefes de lá a oportunidade magnífica que me deram para crescer, tanto profissional como pessoalmente. Ao Prof. António O. S. S. Rangel e à Dra. Susana S. M. P. Vidigal, estarei eternamente agradecida. Fui feliz no laboratório e

também fora. De hecho, me fui de allí con algunas personitas en el corazón, sobretodo Natalia y Jorge. Sem esquecer, claro, a Cristina e a sua troupe de beagles (os nossos bebés). Estou enamorada do Porto, dos seus pores do sol e dos seus becos, dos vinhos verdes no rio e dos passeios de bicicleta. Saudade... Bela palavra... Não vejo a hora de voltar (pela quarta vez).

I ara toca donar les gràcies a les ànimes caritatives a les quals dec, massa literalment, un tros d'això. La portada, per exemple, és del Bernat. I si no trobeu (més) crims gramaticals i ortogràfics és cosa de l'Eva, el Roger i el Jordi (m'has deixat bocabadada). Ari, tu tens un 5% de les accions. Reclama dividends! M'encanta veure la il·lusió que et fa tot plegat i em reconforta saber que puc comptar amb tu per tot. Gracias Tony y Miki por vuestras pequeñas grandes aportaciones. Y, cómo no, gracias, Edu, por las horas que has invertido en esto. Sin ti, la tesis seria "distinta" (dejémoslo así). Eres, sin duda, mi hermanito preferido (y yo tu hermanita preferida, lo sé).

Sé que em deixo moltíssima gent. Sobretot a molts dels que no teniu, potser, una implicació tan directa en la tesi tot i que molta en la meva vida personal. Però també sé que tots els que hauríeu d'estar aquí mencionats ho sabeu i sabeu quant heu significat per a mi durant tot aquest temps. Us val un gràcies general?

Y, ya para terminar, falta a quien más agradecida tengo que estar. Por todo. Porque no estaría aquí si no fuse por ti. Sé que no soy una hija ejemplar, pero tampoco estoy tan mal. Gracias, mami. Te quiero.

Manresa, Novembre de 2018

Natalia Sandez Fernandez

Abstract

During the last few decades analytical chemistry has experienced an extraordinary evolution in order to meet the actual demand of on-time and in-situ information, moving from versatile yet bulky, time-consuming and expensive classical instrumentation towards novel economical miniaturised systems which are capable to fulfill the nowadays requirements. This evolution gave rise to the so-called Lab on a Chip (LOC) systems and micro total analysis systems (μ TAS), these latter integrating all the steps of the analytical procedure in a single microfluidic platform. This high level of integration and miniaturisation has been possible due to the existence of a “toolbox” of microfluidic elements that allow to perform the basic fluidic operations required within a given application.

In this context, the present thesis aims to broaden the scope of the μ TAS applications as well as to contribute to the currently available microfluidic toolbox. This dissertation describes the development of three different microsystems which have been applied to the quantification of various analytes of interest in wine, along with the development of a novel valving system for centrifugal microfluidic platforms. Due to its outstanding properties, Cyclic Olefin Copolymer (COC) has been selected as the substrate material for the construction of the abovementioned systems.

Firstly, an economical, automated and miniaturised system for the spectrophotometric determination of titratable acidity in wines is presented. The developed system permits not only the quantification of titratable acidity in individual wine samples, but also its continuous monitoring during wine-making processes. The microsystem has been optimised for both situations, prioritising, in one case, high throughput and minimal reagent and sample consumptions and, in the second case, high robustness and a complete automation of the system. The same microanalyser has been successfully applied to the measurement of the Primary Amino Nitrogen (PAN) content in wine. Minimal modifications were required, thus demonstrating its high versatility. The obtained results confirm an excellent performance of the microsystem for the three applications studied.

The development of a centrifugal microfluidic system for the parallel enzyme-based analysis of several wine parameters is also presented. L-lactic acid, the analyte selected as proof-of-concept, has been quantified by performing an on-chip standard addition. With that purpose, a double aliquoting structure that allows to split a wine sample into equal sub-volumes and an L-lactic acid standard solution into variable volumes, has

been implemented. The platform is still in the development stage, although promising results have already been obtained.

Finally, a novel magnetically actuated valving system for centrifugal microfluidic platforms is described. The working principle of the valve is based on the deformation of a flexible PDMS disc as a result of the magnetic attractive forces between two magnets, one at each side of the valve. At low rotational speeds, the pressure exerted onto the disc blocks the connection between two channels. At higher rotational speeds, one of the magnets is displaced as a result of an increase in the centrifugal force, thus releasing the pressure that kept the valve closed and allowing the fluid flow. Apart from being easily constructed and integrated, the major strength of this valve lies on its reversibility, which enables a highly sophisticated and flexible fluid management.

The results presented in this dissertation demonstrate the advantages of using miniaturised systems for analytical applications as well as the high potential of using COC as the substrate material for LOC devices. Moreover, the fabrication methodologies employed could potentially be extrapolated to mass production, which is an essential requirement for the commercial viability of these systems.

Resum

Durante las últimas décadas la química analítica ha experimentado una extraordinaria evolución con tal de satisfacer la actual demanda de información en tiempo real e *in situ*, partiendo de la instrumentación clásica (de gran versatilidad aunque voluminosa, cara e implicando largos tiempos de análisis) para alcanzar nuevos sistemas miniaturizados y económicos capaces de satisfacer los requerimientos actuales. Esta evolución ha dado lugar a la aparición de los conocidos sistemas de tipo Lab on a Chip (LOC) y los microsistemas de análisis total (μ TAS), integrando, estos últimos, todas las etapas del procedimiento analítico en una misma plataforma microfluídica. Este alto nivel de integración y miniaturización ha sido posible gracias a la existencia de un conjunto de elementos microfluídicos que permiten realizar las operaciones fluidicas necesarias para una aplicación dada.

En este contexto, la presente tesis pretende ampliar el alcance de las aplicaciones de los μ TAS, así como contribuir al conjunto de elementos microfluídicos existente actualmente. La tesis recoge el desarrollo de tres sistemas microfluídicos que se han aplicado a la cuantificación de diversos analitos de interés en el vino y el desarrollo de una nueva válvula para plataformas microfluídicas centrífugas. Debido a sus excepcionales propiedades, se ha escogido el copolímero de olefina cíclica (COC) como sustrato para la construcción de los sistemas mencionados.

Primeramente, se presenta el desarrollo de un sistema miniaturizado, económico e automatizado para la determinación espectrofotométrica de la acidez titulable en vinos. El sistema desarrollado permite la cuantificación de la acidez en muestras individuales, así como la monitorización de ésta durante los procesos de vinificación. El microsistema se ha optimizado para ambos casos, priorizando, en el primero, un alto rendimiento y un mínimo consumo de muestra y reactivos y, en el segundo, una elevada robustez y la completa automatización del sistema. El mismo microanalizador se ha empleado exitosamente para determinar el contenido de nitrógeno amínico primario (PAN) en vinos, haciendo mínimos cambios en el sistema y demostrando así su gran versatilidad. Los resultados obtenidos confirman un excelente funcionamiento del sistema para las tres aplicaciones estudiadas.

Se presenta, también, el desarrollo de un sistema microfluídico centrífugo para el análisis enzimático y en paralelo de diversos analitos de interés en vinos. El ácido L-láctico, el analito seleccionado como prueba de concepto, se ha cuantificado mediante un método de adición estándar "on-chip". Para ello se ha implementado una estructura de alicuotado doble que permite dividir una muestra de vino y un volumen dado de

disolución patrón en distintos sub-volúmenes. Esta plataforma está todavía en etapa de desarrollo. No obstante, se han obtenido ya resultados muy prometedores.

Finalmente, se describe el desarrollo de una nueva válvula para plataformas de microfluídica centrífuga, el funcionamiento de la cual está basado en la deformación de un disco de polidimetilsiloxano (PDMS) debido a la presión que ejercen dos pequeños imanes, uno a cada lado de la válvula, sobre éste. A bajas revoluciones, la presión deforma el disco bloqueando la conexión entre dos canales. A velocidades de rotación superiores, uno de los imanes se desplaza a consecuencia del incremento de la fuerza centrífuga, liberando la presión sobre el disco y permitiendo, así, el paso del líquido. Aparte de ser fácil de construir e integrar, esta válvula es reversible, permitiendo así una gestión de fluidos altamente flexible y sofisticada.

Los resultados presentados en esta tesis manifiestan las ventajas del uso de sistemas miniaturizados para aplicaciones analíticas, así como el potencial de usar COC como sustrato para sistemas de tipo LOC. Además, los métodos de fabricación empleados son potencialmente extrapolables a la producción en masa, requerimiento esencial para la viabilidad comercial de este tipo de sistemas.

Contents

Financial support	v
Acknowledgements	ix
Abstract	xi
Resum	xiii
Contents	xv
List of Figures	xix
List of Tables	xxix
1 General introduction	1
1.1 Analytical chemistry - Towards miniaturisation	1
1.2 Miniaturisation and Microfluidics	3
1.2.1 Theoretical aspects	4
1.2.2 Microfluidic platforms - Classification	8
1.2.2.1 Pressure driven systems	8
1.2.2.2 Centrifugal microfluidic systems	12
1.3 Microfabrication technologies and materials	16
1.3.1 Silicon and glass	16
1.3.2 Low Temperature Co-fired Ceramics	18
1.3.3 Polymers	18
1.3.3.1 PDMS	21
1.3.3.2 COP/COC	23
1.3.4 Other materials	24
1.4 Microfluidics impact in the “real world”	24
1.5 Molecular absorption spectroscopy	25
1.6 Overview of the dissertation	26
2 Objectives	43

3	Microfabrication methodology	45
3.1	COC as the substrate material	45
3.2	Fabrication process of COC devices	47
3.2.1	Design	48
3.2.2	Microstructuring	50
3.2.2.1	Micromilling	50
3.2.2.2	Hot embossing	51
3.2.2.3	Laser ablation	54
3.2.3	Bonding	55
3.2.4	Additional back-end processes	58
4	Analytical microsystem for the spectrophotometric determination of titratable acidity in wine samples	63
4.1	Organic acids and acidity of wines	63
4.1.1	Titratable acidity in wines	64
4.2	Development of an analytical microsystem for the determination of titratable acidity in must and wine samples	66
4.2.1	Methods	66
4.2.1.1	Reagents and solutions	66
4.2.1.2	Materials	67
4.2.1.3	Experimental setup	67
4.2.1.4	Flow manifold	69
4.2.1.5	Microanalyser design and construction	71
4.2.2	Results and discussion	72
4.2.2.1	Optimisation of the hydrodynamic and chemical conditions	72
4.2.2.2	Wine model solution	81
4.2.2.3	Analytical characterisation of the microsystem	82
4.2.2.4	Real sample analysis	84
4.3	Adaptation of the microsystem for its application to the continuous monitoring of titratable acidity during wine-making processes	86
4.3.1	Methods	86
4.3.1.1	Reagents and solutions	86
4.3.1.2	Materials	87
4.3.1.3	Experimental setup	87
4.3.1.4	Flow manifold	87
4.3.2	Results and discussion	88
4.3.2.1	Optimisation of the hydrodynamic and chemical conditions	88
4.3.2.2	Analytical characterisation of the microsystem	110
4.3.2.3	Real sample analysis	112
4.4	Conclusions & future remarks	114

5	Analytical microsystem for the spectrophotometric determination of Primary Amino Nitrogen in must and wine samples	121
5.1	Nitrogen compounds in wine	121
5.1.1	Alcoholic fermentation and Yeast Assimilable Nitrogen	122
5.1.2	YAN measurement in wine	124
5.2	Development of an analytical microsystem for the spectrophotometric determination of Primary Amino Nitrogen in wine samples	126
5.2.1	Methods	126
5.2.1.1	Reagents and solutions	126
5.2.1.2	Materials	127
5.2.1.3	Experimental setup	127
5.2.1.4	Flow manifold	128
5.2.1.5	Microanalyser design and construction	129
5.2.2	Results and discussion	129
5.2.2.1	Optimisation of the hydrodynamic and chemical conditions	129
5.2.2.2	Analytical characterisation of the microsystem	141
5.2.2.3	Real sample analysis	143
5.3	Conclusions & future remarks	146
6	Novel centrifugo-magnetically actuated valve for centrifugal microfluidic systems	153
6.1	Valving in centrifugal microfluidic systems	153
6.1.1	Passive valving	153
6.1.2	Active valving	155
6.1.3	The need for new valving systems	158
6.1.4	Development of a novel active valving system for centrifugal microfluidic platforms	158
6.2	Materials & methods	159
6.2.1	Materials	159
6.2.2	Experimental setup	160
6.3	Principle of operation	160
6.4	Optimisation of the valve design	162
6.4.1	All-COC prototypes	165
6.4.1.1	Construction process of all-COC valves	166
6.4.1.2	Performance of the all-COC valves	169
6.4.2	Prototypes integrating PDMS discs	173
6.4.2.1	Construction process of prototypes integrating PDMS discs	173
6.4.2.2	Performance of the valves integrating PDMS discs	174
6.4.3	Final prototype	176
6.4.3.1	Construction process of the final valve prototype	176
6.4.3.2	Performance of the final valve prototype	176

6.5	Conclusions & future remarks	178
7	Centrifugal microfluiding system for the implementation of enzyme-based analyses in wine with spectrophotometric detection	187
7.1	Enzyme-based analyses in wine	187
7.2	Parallelisation in centrifugal microfluidic platforms	190
7.3	Lactic acid as the proof-of-concept analyte	191
7.3.1	Lactic acid and the malo-lactic fermentation of wine	192
7.3.2	L-lactic acid enzymatic determination	193
7.4	Development of a centrifugal microfluidic system for the enzymatic determination of L-lactic acid in wine samples using spectrophotometric detection	194
7.4.1	Methods	194
7.4.1.1	Reagents and solutions	194
7.4.1.2	Materials	195
7.4.1.3	Experimental setup	195
7.5	Modular centrifugal microfluidic platform	198
7.5.1	Design and principle of operation	199
7.5.2	Construction	203
7.6	Implementation of the L-lactic acid enzymatic determination into the developed centrifugal microfluidic platforms	204
7.7	Conclusions & future remarks	223
8	Concluding remarks & future challenges	229

List of Figures

1.1	The automation and integration of all steps of the analytical process gave rise to the well-known TAS. μ TAS were the result of the TAS miniaturisation.	2
1.2	The “Lab on a Chip” concept. Several “lab” functionalities can be implemented in a single microfluidic platform.	3
1.3	Example of the effect of downscaling a system on the surface area (S), the volume (V) and the surface area to volume ratio (S/V).	5
1.4	Illustration of the laminar flow regime at the microscale and the turbulent flow regime at the macroscale.	6
1.5	Example of laminar flow and diffusive mixing for two fluids (X and Y) which meet at a T-junction point. Diffusion is responsible for the mixing of fluids at the microscale due to the laminar flow regime.	7
1.6	Some examples of macro-to-micro interfaces: a) a magnetic connector; b) a pin header connector; c) a solder-based connection; and d) an interconnect using Parylene-C. Parylene-C is deposited in the space delimited in red from the second illustration in (d). Images adapted from the respective references.	11
1.7	Three examples of passive micromixers: a) staggered herringbone micromixer, b) 2D serpentine micromixer and c) 3D serpentine micromixer. Redrawn from reference.	12
1.8	Some examples of commercially available centrifugal systems for POC diagnostics: a) Piccolo Xpress by Abaxis (Union City, CA, USA); b) Spinit by Biosurfit (Azambuja, Portugal); c) Revogene by GenePOC (Québec, Canada); d) Cobas b 101 by Roche Diagnostics (Indianapolis, IN, USA); e) LABGEO IB10 by Samsung Healthcare (Seoul, South Korea); and f) Gyrolab xPlore by Gyros Protein Technologies (Uppsala, Sweden). Images adapted from their respective websites.	14
1.9	Pseudo forces acting on a particle inside a spinning disc: the centrifugal force (F_ω), the Coriolis force (F_C) and the Euler force (F_E). F_E can act in both directions depending on the acceleration to which the platform is subjected (which can be either positive or negative). Capital letter F has been used to represent force (instead of force density f).	15

1.10	Schematic representation of basic (a) photolithographic and (b) etching processes. In this example, a positive photoresist is used and, therefore, the areas which are dissolved are the ones previously exposed to light. When a negative photoresist is used, the unexposed areas are the ones which are dissolved. The etching process removes material only from the areas where there is no photoresist.	17
1.11	Top (a), bottom (b) and inner (c) view of an LTCC microreactor for the synthesis of superparamagnetic iron oxide nanoparticles (SPION). The device contained a monolithically integrated gold resistor which was used as a heater. The top side (a) of the microreactor included the fluidic inlets and outlets while the bottom side (b) contained the contact pads for the gold resistor (c) and a temperature sensor. The internal fluidic system is not shown.	19
1.12	PDMS casting.	22
3.1	Reaction scheme for the production of TOPAS. The norbornene and ethylene proportion in the final product (m, n) define the grade of the polymer.	47
3.2	General fabrication process of COC microfluidic devices. Back-end processing may include other steps that are not depicted in this figure for the better understanding of the scheme.	48
3.3	Multilayer approach for the construction of a micromixer. The different layers that will constitute the final structure, a top layer containing the inlet and outlet holes (I), a middle layer containing the main structure (II) and a bottom layer for sealing the device (III), are individually designed. The two possible design strategies are here represented: a) “what you see is what you get” approach, where the equipment software will choose the appropriate microstructuring parameters and tools to create the drawn design; and b) toolpath design approach, where the user is in charge of choosing the microstructuring parameters and tools. In this example, the two designs are equivalent for a 0.8 mm diameter milling tool selection for the toolpath design strategy. The stacking of the different microstructured layers (c) will create the final 3D structure containing the micromixer (d).	49
3.4	Different types of milling tools and their corresponding cut profiles. b) Parameters defining a milling tool.	51
3.5	LTCC master construction and engraving of the master features onto a COC layer.	52
3.6	a) Temperature profile of the sintering process. b) During the second plateau of the sintering process, at 850 ° C, the glass particles melt and cover the alumina particles.	53

3.7	Microscope images of the laser ablated TOPAS layers using the CO ₂ laser K-1030 HPD UHS from Macsa ID. Bulges (a-d), bubbles (b-d) and fractures (b), in addition to incomplete and irregular (c, d) cut profiles can be noticed.	55
3.8	A bonding step of TOPAS 8007 layers (light blue) with structural TOPAS layers (dark blue) before the micromachining process reduces the overall complexity of the construction process by reducing the required micromachining steps. As an example, for a device with three structural layers, this previous step would reduce the micromilling steps from five (a) to three (b).	57
3.9	Bonding setup. Aluminium blocks containing fiducial pins guarantee the correct alignment of the layers; silicone layers ensure homogeneous pressure; polymeric sacrificial plaques avoid the bending of structural layers in devices with high aspect ratio structures; and polymeric foils prevent the sticking of the device to the sacrificial plaques.	59
4.1	Schematic illustration of the experimental setup. PP: peristaltic pump; W: waste.	68
4.2	Insertion structure of the optical detection system based on a lock and key concept. The several PMMA layers that constitute the structure are used for: fixing the LED (a) and the photodiode (e), eliminating the unwanted light emitted by the LED (b), defining the desired sensing area of the photodiode (d) and inserting the microanalyser (c). Four bolts secure the structure.	69
4.3	Construction scheme of the microanalyser and photograph of the final device including the fluidic connections.	70
4.4	Detection chamber design. The arrows indicate the flow direction. . . .	72
4.5	Acid-base equilibrium of BTB.	73
4.6	a) Absorbance spectra of BTB solutions in the pH range from 4.5 to 10.5. b) Linear range for the monitoring of the blue coloration decrease at 616 nm.	74
4.7	Signal record for an injection volume of 7.5 μ L of (a) 0.02 g/L, (b) 0.04 g/L, (c) 0.08 g/L, (d) 0.12 g/L and (e) 0.16 g/L tartaric acid standard solutions. No height differences were found for concentrations over 0.08 g/L (c, d, e).	76
4.8	Influence of the phosphate buffer concentration in the absorbance peak height. a) Representation of the results. b) Linear regression parameters.	77
4.9	Flow rate optimisation. a) Representation of the results. b) Linear regression parameters.	78
4.10	Influence of an increment in the indicator solution pH. a) Representation of the results. b) Linear regression parameters.	79

4.11	Optimisation of the BTB and the phosphate buffer concentrations. Influence of the BTB concentration: a) representation of the results; b) linear regression parameters. Influence of the phosphate buffer concentration: c) representation of the results; d) linear regression parameters.	80
4.12	Calibration curves for tartaric acid standard solutions prepared in a 25-fold diluted WMS or in deionised water. a) Representation of the results. b) Linear regression parameters.	82
4.13	Recorded signal (a) and calibration curve (b) for one of the experiments using the optimised conditions. Standard solutions: (a) 0.005 g/L, (b) 0.010 g/L, (c) 0.025 g/L, (d) 0.050 g/L, (e) 0.100 g/L, (f) 0.200 g/L, (g) 0.300 g/L and (h) 0.400 g/L tartaric acid.	83
4.14	Comparison of the titratable acidity (TA) results obtained by the reference and the developed methods. Error bars correspond to the confidence interval of the results.	85
4.15	Schematic illustration of the experimental setup. PP: peristaltic pump; W: waste; V: valve.	88
4.16	Evolution of the absorbance at 621 nm and the pH of several buffered BTB solutions during 10 days when stored open (O) (a, b) or closed (C) (c, d).	89
4.17	The same concentration of the indicator solution is obtained when the solution enters through two of the channels (a) and when it enters through one channel but it has twice the buffer and BTB content (b).	91
4.18	Optimisation of the BTB and the phosphate buffer concentrations of the indicator solution. a) Representation of the results. b) Linear regression parameters.	92
4.19	Injection volume optimisation. a) Representation of the results. b) Linear regression parameters.	93
4.20	Operation sequence of the valves for both calibration and sample analysis. V_1 and V_2 are in charge of the dilution of the stock standard solution and the sample, respectively; V_3 is used for discarding waste solutions before entering the microanalyser. The times here represented for each step are for guidance purposes only.	96
4.21	First calibration using the multicommutated flow system. a) Recorded signal. b) Representation of the results. c) Linear regression parameters. The height of the peaks was calculated by considering a common constant baseline.	97

4.22	Effect of reducing the length and the diameter of the tubing. a) Representation of the results. b) Comparison of the peak height and the baseline noise of the recorded signal. The plotted peaks correspond to the same standard solution for both cases: two peaks of a 0.04 g/L tartaric acid solution and one peak of a 0.08 g/L tartaric acid solution. An arbitrary intercept has been used for better comprehension of the representation. c) Linear regression parameters.	99
4.23	Influence of the flow rate in the repeatability of the peaks. a) Representation of the results. b) Linear regression parameters. c) RSD values of the peaks obtained for the two flow rates.	100
4.24	Influence of the minimum commutation speed in the repeatability of the peaks and the linearity of the calibration curve. Representation of the results for injection times of: 8.0 s (a, b), 9.6 s (c, d) and 11.2 s (e,f). g) Linear regression parameters.	102
4.25	Injection time optimisation. a) Representation of the results. b) Linear regression parameters.	103
4.26	Sensibility of the calibration curves against the injection time.	104
4.27	Effect of interchanging the roles of V_1 and V_2 valves. a) Representation of the results. b) Linear regression parameters.	105
4.28	Effect of the minimum commutation speed for a 25-fold dilution of the sample. a) Recorded signal for the different commutation cycles. An arbitrary intercept has been used for clearer illustration. b) Experimental parameters and obtained results.	108
4.29	BTB and phosphate buffer concentration optimisation. a) Representation of the results. b) Linear regression parameters.	110
4.30	Recorded signal (I) and calibration curve (II) for one of the experiments using the optimal conditions. Standard solutions: (a) 0.05 g/L, (b) 0.10 g/L, (c) 0.20 g/L, (d) 0.30 g/L and (e) 0.40 g/L tartaric acid.	111
4.31	Introduction of a fourth valve (V_4) for the measurement of the blank.	114
5.1	Transformation of sugars into ethanol and carbon dioxide during the alcoholic fermentation of wine.	122
5.2	Classification of nitrogen-containing compounds in wine.	123
5.3	Schematic illustration of the experimental setup. PP: peristaltic pump; W: waste; V: solenoid valve.	128
5.4	NOPA assay reaction.	129
5.5	Schematic illustration of the flow manifold used during the optimisation of the variables. PP: peristaltic pump; W: waste.	131
5.6	Flow rate optimisation. a) Representation of the results. b) Linear regression parameters.	132
5.7	NOPA reagent solution pH optimisation. a) Representation of the results. b) Linear regression parameters.	133

5.8	Borate buffer optimisation. a) Representation of the results. b) Linear regression parameters.	134
5.9	Optimisation of the OPA and NAC concentrations of the NOPA reagent solution. a) Representation of the results. b) Linear regression parameters.	135
5.10	Effect of varying the NAC concentration of the NOPA reagent solution. a) Representation of the results. b) Linear regression parameters.	137
5.11	Effect of varying the OPA concentration of the NOPA reagent solution. a) Representation of the results. b) Linear regression parameters.	138
5.12	Fluidic schemes for: (a) the introduction of a previously prepared NOPA reagent solution and (b) the in-line preparation of the reagent using separate OPA and NAC solutions. OPA and NAC concentrations are equivalent for both configurations (all channel dimensions and flow rates per channel are equal).	139
5.13	Effect of preparing the NOPA reagent solution in-line. a) Representation of the results. b) Linear regression parameters.	140
5.14	Recorded signal (I) for the first replicate from Table 5.2 and calibration curves (II) for all three replicates using the optimal conditions. Standard solutions: (a) 0.5 mM, (b) 2.5 mM, (c) 5.0 mM, (d) 7.5 mM, (e) 10.0 mM, (f) 12.5 mM, (g) 15.0 mM, (h) 17.5 mM and (i) 20.0 mM.	142
5.15	Schematic illustration of the flow manifold used for the analysis of real samples. PP: peristaltic pump; W: waste; V: solenoid valve.	143
5.16	Measurement of the absorbance of a sample (A_S) and its corresponding blank (A_B). Firstly, the absorbance of the sample is measured using a blank reagent solution (without OPA). Then, the blank reagent solution is automatically substituted by the NOPA reagent solution. The baseline shifts upwards and, once it stabilises, the sample is injected again. A_B is subtracted from A_S	144
5.17	Comparison of the PAN content obtained by using the commercial kit and the developed microsystem. Error bars correspond to the confidence interval of the results.	145
6.1	Schematic representation of the most commonly used passive valving systems: (a) capillary valving, (b) hydrophobic valving, (c) dissolvable-film valving, (d) centrifugo-pneumatic over-pressure valving, (e) centrifugo-pneumatic under-pressure valving and (f) siphon valving.	155
6.2	Two examples of temperature actuated valving systems. a) Sequential actuation of optofluidic valves based on the piercing of a plastic thin film by a laser beam. Adapted from reference. b) Principle of operation of “normally closed” (NC) and “normally open” (NO) laser-irradiated ferrowax microvalves (LIFM). AVC: Assistant valve chamber; LD: Laser diode. Adapted from reference.	156
6.3	Magnetically-actuated valve based on the use of a flyball governor. a) Schematic diagram of the valve system. b) Exploded view of the assembly.	157

6.4	Valving principle of the developed valve. Rotational frequency is represented by ω .	159
6.5	Schematic (I) and actual (II) experimental setup for the evaluation of the valve actuation: support platform (a) and rotatory actuator, including a motor (b), an encoder (c), a positioning controller (d), a power supply (e) and a PC (e). The motor, the encoder and the positioning controller were mounted onto a polymeric perforated base.	161
6.6	Support platform layers. Top and bottom layers impeded the ejection of the devices during the rotation of the platform. The different layers were assembled together by the four outer bolts; the four central ones secured the platform to the aluminium shaft adapter.	162
6.7	Principle of operation of the developed valving system. a) Closed state, where the magnetic force (F_m) is higher than the centrifugal force (F_c). b) Open state, where F_c is higher than F_m . Closed and open states are reversible and can be controlled by changing the rotational frequency (ω) applied to the platform.	163
6.8	Schematic representation of a device placed into the support platform.	164
6.9	Principle of operation of the all-COC valving system. a) Closed state, where the magnetic force (F_m) is higher than the centrifugal force (F_c). b) Open state, where F_c is higher than F_m .	165
6.10	Scheme of the first prototypes developed. TOPAS 8007 bonding layers and TOPAS 5013/6015 structural layers are depicted in dark and light blue, respectively.	166
6.11	Use of a Delrin sacrificial layer for minimising pressure onto the valving area during the bonding of the membrane layer (B) to the previously bonded block (C+D).	167
6.12	Bonding results for some of the tested conditions. a) Poor sealing of the device (see upper part of the image) due to low temperature ($T_{max} = 85 \text{ }^\circ\text{C}$) in spite of high pressure ($P_{max} = 8 \text{ bar}$), along with a partial bonding of the membrane layer in the valving zone. b) Almost total bonding of the membrane layer as a consequence of high temperature ($T_{max} = 105 \text{ }^\circ\text{C}$) even though low pressure was applied ($P_{max} = 3 \text{ bar}$). c) Perfectly defined valving area using the optimised conditions ($T_{max} = 95 \text{ }^\circ\text{C}$ and $P_{max} = 4 \text{ bar}$).	168
6.13	Examples of the low reproducibility of the bonding processes: a, b) partial bonding of the membrane layer in the valving area despite using the optimised conditions; c, d) different degrees of the undesired membrane sealing as a result of the final bonding step for the integration of the magnet layers.	169

6.14	Real and schematic top view of the two valve designs: a) with a higher area and b) with a reduced area through which liquid could reach the valve. These areas are highlighted in red in the schematic view. Channel ends were at 0.5 mm and 1.8 mm distance for designs (a) and (b), respectively. For both designs, the 5 mm diameter valving zone was completely covered by the 6 mm diameter magnet.	171
6.15	Scheme of the second valve design prototypes. The extra 400 μm thick layer required for these prototypes is framed in red.	172
6.16	Placement of a PDMS disc under the top magnet for achieving a homogeneous pressure onto the valving area.	173
6.17	Layers of the prototypes integrating a PDMS disc inside the valve.	174
6.18	Internal structure of the final valve design: (a) schematic view (not at scale) and (b) real microscopic image.	175
6.19	Layers of the final prototypes, where the adhesive plate seal was substituted by a 150 μm thick TOPAS 6015 layer.	177
6.20	Real images of the final prototype. I) The different layers to be assembled inside the support: a) top magnet layer, b) fluidic block and c) bottom magnet layer. II) The assembled valving prototype containing the magnets.	178
7.1	a) Reduced structure of NADH and NADPH coenzymes. b) Redox reaction of the coenzymes.	188
7.2	Enzymatic methods based on NADH and NADPH coenzymes for the spectrophotometric determination of several wine parameters: (a) reaction schemes and (b) the corresponding calibration curves.	189
7.3	Example of a modular centrifugal platform. The platform integrates four different devices, each of them containing an aliquoting structure.	190
7.4	Commonly used two-stage aliquoting strategies: a) continuous zig-zag shaped metering channel and b) interconnected metering chambers. In (a): (I) loading of the metering structures and (II, III) sequential transfer of the metered liquids. In (b): (I) injection, (II) distribution, (III) metering and (IV) transfer of the metered sub-volumes.	192
7.5	General reaction of the transformation of L-malic acid to L-lactic acid during the malolactic fermentation.	193
7.6	Enzymatic reactions involved in the quantification of L-lactic acid.	194

7.7	Schematic (I) and actual (II) experimental setup for the L-lactic acid determination. In (II): support platform (a); rotatory actuator, including a motor (b), an encoder (c), a positioning controller (d) and a power supply (e); and optical detection system, composed of a LED (f) and a photodiode (g) mounted into a polymeric support (h), a PCB (i) and a DAQ (j). The positioning controller of the rotatory actuator and the DAQ of the optical detection system were connected to a PC (k). The rotatory actuator and the optical detection system (with exception of the power supply and the DAQ, respectively) were fixed onto a polymeric perforated base.	196
7.8	a) Support platform layers. The different layers were assembled together using several bolts and magnets; the four internal bolts secured the platform to the aluminium shaft adapter. b) PMMA structure of the optical detection system. The LED was embedded inside the top layers, whereas the photodiode was fixed into the bottom layers. The central layers permitted the free rotation of the support platform between the LED and the photodiode. Several bolts assembled the different layers and secured the structure to the setup.	198
7.9	Schematic representation of the developed modules: a) 2D view and b) 3D view. To obtain a clear representation, some details of the receiving chambers have been omitted in the 3D view.	200
7.10	Microscopic image of the microchannels being used as hydrophobic valves.	201
7.11	Two-stage aliquoting process. A first metering phase is carried out at a rotational frequency ω_m below the burst frequency of the hydrophobic valves (ω_b). The final transfer phase is carried out at a rotational frequency ω_t above ω_b . The different sample (pink) and standard (blue) aliquoted volumes produce a gradual decrease in the analyte concentration at the final volume (purple).	201
7.12	Fabrication scheme of the developed devices. TOPAS 8007 bonding layers and TOPAS 6013 structural layers are represented in grey and blue, respectively.	202
7.13	Linear working range for the absorbance measurement of NADH solutions at 340 nm using the developed setup. Error bars represent the standard deviation of two replicate measurements.	205
7.14	Linear working range of the L-lactic acid determination using the kit reagents and the developed setup. The L-lactic acid concentration here represented corresponds to the analyte concentration at the final volume. Error bars represent the standard deviation of two replicate measurements.	207

7.15 Standard addition calibration plots for the six on-chip L-lactic acid enzymatic determinations. The concentration of the standard solution added to the sample was 1.00 mM for replicates (a) to (e) and 0.50 mM for replicate (f).	211
7.16 Microscopic image of two microchannels. The one in the left is completely clogged, whereas the one in the right is properly sealed.	213
7.17 On-chip standard addition calibration for the determination of the L-lactic acid content of a commercial wine sample.	217
7.18 Calibration for the determination of the L-lactic acid content of a commercial wine sample using the procedure described by the kit manufacturer.	217
7.19 New design of the modules for increasing the precision of the method and minimising the effect of the matrix dilution.	218
7.20 Standard addition calibration plots for the eight on-chip L-lactic acid enzymatic determinations using the new prototypes. The concentration of the standard solution added to the sample was 3.00 mM for replicates (a) to (f) and 2.00 mM for replicates (g) and (h). Error bars represent the standard deviation ($n = 3$).	221
7.21 Latest developed prototypes for the L-lactic acid enzymatic determination.	222

List of Tables

1.1	Summary of some properties of interest of the most commonly used polymer materials. The qualitative metrics shown in this chart are provided only as a general guide. Particularly, solvent resistance can be highly dependent upon the solvent type.	20
3.1	Thermal properties of TOPAS grades. TOPAS extruded layers are available in several thicknesses; purchased layers are here indicated.	47
4.1	Characteristics of the main organic acids in wine.	64
4.2	Main characteristics of the tested LEDs.	74
4.3	Optimisation of variables.	81
4.4	Analytical characterisation of the microsystem. Linear regression parameters and limits of detection (LOD) and quantification (LOQ) for the four calibration experiments using the optimal conditions. LOD and LOQ were calculated as 3 times and 10 times the standard deviation of the baseline, respectively.	84
4.5	Titrateable acidity of eleven wine samples determined by the reference method and the developed method.	85
4.6	Reduction of the working range as a result of a decrease in the pH.	90
4.7	Diluted standard solutions obtained from a stock standard solution (stock ss) of 0.40 g/L tartaric acid for an injection time of 10 s. The actuation of the valve for a 25-fold dilution of the sample is also included.	95
4.8	Actuation of the valves for a minimum commutation speed of 0.1 s and 0.2 s for preparing standard solutions of 0.05 g/L, 0.10 g/L, 0.20 g/L and 0.30 g/L tartaric acid from a 0.40 g/L tartaric acid stock solution.	101
4.9	Interpolated concentration of a synthetic sample of 5 g/L tartaric acid. The sample was injected in triplicate for each experiment.	104
4.10	Interpolated concentration of a synthetic sample of 5 g/L tartaric acid. The sample was injected in triplicate for each commutation speed.	105
4.11	Average peak height and RSD for 10 injections of a 0.20 g/L tartaric acid solution carried out by V_1 and V_2	106

4.12	Programming of the actuation of V_1 for obtaining diluted solutions of 0.05 g/L to 0.40 g/L from a stock solution of 0.50 g/L tartaric acid for 40.0 s injection time and 20 commutation cycles per dilution.	107
4.13	Analytical characterisation of the microsystem. Linear regression parameters, LOD and LOQ for three calibration experiments. LOD and LOQ were calculated as 3 times and 10 times the standard deviation of the baseline, respectively.	112
4.14	Results for the titratable acidity determination of twenty-five wine samples obtained by BioSystems and by the system here presented. No confidence interval was given for the BioSystems results.	113
4.15	Effect of the colour correction for some of the analysed samples.	114
5.1	Optimisation of variables.	141
5.2	Analytical characterisation of the microsystem. Linear regression parameters and limits of detection (LOD) and quantification (LOQ) for three calibration experiments. LOD and LOQ were calculated as 3 times and 10 times the standard deviation of the baseline.	141
5.3	Results for the PAN determination of six wine samples obtained by using the BioSystems kit and the microsystem presented in this chapter.	145
6.1	Optimisation of the construction process for the all-COC valving prototypes.	168
7.1	L-lactic acid (L-lactate) assay kit K-LATE 07/14 (Megazyme) reagents and recommended procedure.	206
7.2	Measured volumes for the aliquoting of water by using the equal volume and the variable volume aliquoting subsystems. Volumes correspond to the average value of five experiment replicates.	209
7.3	Volumes and concentrations used for the on-chip standard addition calibrations. L-lactic acid concentrations at the final volume are also indicated for the two standard solutions used.	210
7.4	Linear regression parameters of the calibration plots from Figure 7.15 and the corresponding extrapolated concentrations of L-lactic acid.	210
7.5	Linear regression parameters and calculated L-lactic acid concentration for the two different procedures.	216
7.6	Measured volumes for the aliquoting of water by using the equal volume and the variable volume aliquoting subsystems. Volumes correspond to the average value of three experiment replicates.	219
7.7	Volumes and concentrations used for the on-chip standard addition calibrations using the new prototypes. L-lactic acid concentrations at the final volume are also indicated for the two standard solutions used.	219
7.8	Linear regression parameters of the calibration plots from Figure 7.20 and the corresponding extrapolated concentrations of L-lactic acid.	220

Chapter 1

General introduction

1.1 Analytical chemistry - Towards miniaturisation

Analytical chemistry can be described as the metrological science that develops, optimises and applies methodologies, strategies and instrumentation for obtaining quality spatio-temporal information of biological, chemical and biochemical systems.¹⁻³ Although it has been frequently considered as a chemical sub-discipline,⁴ some authors prefer to define analytical chemistry as an interdisciplinary yet individual science^{3,5-7} in order to give it its well-merited relevance. Analytical chemistry, which at the beginning was mainly focused on obtaining information about chemical systems, has nowadays a strong impact in almost all existing scientific, technologic and social areas, including biology, biotechnology, medicine, environmental sciences and industry, among many others.^{8,9}

During the last few decades, analytical chemistry has experienced an enormous evolution in order to meet the increased demand of information as well as to fulfill the new analytical requirements, which include lower detection and quantification limits, lower reagent consumption, higher portability, higher automation and shorter analysis times. Consequently, analytical chemistry has moved from versatile yet complex classical instrumental techniques, which were very powerful tools but did not cover the current on-time and in-situ information needs, to new miniaturised instrumental techniques which are able to solve some of the classical instrumentation challenges.

The analytical process comprises the series of operations that have to be performed for obtaining the desired information from a concrete system and it can be divided into three different steps: the preliminary operations (e.g. sampling, sample transport, analyte separation, preconcentration and derivatisation, etc.), the measurement and transduction of the analytical signal and the data acquisition and processing.^{10,11} The integration and automation of all these steps in a single system led to the well-known Total Analysis Systems (TAS).¹² These systems reduced the complexity of the process and the analysis time and gave traceability, reproducibility and exactitude to the measurements. However, TAS were noticeably bulky, involved dealing with considerable

amounts of samples, reagents and waste, and required the fabrication of interfaces between the distinct components.^{13–15}

The latest revolution of analytical chemistry came with the miniaturisation of TAS, giving rise to the popular Micro Total Analysis Systems (μ TAS). Although the first investigations on integrated, automated and miniaturised analytical systems date from the seventies,¹⁶ it was not until 1990 when the μ TAS concept was firstly introduced by Manz et al.¹⁷ The advantages of miniaturising TAS were already outlined and included shorter analysis times, reduced reagent and sample consumption, minimised production of waste and higher portability.^{13,17} Since that moment, thousands of articles have been published about the miniaturisation of analytical systems, giving rise to new concepts such as the widespread “Lab on a Chip” (LOC).

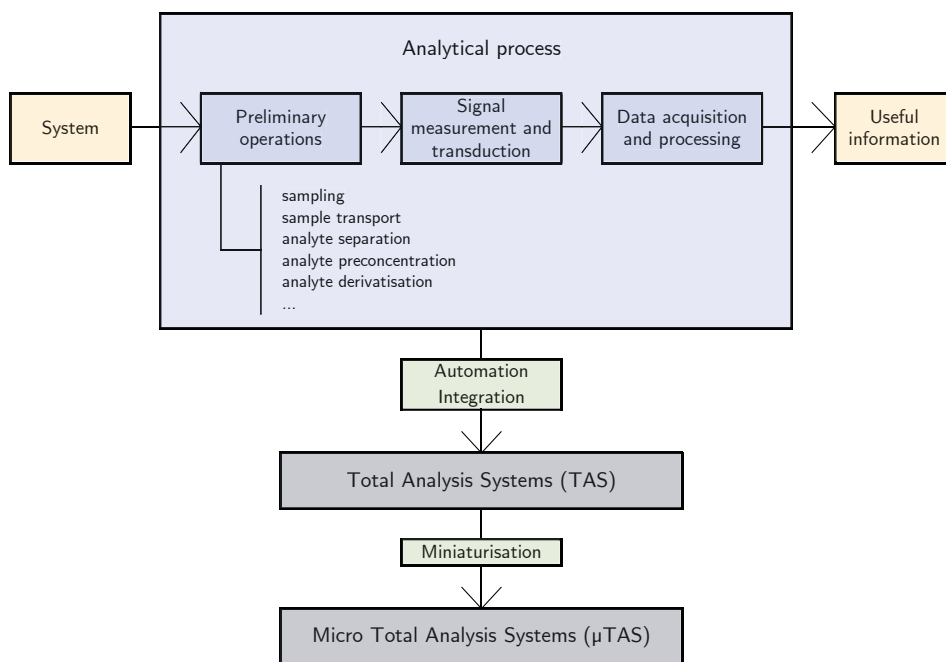


Figure 1.1: The automation and integration of all steps of the analytical process gave rise to the well-known TAS. μ TAS were the result of the TAS miniaturisation.

μ TAS and LOC have been frequently used as synonyms. Nonetheless, μ TAS are miniaturised, automated and integrated systems dedicated to analysis, whereas the LOC concept covers a wider spectrum of systems which are not exclusively focused on analytical purposes.^{18,19} A large number of LOC devices have been developed for many

other applications such as synthesis,^{20–22} drug delivery^{23–25} and the study of in-vitro cell culture systems in the frequently referred to as Organ-on-a-Chip^{26–29} devices.



Figure 1.2: The “Lab on a Chip” concept. Several “lab” functionalities can be implemented in a single microfluidic platform.

1.2 Miniaturisation and Microfluidics

Miniaturisation of analytical systems led to the development of a new research field that provided the necessary tools to connect all steps of any analytical procedure. This field, which is known as Microfluidics, copes with the study of the behaviour of fluids at the microscale and includes any experimental and theoretical research related to the development of new miniaturised fluidic systems, including their fabrication and practical application.^{19,30}

Microfluidic platforms are the result of the miniaturisation of fluidic systems and they are conformed by a set of microfluidic elements that are able to perform the basic fluidic unit operations required within a given application.³¹ These elements, which are designed for their easy combination within a well-defined fabrication technology, are the building blocks of microfluidic platforms and they provide a generic and consistent way for the miniaturisation, integration, automation and parallelisation of (bio)chemical processes.³² Some of the basic fluidic unit operations are: fluid transport, metering, valving, mixing, reagent storage and release, and separation and preconcentration of molecules or particles.^{31,32}

A significant part of the research has been focused on the development of new tools for improving the execution of the different fluidic operations and for implementing new fluidic functionalities. A considerable effort has been put into the improvement of the connectivity between the different fluidic elements that are to be combined within a microfluidic platform, as well as into the development of more efficient construction methods for their easier fabrication and integration.

1.2.1 Theoretical aspects

In order to develop functional microfluidic elements and operational miniaturised fluidic devices, we first need to understand the behaviour of fluids at the microscale. At this scale, the physical phenomena that dominate fluids are substantially different from those that dominate at the macroscale. An overview of some of the most relevant effects of downscaling is provided hereunder.

Surface area to volume ratio

The differences in the behaviour of fluids at the microscale compared to the macroscale are related to the dramatic increase in the surface area to volume ratio when a system is downscaled (see [Figure 1.3](#)). For a system with a characteristic dimension l , the basic scaling law for the surface area to volume ratio can be expressed as:³³

$$\frac{\text{Surface area}}{\text{Volume}} = \frac{S}{V} \propto \frac{l^2}{l^3} = l^{-1} \xrightarrow{l \rightarrow 0} \infty \quad (1.1)$$

Equivalently, for surface forces (e.g. surface tension and viscosity) and volume forces (e.g. gravity and inertia):³⁴

$$\frac{\text{Surface forces}}{\text{Volume forces}} \propto \frac{l^2}{l^3} = l^{-1} \xrightarrow{l \rightarrow 0} \infty \quad (1.2)$$

[Equation 1.1](#) and [Equation 1.2](#) evidence the increase in the S/V ratio and the surface forces to volume forces ratio when l decreases. The microscale, where $l \rightarrow 0$, is therefore controlled by surface dependent phenomena, whereas volume dependent phenomena become negligible.

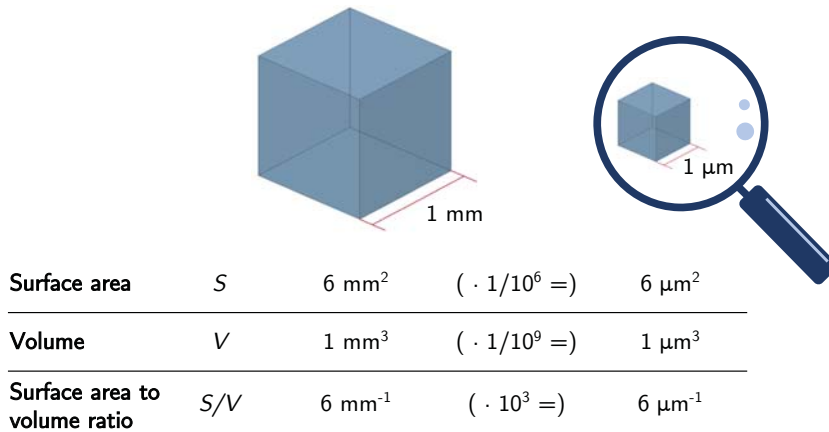


Figure 1.3: Example of the effect of downscaling a system on the surface area (S), the volume (V) and the surface area to volume ratio (S/V).

Laminar flow

In microfluidic channels, mass transport is dominated by viscous forces, whereas inertial forces dominating at the macroscale become negligible. The reduced influence of inertia at the microscopic scale, which is the main reason for the chaotic behaviour of fluids at the macroscale, leads to a laminar flow of fluids rather than the turbulent flow we are used to see in macroscopic channels.³⁵

The Reynolds number (Re) establishes the relationship between the inertial forces and the viscous forces that a fluid of a density ρ and a viscosity η experiments when flowing at a velocity v inside a channel with a hydraulic diameter D_h , and it can be calculated from the following expression:³⁶

$$Re = \frac{\rho v D_h}{\eta} \quad (1.3)$$

The hydraulic diameter of a circular channel corresponds to the channel diameter, whereas for channels presenting other shapes it can be calculated as:³⁶

$$D_h = \frac{4A}{P} \quad (1.4)$$

where A is the cross-sectional area and P is the wetted perimeter (i.e. the total perimeter of all channel walls which are in contact with the liquid).

Re is a dimensionless number which is frequently used to predict the behaviour of a fluid inside a microchannel. At low Re values, typically below 2000, the inertial effects causing turbulence and secondary fluid flows are negligible and viscous effects

dominate the dynamics of the fluid. Conversely, at higher Re values, generally above 3000, the flow becomes turbulent since the inertial effects come to be dominant.³⁷ Owing to the reduced dimensions of the channels, Re is generally in the laminar flow regime for microfluidic systems.^{35,38}

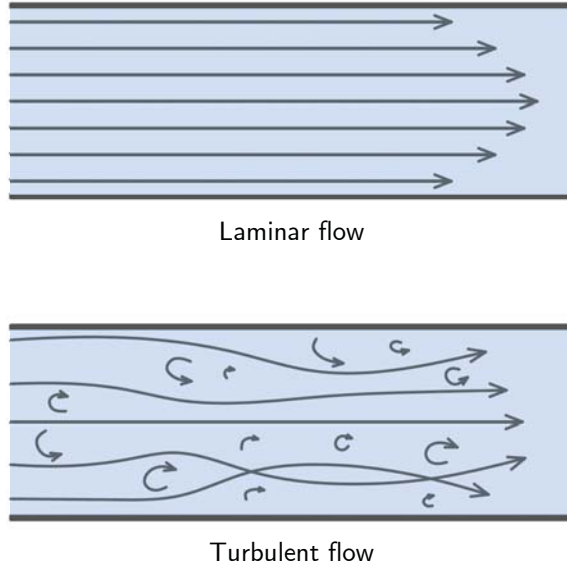


Figure 1.4: Illustration of the laminar flow regime at the microscale and the turbulent flow regime at the macroscale.

Diffusion

As a consequence of the laminar flow regime, convective mixing does not occur at the microscale. Molecular transport is therefore governed by diffusion, which is a less efficient yet higher predictable mixing process.³⁹ Diffusion is the fluidic transport phenomenon resulting from concentration gradients and it is described by Fick's first law, which can be found elsewhere.⁴⁰

The time τ_D it takes for a molecule with a diffusion coefficient D to move a distance l is described as:⁴¹

$$\tau_D = \frac{l^2}{D} \quad (1.5)$$

At the macroscale, diffusion is a slow mixing process since the distances that molecules need to travel are enormous. In contrast, at the microscale, the reduced channel dimensions lead to reduced diffusion times, enabling a relatively effective mixing of fluids via diffusive mixing.

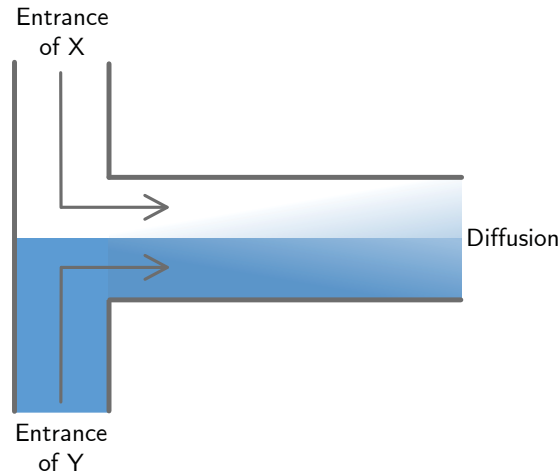


Figure 1.5: Example of laminar flow and diffusive mixing for two fluids (X and Y) which meet at a T-junction point. Diffusion is responsible for the mixing of fluids at the microscale due to the laminar flow regime.

Surface tension and capillarity

Capillarity refers to the ability of a fluid to flow through narrow spaces without the aid of external driving forces.⁴² Capillary motion mainly depends on the surface tension forces, which are the result of two competitive forces at an interface: the cohesive forces between the molecules of a fluid and the adhesion forces between the fluid and the surfaces in contact with it.³⁶ The first ones solely depend on the fluid properties, whereas the second ones depend on both the fluid and the surface properties. Surface tension forces (l^2 dependant) play a major role in the fluid behaviour at the microscale since they become progressively more dominant with the reduction of the system dimensions.

When a narrow circular tube is immersed vertically inside a liquid source, liquid rises (or descends) through the tube as a consequence of the capillary effect. The height h of the liquid column can be described by the following expression:⁴³

$$h = \frac{2\gamma \cos \theta}{\rho g r} \quad (1.6)$$

Where γ corresponds to the liquid-air surface tension, θ is the contact angle of the liquid-air-surface interface, g is the gravitational constant and r is the radius of the channel. Whilst for macroscopic channels h is negligible ($r \rightarrow \infty$, $h \rightarrow 0$), when the dimensions of the channels are reduced to the microscopic scale, h drastically increases ($r \rightarrow 0$, $h \rightarrow \infty$).

Although Equation 1.6 cannot be used to describe capillary motion in horizontal systems, it illustrates the importance of capillary flow at the microscopic scale.

Several other phenomena can be used to describe the behaviour of fluids at the microscale. Nonetheless, due to their minor relevance in the work presented in this dissertation, they have been deliberately omitted. A thorough description of these phenomena can be found elsewhere.^{34,42,43}

Although generally the miniaturisation of a fluidic system cannot be directly performed by scaling it down due to the different behaviour of fluids at the microscale with respect to the macroscale, the microfluidics community has taken advantage of these differences and has used these particular phenomena to develop new applications as well as to achieve new functionalities which were unattainable at the macroscopic scale. Some examples can be found below.

Large surface area to volume ratios are particularly useful in electroosmotic flow,^{44,45} where liquids are dragged along a surface by mobile ions in close proximity to them, and in surface acoustic wave systems,^{46,47} where the reduced volumes compared to the high interfacial areas allow acoustic energy to displace droplets. Surface tension forces have enabled the development of lateral flow tests, where capillary forces are used to transport fluids along porous materials, and electrowetting flow based systems,^{48,49} where droplets are moved by electrically induced changes in the contact angle. The laminar flow and the diffusive mixing dominating at the microscale have been used for the effective separation of particles with different diffusion coefficients without requiring membranes or centrifuge methods.^{50,51}

1.2.2 Microfluidic platforms - Classification

According to their main liquid propulsion principle, microfluidic platforms can be classified into capillary systems, pressure driven systems, electrokinetic systems, acoustic systems and centrifugal systems.³² In the work here presented, two different types of microfluidic platforms have been used: pressure driven systems, where fluids are actuated by applying positive or negative pressure gradients, and centrifugal systems, where fluid flow is mainly controlled by centrifugally induced forces. These two types of platforms are described in detail hereafter.

1.2.2.1 Pressure driven systems

As mentioned before, pressure driven systems use negative or positive pressure gradients for fluid transport. The pumping and gathering of fluids is achieved by using internal or external actuators (e.g. pumps and valves).

Ideally, these actuators should be monolithically integrated into the platform in order to minimise the external instrumentation required and therefore reduce the size of the system, the fluid consumption and the overall costs. However, the monolithic

integration of these actuators is still a technological challenge not only due to the high degree of miniaturisation required but also due to the actual complex connection of these actuators to the rest of the elements that conform a system.^{32,52} Besides, the integration of these actuators generally implies complex fabrication processes which may become prohibitively expensive or even inviable when scaled to mass production.^{41,53}

A huge amount of effort has been put into the development of integrable miniaturised actuators, and several monolithically integrated micropumps and microvalves have been reported.^{54–59} However, the integration of these microactuators is still extremely challenging due to incompatibilities on materials and fabrication procedures between the microactuators and the microfluidic platforms. Consequently, most pressure driven systems found in the literature are “hybrid” and combine the use of microfluidic platforms with external macroactuators such as conventional peristaltic pumps and manual injection valves commonly used in classical flow analysis techniques.

Flow analysis techniques constitute the basis of most of the pressure driven μ TAS and have been an essential tool for the miniaturisation and automation of the analytical process. Among the existing flow analysis techniques,⁶⁰ flow injection analysis (FIA) has probably been the most widely applied one due to its high simplicity. This technique consists in the injection of a small volume of sample into a carrier stream which is directed towards a detector. Before reaching the detector, the sample is mixed, when required, with one or more reagent solutions that meet the carrier stream in one or more confluence points.⁶¹

In order to solve the major drawbacks of FIA, which were mainly related to the high dimension of the actuators as well as to the relatively limited applicability of these systems (concerning, for instance, the high reagent and sample consumption), new methodologies were developed. The bulky conventional peristaltic pumps and manual injection valves were substituted by solenoid micropumps and microvalves, therefore diminishing the dimensions of the systems as well as increasing the versatility of the fluid management. Numerous new techniques arose from the use of these new type of actuators, including multipumping flow systems (MPFS)^{62–64} and multicommutated flow injection analysis (MCFIA) systems,^{65–67} among others.^{68–72} Apart from the evident high degree of miniaturisation, other benefits of using micropumps and microvalves are: a more efficient mixture of the solutions due to the pulsating flow, a reduced reagent and sample consumption, an easier automation and an increased robustness of the system. Furthermore, these actuators offer high versatility to the flow system due to an easier modification of the hydrodynamic parameters (e.g. the flow rate and the injection volume) and a simpler reconfiguration of the system network.⁶⁰

Therefore, despite not being monolithically integrated, the combined use of external microactuators and microfluidic platforms enables the development of highly miniaturised, automated and economical hybrid analytical systems.

Apart from fluid transport, the other two key unit operations of pressure driven platforms are fluid introduction and fluid mixing.

Fluid introduction – Connection to the external world

One important hurdle for the effective application of a microfluidic system is the connection between the microfluidic platform and the peripherals (e.g. pumps, valves, etc.), which is commonly referred to as the “world-to-chip” or the “macro-to-micro” interface. These interfaces, which should apparently be functional, robust and reliable, often turn out to be responsible for compromising the overall performance of the systems.^{73,74} Some attempts to develop universal fluidic connectors have been carried out (e.g. the Luer Lock system). However, these interfaces are generally suitable for a limited number of applications and are not compatible with most fabrication techniques.⁷⁴

Several aspects have to be considered for the design of a suitable interface. Ideally, a connector should be simple, easily plugged and removed, have minimal dead volume, allow to work with a wide variety of flow rates and pressures and present chemical compatibility with the reagents and samples to be used. Besides, it should be inexpensive and it should provide the maximum possible compatibility with other commercial fluidic connectors.⁷⁴

Some examples of connectors for pressure-driven microsystems are: a magnetic connector based on the sealing of the tubing against inlets/outlets by the attractive forces between to magnets (Figure 1.6.a);⁷⁵ a connector based on standard pin header electrical connectors (Figure 1.6.b);⁷⁶ a solder-based connection where metal ferrules are soldered to silicon/glass chips using an intermediate solder layer (Figure 1.6.c);⁷⁷ and an in-plane interconnect where polyimide tubing is inserted into a glass/silicon device and fixed by the deposition of Parylene-C (Figure 1.6.d).⁷⁸

The devices that will be presented in this dissertation use modular polymeric connectors for the introduction of fluids into the microfluidic platforms.

Mixing

Although diffusive mixing is considered a relatively efficient mixing method in microfluidic systems due to the reduced dimensions of the microchannels, most microfluidic platforms integrate structures in order to accelerate this process. These structures, commonly referred to as micromixers, are generally aimed to favour the turbulent flow of the fluids (instead of the typical laminar flow of the microscale), therefore enhancing the effective mixing of the solutions in a reduced time.

Micromixers can be classified into active and passive. Active micromixers use external energy sources in order to disrupt the flow, increase the contact area or induce chaotic advection. Despite their high mixing efficiency, the involved structures are frequently complicated, thus increasing the complexity of the overall construction process.⁷⁹ This fact, along with the need for external energy sources, has limited the actual applicability of this type of micromixers. Conversely, passive micromixers are based on the microstructuring of certain channel geometries to favour the disturbance of the flow and do not require any external energy source.⁸⁰ This type of micromixers have been widely used due to their simplicity, robustness and easy integration.

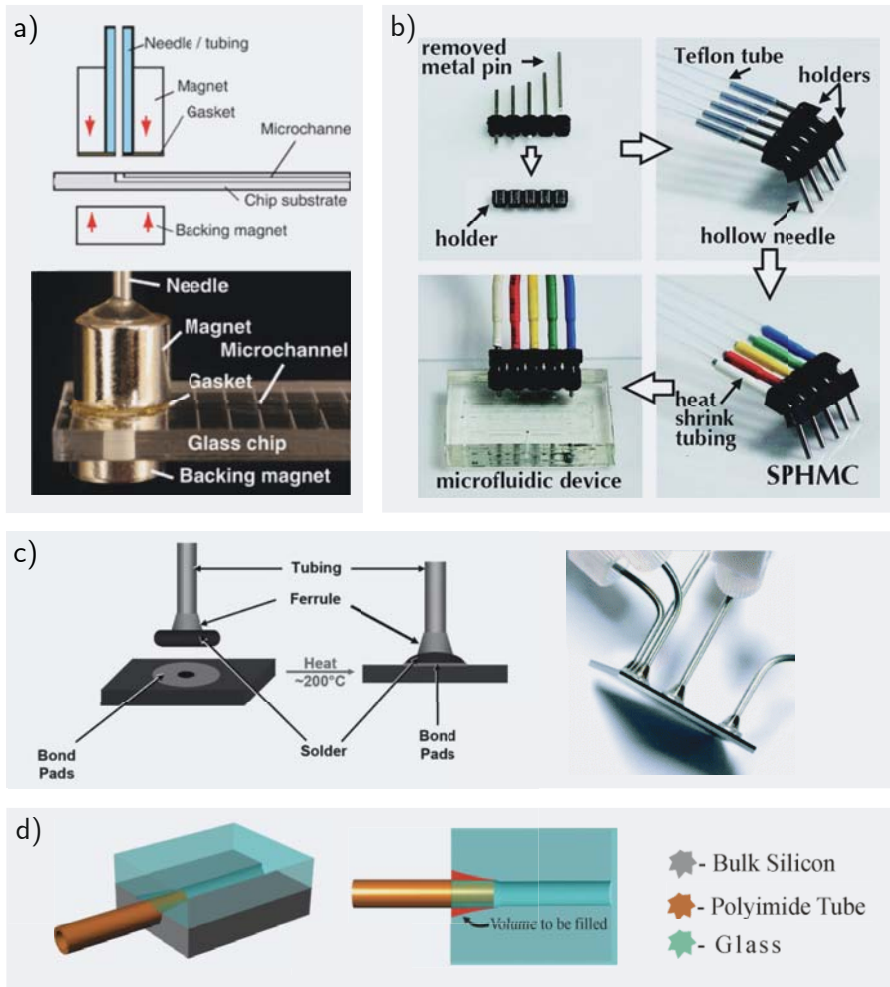


Figure 1.6: Some examples of macro-to-micro interfaces: a) a magnetic connector;⁷⁵ b) a pin header connector;⁷⁶ c) a solder-based connection;⁷⁷ and d) an interconnect using Parylene-C⁷⁸. Parylene-C is deposited in the space delimited in red from the second illustration in (d). Images adapted from the respective references.

Numerous active and passive micromixers can be found in the literature.^{80–82} **Figure 1.7** shows three examples of passive micromixers. The pressure-driven microfluidic platforms presented in this dissertation integrate 2D serpentine micromixers due to their high efficiency yet simple construction.

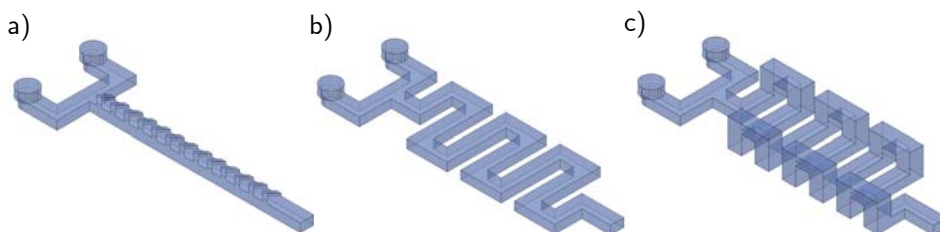


Figure 1.7: Three examples of passive micromixers: a) staggered herringbone micromixer, b) 2D serpentine micromixer and c) 3D serpentine micromixer. Redrawn from reference [79].

1.2.2.2 Centrifugal microfluidic systems

Centrifugal microfluidic systems, also known as Lab on a CD or Lab on a disc due to their frequent resemblance to conventional compact discs (CD), use centrifugally induced forces for fluid transport. Fluid motion is controlled by the frequency of rotation of a platform and depends on the geometry of the channels and chambers as well as on the properties of the fluids and the surfaces in direct contact with them.

Centrifugal microfluidic platforms offer many advantages compared to other common microfluidic systems. The most relevant one is related to the “chip-in-a-lab”⁵³ concept, which refers to the general need for bulky external instrumentation for fluid handling and detection. Centrifugal pumping involves minimum external instrumentation, requiring only a rotatory motor as actuator and therefore eliminating any external fluidic interconnection (the “world-to-chip” interfaces introduced in the previous section).

Besides, unlike electrokinetic and acoustic pumping, centrifugal pumping is relatively insensitive to various physicochemical properties such as pH, ionic strength or chemical composition, hence enabling the effective transport of a wide variety of fluids, from aqueous solutions to biological fluids such as blood^{83–85} and urine^{85,86}. Fluid transport in centrifugal systems is also highly efficient: a wide range of flow rates can be achieved, formed bubbles are easily eliminated and reagent and sample consumptions are minimised. Moreover, multiplexing is quite easily implemented by means of integrating multiple parallel structures in a single disc.[†]

Many fluidic functions have been successfully integrated into centrifugal microfluidic platforms. These include pumping,^{87–89} valving,^{90–92} mixing,^{93,94} flow switching,^{95,96} metering and aliquoting,^{97–99} reagent storage,^{100,101} analyte separation^{102–104} and pre-concentration,^{86,105} among others. Furthermore, several optical (e.g. molecular absorption spectroscopy,^{84,106} molecular fluorescence spectroscopy,^{107,108} surface plasmon

[†]Parallelisation in centrifugal platforms is examined in more detail in § 7.2.

resonance (SPR) spectroscopy^{109,110} and Raman spectroscopy^{111,112}) and electrochemical^{113–115} detection methods have been demonstrated.[†]

The wide range of available functions for fluid handling and the multiple analytical detection methods demonstrated enable the development of dedicated systems for many specific applications by means of the appropriate selection and combination of these tools. Centrifugal microfluidic platforms have been applied to numerous fields, such as environmental monitoring¹²⁰ and medical diagnosis.¹²¹

One of the major advantages of using centrifugal microfluidic platforms lies on the possibility of developing inexpensive dedicated disposable devices. This fact, along with the minimal external instrumentation required, make these platforms especially suitable for point of care (POC) applications.¹²² The potential of these platforms in POC diagnostics rapidly caught the attention of several companies, which developed various centrifugal systems that are now commercially available. Some examples are: Piccolo Xpress¹²³ by Abaxis (Union City, CA, USA); Spinit¹²⁴ by Biosurfit (Azambuja, Portugal); Revogene¹²⁵ by GenePOC (Québec, Canada); Cobas b 101¹²⁶ by Roche Diagnostics (Indianapolis, IN, USA); LABGEO IB10¹²⁷ by Samsung Healthcare (Seoul, South Korea); and Gyrolab xPlore¹²⁸ by Gyros Protein Technologies (Uppsala, Sweden).

Theoretical aspects - Centrifugal hydrodynamics

As mentioned earlier, in centrifugal microfluidic systems fluids are controlled by the frequency of rotation of a microstructured circular platform. Fluid flow is mainly governed by three different pseudo forces[†]: the centrifugal force, the Coriolis force and the Euler force.

[†]Pseudo forces, also called fictitious or inertial forces, refer to apparent forces which act on masses whose motion is described using a non-inertial frame of reference (i.e. the coordinate system where the motion of an object is being analysed).¹²⁹ In order to describe the mechanics of fluids and particles in rotating platforms, a rotating reference frame is generally used.

A fluid of a mass density ρ on a planar substrate rotating at a distance r from the central axis at an angular velocity ω experiences three fictitious force densities (i.e. per unit volume):^{42,130}

$$f_{\omega} = \rho r \omega^2 \quad (1.7) \text{ The centrifugal force (density), which is directed outwards from the centre of rotation along the radius of the disc. This force is contained in the plane perpendicular to the rotation axis, and it}$$

[†]Only few novel/relevant examples are referenced. Further information about the different unit operations and detection methods can be found in references [116] and [117], and [116], [118] and [119], respectively.



Figure 1.8: Some examples of commercially available centrifugal systems for POC diagnostics: a) Piccolo Xpress¹²³ by Abaxis (Union City, CA, USA); b) Spinit¹²⁴ by Biosurfit (Azambuja, Portugal); c) Revogene¹²⁵ by GenePOC (Québec, Canada); d) Cobas b 101¹²⁶ by Roche Diagnostics (Indianapolis, IN, USA); e) LABGEO IB10¹²⁷ by Samsung Healthcare (Seoul, South Korea); and f) Gyrolab xPlore¹²⁸ by Gyros Protein Technologies (Uppsala, Sweden). Images adapted from their respective websites.

drives fluids outwards from the centre towards the periphery of the platform.

$$f_C = 2\rho\omega v$$

(1.8) The Coriolis force (density), which acts in a direction perpendicular to the rotation axis and to the linear velocity of the fluid (v) in the rotating platform. This force deflects the fluid movement in the transversal direction and becomes dominant at high rotational speeds.¹³¹

$$f_E = \rho r \frac{d\omega}{dt}$$

(1.9) The Euler force (density), which appears when the angular velocity changes with time and it is normal to the direction of the centrifugal force. This force drives fluids in a direction opposite to rotation and increases proportionally to the radius. It becomes significant when high acceleration/deacceleration profiles are used.^{132,133}

These three pseudo forces can be directly controlled by the frequency of rotation of the platform ν . The relationship between the angular velocity ω and the frequency of rotation ν is:

$$\omega = 2\pi\nu. \quad (1.10)$$

The aforementioned pseudo forces are illustrated in [Figure 1.9](#) for a particle inside a rotating platform.

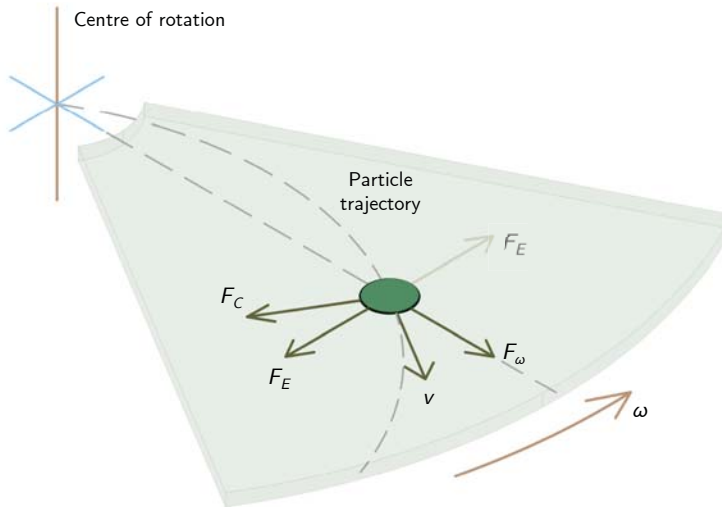


Figure 1.9: Pseudo forces acting on a particle inside a spinning disc: the centrifugal force (F_ω), the Coriolis force (F_C) and the Euler force (F_E). F_E can act in both directions depending on the acceleration to which the platform is subjected (which can be either positive or negative). Capital letter F has been used to represent force (instead of force density f).

In addition to the inertial forces previously described, centrifugal platforms have benefited from other forces for the development of several fluidic applications. These forces include capillary force,^{134,135} electrostatic force¹³⁶ and magnetic force,^{137–139} among others. Out of all these, capillary force has been the most widely exploited. Fluid control in most passive valves is actually achieved by the interplay between capillary forces and centrifugally induced forces.[†]

[†]Valving in centrifugal platforms is examined in more detail in [§ 6.1](#).

1.3 Microfabrication technologies and materials

Over the last decades, LOC microfabrication technologies have experienced a significant evolution and new materials have emerged as a consequence of the search for enhanced LOC characteristics, new LOC applications, and more precise, economical and faster construction methods. In this section, a brief overview of the main substrate materials, including their strengths and weaknesses as well as their respective most common microfabrication methodologies, is given.

It is important to emphasize that there is no ideal material (and therefore no ideal microfabrication methodology) that can fulfill all the requirements for every application. Generally, the selection of the suitable material is carried out by considering the final application of the device. The selected material has to meet the required optical, electrical, mechanical, thermal and chemical properties, including toxicity and biocompatibility, apart from taking into account the available fabrication methods (both at the prototyping and the mass production scale) and the costs of the material and the fabrication procedure.¹⁴⁰ The critical design dimensions along with the manufacturing time and costs play an important role in the selection of the fabrication method. Besides, the accessibility to equipment and techniques is often a limiting factor (e.g., the use of clean room facilities is not always plausible).³⁸

1.3.1 Silicon and glass

Some of the earliest works in microfluidics used silicon and glass as substrate materials due to the well-established fabrication methods inherited from the microelectronics industry.¹⁴¹

The usual microfabrication process of silicon and glass devices consists in a first photolithographic step, followed by (dry or wet) etching and a final anodic bonding.^{142,143} During the photolithographic process (see [Figure 1.10.a](#)), the areas that will be etched later on are defined by using a photosensitive polymer layer deposited onto the substrate by spin-coating. This layer is then exposed to intense light through a photomask and, consecutively, the exposed or unexposed photoresist (depending on whether a positive or a negative photoresist is used) is dissolved. During the etching (see [Figure 1.10.b](#)), the patterns are created by the removal of the material in the parts that are not covered by the photoresist layer. The pieces that conform the final device are then sealed together by anodic bonding. The described fabrication methodology allows precise machining of channels with high resolution down to less than 100 nm and high aspect ratio structures up to 20:1.^{143,144}

Other microstructuring techniques such as femtosecond laser 3D micromachining,¹⁴⁶ the use of xurography¹⁴⁷ as an alternative to photolithography, and some other bonding strategies¹⁴³ including direct bonding and adhesive bonding, are also available for the construction of silicon/glass devices.

The use of silicon and glass as substrate materials for LOC devices is nowadays modest and it is mainly restricted to applications where strong solvents or high temperatures

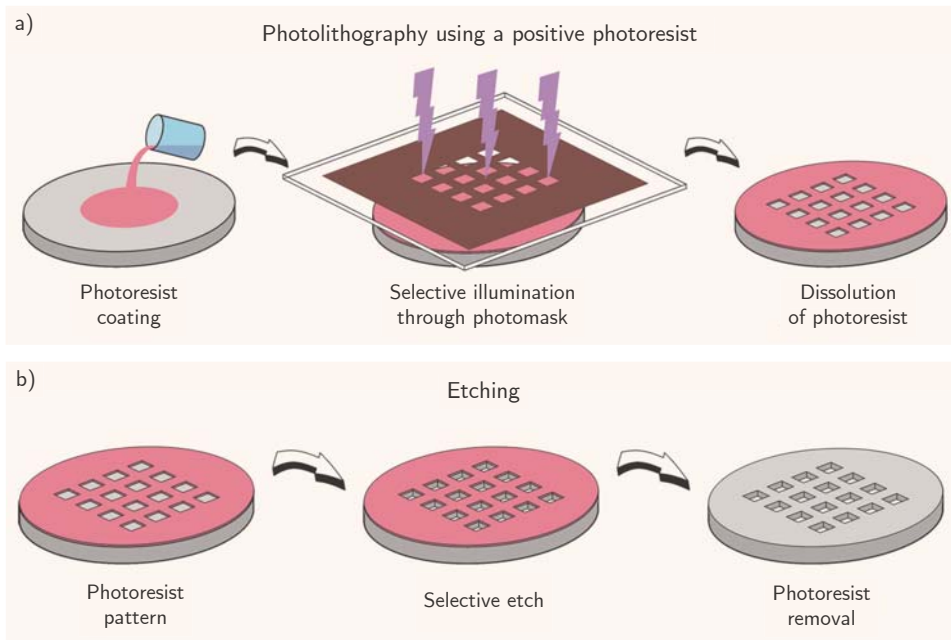


Figure 1.10: Schematic representation of basic (a) photolithographic and (b) etching processes. In this example, a positive photoresist is used and, therefore, the areas which are dissolved are the ones previously exposed to light. When a negative photoresist is used, the unexposed areas are the ones which are dissolved. The etching process removes material only from the areas where there is no photoresist. Adapted from reference [145].

are required. Glass is the preferred material for on-chip capillary electrophoresis, where the surface properties of the channels play an important role, and for some biological applications due to its high compatibility with biological samples.^{35,38} The current limited application of these materials (apart from the ones mentioned before) is a direct consequence of the several drawbacks they suffer from.^{35,143} Silicon devices are expensive, they require especial microfabrication facilities (clean rooms) and trained personnel to be constructed and they are optically opaque to visible light. Although glass is transparent at the UV-visible range of the spectrum, the manufacturing costs are equivalent to those from silicon since special facilities and trained personnel are also required. Furthermore, the construction process of both silicon and glass devices is not only expensive but also highly time-consuming.

1.3.2 Low Temperature Co-fired Ceramics

Low Temperature Co-fired Ceramics (LTCC), which were originally used for electronic multilayer packaging, were introduced as substrate materials for LOC devices due to the high compatibility with conductive materials, the easy integration of electronic components and the simple and fast prototyping of 3D structures.^{148–150} The Group of Sensors and Biosensors (GSB) has an extensive experience in the use of LTCC to develop highly integrated microanalysers, being one of the pioneer research groups in applying this material to microfluidics.^{150–154}

LTCC are polycrystalline solids mainly containing alumina (Al_2O_3 , 45%) and glass (SiO_2 40%). In their “green” state (i.e. pre-fired, pre-sintered), they contain a small percentage of organic compounds (15%) which confer this material the adequate properties for its manipulation.¹⁵⁰

LTCC are generally manufactured in malleable sheets of different thicknesses. Therefore, LTCC devices are generally constructed by using a multilayer approach. The general construction process can be divided into three main steps: firstly, the individual microstructuring of the different layers in their green state; then, the lamination of these layers by applying temperature and pressure; and, finally, the sintering of the obtained LTCC block at about 900 °C.¹⁵⁰ The name of this material is actually related to the sintering temperature, which is considerably lower than that of classic alumina ceramic substrates (1600 °C to 1800 °C).¹⁴⁸ When required, conductive pastes are screen printed onto the surface of the ceramics layers in their green state.

The microstructuring of LTCC sheets is generally carried out through laser ablation, although other techniques such as micromilling and jet vapour etching are also feasible.¹⁵⁵

Apart from the possibility of integrating conductive materials and electronic components, LTCC devices present other advantageous characteristics such as high chemical inertness and high temperature stability, enabling them to be applied to syntheses requiring harsh conditions (see [Figure 1.11](#)).^{156–158} Besides, these devices are easily prototyped with no need for special facilities. The main disadvantages of these systems are their relatively high fragility and their optical opacity. Nonetheless, the possibility of monitoring absorbance and fluorescence by using thin LTCC layers has been demonstrated by the GSB.^{159,160}

Due to their fast and precise prototyping, LTCC have been used in the work here presented for the construction of masters for the later hot embossing of microchannels onto polymeric substrates.

1.3.3 Polymers

The use of polymers has grown rapidly over the last few years due to their low cost and the vast variety of available materials and fabrication methodologies. Polymers have attracted attention not only in the research field but also in industry due to the possibility of developing cost-effective disposable devices.^{161,162} Besides, the wide range

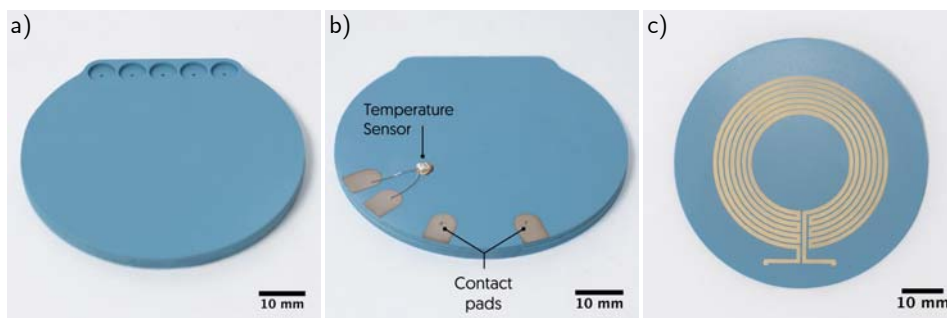


Figure 1.11: Top (a), bottom (b) and inner (c) view of an LTCC microreactor for the synthesis of superparamagnetic iron oxide nanoparticles (SPION). The device contained a monolithically integrated gold resistor which was used as a heater. The top side (a) of the microreactor included the fluidic inlets and outlets while the bottom side (b) contained the contact pads for the gold resistor (c) and a temperature sensor. The internal fluidic system is not shown. Adapted from reference [158].

of available polymers presenting a wide diversity of mechanical, thermal and chemical properties offers great flexibility in choosing the suitable material for each specific application.

Among all available polymers, polydimethylsiloxane (PDMS), poly(methyl methacrylate) (PMMA), polystyrene (PS), polycarbonate (PC) and cyclic olefin (co)polymers (COP, COC) are the most commonly used ones.¹⁶³ PDMS is, by far, the most often utilised due to its extremely easy and fast prototyping.

An overview of some properties of these polymers is provided in Table 1.1. In the following sections, the use of PDMS and COP/COC as substrate materials for LOC will be presented due to their importance in the microfluidics field as well as because of their relevance in this dissertation, particularly in the case of COC.[†]

[†]A more detailed and complete description of the available polymeric materials for microfluidic devices and their fabrication methods can be found elsewhere.^{163,164}

[†]Thermal property refers to the curing temperature of PDMS and the glass transition temperature (T_g)

Table 1.1: Summary of some properties of interest of the most commonly used polymer materials.¹⁶³ The qualitative metrics shown in this chart are provided only as a general guide. Particularly, solvent resistance can be highly dependent upon the solvent type. A more complete description of the chemical resistance of these polymers (among other materials) can be found in reference [165].

	PDMS	Thermoplastics			
		PS	PMMA	PC	COP/COC
Mechanical property	Elastomer	Rigid	Rigid	Rigid	Rigid
Thermal property [†]	~ 80 °C	90 ~ 100 °C	100 ~ 125 °C	140 ~ 150 °C	70 ~ 155 °C
Solvent resistance	Poor	Poor	Good	Good	Excellent
Acid/base resistance	Poor	Good	Good	Good	Good
Optical transmissivity					
Visible	Excellent	Excellent	Excellent	Excellent	Excellent
UV	Good	Poor	Good	Poor	Excellent
Biocompatibility	Good	Good	Good	Good	Good
Material cost	150 \$/kg	<3 \$/kg	2 - 4 \$/kg	<3 \$/kg	20 - 25 \$/kg

Polymer classification^{161,165}

Based on their physical properties, polymers can be classified into three groups: thermoplastics, elastomers and thermosets. These mainly differ in the degree of cross-linking of the polymer chains, which results in a difference in the final physical characteristics of the polymers.

Thermoplastics are polymers with unlinked chains whose polymeric network is easily broken by heat. Therefore, when heated above the glass transition temperature (T_g), they become plastic and can be easily moulded into specific shapes which will be retained once temperature descends. Most of the polymers used in microfluidics belong to this group (e.g. PMMA, PS, PC, COP/COC).

Elastomers are weak to moderate cross-linked polymers which are characterised by their capability to stretch or compress when an external force is applied and return to their original shape once the force is withdrawn. The most popular elastomer in microfluidics is PDMS.

Thermosets present high cross-linking of the polymer chains, thus impeding their free movement. This results in hard and brittle materials which are usually temperature stable. As a consequence, this type of polymers are rarely employed as substrate materials for LOC devices, although they are frequently used as photoresists for photolithography.

The general microfabrication methods of polymeric devices include casting (also known as soft lithography), injection moulding, thermoforming and hot embossing, all of them requiring the fabrication of a master mould.^{164,166} For prototyping purposes, alternative techniques which avoid the need for a master are generally preferred.^{163,164} These techniques are usually based on a multilayer approach, in which complex 3D structures are easily obtained by the overlapping of several 2D microstructured layers. The individual machining of these layers is typically carried out by direct microstructuring techniques such as laser ablation and micromilling. The sealing of the different layers/parts that constitute the final device can be performed by thermal bonding, solvent bonding and adhesive bonding, among others.¹⁶⁷ Multilayer construction methods are widely used due to their broad applicability, material compatibility and high simplicity.

It is important to highlight that not all the aforementioned construction methods are feasible for every polymer. The selection of the adequate construction method will, therefore, depend on the polymer selected. Other aspects such as the available infrastructure or the required resolution of the final structures may also be considered.

3D printing techniques have recently emerged and are rapidly growing in the microfluidics field due to the possibility of creating complex 3D structures in an automated way and without the need for later bonding or assembly.^{168,169} 3D printing refers to a set of additive manufacturing techniques where 3D objects are created from a computer aided design (CAD) in a single process and includes stereolithography, photopolymer inkjet printing and fused deposition modelling, among many others.^{168,170} Relatively low-cost 3D printers are commercially available, allowing a rapid and cost-effective prototyping.¹⁷¹ The major drawbacks of these techniques are principally related to the resolution of the obtained structures and the properties of the compatible materials (e.g. their optical transparency and biocompatibility). Notwithstanding, both issues are rapidly being improved. The possibilities and applications of these techniques are expected to rapidly increase during the next few years.¹⁷⁰

1.3.3.1 PDMS

PDMS is the most popular material in research laboratories due to its easy and low cost prototyping.

PDMS pieces are commonly produced by casting (see [Figure 1.12](#)).¹⁴⁵ This process consists in pouring the liquid PDMS prepolymer onto a mould which is generally fabricated by photolithography (although other techniques are also available). The PDMS piece is then cured for a few hours at mild temperature and, after the curing process, it is peeled off the mould. The obtained PDMS piece can be directly (and reversibly) bonded to other PDMS pieces or other materials such as glass and silicon.¹⁷² The easy replication of these pieces along with a simple bonding where no additional material or special process are required confer this material an exceptional usefulness for prototyping purposes. Furthermore, PDMS casting and bonding involve neither special facilities

nor expensive instrumentation. It is important to highlight that the direct bonding previously described is not always suitable and that alternative bonding processes such as O_2 plasma bonding are available for applications where a stronger sealing is required. The O_2 plasma bonding is also a simple and fast sealing process.¹⁷²

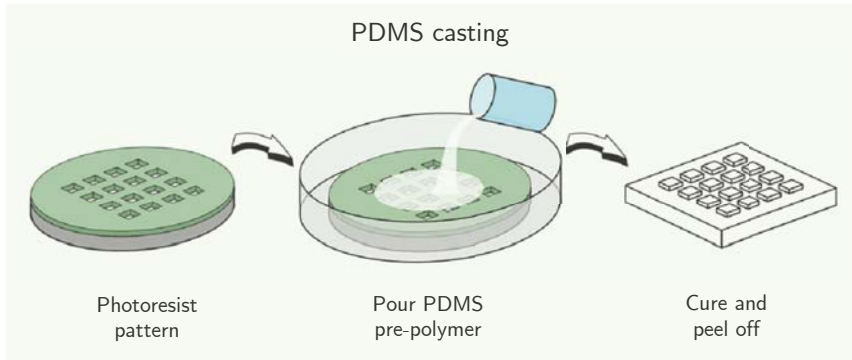


Figure 1.12: PDMS casting. Adapted from reference [145].

Apart from the easy replication and bonding of PDMS, this polymer possesses other interesting characteristics such as good optical transparency and biocompatibility. However, PDMS exhibits some double-edged properties which can be beneficial for some applications yet counterproductive for many others. Two examples of these characteristics are its elasticity and its permeability to gases. The high elasticity of PDMS has enabled the development of microvalves and micropumps based on thin flexible PDMS layers.^{145,173,174} Notwithstanding, this property can become problematic when internal or external pressures are applied to a PDMS microfluidic device, since it would lead to a change in the dimensions of the patterned microstructures and, therefore, to changes in the flow rate, the volume of the chambers, etc.¹⁷⁴ Its permeability to gases is considered advantageous for some cellular studies where the free diffusion of O_2 and CO_2 is desired.¹⁷⁵ However, it may alter the measurements in microfluidic analytical devices as a result of vapour loss or changes in pH due to CO_2 diffusion.¹⁷⁴ The high hydrophobicity of the material is generally considered detrimental, since it promotes the absorption of small hydrophobic molecules and biomolecules.¹⁷⁴ Furthermore, it is poorly resistant to organic solvents and its use is mainly restricted to aqueous solutions.¹⁴⁴

Additionally, one of the major drawbacks of using PDMS is the difficulty to transfer the construction methodology at the prototyping scale to mass manufacturing. Casting has only very little initial equipment costs. However, whilst for other replication technologies such as injection moulding or hot embossing the cost per device is drastically reduced with the increase of the number of devices, in this case, the cost per device remains almost constant.¹⁷⁶ As a consequence, industry has opted for other polymer materials and the use of PDMS has been basically restricted to research labs.⁷⁴

1.3.3.2 COP/COC

During the last decades, the use of cyclic olefin polymers (COPs) as substrate materials for LOC applications has become more and more extensive due to their promising properties which include high chemical resistance, low water absorption, good optical transparency in the visible and near UV range, high biocompatibility and an easy fabrication, among others.^{177,178}

Different COP materials are commercially available from several suppliers and under different brand names, being TOPAS¹⁷⁹ by Topas Advanced Polymers and Zeonex and Zeonor¹⁸⁰ by Zeon Chemicals the most commonly employed. COPs are synthesised by using two different polymerisation processes. The first consists in a ring-opening metathesis polymerisation of cyclic monomers followed by hydrogenation (e.g. Zeonex and Zeonor), while the second consists in the chain copolymerisation of the cyclic olefin monomers with ethene (e.g. TOPAS).¹⁷⁷ The polymers resulting from this second synthesis are frequently referred to as cyclic olefin copolymers (COCs).

One of the most important characteristics of COPs/COCs is the availability of a wide range of materials with different glass transition temperatures (T_g). The T_g of COP/COC can be tuned without altering other interesting properties (such as the structural or the optical ones) by applying some modifications to the synthesis. In the case of Zeonex and Zeonor, the T_g is tuned by changing the substituents of the norbornene,¹⁸¹ whereas for TOPAS, the T_g is tuned by modifying the norbornene to ethylene ratio.¹⁷⁷

As previously mentioned, thermal bonding is one of the usual bonding strategies for polymer devices. This technique is based on the increase in temperature up to or above the T_g of the substrate material while pressure is being applied in order to achieve the interdiffusion of the polymer chains between the surfaces. The main drawback of thermal bonding is the possible deformation of the internal structures due to applied temperature and pressure. However, this can be avoided by the combined use of COPs/COCs with different T_g .^{177,178,182} In this bonding approach, high T_g COP/COC layers containing the microfluidic structures are sealed together by using low T_g COP/COC sheets as bonding layers. Hence, the applied temperature must be above the T_g of the bonding layers but below that of the structural ones. This strategy avoids not only the deformation of the microstructured features but also the use of auxiliary bonding materials such as solvents, adhesives or glues.

COC devices are generally prototyped using direct microstructuring methods such as micromilling and laser ablation. For their mass production, replication techniques such as hot embossing and injection moulding are preferred.^{177,178}

Due to its outstanding properties, COC was selected as the substrate material for the construction of the devices presented in this dissertation. The microstructuring of the material was principally carried out by micromilling and hot embossing. The combined use of COC layers with different T_g was chosen as the bonding method.

1.3.4 Other materials

Apart from the aforementioned, other materials have been used for developing LOC systems. Paper and hydrogels are two examples worth-mentioning.

Microfluidic Paper-based Analytical Devices (μ PADs) have attracted notable interest due to their low cost and their user-friendly operation. The pumping of liquids is achieved by capillarity, therefore avoiding the need for any external actuator. This fact, along with the low cost of the material, promoted the use of paper as the substrate material for many POC applications.¹⁸³⁻¹⁸⁵

Hydrogels are 3D networks of hydrophilic polymer chains containing up to 99% of water. Their high porosity and controllable pore size allow small molecules or even bioparticles to diffuse through. As a consequence, hydrogels are considered the perfect candidates for encapsulating cells for 3D culture.¹⁴⁴ The use of hydrogels for tissue-engineering is nowadays growing fast due to their interesting properties for mimicking biological conditions.^{186,187}

1.4 Microfluidics impact in the “real world”

Over the last decades, a great part of the microfluidics research has been focused on the development, optimisation and application of new miniaturised analytical systems for solving the current hunger for on-time and in-situ information. Microfluidic analytical systems have been applied to a wide variety of fields and have demonstrated a great potential in several areas with commercial appeal such as POC diagnostics. However, the number of commercially available LOC systems is low and their actual impact on the real world is still reduced.

An interesting discussion is currently being held about the actual applicability and commercialisation of these systems. The lack of commercial LOC systems is generally attributed to economic issues. In most cases, microfluidic devices are considered novel solutions to problems which had already been solved.¹⁷⁶ The previous solutions were, probably, not so “elegant” in one or more aspects (e.g. miniaturisation, time response, sensibility, etc.). However, if the proposed solution does not substantially improve the former ones and cannot economically compete against the conventional solutions, the investment that would be required for the development and commercialisation of these new systems is considered worthless.^{176,188}

Apart from the economic aspects, another important obstacle for the real application of these systems relies on the “chip-on-a-lab” concept.⁵³ The unspoken reality of many LOC devices is that they need a large amount of ancillary equipment to be operative, including fluidic actuators, power supplies and detection systems, among others. Frequently, this external instrumentation is larger than the LOC itself, thus contradicting some of the premises of miniaturisation.

Nevertheless, the effort put into solving some of the aforementioned challenges is broadly compensated by the benefits reported once the final targets are achieved.

Intelligent insulin dosing systems for patients suffering from diabetes are one of the best examples of the unquestionable success of this effort. These devices are able to measure the glucose levels in blood, decide whether an insulin dose is necessary or not, and administrate the dose to the patient when deemed necessary, all in an autonomous, automated and miniaturised fashion. Intelligent insulin dosing systems, which have considerably improved the quality of life of patients with diabetes, exemplify the enormous potential of miniaturised analytical microsystems in order to solve some of the current needs of the "real world".

1.5 Molecular absorption spectroscopy

Due to the relevance of molecular absorption spectroscopy in the work presented in this dissertation, it has been deemed necessary to give a quite brief overview on this optical detection method.

Among all the existing spectrometric detection methods, molecular absorption spectroscopy is one of the most commonly used ones. This technique is based on the measurement of the interaction between electromagnetic radiation and matter, making it possible to establish a proportional relationship between the amount of radiation absorbed (or transmitted) at a certain wavelength by a specie and the concentration of this specie in a sample. This relationship is known as Beer's law[†] and can be described as:^{189,190}

$$A = \varepsilon \cdot c \cdot l \quad (1.11)$$

Where A is the measured absorbance, ε is the molar absorptivity of the specie and l is the path length of radiation through the sample. Although absorbance is a dimensionless parameter, Absorbance Units (AU) are frequently used.¹⁹⁰

The experimental value that is actually measured is transmittance, which can be calculated as:^{189,190}

$$T = \frac{P}{P_0} \quad (1.12)$$

This expression relates the power of the light beam before (P_0) and after (P) passing through the sample. Absorbance and transmittance are related by the following expression:^{189,190}

$$A = -\log T = \log \frac{P_0}{P} \quad (1.13)$$

The selectivity of this technique can be modulated by the appropriate selection of the measurement wavelength. When other matrix species may potentially interfere with the absorbance measurement of the analyte of interest, the use of colorimetric reagents which can selectively react with the analyte are frequently used.

The basic components of an optical detection system for measuring absorbance are, basically, a radiation source capable of emitting light at the desired wavelength and

[†]Limitations of Beer's law can be found elsewhere.¹⁸⁹

a detector capable of distinguish the power changes resulting from the interaction of the radiation with the analyte.¹⁹⁰ Traditionally, the equipment used for measuring absorbance was bulky, expensive and high energy-demanding. Nowadays, the availability of smaller light sources (e.g light emitting diodes (LEDs)) and smaller photodetectors (e.g. photodiodes) has enabled the development of portable, miniaturised and low-cost optical detection systems.^{191–195} Evidently, these miniaturised components reduce the versatility of the equipment but, on the other hand, they allow the implementation of dedicated instruments for concrete applications.

The analytical microsystems presented in this dissertation use molecular absorption spectroscopy for the detection and monitoring of the analytes of interest. A miniaturised optical detection system based on an interchangeable LED and a small photodiode is used.¹⁹⁶ For the calibration of the microsystems, the absorbance values of standard solutions of the analyte are represented against the analyte concentration of these solutions. The data points are fitted to a linear relationship such as:

$$A = a + b \cdot x \quad (1.14)$$

Where A is the measured absorbance, a corresponds to the intercept, b is the sensibility of the method and x is the concentration of the analyte in the solution; the path length (l) and the molar absorptivity (ϵ) are included in b .

1.6 Overview of the dissertation

This doctoral thesis reports on the development of a novel magnetically actuated valve for centrifugal microfluidic systems as well as on the development of novel LOC systems which have been principally applied to wine industry. These LOC systems include pressure-driven systems and centrifugal systems. Each chapter contains a brief introduction to the specific problem it is addressed to.

Chapter 2 (§ 2) introduces the general objectives of the thesis. Chapter 3 (§ 3) describes the general fabrication method of the devices presented in the following chapters. Chapter 4 (§ 4) presents a microsystem for the determination of titratable acidity in wine samples and for the continuous monitoring of this parameter during wine-making processes. In Chapter 5 (§ 5), the microsystem described in Chapter 4 is used for the measurement of the primary amino nitrogen content in wine. Chapter 6 (§ 6) reports on the development of a novel valving system for centrifugal microfluidic platforms. Chapter 7 (§ 7) presents the first works on the development of a centrifugal microfluidic system for the parallel analysis of several wine parameters by using enzymatic methods. Finally, Chapter 8 (§ 8) highlights the main conclusions and discusses future challenges and perspectives.

References

- (1) Niessner, R. Analytical Chemistry: Current Trends in Light of the Historic Beginnings. *Angewandte Chemie International Edition* **2018**, *57*, 14328–14336.
- (2) Valcárcel, M. Quo vadis, analytical chemistry? *Analytical and Bioanalytical Chemistry* **2016**, *408*, 13–21.
- (3) Zuckerman, A. M. Analytical Chemistry - today's definition and interpretation. *Fresenius' Journal of Analytical Chemistry* **1992**, *343*, 817–818.
- (4) Cammann, K. Analytical Chemistry - today's definition and interpretation. *Fresenius' Journal of Analytical Chemistry* **1992**, *343*, 812–813.
- (5) Karayannis, M. I.; Efstathiou, C. E. Significant steps in the evolution of analytical chemistry—Is the today's analytical chemistry only chemistry? *Talanta* **2012**, *102*, 7–15.
- (6) Zolotov, Y. A. General methodological aspects of present-day analytical chemistry. *Journal of Analytical Chemistry* **2001**, *56*, 885.
- (7) Valcárcel, M. A modern definition of analytical chemistry. *TrAC Trends in Analytical Chemistry* **1997**, *16*, 124–131.
- (8) Bergquist, J.; Turner, C. Analytical chemistry for a sustainable society – trends and implications. *Analytical and Bioanalytical Chemistry* **2018**, *410*, 3235–3237.
- (9) Šíma, J. Modern analytical chemistry in the contemporary world. *Cultural Studies of Science Education* **2016**, *11*, 1269–1273.
- (10) Valcárcel, M., *Principles of Analytical Chemistry*, 1st; Springer - Verlag Berlin Heidelberg: New York, NY, 2000, p 371.
- (11) De Castro, M. D. L. Preliminary steps of the analytical process. From sampling to detection. *Pure and Applied Chemistry* **2002**, *74*, 2293–2298.
- (12) Widmer, H. Trends in industrial analytical chemistry. *TrAC Trends in Analytical Chemistry* **1983**, *2*, VIII–X.
- (13) Kopp, M. U.; Crabtree, H. J.; Manz, A. Developments in technology and applications of microsystems. *Current Opinion in Chemical Biology* **1997**, *1*, 410–419.
- (14) Ríos, Á.; Zougagh, M. Sample preparation for micro total analytical systems (μ -TASs). *TrAC Trends in Analytical Chemistry* **2013**, *43*, 174–188.
- (15) Alegret, S. In *Comprehensive Analytical Chemistry*; Elsevier B.V.: Oxford, UK, 2003; Vol. 39; Chapter 1, pp 1–36.
- (16) Terry, S.; Jerman, J.; Angell, J. A gas chromatographic air analyzer fabricated on a silicon wafer. *IEEE Transactions on Electron Devices* **1979**, *26*, 1880–1886.

- (17) Manz, A.; Graber, N.; Widmer, H. Miniaturized total chemical analysis systems: A novel concept for chemical sensing. *Sensors and Actuators B: Chemical* **1990**, *1*, 244–248.
- (18) Ghallab, Y.; Badawy, W., *Lab-On-A-Chip - Techniques, Circuits, and Biomedical Applications*, 1st; Artech House: Norwood, MA, USA, 2010, p 220.
- (19) Dittrich, P. S.; Manz, A. Lab-on-a-chip: microfluidics in drug discovery. *Nature Reviews Drug Discovery* **2006**, *5*, 210–218.
- (20) Liu, Y.; Jiang, X. Why microfluidics? Merits and trends in chemical synthesis. *Lab on a Chip* **2017**, *17*, 3960–3978.
- (21) Pan, L.-J.; Tu, J.-W.; Ma, H.-T.; Yang, Y.-J.; Tian, Z.-Q.; Pang, D.-W.; Zhang, Z.-L. Controllable synthesis of nanocrystals in droplet reactors. *Lab on a Chip* **2018**, *18*, 41–56.
- (22) Ma, J.; Lee, S. M.-Y.; Yi, C.; Li, C.-W. Controllable synthesis of functional nanoparticles by microfluidic platforms for biomedical applications – a review. *Lab on a Chip* **2017**, *17*, 209–226.
- (23) Nielsen, L. H.; Keller, S. S.; Boisen, A. Microfabricated devices for oral drug delivery. *Lab on a Chip* **2018**, *18*, 2348–2358.
- (24) Wang, M.; Hu, L.; Xu, C. Recent advances in the design of polymeric microneedles for transdermal drug delivery and biosensing. *Lab on a Chip* **2017**, *17*, 1373–1387.
- (25) Riahi, R.; Tamayol, A.; Shaegh, S. A. M.; Ghaemmaghami, A. M.; Dokmeci, M. R.; Khademhosseini, A. Microfluidics for advanced drug delivery systems. *Current Opinion in Chemical Engineering* **2015**, *7*, 101–112.
- (26) Zhang, B.; Radisic, M. Organ-on-a-chip devices advance to market. *Lab on a Chip* **2017**, *17*, 2395–2420.
- (27) Rothbauer, M.; Zirath, H.; Ertl, P. Recent advances in microfluidic technologies for cell-to-cell interaction studies. *Lab on a Chip* **2018**, *18*, 249–270.
- (28) Caballero, D.; Blackburn, S. M.; de Pablo, M.; Samitier, J.; Albertazzi, L. Tumour-vessel-on-a-chip models for drug delivery. *Lab on a Chip* **2017**, *17*, 3760–3771.
- (29) McLean, I. C.; Schwerdtfeger, L. A.; Tobet, S. A.; Henry, C. S. Powering ex vivo tissue models in microfluidic systems. *Lab on a Chip* **2018**, *18*, 1399–1410.
- (30) Yeo, L. Y.; Chang, H.-C.; Chan, P. P. Y.; Friend, J. R. Microfluidic Devices for Bioapplications. *Small* **2011**, *7*, 12–48.
- (31) Haeberle, S.; Zengerle, R. Microfluidic platforms for lab-on-a-chip applications. *Lab on a Chip* **2007**, *7*, 1094–1110.
- (32) Mark, D.; Haeberle, S.; Roth, G.; von Stetten, F.; Zengerle, R. Microfluidic lab-on-a-chip platforms: requirements, characteristics and applications. *Chemical Society Reviews* **2010**, *39*, 1153–1182.

- (33) Prakash, S.; Yeom, J., *Nanofluidics and Microfluidics*, 1st; Elsevier: Oxford, UK, 2014.
- (34) Henrik, B., *Theoretical Microfluidics*, 1st; Oxford University Press: New York, NY, USA, 2008.
- (35) Holmes, D.; Gawad, S. In *Microengineering in Biotechnology*, Hughes, M. P., Hoettges, K. F., Eds.; Methods in Molecular Biology, Vol. 583; Humana Press: Totowa, NJ, USA, 2010, pp 55–80.
- (36) *Microfluidics in Detection Science - Lab-on-a-chip Technologies*; Labeed, F. H., Fatoyinbo, H. O., Eds.; Royal Society of Chemistry: Cambridge, UK, 2015.
- (37) Rios, A.; Escarpa, A.; Simonet, B., *Miniaturization of Analytical Systems: Principles, Designs and Applications*, 1st; John Wiley & Sons, Ltd: Chichester, UK, 2009, p 371.
- (38) *Microfluidics for Biologists - Fundamentals and Applications*, 1st; Dixit, C. K., Kaushik, A., Eds.; Springer International Publishing: Cham, Switzerland, 2016.
- (39) Sackmann, E. K.; Fulton, A. L.; Beebe, D. J. The present and future role of microfluidics in biomedical research. *Nature* **2014**, *507*, 181–189.
- (40) Lee, S.-J. J.; Sundararajan, N., *Microfabrication for Microfluidics*, 1st; Artech House: Norwood, MA, USA, 2010.
- (41) *Lab-on-a-Chip Devices and Micro-Total Analysis Systems*; Castillo-León, J., Svendsen, W. E., Eds.; Springer International Publishing: Cham, Switzerland, 2015.
- (42) *Microfluidics and Microscale Transport Processes*, 1st; Chakraborty, S., Ed.; CRC Press: Boca Raton, FL, USA, 2013.
- (43) Kleinstreuer, C., *Microfluidics and Nanofluidics*; John Wiley & Sons, Ltd: Hoboken, NJ, USA, 2014.
- (44) Slater, G. W.; Tessier, F.; Kopecka, K. In *Microengineering in Biotechnology*, Hughes, M. P., Hoettges, K. F., Eds.; Humana Press: Totowa, NJ, USA, 2010; Vol. 583, pp 121–134.
- (45) Manz, A.; Effenhauser, C. S.; Burggraf, N.; Harrison, D. J.; Seiler, K.; Fluri, K. Electroosmotic pumping and electrophoretic separations for miniaturized chemical analysis systems. *Journal of Micromechanics and Microengineering* **1994**, *4*, 257–265.
- (46) Go, D. B.; Atashbar, M. Z.; Ramshani, Z.; Chang, H.-C. Surface acoustic wave devices for chemical sensing and microfluidics: a review and perspective. *Analytical Methods* **2017**, *9*, 4112–4134.
- (47) Yeo, L. Y.; Friend, J. R. Surface acoustic wave microfluidics. *Annual Reviews of Fluid Mechanics* **2014**, *46*, 379–406.

- (48) Pollack, M. G.; Pamula, V. K.; Srinivasan, V.; Eckhardt, A. E. Applications of electrowetting-based digital microfluidics in clinical diagnostics. *Expert Review of Molecular Diagnostics* **2011**, *11*, 393–407.
- (49) Mugele, F.; Baret, J.-C. Electrowetting: from basics to applications. *Journal of Physics: Condensed Matter* **2005**, *17*, R705–R774.
- (50) Weigl, B. H. MICROFLUIDICS: Microfluidic Diffusion-Based Separation and Detection. *Science* **1999**, *283*, 346–347.
- (51) Brody, J. P.; Yager, P. Diffusion-based extraction in a microfabricated device. *Sensors and Actuators A: Physical* **1997**, *58*, 13–18.
- (52) Ghosh, A.; Corves, B., *Introduction to Micromechanisms and Microactuators*; Mechanisms and Machine Science, Vol. 28; Springer India: New Delhi, India, 2015.
- (53) Mohammed, M. I.; Haswell, S.; Gibson, I. Lab-on-a-chip or Chip-in-a-lab: Challenges of Commercialization Lost in Translation. *Procedia Technology* **2015**, *20*, 54–59.
- (54) Zhang, C.; Xing, D.; Li, Y. Micropumps, microvalves, and micromixers within PCR microfluidic chips: Advances and trends. *Biotechnology Advances* **2007**, *25*, 483–514.
- (55) Woias, P. Micropumps—past, progress and future prospects. *Sensors and Actuators B: Chemical* **2005**, *105*, 28–38.
- (56) Oh, K. W.; Ahn, C. H. A review of microvalves. *Journal of Micromechanics and Microengineering* **2006**, *16*, R13–R39.
- (57) Au, A. K.; Lai, H.; Utela, B. R.; Folch, A. Microvalves and Micropumps for BioMEMS. *Micromachines* **2011**, *2*, 179–220.
- (58) Wilhelm, E.; Richter, C.; Rapp, B. Phase change materials in microactuators: Basics, applications and perspectives. *Sensors and Actuators A: Physical* **2018**, *271*, 303–347.
- (59) Wang, Y.-N.; Fu, L.-M. Micropumps and biomedical applications – A review. *Microelectronic Engineering* **2018**, *195*, 121–138.
- (60) Cerdà, V.; Ferrer, L.; Avivar, J.; Cerdà, A., *Flow Analysis: A Practical Guide*, 1st; Elsevier: Amsterdam, Netherlands, 2014, p 278.
- (61) *Advances in Flow Injection Analysis and Related Techniques*, 1st; Kolev, S. D., McKelvie, I. D., Eds.; Elsevier B.V.: Oxford, UK, 2008; Vol. 54, p 777.
- (62) Santos, J. L.; Ribeiro, M. F.; Dias, A. C.; Lima, J. L.; Zagatto, E. E. Multi-pumping flow systems: The potential of simplicity. *Analytica Chimica Acta* **2007**, *600*, 21–28.
- (63) Lima, J. L.; Santos, J. L.; Dias, A. C.; Ribeiro, M. F.; Zagatto, E. A. Multi-pumping flow systems: an automation tool. *Talanta* **2004**, *64*, 1091–1098.

- (64) Silva Júnior, J. J.; Farias, M. A.; Silva, V. L.; Montenegro, M. C. B. S. M.; Araújo, A. N.; Lavorante, A. F.; Paim, A. P. S. Spectrophotometric Determination of Thiocyanate in Human Saliva Employing Micropumping Multicommutation Flow System. *Spectroscopy Letters* **2010**, *43*, 213–219.
- (65) Rocha, F. R.; Reis, B. F.; Zagatto, E. A.; Lima, J. L.; Lapa, R. A.; Santos, J. L. Multicommutation in flow analysis: concepts, applications and trends. *Analytica Chimica Acta* **2002**, *468*, 119–131.
- (66) Feres, M. A.; Fortes, P. R.; Zagatto, E. A.; Santos, J. L.; Lima, J. L. Multicommutation in flow analysis: Recent developments and applications. *Analytica Chimica Acta* **2008**, *618*, 1–17.
- (67) Freitas, S. K. B.; da Silva, V. L.; Araújo, A. N.; Montenegro, M. C. B. S. M.; Reis, B. F.; Paim, A. P. S. A multicommutated flow analysis method for the photometric determination of amoxicillin in pharmaceutical formulations using a diazo coupling reaction. *Journal of the Brazilian Chemical Society* **2011**, *22*, 279–285.
- (68) Šrámková, I.; Amorim, C. G.; Sklenářová, H.; Montenegro, M. C.; Horstkotte, B.; Araújo, A. N.; Solich, P. Fully automated analytical procedure for propofol determination by sequential injection technique with spectrophotometric and fluorimetric detections. *Talanta* **2014**, *118*, 104–110.
- (69) Amorim, C.; Souza, R.; Araújo, A.; Montenegro, M.; Silva, V. SI lab-on-valve analysis of histamine using potentiometric detection for food quality control. *Food Chemistry* **2010**, *122*, 871–876.
- (70) Oliveira, H. M.; Segundo, M. A.; Lima, J. L. Automatic flow system for evaluation of polystyrene-divinylbenzene sorbents applied to preconcentration of phenolic pollutants. *International Journal of Environmental Analytical Chemistry* **2011**, *91*, 884–899.
- (71) Mesquita, R. B. R.; Machado, A.; Santos, I. C.; Bordalo, A. A.; Rangel, A. O. S. S. Seasonal monitoring of inland bathing waters using a sequential injection method as a fast and effective tool for nutrient quantification (N : P). *Analytical Methods* **2016**, *8*, 1973–1980.
- (72) Vidigal, S. S.; Tóth, I. V.; Rangel, A. O. Determination of total protein content in white wines by solid phase spectrometry in a SI-LOV system. *Talanta* **2012**, *96*, 102–106.
- (73) Fredrickson, C. K.; Fan, Z. H. Macro-to-micro interfaces for microfluidic devices. *Lab on a Chip* **2004**, *4*, 526–533.
- (74) Temiz, Y.; Lovchik, R. D.; Kaigala, G. V.; Delamarche, E. Lab-on-a-chip devices: How to close and plug the lab? *Microelectronic Engineering* **2015**, *132*, 156–175.

- (75) Atencia, J.; Cooksey, G. A.; Jahn, A.; Zook, J. M.; Vreeland, W. N.; Locascio, L. E. Magnetic connectors for microfluidic applications. *Lab Chip* **2010**, *10*, 246–249.
- (76) Zhao, S. K.; Chen, R.; Yu, Y.; He, L.; Liu, J. Q.; Chen, X.; Qin, S. Y. A multi-functional, plug-and-play and low-cost microfluidic connector system based on electronics standard. *RSC Advances* **2015**, *5*, 97422–97426.
- (77) Murphy, E. R.; Inoue, T.; Sahoo, H. R.; Zaborenko, N.; Jensen, K. F. Solder-based chip-to-tube and chip-to-chip packaging for microfluidic devices. *Lab on a Chip* **2007**, *7*, 1309–1314.
- (78) Johnson, D. G.; Frisina, R. D.; Borkholder, D. A. In-Plane Biocompatible Microfluidic Interconnects for Implantable Microsystems. *IEEE Transactions on Biomedical Engineering* **2011**, *58*, 943–948.
- (79) Nguyen, N.-T.; Wu, Z. Micromixers—a review. *Journal of Micromechanics and Microengineering* **2005**, *15*, R1–R16.
- (80) Lee, C.-Y.; Wang, W.-T.; Liu, C.-C.; Fu, L.-M. Passive mixers in microfluidic systems: A review. *Chemical Engineering Journal* **2016**, *288*, 146–160.
- (81) Cai, G.; Xue, L.; Zhang, H.; Lin, J. A Review on Micromixers. *Micromachines* **2017**, *8*, 274.
- (82) Lee, C.-Y.; Chang, C.-L.; Wang, Y.-N.; Fu, L.-M. Microfluidic Mixing: A Review. *International Journal of Molecular Sciences* **2011**, *12*, 3263–3287.
- (83) Uddin, R.; Donolato, M.; Hwu, E.-T.; Hansen, M. F.; Boisen, A. Combined detection of C-reactive protein and PBMC quantification from whole blood in an integrated lab-on-a-disc microfluidic platform. *Sensors and Actuators B: Chemical* **2018**, *272*, 634–642.
- (84) Mahmodi Arjmand, E.; Saadatmand, M.; Bakhtiari, M.; Eghbal, M. Design and fabrication of a centrifugal microfluidic disc including septum valve for measuring hemoglobin A1c in human whole blood using immunoturbidimetry method. *Talanta* **2018**, *190*, 134–139.
- (85) Phaneuf, C.; Mangadu, B.; Piccini, M.; Singh, A.; Koh, C.-Y. Rapid, Portable, Multiplexed Detection of Bacterial Pathogens Directly from Clinical Sample Matrices. *Biosensors* **2016**, *6*, 49.
- (86) Duffy, E.; Padovani, R.; He, X.; Gorkin, R.; Vereshchagina, E.; Ducrée, J.; Nesterenko, E.; Nesterenko, P. N.; Brabazon, D.; Paull, B.; Vázquez, M. New strategies for stationary phase integration within centrifugal microfluidic platforms for applications in sample preparation and pre-concentration. *Analytical Methods* **2017**, *9*, 1998–2006.
- (87) Cai, Z.; Xiang, J.; Chen, H.; Wang, W. Membrane-based valves and inward-pumping system for centrifugal microfluidic platforms. *Sensors and Actuators B: Chemical* **2016**, *228*, 251–258.

- (88) Schwemmer, F.; Zehle, S.; Mark, D.; von Stetten, F.; Zengerle, R.; Paust, N. A microfluidic timer for timed valving and pumping in centrifugal microfluidics. *Lab on a Chip* **2015**, *15*, 1545–1553.
- (89) Aeinehvand, M. M.; Ibrahim, F.; Harun, S. W.; Al-Faqheri, W.; Thio, T. H. G.; Kazemzadeh, A.; Madou, M. Latex micro-balloon pumping in centrifugal microfluidic platforms. *Lab on a Chip* **2014**, *14*, 988.
- (90) Liu, Q.; Zhang, X.; Chen, L.; Yao, Y.; Ke, S.; Zhao, W.; Yang, Z.; Sui, G. A sample-to-answer labdisc platform integrated novel membrane-resistance valves for detection of highly pathogenic avian influenza viruses. *Sensors and Actuators B: Chemical* **2018**, *270*, 371–381.
- (91) Kinahan, D. J.; Delgado, S. M.; Julius, L. A.; Mallette, A.; Saenz-Ardila, D.; Mishra, R.; Miyazaki, C. M.; Korvink, J.; Mager, D.; Ducree, J. In *2018 IEEE Micro Electro Mechanical Systems (MEMS)*, IEEE: 2018, pp 1213–1216.
- (92) Aeinehvand, M. M.; Magaña, P.; Aeinehvand, M. S.; Aguilar, O.; Madou, M. J.; Martinez-Chapa, S. O. Ultra-rapid and low-cost fabrication of centrifugal microfluidic platforms with active mechanical valves. *RSC Advances* **2017**, *7*, 55400–55407.
- (93) Clark, J.; Kaufman, M.; Fodor, P. S. Mixing Enhancement in Serpentine Micromixers with a Non-Rectangular Cross-Section. *Micromachines* **2018**, *9*, 107–118.
- (94) Mortazavi, S. M. A.; Tirandazi, P.; Normandie, M.; Saidi, M. S. Efficient batch-mode mixing and flow patterns in a microfluidic centrifugal platform: a numerical and experimental study. *Microsystem Technologies* **2017**, *23*, 2767–2779.
- (95) Xiang, J.; Cai, Z.; Zhang, Y.; Wang, W. Mechanically programmed valving technology and the active flow switching application in centrifugal microfluidics. *Sensors and Actuators B: Chemical* **2018**, *259*, 325–331.
- (96) Kim, J.; Kido, H.; Rangel, R. H.; Madou, M. J. Passive flow switching valves on a centrifugal microfluidic platform. *Sensors and Actuators B: Chemical* **2008**, *128*, 613–621.
- (97) Oh, S. J.; Park, B. H.; Jung, J. H.; Choi, G.; Lee, D. C.; Kim, D. H.; Seo, T. S. Centrifugal loop-mediated isothermal amplification microdevice for rapid, multiplex and colorimetric foodborne pathogen detection. *Biosensors and Bioelectronics* **2016**, *75*, 293–300.
- (98) Schwemmer, F.; Blanchet, C. E.; Spilotros, A.; Kosse, D.; Zehle, S.; Mertens, H. D. T.; Graewert, M. A.; Rössle, M.; Paust, N.; Svergun, D. I.; von Stetten, F.; Zengerle, R.; Mark, D. LabDisk for SAXS: a centrifugal microfluidic sample preparation platform for small-angle X-ray scattering. *Lab on a Chip* **2016**, *16*, 1161–1170.

- (99) Keller, M.; Wadle, S.; Paust, N.; Dreesen, L.; Nuese, C.; Strohmeier, O.; Zengerle, R.; von Stetten, F. Centrifugo-thermopneumatic fluid control for valving and aliquoting applied to multiplex real-time PCR on off-the-shelf centrifugal thermocycler. *RSC Advances* **2015**, *5*, 89603–89611.
- (100) Zhao, Y.; Czilwik, G.; Klein, V.; Mitsakakis, K.; Zengerle, R.; Paust, N. C-reactive protein and interleukin 6 microfluidic immunoassays with on-chip pre-stored reagents and centrifugo-pneumatic liquid control. *Lab on a Chip* **2017**, *17*, 1666–1677.
- (101) Hoffmann, J.; Mark, D.; Lutz, S.; Zengerle, R.; von Stetten, F. Pre-storage of liquid reagents in glass ampoules for DNA extraction on a fully integrated lab-on-a-chip cartridge. *Lab on a Chip* **2010**, *10*, 1480–1484.
- (102) Hin, S.; Loskyll, M.; Klein, V.; Keller, M.; Strohmeier, O.; von Stetten, F.; Zengerle, R.; Mitsakakis, K. Membrane-based sample inlet for centrifugal microfluidic cartridges. *Microelectronic Engineering* **2018**, *187-188*, 78–83.
- (103) Ymbern, O.; Sández, N.; Calvo-López, A.; Puyol, M.; Alonso-Chamarro, J. Gas diffusion as a new fluidic unit operation for centrifugal microfluidic platforms. *Lab on a Chip* **2014**, *14*, 1014–1022.
- (104) Ukita, Y.; Oguro, T.; Takamura, Y. Density-gradient-assisted centrifugal microfluidics: an approach to continuous-mode particle separation. *Biomedical Microdevices* **2017**, *19*, 24.
- (105) Chen, Y.-Y.; Fang, Y.-C.; Lin, S.-Y.; Lin, Y.-J.; Yen, S.-Y.; Huang, C.-H.; Yang, C.-Y.; Chau, L.-K.; Wang, S.-C. Corona-induced micro-centrifugal flows for concentration of *Neisseria* and *Salmonella* bacteria prior to their quantitation using antibody-functionalized SERS-reporter nanobeads. *Microchimica Acta* **2017**, *184*, 1021–1028.
- (106) Duffy, G.; Maguire, I.; Heery, B.; Gers, P.; Ducrée, J.; Regan, F. ChromiSense: A colourimetric lab-on-a-disc sensor for chromium speciation in water. *Talanta* **2018**, *178*, 392–399.
- (107) Huang, G.; Huang, Q.; Xie, L.; Xiang, G.; Wang, L.; Xu, H.; Ma, L.; Luo, X.; Xin, J.; Zhou, X.; Jin, X.; Zhang, L. A rapid, low-cost, and microfluidic chip-based system for parallel identification of multiple pathogens related to clinical pneumonia. *Scientific Reports* **2017**, *7*, 6441.
- (108) Koh, C.-Y.; Schaff, U. Y.; Piccini, M. E.; Stanker, L. H.; Cheng, L. W.; Ravichandran, E.; Singh, B.-R.; Sommer, G. J.; Singh, A. K. Centrifugal Microfluidic Platform for Ultrasensitive Detection of Botulinum Toxin. *Analytical Chemistry* **2015**, *87*, 922–928.
- (109) Miyazaki, C. M.; Kinahan, D. J.; Mishra, R.; Mangwanya, F.; Kilcawley, N.; Ferreira, M.; Ducrée, J. Label-free, spatially multiplexed SPR detection of immunoassays on a highly integrated centrifugal Lab-on-a-Disc platform. *Biosensors and Bioelectronics* **2018**, *119*, 86–93.

- (110) Hemmi, A.; Usui, T.; Moto, A.; Tobita, T.; Soh, N.; Nakano, K.; Zeng, H.; Uchiyama, K.; Imato, T.; Nakajima, H. A surface plasmon resonance sensor on a compact disk-type microfluidic device. *Journal of Separation Science* **2011**, *34*, 2913–2919.
- (111) Martin, J. W.; Nieuwoudt, M. K.; Vargas, M. J. T.; Bodley, O. L. C.; Yohendiran, T. S.; Oosterbeek, R. N.; Williams, D. E.; Cather Simpson, M. Raman on a disc: high-quality Raman spectroscopy in an open channel on a centrifugal microfluidic disc. *The Analyst* **2017**, *142*, 1682–1688.
- (112) Yue, S.; Sun, X.; Wang, N.; Wang, Y.; Wang, Y.; Xu, Z.; Chen, M.; Wang, J. SERS–Fluorescence Dual-Mode pH-Sensing Method Based on Janus Microparticles. *ACS Applied Materials & Interfaces* **2017**, *9*, 39699–39707.
- (113) Sanger, K.; Zór, K.; Bille Jendresen, C.; Heiskanen, A.; Amato, L.; Toftgaard Nielsen, A.; Boisen, A. Lab-on-a-disc platform for screening of genetically modified *E. coli* cells via cell-free electrochemical detection of p-Coumaric acid. *Sensors and Actuators B: Chemical* **2017**, *253*, 999–1005.
- (114) McArdle, H.; Jimenez-Mateos, E. M.; Raof, R.; Carthy, E.; Boyle, D.; ElNaggar, H.; Delanty, N.; Hamer, H.; Dogan, M.; Huchtemann, T.; Körtvelyessy, P.; Rosenow, F.; Forster, R. J.; Henshall, D. C.; Spain, E. “TORNADO” – Theranostic One-Step RNA Detector; microfluidic disc for the direct detection of microRNA-134 in plasma and cerebrospinal fluid. *Scientific Reports* **2017**, *7*, 1750.
- (115) Andreasen, S. Z.; Kwasny, D.; Amato, L.; Brøgger, A. L.; Bosco, F. G.; Andersen, K. B.; Svendsen, W. E.; Boisen, A. Integrating electrochemical detection with centrifugal microfluidics for real-time and fully automated sample testing. *RSC Advances* **2015**, *5*, 17187–17193.
- (116) Kong, L. X.; Perebikovskiy, A.; Moebius, J.; Kulinsky, L.; Madou, M. Lab-on-a-CD: A Fully Integrated Molecular Diagnostic System. *Journal of Laboratory Automation* **2016**, *21*, 323–355.
- (117) Strohmeier, O.; Keller, M.; Schwemmer, F.; Zehnle, S.; Mark, D.; von Stetten, F.; Zengerle, R.; Paust, N. Centrifugal microfluidic platforms: advanced unit operations and applications. *Chemical Society Reviews* **2015**, *44*, 6187–6229.
- (118) Burger, R.; Amato, L.; Boisen, A. Detection methods for centrifugal microfluidic platforms. *Biosensors and Bioelectronics* **2016**, *76*, 54–67.
- (119) King, D.; O’Sullivan, M.; Ducrée, J. Optical detection strategies for centrifugal microfluidic platforms. *Journal of Modern Optics* **2014**, *61*, 85–101.
- (120) Maguire, I.; O’Kennedy, R.; Ducrée, J.; Regan, F. A review of centrifugal microfluidics in environmental monitoring. *Analytical Methods* **2018**, *10*, 1497–1515.
- (121) Tang, M.; Wang, G.; Kong, S.-K.; Ho, H.-P. A Review of Biomedical Centrifugal Microfluidic Platforms. *Micromachines* **2016**, *7*, 26.

- (122) Michael, I.; Kim, T.-H.; Sunkara, V.; Cho, Y.-K. Challenges and Opportunities of Centrifugal Microfluidics for Extreme Point-of-Care Testing. *Micromachines* **2016**, *7*, 32.
- (123) Abaxis Piccolo Xpress.
- (124) Biosurfit Spinit.
- (125) GenePOC Revogene.
- (126) Roche Cobas b 101.
- (127) Samsung LABGEO IB10.
- (128) Technologies, G. P. Gyrolab xPlore.
- (129) Nolting, W., *Theoretical Physics 1 - Classical Mechanics*; Springer International Publishing: Cham, Switzerland, 2016.
- (130) Ducrée, J.; Haeberle, S.; Lutz, S.; Pausch, S.; Stetten, F. V.; Zengerle, R. The centrifugal microfluidic Bio-Disk platform. *Journal of Micromechanics and Microengineering* **2007**, *17*, S103–S115.
- (131) Ducrée, J.; Haeberle, S.; Brenner, T.; Glatzel, T.; Zengerle, R. Patterning of flow and mixing in rotating radial microchannels. *Microfluidics and Nanofluidics* **2006**, *2*, 97–105.
- (132) Ren, Y.; Leung, W. W.-F. Numerical and experimental investigation on flow and mixing in batch-mode centrifugal microfluidics. *International Journal of Heat and Mass Transfer* **2013**, *60*, 95–104.
- (133) Ren, Y.; Leung, W. W.-F. Vortical flow and mixing in rotating milli- and micro-chambers. *Computers & Fluids* **2013**, *79*, 150–166.
- (134) Moore, J. L.; McCuiston, A.; Mittendorf, I.; Ottway, R.; Johnson, R. D. Behavior of capillary valves in centrifugal microfluidic devices prepared by three-dimensional printing. *Microfluidics and Nanofluidics* **2011**, *10*, 877–888.
- (135) Zehnle, S.; Schwemmer, F.; Bergmann, R.; von Stetten, F.; Zengerle, R.; Paust, N. Pneumatic siphon valving and switching in centrifugal microfluidics controlled by rotational frequency or rotational acceleration. *Microfluidics and Nanofluidics* **2015**, *19*, 1259–1269.
- (136) Martinez-Duarte, R.; Gorkin III, R. A.; Abi-Samra, K.; Madou, M. J. The integration of 3D carbon-electrode dielectrophoresis on a CD-like centrifugal microfluidic platform. *Lab on a Chip* **2010**, *10*, 1030.
- (137) Czilwik, G.; Vashist, S. K.; Klein, V.; Buderer, A.; Roth, G.; von Stetten, F.; Zengerle, R.; Mark, D. Magnetic chemiluminescent immunoassay for human C-reactive protein on the centrifugal microfluidics platform. *RSC Advances* **2015**, *5*, 61906–61912.

- (138) Kirby, D.; Siegrist, J.; Kijanka, G.; Zavattoni, L.; Sheils, O.; O'Leary, J.; Burger, R.; Ducrée, J. Centrifugo-magnetophoretic particle separation. *Microfluidics and Nanofluidics* **2012**, *13*, 899–908.
- (139) Carpentras, D.; Kulinsky, L.; Madou, M. A Novel Magnetic Active Valve for Lab-on-CD Technology. *Journal of Microelectromechanical Systems* **2015**, *24*, 1322–1330.
- (140) *Unravelling Single Cell Genomics*, 1st; Bontoux, N., Dauphinot, L., Potier, M.-C., Eds.; Royal Society of Chemistry: Cambridge, UK, 2010.
- (141) Petersen, K. Silicon as a mechanical material. *Proceedings of the IEEE* **1982**, *70*, 420–457.
- (142) Gardeniers, J.; Oosterbroek, R.; van den Berg, A. In *Lab-on-a-Chip*, Oosterbroek, R. E., van den Berg, A., Eds.; Elsevier B.V.: Oxford, UK, 2003, pp 37–64.
- (143) Iliescu, C.; Taylor, H.; Avram, M.; Miao, J.; Franssila, S. A practical guide for the fabrication of microfluidic devices using glass and silicon. *Biomicrofluidics* **2012**, *6*, 016505.
- (144) Ren, K.; Zhou, J.; Wu, H. Materials for Microfluidic Chip Fabrication. *Accounts of Chemical Research* **2013**, *46*, 2396–2406.
- (145) Folch, A., *Introduction to BioMEMS*; CRC Press: Boca Raton, FL, USA, 2013, p 528.
- (146) Sugioka, K.; Xu, J.; Wu, D.; Hanada, Y.; Wang, Z.; Cheng, Y.; Midorikawa, K. Femtosecond laser 3D micromachining: a powerful tool for the fabrication of microfluidic, optofluidic, and electrofluidic devices based on glass. *Lab Chip* **2014**, *14*, 3447–3458.
- (147) Pessoa de Santana, P.; Segato, T. P.; Carrilho, E.; Lima, R. S.; Dossi, N.; Kamogawa, M. Y.; Gobbi, A. L.; Piazzeta, M. H.; Piccin, E. Fabrication of glass microchannels by xurography for electrophoresis applications. *The Analyst* **2013**, *138*, 1660–1664.
- (148) Imanaka, Y., *Multilayered Low Temperature Cofired Ceramics (LTCC) Technology*; Springer: New York, NY, USA, 2005.
- (149) Vasudev, A.; Kaushik, A.; Jones, K.; Bhansali, S. Prospects of low temperature co-fired ceramic (LTCC) based microfluidic systems for point-of-care biosensing and environmental sensing. *Microfluidics and Nanofluidics* **2013**, *14*, 683–702.
- (150) Ibáñez-García, N.; Alonso, J.; Martínez-Cisneros, C. S.; Valdés, F. Green-tape ceramics. New technological approach for integrating electronics and fluidics in microsystems. *TrAC Trends in Analytical Chemistry* **2008**, *27*, 24–33.

- (151) Calvo-López, A.; Arasa-Puig, E.; Puyol, M.; Casalta, J. M.; Alonso-Chamarro, J. Biparametric potentiometric analytical microsystem for nitrate and potassium monitoring in water recycling processes for manned space missions. *Analytica Chimica Acta* **2013**, *804*, 190–196.
- (152) Da Rocha, Z. M.; Martínez-Cisneros, C. S.; Seabra, A. C.; Valdés, F.; Gongora-Rubio, M. R.; Alonso-Chamarro, J. Compact and autonomous multiwavelength microanalyzer for in-line and in situ colorimetric determinations. *Lab Chip* **2012**, *12*, 109–117.
- (153) Pedro, S. G.-d.; Puyol, M.; Izquierdo, D.; Salinas, I.; de la Fuente, J. M.; Alonso-Chamarro, J. A ceramic microreactor for the synthesis of water soluble CdS and CdS/ZnS nanocrystals with on-line optical characterization. *Nanoscale* **2012**, *4*, 1328.
- (154) Martínez-Cisneros, C. S.; Pedro, S. G.-d.; Puyol, M.; García-García, J.; Alonso-Chamarro, J. Design, fabrication and characterization of microreactors for high temperature syntheses. *Chemical Engineering Journal* **2012**, *211-212*, 432–441.
- (155) Gongora-Rubio, M.; Espinoza-Vallejos, P.; Sola-Laguna, L.; Santiago-Avilés, J. Overview of low temperature co-fired ceramics tape technology for meso-system technology (MsST). *Sensors and Actuators A: Physical* **2001**, *89*, 222–241.
- (156) Jiang, B.; Maeder, T.; Santis-Alvarez, A. J.; Poulidakos, D.; Mural, P. A low-temperature co-fired ceramic micro-reactor system for high-efficiency on-site hydrogen production. *Journal of Power Sources* **2015**, *273*, 1202–1217.
- (157) Pedro, S. G.-d.; Salinas-Castillo, A.; Ariza-Avidad, M.; Lapresta-Fernández, A.; Sánchez-González, C.; Martínez-Cisneros, C. S.; Puyol, M.; Capitan-Vallvey, L. F.; Alonso-Chamarro, J. Microsystem-assisted synthesis of carbon dots with fluorescent and colorimetric properties for pH detection. *Nanoscale* **2014**, *6*, 6018–6024.
- (158) Berenguel Alonso, M. Lab on a Chip Systems for Biochemical Analysis, Biology and Synthesis., Ph.D. Thesis, Universitat Autònoma de Barcelona, 2017.
- (159) Couceiro, P.; Alonso-Chamarro, J. Microfabrication of Monolithic Microfluidic Platforms Using Low Temperature Co-Fired Ceramics Suitable for Fluorescence Imaging. *Analytical Chemistry* **2017**, *89*, 9147–9153.
- (160) Couceiro, P.; Gómez-de Pedro, S.; Alonso-Chamarro, J. All-ceramic analytical microsystems with monolithically integrated optical detection microflow cells. *Microfluidics and Nanofluidics* **2015**, *18*, 649–656.
- (161) Becker, H.; Gärtner, C. Polymer microfabrication methods for microfluidic analytical applications. *Electrophoresis* **2000**, *21*, 12–26.
- (162) Fiorini, G. S.; Chiu, D. T. Disposable microfluidic devices: fabrication, function, and application. *BioTechniques* **2005**, *38*, 429–446.

- (163) Tsao, C.-W. Polymer Microfluidics: Simple, Low-Cost Fabrication Process Bridging Academic Lab Research to Commercialized Production. *Micromachines* **2016**, *7*, 225.
- (164) Becker, H.; Gärtner, C. Polymer microfabrication technologies for microfluidic systems. *Analytical and Bioanalytical Chemistry* **2008**, *390*, 89–111.
- (165) Waldbaur, A.; Rapp, H.; Länge, K.; Rapp, B. E. Let there be chip—towards rapid prototyping of microfluidic devices: one-step manufacturing processes. *Analytical Methods* **2011**, *3*, 2681–2716.
- (166) Sollier, E.; Murray, C.; Maoddi, P.; Di Carlo, D. Rapid prototyping polymers for microfluidic devices and high pressure injections. *Lab on a Chip* **2011**, *11*, 3752.
- (167) Tsao, C. W.; DeVoe, D. L. Bonding of thermoplastic polymer microfluidics. *Microfluidics and Nanofluidics* **2009**, *6*, 1–16.
- (168) Bhattacharjee, N.; Urrios, A.; Kang, S.; Folch, A. The upcoming 3D-printing revolution in microfluidics. *Lab on a Chip* **2016**, *16*, 1720–1742.
- (169) Chen, C.; Mehl, B. T.; Munshi, A. S.; Townsend, A. D.; Spence, D. M.; Martin, R. S. 3D-printed microfluidic devices: fabrication, advantages and limitations—a mini review. *Analytical Methods* **2016**, *8*, 6005–6012.
- (170) Au, A. K.; Huynh, W.; Horowitz, L. F.; Folch, A. 3D-Printed Microfluidics. *Angewandte Chemie International Edition* **2016**, *55*, 3862–3881.
- (171) Waheed, S.; Cabot, J. M.; Macdonald, N. P.; Lewis, T.; Guijt, R. M.; Paull, B.; Breadmore, M. C. 3D printed microfluidic devices: enablers and barriers. *Lab on a Chip* **2016**, *16*, 1993–2013.
- (172) McDonald, J. C.; Duffy, D. C.; Anderson, J. R.; Chiu, D. T.; Wu, H.; Schueller, O. J. A.; Whitesides, G. M. Fabrication of microfluidic systems in poly(dimethylsiloxane). *Electrophoresis* **2000**, *21*, 27–40.
- (173) McDonald, J. C.; Whitesides, G. M. Poly(dimethylsiloxane) as a Material for Fabricating Microfluidic Devices. *Accounts of Chemical Research* **2002**, *35*, 491–499.
- (174) Kuncova-Kallio, J.; Kallio, P. J. In *2006 International Conference of the IEEE Engineering in Medicine and Biology Society*, IEEE: 2006, pp 2486–2489.
- (175) Mukhopadhyay, R. When PDMS isn't the best. *Analytical Chemistry* **2007**, *79*, 3248–3253.
- (176) Becker, H. It's the economy... *Lab on a Chip* **2009**, *9*, 2759.
- (177) Nunes, P. S.; Ohlsson, P. D.; Ordeig, O.; Kutter, J. P. Cyclic olefin polymers: emerging materials for lab-on-a-chip applications. *Microfluidics and Nanofluidics* **2010**, *9*, 145–161.

- (178) Bundgaard, F.; Perozziello, G.; Geschke, O. Rapid prototyping tools and methods for all-Topas® cyclic olefin copolymer fluidic microsystems. *Proceedings of the Institution of Mechanical Engineers, Part C: Journal of Mechanical Engineering Science* **2006**, *220*, 1625–1632.
- (179) TOPAS Advanced Polymers TOPAS.
- (180) Zeon Chemicals ZEONEX.
- (181) Yamazaki, M Industrialization and application development of cyclo-olefin polymer. *Journal of Molecular Catalysis A: Chemical* **2004**, *213*, 81–87.
- (182) Steigert, J.; Haeberle, S.; Brenner, T.; Müller, C.; Steinert, C. P.; Koltay, P.; Gottschlich, N.; Reinecke, H.; Rühle, J.; Zengerle, R.; Ducrée, J Rapid prototyping of microfluidic chips in COC. *Journal of Micromechanics and Microengineering* **2007**, *17*, 333–341.
- (183) Akyazi, T.; Basabe-Desmonts, L.; Benito-Lopez, F. Review on microfluidic paper-based analytical devices towards commercialisation. *Analytica Chimica Acta* **2018**, *1001*, 1–17.
- (184) Ballerini, D. R.; Li, X.; Shen, W. Patterned paper and alternative materials as substrates for low-cost microfluidic diagnostics. *Microfluidics and Nanofluidics* **2012**, *13*, 769–787.
- (185) He, Y.; Wu, Y.; Fu, J.-Z.; Wu, W.-B. Fabrication of paper-based microfluidic analysis devices: a review. *RSC Advances* **2015**, *5*, 78109–78127.
- (186) Yanagawa, F.; Sugiura, S.; Kanamori, T. Hydrogel microfabrication technology toward three dimensional tissue engineering. *Regenerative Therapy* **2016**, *3*, 45–57.
- (187) Chung, B. G.; Lee, K.-H.; Khademhosseini, A.; Lee, S.-H. Microfluidic fabrication of microengineered hydrogels and their application in tissue engineering. *Lab Chip* **2012**, *12*, 45–59.
- (188) Caicedo, H. H.; Brady, S. T. Microfluidics: The Challenge Is to Bridge the Gap Instead of Looking for a 'Killer App'. *Trends in Biotechnology* **2016**, *34*, 1–3.
- (189) Skoog, D. A.; Holler, F. J.; Crouch, S. R., *Principles of Instrumental Analysis*, 6th; Cengage Learning: Boston, MA, USA, 2006.
- (190) Harris, D. C., *Quantitative Chemical Analysis*, 7th; W. H. Freeman and Company: New York, NY, USA, 2007.
- (191) Dasgupta, P. K.; Eom, I.-Y.; Morris, K. J.; Li, J. Light emitting diode-based detectors. *Analytica Chimica Acta* **2003**, *500*, 337–364.
- (192) Yang, F.-B.; Pan, J.-Z.; Zhang, T.; Fang, Q. A low-cost light-emitting diode induced fluorescence detector for capillary electrophoresis based on an orthogonal optical arrangement. *Talanta* **2009**, *78*, 1155–1158.

-
- (193) De Lima, K. M. G. A portable photometer based on LED for the determination of aromatic hydrocarbons in water. *Microchemical Journal* **2012**, *103*, 62–67.
- (194) O'Toole, M.; Lau, K. T.; Shepherd, R.; Slater, C.; Diamond, D. Determination of phosphate using a highly sensitive paired emitter–detector diode photometric flow detector. *Analytica Chimica Acta* **2007**, *597*, 290–294.
- (195) Pujol-Vila, F.; Giménez-Gómez, P.; Santamaria, N.; Antúnez, B.; Vigués, N.; Díaz-González, M.; Jiménez-Jorquera, C.; Mas, J.; Sacristán, J.; Muñoz-Berbel, X. Portable and miniaturized optofluidic analysis system with ambient light correction for fast in situ determination of environmental pollution. *Sensors and Actuators B: Chemical* **2016**, *222*, 55–62.
- (196) Ymbern, O.; Berenguel-Alonso, M.; Calvo-López, A.; Gómez-de Pedro, S.; Izquierdo, D.; Alonso-Chamarro, J. Versatile Lock and Key Assembly for Optical Measurements with Microfluidic Platforms and Cartridges. *Analytical Chemistry* **2015**, *87*, 1503–1508.

Chapter 2

Objectives

The Group of Sensors and Biosensors from the Universitat Autònoma de Barcelona has extensive experience in the development of LOC systems, which have been successfully applied to a wide variety of fields including biomedicine, environmental monitoring and astronautics. The development of these microsystems has been possible due to a proprietary fabrication methodology which has been progressively developed during the last few years and which is continuously increasing its potential as a result of the accumulative contribution of the different members of the group.

In this context, the work presented in this dissertation aims to contribute to the existing fabrication methodology by providing new tools with enhanced characteristics to the currently available microfluidic toolbox, as well as to broaden the scope of the LOC applications. In this particular case, wine industry is the targeted field, having a major impact in the economy of both Catalonia and Spain.

The main purpose of this work is divided into several intermediate objectives which can be summarised as:

- The development of a versatile pressure-driven microfluidic system for the continuous monitoring of several parameters of interest in must and wine during wine-making processes.
- The development of a versatile centrifugal microfluidic system for the parallel enzymatic analysis of several parameters of interest in must and wine samples.
- The development of a novel valving system for centrifugal microfluidic platforms with enhanced characteristics.

Chapter 3

Microfabrication methodology

All the devices presented in this dissertation have been fabricated using COC as the substrate material. This thermoplastic is becoming extensively used in microfluidics owing to its promising properties, previously exposed in § 1.3.3.2.

The selection of this material for the construction of the devices was mainly due to its thermal and optical properties. The possibility of using a multilayer approach for a rapid and simple construction of devices makes COC an excellent material for working at the prototyping scale. Furthermore, its high transparency in the visible and near ultraviolet regions of the spectrum¹ enables optical measurements through layers. Both qualities of COC have been extensively exploited over the course of this work. Apart from COC, other materials such as LTCC or PDMS have been used for punctual fabrication steps or applications. A microstructuring process using LTCC masters has been developed for engraving small features into COC layers (see § 3.2.2.2), while PDMS has been used for the development of a new type of valve for centrifugal microfluidic platforms (see § 6).

The construction of the devices has been carried out in the microfabrication facilities of the group. The infrastructure that we have at our disposal permits us to perform not only all the fabrication processes described in this chapter, but also other interesting techniques such as the screen-printing of electrodes²⁻⁴ and the integration of gas diffusion membranes^{3,5,6}. A thorough description of the COC fabrication methodology employed is provided hereafter. Specific particularities of each device will be discussed later on in the corresponding chapters.

3.1 COC as the substrate material

Thermal properties of cyclic olefin copolymers depend on the cyclic monomer and the polymerisation process used for their synthesis.⁷ Hence, by tuning the polymerisation conditions, a range of polymer grades that basically differ on the glass transition temperature (T_g) and the heat distortion (or deflection) temperature (HDT) can be easily obtained. Taking advantage of this property, a multilayer approach that consists in the

creation of 3D structures by means of the stacking of several 2D layers has been used for the construction of the devices.

Glass transition temperature versus heat distortion temperature^{8–10}

The *glass transition temperature* (T_g) of an amorphous polymer is defined as the temperature at which the polymer changes from a rigid amorphous glassy solid to a bendable and soft material. Normally, amorphous polymers do not have a sharp softening point. Instead, this change slowly occurs over a range of temperatures, hence being the T_g the temperature at which this change starts.

Heat distortion temperature (HDT) is defined as the temperature at which a polymer distorts by a certain amount under controlled stress. Therefore, it describes the maximum temperature at which the material can be used for structural applications.

Despite both parameters are used to define the thermal properties of a polymer, they should not be confused. T_g is related to the movement of the polymer chains that conform the material, thus being related to its internal structure, whereas HDT is associated to the macroscopic behaviour of the material. For amorphous polymers, which is the case of COC, HDT is somewhat lower than T_g .

Extruded COC layers were purchased from TOPAS Advanced Polymers (Florence, USA). TOPAS[®] is a registered trademark and stands for Thermoplastic Olefin Polymer of Amorphous Structure. TOPAS is obtained by the chain copolymerisation of norbornene and ethylene using a metallocene catalyst (see [Figure 3.1](#)).¹¹ Different TOPAS grades showing different thermal properties are obtained by changing the norbornene/ethylene proportion.

A broad diversity of TOPAS products are commercially available. The purchased layers (see [Table 3.1](#)) covered a range from 78 °C to 178 °C in T_g and from 25 µm to 2 mm in thickness. The multiple combination possibilities arising from this wide variety of TOPAS layers gave flexibility to the whole construction process and, especially, to the bonding process, where the use of layers with different T_g values was particularly advantageous in order to prevent the deformation of the internal structures of the devices. Generally, TOPAS layers presenting high T_g values (TOPAS 5013, 6013, 6016 and 6017) were used as structural layers, whereas TOPAS layers with lower T_g values (TOPAS 8007) were used as bonding layers.^{12,13}

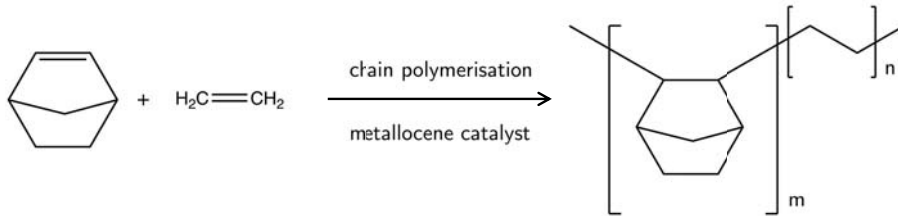


Figure 3.1: Reaction scheme for the production of TOPAS. The norbornene and ethylene proportion in the final product (m, n) define the grade of the polymer. Redrawn and adapted from reference [1].

Table 3.1: Thermal properties of TOPAS grades.^{11,14} TOPAS extruded layers are available in several thicknesses; purchased layers are here indicated.

	TOPAS grade					
	Unit	8007	5013	6013	6015	6017
Norbornene content	mol %	36	50	52	56	62
Glass transition temperature (T_g)	$^{\circ}\text{C}$	79	135	142	161	181
Heat deflection temperature (HDT) at 4.5 bar	$^{\circ}\text{C}$	75	130	130	150	170
Extruded layer thickness (μm)						
	25	✓				
	50	✓				
	100		✓		✓	
	150		✓	✓	✓	
	300	✓		✓		
	400		✓	✓		
	500		✓	✓	✓	
	1000		✓	✓	✓	✓
	2000		✓	✓	✓	✓

3.2 Fabrication process of COC devices

The general fabrication process of polymeric devices can be divided into three main steps: design, microstructuring and back-end processing.¹⁵ The fabrication process that has been followed for the development of COC devices follows the same scheme (see Figure 3.2). The process started with the design of the different layers of the prototypes, followed by the individual microstructuring of these layers. Afterwards, a thermocompression process was carried out for bonding the layers and sealing the device. A last machining step was usually required for defining the final shape of the

device.

If necessary, other components such as electrodes^{3,4} or separation membranes^{3,5,6} could be integrated before the thermocompression process. Elements that did not resist temperature and/or pressure or that were placed on the external part of the device were added once the device was finished.

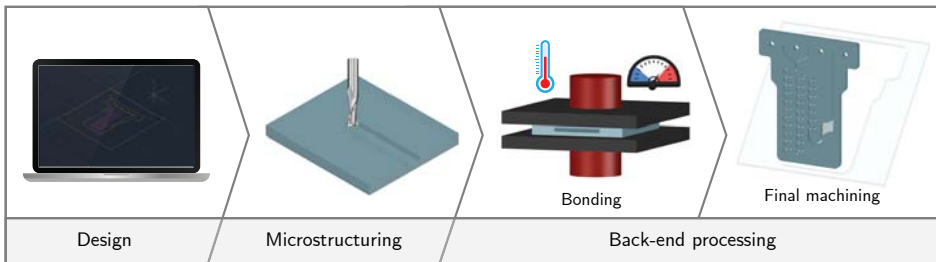


Figure 3.2: General fabrication process of COC microfluidic devices. Back-end processing may include other steps that are not depicted in this figure for the better understanding of the scheme.

Three different techniques have been employed for the microstructuring of the layers: micromilling, hot embossing and laser ablation. Micromilling has been the main used technique, while hot embossing was only required when features with smaller dimensions than the micromilling resolution were needed. Some experiments were performed for the direct laser ablation of COC with no successful results.

A detailed description of the main fabrication steps, design, microstructuring and bonding, is provided below. A brief summary of additional back-end processes is found at the end of this chapter.

3.2.1 Design

As previously mentioned, the fabrication method of the COC devices was based on a multilayer approach, where the final 3D structures were obtained by the overlapping of several individually micromachined layers. Thus, the fabrication process started with the design of the different layers that constituted the complete device. This step was performed by using computer aided design (CAD) software.

Principally, two different strategies can be used for the design of the layers. The selection of the appropriate strategy depends on the micromachining equipment to be used and its corresponding software. The first approach consists in drawing the motifs in the desired final dimensions, which could be understood as a “what you see is what you get” strategy (see [Figure 3.3.a](#)). In this case, the software of the equipment is in charge of choosing the appropriate microstructuring parameters and tools to create the motifs. Alternatively, the design can be constituted by the different lines where the

microstructuring tool has to pass through to produce the motifs (see Figure 3.3.b). These lines are commonly known as toolpaths. For the toolpath design approach, the selection of the micromachining parameters and tools is depending on the user. The devices presented in this work have been designed by using this second approach.

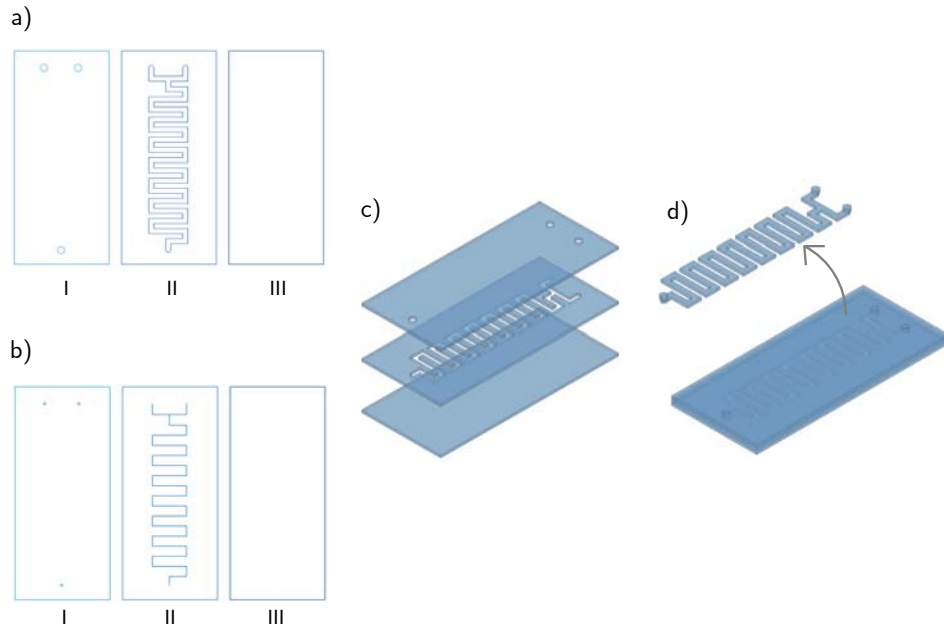


Figure 3.3: Multilayer approach for the construction of a micromixer. The different layers that will constitute the final structure, a top layer containing the inlet and outlet holes (I), a middle layer containing the main structure (II) and a bottom layer for sealing the device (III), are individually designed. The two possible design strategies are here represented: a) “what you see is what you get” approach, where the equipment software will choose the appropriate microstructuring parameters and tools to create the drawn design; and b) toolpath design approach, where the user is in charge of choosing the microstructuring parameters and tools. In this example, the two designs are equivalent for a 0.8 mm diameter milling tool selection for the toolpath design strategy. The stacking of the different microstructured layers (c) will create the final 3D structure containing the micromixer (d).

In the case of micromilling, the width and depth of the cut were determined by the diameter of the tool being used and the selection of its penetration, respectively. On the other hand, for laser ablation, the width of the cut was determined by the laser beam diameter, which had a fixed value. The penetration of the laser beam could be tuned by changing different parameters such as the power or the mark speed. However,

it presented some limitation and, in order to obtain deeper motifs, several overlapped lines had to be drawn.

Once the design was finished, the individual layer designs were processed using computer-aided manufacturing (CAM) software. This software created a CAM file that could be transferred and interpreted by the microstructuring machine.

3.2.2 Microstructuring

The three different COC microstructuring methods used during this work are presented in the next sections: micromilling, hot embossing and laser ablation. Two of them, micromilling and hot embossing, were used for the construction of the devices, whereas direct laser ablation of COC was only studied.

3.2.2.1 Micromilling

All the devices presented in this thesis were totally or partially microstructured by micromilling. Despite presenting some limitations concerning the roughness of the surfaces and the resolution of the structures, this technique is considered a powerful method for the construction of polymeric devices at the prototyping scale due to its rapidity and simplicity.^{16–18}

A computer numerically controlled (CNC) micromilling machine Protomat C100/HF from LPKF Laser & Electronics (Garbsen, Germany) was employed. This equipment allowed the control of several working parameters such as the rotation speed and the XY displacement speed of the tool, among others. The adjustment of these parameters depended on the selected tool, the required precision for the motif and the grade and thickness of the TOPAS layer.

As mentioned before, the width of the cut was determined by the diameter of the tool. A wide range of milling and drilling tools with different cut profiles and diameters is commercially available (see [Figure 3.4](#)). For the devices presented in this work, end mill tools from 0.4 mm to 3 mm in diameter were chosen for the microstructuring of channels and chambers, whereas spiral drill tools from 0.4 mm to 2 mm in diameter were used for through-layer holes.

The tool penetration distance was manually adjusted using a micrometre with a 10 μm resolution. This precision in the Z axis permitted not only the microstructuring of through-layer motifs, but also the micromilling of bas-relief structures. Normally, several steps with accumulative penetration distances were carried out in order to achieve the desired depth of the motifs but avoiding the damage of the tool. The selection of this distance was mainly determined by the diameter of the tool being used: the thinner the tool was, the lower the penetration per step was selected.

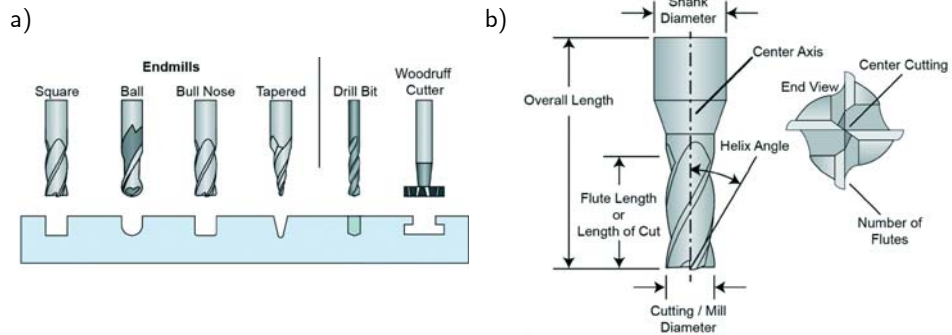


Figure 3.4: a) Different types of milling tools and their corresponding cut profiles.
b) Parameters defining a milling tool. Adapted from reference¹⁷.

Some of the devices that will be presented required the patterning of microchannels of less than 100 μm in both height and width. Since such small dimensions were not achievable by common micromilling equipment,¹⁷ we developed an hybrid fabrication method that combined hot embossing for the smallest features and micromilling for the large motifs.¹⁹

3.2.2.2 Hot embossing

Taking advantage of the experience of the group and the infrastructure we had at our disposal, we developed a simple and cost-effective method for engraving small features into COC layers which consisted in the hot embossing of the motifs using home-made LTCC masters.

Despite being considered a fast and inexpensive microstructuring method for mass production, hot embossing processes are generally not suitable at the prototyping scale owing to the expensive and time-consuming fabrication of masters.^{20,21} Nonetheless, alternatives to classic mould materials and mould fabrication processes in order to lower costs and reduce manufacturing time have already been proposed.^{22,23} In our case, the novel use of LTCC as the substrate material for the construction of the master enabled a rapid and low-cost master prototyping, thereby simplifying the overall process and making it suitable for prototyping purposes. Besides, the constructed masters demonstrated excellent performance, remaining completely functional and showing no evident deterioration after more than 30 hot embossing runs.

The LTCC master construction and the later engraving of the features into a COC layer are schematically depicted in [Figure 3.5](#).

The master construction started with the lamination of eight 254 μm thick Green-TapeTM 951 LTCC layers (DuPontTM, Wilmington, USA) in a uniaxial hydraulic press (Francisco Camps, Granollers, Spain) at 70 $^{\circ}\text{C}$ and 30 bar for 5 minutes, obtaining a

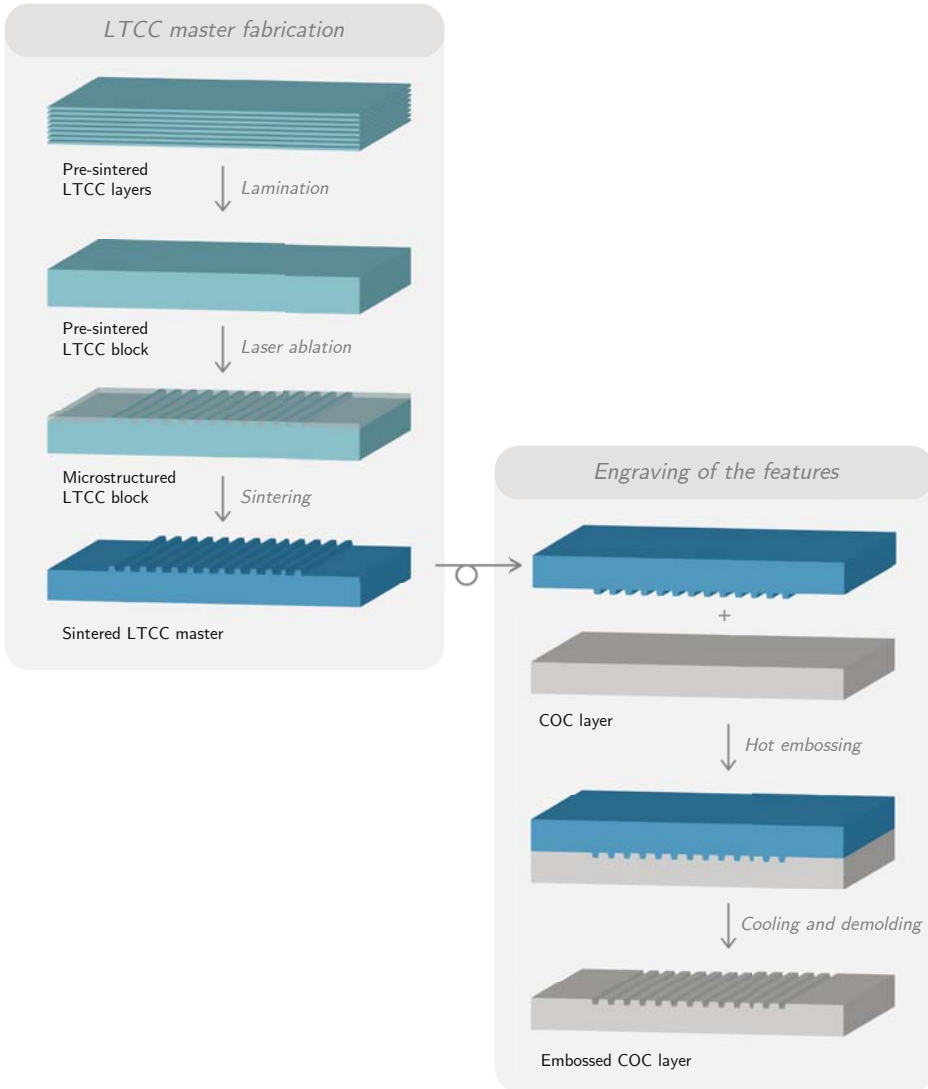


Figure 3.5: LTCC master construction and engraving of the master features onto a COC layer.

compact and indivisible LTCC block. Then, the surface of the ceramic block was etched by using a Protolaser 200 laser (LPKF Laser & Electronics). This neodymium-doped yttrium aluminium garnet (Nd:YAG) laser, working at 1064 nm, had a 25 μm resolution

(corresponding to the laser beam diameter). Thus, the design of the ablation pattern consisted in several arrays of lines at 25 μm distance between them creating the negative image of the design to be engraved onto the COC surface. The shrinkage of the LTCC during the sintering process (12.7% in the XY plane and 15% in the Z plane according to DuPont²⁴) had to be considered when designing the pattern. The sintering process was performed in a programmable box furnace CBCWF11/23P16 (Carbolite, Afora, Spain). The temperature profile of the sintering process is shown in Figure 3.6.a. As mentioned in § 1.3.2, LTCC are mainly composed of Al_2O_3 (45%), SiO_2 (40%) and organic components (15%).²⁵ During the first plateau at 350 °C, the organic components of the material volatilise. During the second plateau, at 850 °C, the glass particles melt and cover the alumina particles (see Figure 3.6.b). When temperature descends, glass particles vitrify, resulting in a rigid and compact final structure.

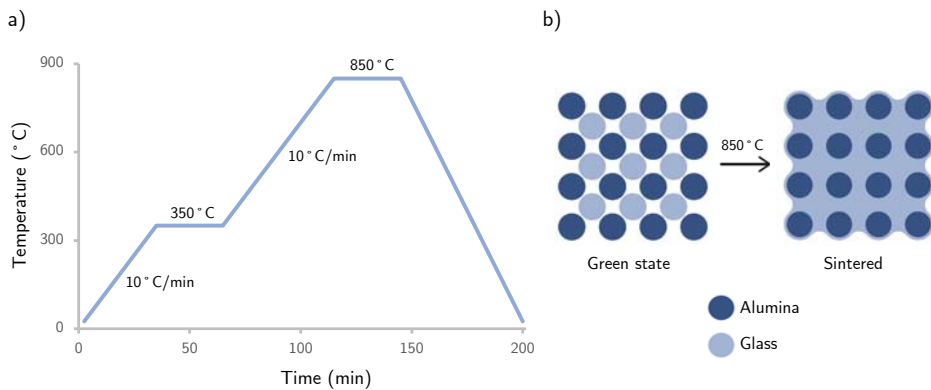


Figure 3.6: a) Temperature profile of the sintering process.²⁴ b) During the second plateau of the sintering process, at 850 °C, the glass particles melt and cover the alumina particles.

For the engraving of the motifs into the polymer layer, a thermocompression process (the actual hot embossing) was carried out. With that purpose, the master and a COC structural layer were thermocompressed together in the hydraulic press at $P_{\text{max}} = 6$ bar and $T_{\text{max}} > T_g$, thus depending the applied temperature on the selected TOPAS layer grade. As an example, for TOPAS 6013 layers, with a T_g of 142 °C, the thermocompression conditions were $P_{\text{max}} = 6$ bar and $T_{\text{max}} = 155$ °C. Once room temperature was reached, the COC layer containing the embossed motifs was easily released requiring no demoulding agent. A further bonding step was required in order to seal the engraved microfluidic motifs.

3.2.2.3 Laser ablation

Laser ablation is considered a suitable method for the fast prototyping of polymeric devices, since it has proven to be a simple and rapid microstructuring process.^{26–28} Nonetheless, several limitations have been found regarding, for example, the polymeric materials being compatible with this microstructuring technique.²⁹ Besides, the formation of bulges at the rim of the channels during the ablation process has been frequently reported.^{30–35} Bulges are a consequence of the melting and re-solidification of the polymer and can result in the clogging of the channels during the bonding process as well as in a poorly bonded final device due to an incomplete sealing of the layers. Diverse methods have already been proposed to improve the ablation process and minimise bulge formation.^{31,35}

Several works have been published with regard to the microstructuring of COP and COC substrates by using direct laser ablation. Microstructuring by using KrF excimer laser³⁶, ArF excimer laser³⁷ and Ti:Sapphire laser²⁹ have been reported, although the majority of the research has been focused on CO₂ and Nd:YAG lasers. Recent publications stated the feasibility of using a CO₂ laser for the ablation of COP^{33–35}, despite first attempts with TOPAS substrate seemed to be unsuccessful¹³. The possibility of employing Nd:YAG lasers for COP rapid prototyping has also been demonstrated in several works.^{38–42}

Owing to the apparent advantages of laser ablation and its demonstrated feasibility over COP and COC substrates, experiments on the microstructuring of TOPAS by using three different lasers were carried out by members of our research group. The first laser tested was the one being used for the laser ablation of LTCC, a Nd:YAG infrared laser (1064 nm) Protolaser 200 from LPKF Laser & Electronics, observing no interaction of the laser with the COC substrate. Some experiments were carried out with a Nd:YAG ultraviolet laser (355 nm) from the same company (Protolaser U3). However, the poor interaction of the laser with the material resulted in irregular ablated surfaces, bubbles and bulges. A CO₂ infrared laser (10.6 µm) Epilog Laser Mini (Epilog Laser, Golden, CO, USA), which was capable to ablate other transparent thermoplastics such as PC, PET and PMMA, was also tested. Although a better interaction with the polymer surface could be observed by using this laser in comparison to the previous one, the same type of defects appeared in all the applied conditions.

Ablation experiments with a fourth laser were performed during the development of this work. A CO₂ laser K-1030 HPD UHS PLUS from Macsa ID (Manresa, Spain), which is usually employed for cutting and perforating flexible plastic films and foils, was tested for the microstructuring of TOPAS layers of different grades and thicknesses. The wavelength of the laser was 10.6 µm, with a maximum power output of 30 W. The focal length of the laser head was set to 60 mm, with a corresponding minimum diameter of 100 µm of the focused spot. Different setups of power, resolution and mark speed were trialled during the experiments. Unfortunately, none of the combinations led to suitable marking profiles. Bulges, bubbles and fractures on the material could be easily noticed. Furthermore, difficulties regarding the reproducibility of the ablated

features as well as incomplete or irregular cut profiles were also found. Some examples of the aforementioned defects are shown in [Figure 3.7](#).

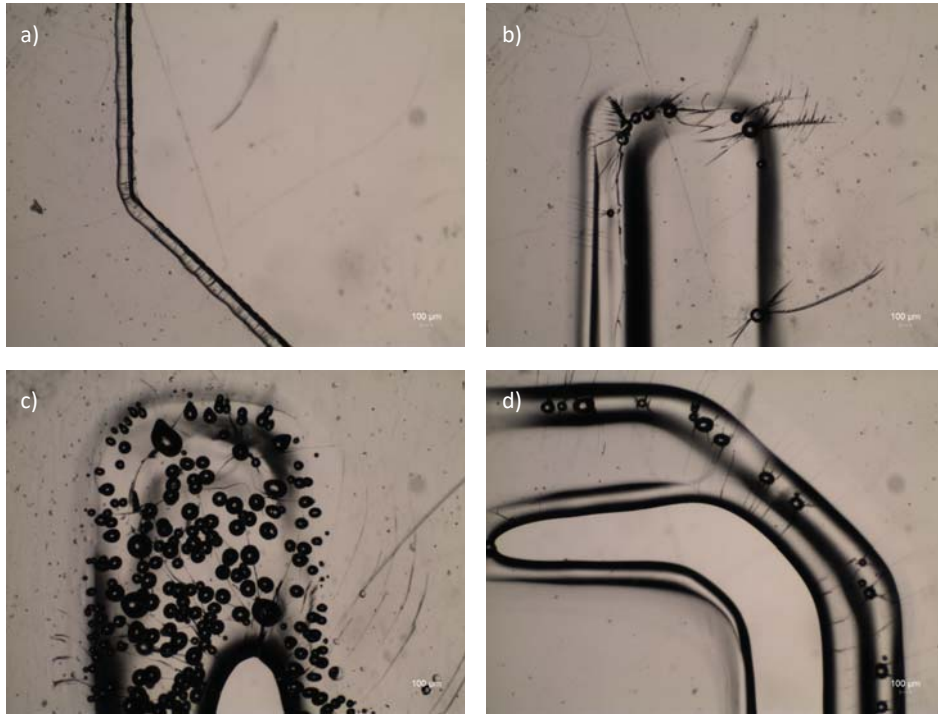


Figure 3.7: Microscope images of the laser ablated TOPAS layers using the CO₂ laser K-1030 HPD UHS from Macsa ID. Bulges (a-d), bubbles (b-d) and fractures (b), in addition to incomplete and irregular (c, d) cut profiles can be noticed.

None of the four lasers tested proved to be useful for the direct microstructuring of TOPAS. Further attempts with other equipment may be carried out in order to obtain adequate results for the direct laser ablation of this material.

3.2.3 Bonding

The final internal 3D structures of a device were defined once the individual COC layers that conformed the whole system were sealed together. Diverse bonding strategies for COC devices have been proposed, including, for example, adhesive bonding, solvent bonding, ultrasonic bonding and thermal bonding, this latter being the most widely used due to its simplicity and relatively high bond strength.^{18,43} Thermal bonding presents several advantages in comparison to other commonly used methods, as it does not

involve the use of solvents or other additional materials such as glues, adhesives or epoxy resins that might lead to the clogging of the channels. Besides, it does not require the use of expensive instrumentation or special facilities.

Thermal bonding is based on the increase of the temperature up to or above the T_g of the substrate material while pressure is being applied in order to achieve the inter-diffusion of the polymer chains between the surfaces. As a consequence, a monolithic and irreversibly sealed device is obtained. The combination of different grades of COC as the bonding strategy is considered advantageous in comparison to the use of a single COC grade, as it might prevent the deformation of the features microstructured onto the COC layers with higher T_g .^{12,13}

A proper sealing process is crucial to obtain of a completely operational device. Hence, an accurate optimisation of the bonding process, including the alignment of the layers and the thermocompression conditions, are of great importance.

The thermocompression processes were carried out in a uniaxial hydraulic press where temperature and pressure could be manually adjusted. A digital display and a manometer showed the actual temperature and pressure values, respectively.

Bonding processes started at a mild temperature, generally at 60 °C, and at a fixed pressure. Once temperature was stable for 10 minutes, it was set to a value over the T_g of the bonding TOPAS layers and, when this temperature was reached, it was set to the initial value again. After 10 minutes at 60 °C, pressure could be released and the bonded layers could be removed from the press. Due to residual heat of the press and thermal expansion of the materials, observed maximum temperature and pressure values often surpassed the pre-set ones. This difference between the actual and the set values had to be considered when adjusting the press parameters.[†]

The choice of the thermocompression conditions depended on the TOPAS grades and the structural motifs of the layers. Pressure had to ensure an appropriate and homogeneous contact between the different layers, while temperature had to ensure the melting of the bonding layers yet avoiding the deformation of the structural ones. As explained before, TOPAS layers with high T_g were used as structural layers, whereas TOPAS layers with low T_g , generally TOPAS 8007 layers of 25 µm in thickness, were used as bonding layers. Despite the fact that a considerably wide range of temperatures and pressures could seem to be suitable, it is important to note that the milder the conditions were, the larger the risk of an incomplete bonding of the layers was. On the other hand, too harsh conditions could lead to the deformation of the structural layers and the consequent alteration of the internal 3D motifs.

The dimensions of the internal structures played an important role when choosing the thermocompression conditions. Due to pressure and temperature, TOPAS 8007 layers penetrated into the features of the structural layers by several microns. This penetration was usually not significant for the operation of the devices, as it did not substantially affect the structure dimensions. However, in some cases this penetration

[†]Unless otherwise specified, actual maximum temperature and pressure values (rather than pre-set values) will be detailed for the bonding steps described along this dissertation.

had a relevant effect and, therefore, had to be controlled and/or minimised. As an example, for one of the applications presented in this dissertation microchannels of less than 100 μm were constructed by a hot embossing process and a later sealing of the embossed layer. Due to the reduced dimensions of the engraved motifs, thermocompression conditions were crucial to avoid channel collapse during the sealing process. Hence, in this particular case, mild and strictly controlled thermocompression conditions were applied (see § 7.5.2).

Usually, before the microstructuring process, TOPAS structural layers were (pre)bonded to TOPAS bonding layers, hence reducing the later micromachining steps and the overall complexity of the fabrication process (see Figure 3.7). In this case, the thermocompression conditions were more flexible as there were no structures to collapse or deform. For this initial bonding step, temperature and pressure conditions were $T_{\text{max}} = 108\text{ }^{\circ}\text{C}$ and $P_{\text{max}} = 25\text{ bar}$.

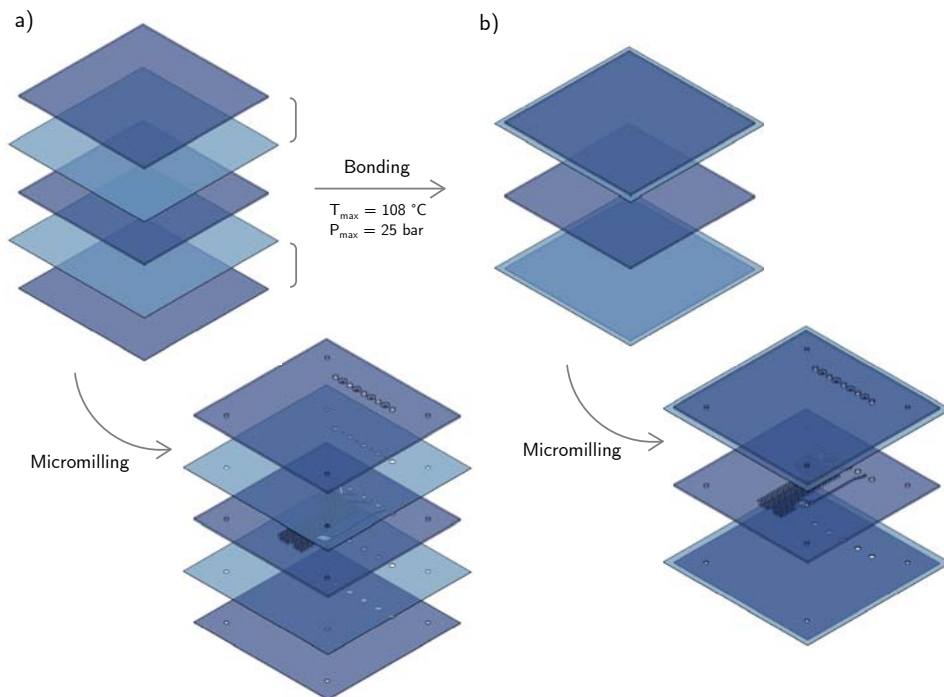


Figure 3.8: A bonding step of TOPAS 8007 layers (light blue) with structural TOPAS layers (dark blue) before the micromachining process reduces the overall complexity of the construction process by reducing the required micromachining steps. As an example, for a device with three structural layers, this previous step would reduce the micromilling steps from five (a) to three (b).

As mentioned before, one of the key features of the bonding processes was the precise alignment of the layers previous to thermocompression in order to obtain a proper alignment of the internal 3D structures of the device. The method had to ensure an accurate positioning of the layers while avoiding their misalignment during the thermocompression process. With that purpose, aluminium blocks containing fiducial pins were used. Fiducial holes fitting these pins were designed and machined to each polymeric layer, allowing the placement of the layers with minimum alignment error and impeding their movement during the whole bonding process.

Apart from the aforementioned aluminium blocks, other auxiliary materials were also used for guaranteeing a proper sealing of the devices. Flexible silicon layers of about 5 mm in thickness were placed onto the aluminium blocks in order to homogenise the applied pressure. Non-stick polymer foils were placed between the silicon layers and the TOPAS layers. These foils avoided the sticking of the device to the silicon layers. In order to prevent the bending of the structural layers in devices with high aspect ratio structures, Delrin acetal resin plaques from DuPont were used as sacrificial layers. The plaques, previously micromilled in the areas where no pressure had to be applied, were placed between the silicon layers and the non-stick polymeric foils during thermocompression processes.

The complete setup for the bonding processes, including all materials employed for ensuring an accurate alignment of the layers and avoiding the deformation of the internal structures, is illustrated in [Figure 3.9](#).

3.2.4 Additional back-end processes

A last micromachining step to give the devices the desired final shape was generally performed after the bonding process. Besides, the integration of other elements was usually required for the actual operation of the devices. Some examples of different back-end processes can be found along this dissertation, including the integration of fluidic connections, the sealing of fluidic structures by using adhesive plate seals and the integration of PDMS discs and magnets. Each back-end process will be addressed in the corresponding section.

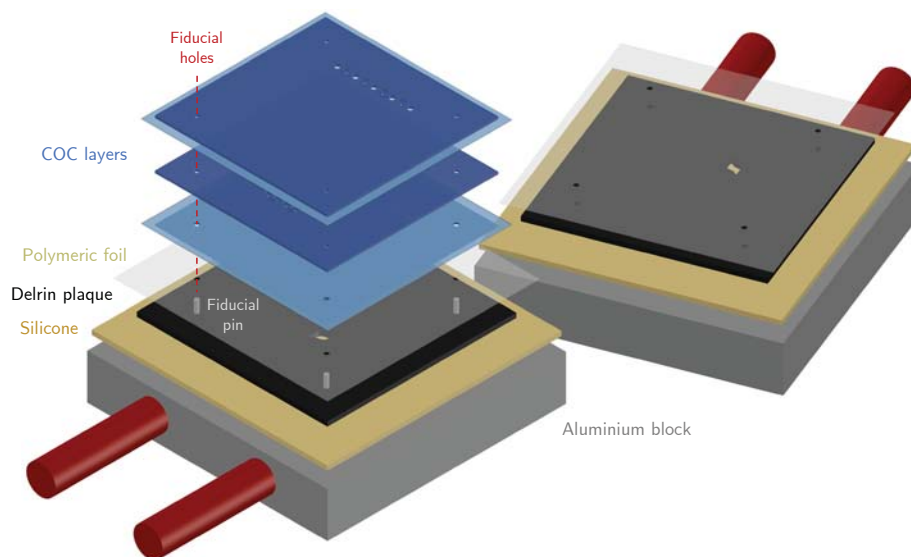


Figure 3.9: Bonding setup. Aluminium blocks containing fiducial pins guarantee the correct alignment of the layers; silicone layers ensure homogeneous pressure; polymeric sacrificial plaques avoid the bending of structural layers in devices with high aspect ratio structures; and polymeric foils prevent the sticking of the device to the sacrificial plaques.

References

- (1) Khanarian, G. Optical properties of cyclic olefin copolymers. *Optical Engineering* **2001**, *40*, 1024–1029.
- (2) Calvo-López, A.; Puyol, M.; Casalta, J. M.; Alonso-Chamarro, J. Multi-parametric polymer-based potentiometric analytical microsystem for future manned space missions. *Analytica Chimica Acta* **2017**, *995*, 77–84.
- (3) Calvo-López, A.; Ymbern, O.; Puyol, M.; Casalta, J. M.; Alonso-Chamarro, J. Potentiometric analytical microsystem based on the integration of a gas-diffusion step for on-line ammonium determination in water recycling processes in manned space missions. *Analytica Chimica Acta* **2015**, *874*, 26–32.
- (4) Calvo-López, A.; Arasa-Puig, E.; Puyol, M.; Casalta, J. M.; Alonso-Chamarro, J. Biparametric potentiometric analytical microsystem for nitrate and potassium monitoring in water recycling processes for manned space missions. *Analytica Chimica Acta* **2013**, *804*, 190–196.

- (5) Calvo-López, A.; Ymbern, O.; Izquierdo, D.; Alonso-Chamarro, J. Low cost and compact analytical microsystem for carbon dioxide determination in production processes of wine and beer. *Analytica Chimica Acta* **2016**, *931*, 64–69.
- (6) Ymbern, O.; Sáñez, N.; Calvo-López, A.; Puyol, M.; Alonso-Chamarro, J. Gas diffusion as a new fluidic unit operation for centrifugal microfluidic platforms. *Lab on a Chip* **2014**, *14*, 1014–1022.
- (7) Shin, J. Y.; Park, J. Y.; Liu, C.; He, J.; Kim, S. C. Chemical structure and physical properties of cyclic olefin copolymers (IUPAC Technical Report). *Pure and Applied Chemistry* **2005**, *77*, 801–814.
- (8) Candlin, J. In *Comprehensive Analytical Chemistry*; 08; Elsevier B.V.: Amsterdam, Netherlands, 2008; Vol. 53; Chapter 3, pp 65–119.
- (9) Kemmish, D. J. In *Rapra Review Reports*; 2; Pergamon: Oxford, UK, 1995; Vol. 8.
- (10) Takemori, M. T. Towards an understanding of the heat distortion temperature of thermoplastics. *Polymer Engineering and Science* **1979**, *19*, 1104–1109.
- (11) TOPAS® COC - Company and Product Brochure., Florence, KY, USA, 2011.
- (12) Steigert, J.; Haerberle, S.; Brenner, T.; Müller, C.; Steinert, C. P.; Koltay, P.; Gottschlich, N.; Reinecke, H.; Rühle, J.; Zengerle, R.; Ducrée, J Rapid prototyping of microfluidic chips in COC. *Journal of Micromechanics and Microengineering* **2007**, *17*, 333–341.
- (13) Bundgaard, F.; Perozziello, G.; Geschke, O. Rapid prototyping tools and methods for all-Topas® cyclic olefin copolymer fluidic microsystems. *Proceedings of the Institution of Mechanical Engineers, Part C: Journal of Mechanical Engineering Science* **2006**, *220*, 1625–1632.
- (14) Błochowiak, M. Structure and properties of norbornene-ethylene copolymers., PhD Thesis, Max Planck Institute for Polymer Research, 2006.
- (15) Becker, H.; Gärtner, C. Polymer microfabrication technologies for microfluidic systems. *Analytical and Bioanalytical Chemistry* **2008**, *390*, 89–111.
- (16) Tsao, C.-W. Polymer Microfluidics: Simple, Low-Cost Fabrication Process Bridging Academic Lab Research to Commercialized Production. *Micromachines* **2016**, *7*, 225.
- (17) Guckenberger, D. J.; de Groot, T. E.; Wan, A. M. D.; Beebe, D. J.; Young, E. W. K. Micromilling: a method for ultra-rapid prototyping of plastic microfluidic devices. *Lab on a Chip* **2015**, *15*, 2364–2378.
- (18) Nunes, P. S.; Ohlsson, P. D.; Ordeig, O.; Kutter, J. P. Cyclic olefin polymers: emerging materials for lab-on-a-chip applications. *Microfluidics and Nanofluidics* **2010**, *9*, 145–161.

- (19) Berenguel-Alonso, M.; Sabés-Alsina, M.; Morató, R.; Ymber, O.; Rodríguez-Vázquez, L.; Talló-Parra, O.; Alonso-Chamarro, J.; Puyol, M.; López-Béjar, M. Rapid Prototyping of a Cyclic Olefin Copolymer Microfluidic Device for Automated Oocyte Culturing. *SLAS Technology* **2017**, 1–11.
- (20) Waldbaur, A.; Rapp, H.; Länge, K.; Rapp, B. E. Let there be chip—towards rapid prototyping of microfluidic devices: one-step manufacturing processes. *Analytical Methods* **2011**, *3*, 2681–2716.
- (21) Fiorini, G. S.; Chiu, D. T. Disposable microfluidic devices: fabrication, function, and application. *BioTechniques* **2005**, *38*, 429–446.
- (22) Lin, T.-Y.; Do, T.; Kwon, P.; Lillehoj, P. B. 3D printed metal molds for hot embossing plastic microfluidic devices. *Lab on a Chip* **2017**, *17*, 241–247.
- (23) Jensen, M. F.; McCormack, J. E.; Helbo, B.; Christensen, L. H.; Christensen, T. R.; Geschke, O. Rapid prototyping of polymer microsystems via excimer laser ablation of polymeric moulds. *Lab on a Chip* **2004**, *4*, 391–395.
- (24) DuPont™ GreenTape™ - Design and Layout Guidelines., Wilmington, DE, USA, 2009.
- (25) Ibáñez-García, N.; Alonso, J.; Martínez-Cisneros, C. S.; Valdés, F. Green-tape ceramics. New technological approach for integrating electronics and fluidics in microsystems. *TrAC Trends in Analytical Chemistry* **2008**, *27*, 24–33.
- (26) Qi, H.; Chen, T.; Yao, L.; Zuo, T. Micromachining of microchannel on the polycarbonate substrate with CO₂ laser direct-writing ablation. *Optics and Lasers in Engineering* **2009**, *47*, 594–598.
- (27) Pflöging, W.; Baldus, O. In *Proc. SPIE 6107, Laser-based Micropackaging*, ed. by Bachmann, F. G.; Hoving, W.; Lu, Y.; Washio, K., 2006, (610705)1–(610705)12.
- (28) Klank, H.; Kutter, J. P.; Geschke, O. CO₂-laser micromachining and back-end processing for rapid production of PMMA-based microfluidic systems. *Lab on a Chip* **2002**, *2*, 242–246.
- (29) Suriano, R.; Kuznetsov, A.; Eaton, S. M.; Kiyon, R.; Cerullo, G.; Osellame, R.; Chichkov, B. N.; Levi, M.; Turri, S. Femtosecond laser ablation of polymeric substrates for the fabrication of microfluidic channels. *Applied Surface Science* **2011**, *257*, 6243–6250.
- (30) Snakenborg, D.; Klank, H.; Kutter, J. P. Microstructure fabrication with a CO₂ laser system. *Journal of Micromechanics and Microengineering* **2004**, *14*, 182–189.
- (31) Chung, C. K.; Lin, Y. C.; Huang, G. R. Bulge formation and improvement of the polymer in CO₂ laser micromachining. *Journal of Micromechanics and Microengineering* **2005**, *15*, 1878–1884.

- (32) Li, J.; Liu, C.; Zhu, L. The formation and elimination of polymer bulges in CO₂ laser microfabrication. *Journal of Materials Processing Technology* **2009**, *209*, 4814–4821.
- (33) Cai, J.; Jiang, J.; Gao, F.; Jia, G.; Zhuang, J.; Tang, G.; Fan, Y. Rapid prototyping of cyclic olefin copolymer based microfluidic system with CO₂ laser ablation. *Microsystem Technologies* **2017**, *23*, 5063–5069.
- (34) Liu, S.; Fan, Y.; Gao, K.; Zhang, Y. Fabrication of cyclo-olefin polymer-based microfluidic devices using CO₂ laser ablation. *Materials Research Express* **2018**, *5*, 095305.
- (35) Gu, L.; Yu, G.; Li, C.-W. A fast and low-cost microfabrication approach for six types of thermoplastic substrates with reduced feature size and minimized bulges using sacrificial layer assisted laser engraving. *Analytica Chimica Acta* **2018**, *997*, 24–34.
- (36) Leech, P. W. Effect of norbornene content on laser ablation of cyclic olefin copolymers. *Materials and Design* **2010**, *31*, 4858–4861.
- (37) Sabbert, D.; Landsiedel, J.; Bauer, H.-D.; Ehrfeld, W. ArF-excimer laser ablation experiments on Cycloolefin Copolymer (COC). *Applied Surface Science* **1999**, *150*, 185–189.
- (38) McCann, R.; Bagga, K.; Duaux, G.; Stalcup, A.; Vázquez, M.; Brabazon, D. Taguchi method modelling of Nd:YAG laser ablation of microchannels on cyclic olefin polymer film. *Optics and Laser Technology* **2018**, *106*, 265–271.
- (39) McCann, R.; Bagga, K.; McCarthy, E.; Groarke, R.; Al-Hamaoy, A.; Stalcup, A.; Vázquez, M.; Brabazon, D. Carbon Nanoparticle Functionalization of Laser Textured Polymer Surfaces for Chemical and Biological Speciation. *Lasers in Engineering* **2017**, *36*, 63–72.
- (40) Bagga, K.; McCann, R.; O’Sullivan, F.; Ghosh, P.; Krishnamurthy, S.; Stalcup, A.; Vázquez, M.; Brabazon, D. Nanoparticle functionalized laser patterned substrate: an innovative route towards low cost biomimetic platforms. *RSC Advances* **2017**, *7*, 8060–8069.
- (41) McCann, R.; Bagga, K.; Groarke, R.; Stalcup, A.; Vázquez, M.; Brabazon, D. Microchannel fabrication on cyclic olefin polymer substrates via 1064 nm Nd:YAG laser ablation. *Applied Surface Science* **2016**, *387*, 603–608.
- (42) McCann, R.; Bagga, K.; Stalcup, A.; Vázquez, M.; Brabazon, D. In *Proc. SPIE 9351, Laser-based Micro- and Nanoprocessing IX*, ed. by Klotzbach, U.; Washio, K.; Arnold, C. B., 2015, 93511N.
- (43) Tsao, C. W.; DeVoe, D. L. Bonding of thermoplastic polymer microfluidics. *Microfluidics and Nanofluidics* **2009**, *6*, 1–16.

Chapter 4

Analytical microsystem for the spectrophotometric determination of titratable acidity in wine samples

4.1 Organic acids and acidity of wines

Organic acids are one of the major components of wine, whose variety and quantity depend on multiple factors including grape variety, climatic conditions, type of soil and orientation of the vineyard, applied production methods and storage conditions, among others.¹ The principal characteristics of the main organic acids which are found in wine are shown in [Table 4.1](#).

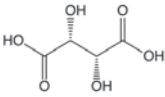
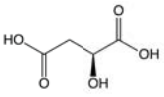
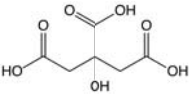
Organic acids are the main contributors to wine acidity and are responsible of its buffer capacity. Both wine acidity and buffer capacity have an important and complex influence on several properties and characteristics of wine, being directly related to its microbiological and chemical stability and having a strong impact on the organoleptic attributes of the final product.⁴ Owing to this important role, acidity levels are controlled and even modified at several steps of the production process.^{1,4}

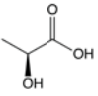
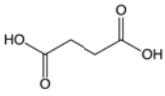
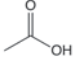
Acidity of musts and wines can be assessed by the determination of the following parameters: total acidity, titratable acidity, fixed acidity, volatile acidity and pH.⁵

Volatile acidity refers to the steam distillable organic acids of wine. It is constituted by the fatty acids belonging to the acetic series⁶ and its importance relies on the relationship of this parameter with possible bacteriological contamination¹. Fixed (or non-volatile) acidity includes all other acids, therefore being the total acidity the sum of both fixed and volatile acidity.

Titratable acidity is a measure of the number of protons which are recovered during a titration with a strong base to a specified endpoint. It is normally expressed as g/L of tartaric acid, being this component the major contributor. Despite it is frequently

Table 4.1: Characteristics of the main organic acids in wine.¹⁻³

Name	L-(+)-Tartaric acid	L-(-)-Malic acid	Citric acid
Structure			
Origin	Grape	Grape	Grape
Must content (g/L)	2 - 6	1 - 6.5	0.5 - 1
Wine content (g/L)	1.5 - 4	0 - 4	0 - 0.5
pKa	3.01, 4.05	3.46, 5.05	3.09, 4.39, 5.74

Name	L-(+)-Lactic acid	Succinic acid	Acetic acid
Structure			
Origin	Malolactic fermentation	Alcoholic fermentation	Alcoholic and malolactic fermentation
Must content (g/L)	-	-	-
Wine content (g/L)	0.1 - 3	0 - 2	> 0.2
pKa	3.81	4.18, 5.23	4.73

used as a synonym of total acidity, titratable acidity is not a measure of the total acid content of wine.^{7,8} The relationship between these two parameters can be found elsewhere.^{9,10}

pH measures the activity of free hydrogen ions of wine and, even though it is a measure of its acidity, there is a complex relationship between pH and the other parameters.¹¹ This non-direct correlation is a result of the complex composition of wine and the different contribution of the various species to the overall acidity.

4.1.1 Titratable acidity in wines

Among the various parameters that can be used to assess wine acidity, titratable acidity is considered one of the most important ones owing to its strong relationship, along with pH, with the stability and the organoleptic characteristics of wine.^{1,4,5,12-14} The measurement and adjustment (when necessary) of this parameter is performed at several steps of the wine-making process in order to guarantee a high quality of the final product. Titratable acidity in musts and wines is commonly in the range of 6 g/L to 9 g/L and 4 g/L to 6.5 g/L expressed as tartaric acid, respectively.¹¹

As mentioned before, titratable acidity is measured by the titration of wine samples to a specified endpoint. Since organic acids of musts and wines are relatively weak, the pH at the equivalence point when titrated with a strong base is greater than

7, commonly between 7.8 and 8.3.¹¹ As a consequence, the American Society for Enology and Viticulture (ASEV) and the Association of Official Analytical Chemists (AOAC) suggested the titration of the samples to an endpoint of 8.2 by potentiometric or colorimetric detection using phenolphthalein as pH indicator.^{15,16} Nonetheless, the official method proposed by the International Organisation of Vine and Wine (OIV, standing for Office International de la Vigne et du Vin) established the endpoint at pH 7, also by potentiometric detection or using bromothymol blue (BTB) as pH indicator.¹⁷ Significant differences between the use of 8.2 or 7 as endpoint pH values have been reported.^{18–20}

Potentiometric methods based on the titration of wine samples to the equivalence point were compared to those based on the titration to a specific pH.^{7,8,21} Higher titratable acidity values were obtained for most of the samples, since their equivalence points were found to be over pH 8.2. Although the titration to the equivalence point could be considered more reliable than the titration to an arbitrary endpoint, the determination of the equivalence point was sometimes challenging.²² Samples containing several weak organic acids display titration curves with subtle inflection points due to their buffer capacity.²³ Therefore, the titration of this type of samples usually requires an experienced analyst to adequately perform the titrant additions as well as a careful record of the pH vs. titrant curve.²³

The above described methods for the titratable acidity determination are laborious and time-consuming, require large sample and titrant volumes and usually involve skilled personnel. Considering the obvious need for simple, rapid and cost-effective methods displaying a high degree of automation and that could be easily implemented in routine analysis, several alternative methods to the classical acid-base titrations have been proposed over the last decades.

Flow based systems for the automated titration of samples with potentiometric²² and colorimetric^{24–29} endpoint determinations have been described. A digital image based detection system that measures the colour change of anthocyanins at the endpoint of the titration has also been proposed.³⁰ The degree of automation of these methods widely differs (from low³⁰ to total²⁴), as well as the simplicity of the system (from complex²² to very simple manifolds²⁸) or the sample/titrant required volume (from several milliliters³⁰ to few microliters²⁵), among others.

Several alternative flow based methods that do not involve the titration of the samples but the construction of a calibration curve by potentiometric³¹ or colorimetric^{32–36} detection have also been proposed. The latter are based on the monitoring of the absorbance of a solution containing an acid-base indicator when it is mixed with a standard solution or a sample, being the change in the absorbance proportional to the acidity of the solution. These methods presented several advantages in comparison to the classical ones, including high automation of the system, low reagent and sample consumption and high throughput. However, some of them required in-line dialysis^{35,36}, involved some sort of sample pretreatment³⁴ or displayed narrow working ranges^{32,33}.

The purpose of the work described in this chapter was the development of a miniaturised, versatile and simple flow based microsystem for the determination of titratable acidity in musts and wines requiring no sample pretreatment and displaying wider working ranges. The determination method of the proposed system was based on the monitoring of the blue coloration decrease of a buffered BTB solution in the presence of acid compounds.

Two main targets were addressed: the determination of the titratable acidity in individual wine and must samples on one hand, and the continuous monitoring of titratable acidity during wine-making processes on the other. Two different systems were developed in order to meet these two targets, both using the same microanalyser and detection system. Fluid management peripherals and hydrodynamic and chemical conditions were adapted and optimised for each of the situations.

This chapter is divided in two main parts. The first part describes the development of the microsystem for the determination of titratable acidity in must and wine samples, where minimum reagent and sample consumption along with high throughput were prioritised. The second part of the chapter focuses on the adaptation of the previous system to the continuous monitoring of titratable acidity during wine-making processes, where robustness and automation were mainly required.

4.2 Development of an analytical microsystem for the determination of titratable acidity in must and wine samples

4.2.1 Methods

4.2.1.1 Reagents and solutions

All used chemicals were of analytical reagent grade and all solutions were prepared in boiled deionised water.

BTB (Merk, Darmstadt, Germany) stock solutions were prepared by accurate weighing and dissolution in ethanol (Panreac, Castellar del Vallès, Spain). The working BTB solutions were prepared by dilution of the stock solution in phosphate buffer aqueous solutions. Potassium phosphate monobasic (KH_2PO_4) (Merk) and potassium phosphate dibasic trihydrate ($\text{K}_2\text{HPO}_4 \cdot 3\text{H}_2\text{O}$, Merk) were used for preparing the phosphate buffer solutions. Aqueous solutions of 1 M sodium hydroxide (NaOH, Panreac) and 1 M hydrochloric acid (HCl, Merk) were used for pH adjustment.

Standard solutions of L-(+)-tartaric acid (Merck) were prepared by dilution of a stock standard solution of 10 g/L. Ethanol, glucose (Merk), fructose (Sigma-Aldrich, Saint Louis, USA), glycerol 99% (Sigma-Aldrich), magnesium sulphate (MgSO_4 , Merk), calcium chloride dihydrate ($\text{CaCl}_2 \cdot 2\text{H}_2\text{O}$, Merk) and sodium chloride (NaCl, Merk) were used for preparing a wine model solution (WMS) for the interference studies.

All tested samples were commercially available. A 25-fold dilution step was required prior to analysis.

For the official method, a 0.1 M NaOH aqueous solution was prepared and standardised by using potassium hydrogen phthalate (KHP, Merk) and phenolphthalein (Panreac) as pH indicator.

4.2.1.2 Materials

The microanalyser was constructed by using COC layers from TOPAS Advanced Polymers (Florence, KY, USA) of diverse thicknesses and grades. Two 1 mm and one 400 μm TOPAS 5013 layers were used as structural layers, while two 25 μm TOPAS 8007 layers were used as bonding layers. All material was cleaned with MilliQ water and ethanol before bonding. Delrin plaques of 2 mm in thickness (DuPont, Wilmington, USA) were used as sacrificial layers for the thermocompression process. Several 3 mm thick PMMA layers (Plásticos Ferplast, Terrassa, Spain) were used for the construction of the detection system support.

4.2.1.3 Experimental setup

The experimental setup, which is depicted in [Figure 4.1](#), can be divided into three main parts: the fluid management peripherals, the microanalyser and the optical detection system.

The peripherals consisted of a four channel peristaltic pump Gilson Miniplus 3 (Gilson, Wisconsin, USA) equipped with 1.02 mm internal diameter Tygon tubing (Ismatec, Wertheim, Germany) and a 6-way injection valve (Hamilton, Bonaduz, Switzerland). Teflon tubing of 0.80 mm internal diameter (Scharlab SL, Setmenat, Spain) was used for connecting the peripherals to the microanalyser.

The optical detection system was developed by the GSB in collaboration with the Grupo de Tecnologías Fotónicas (GFT) from the Universidad de Zaragoza and was subsequently adapted to this work. The system consisted of a light emitting diode (LED) and a photodiode mounted into a compact PMMA structure where the microanalyser was inserted into. The LED and the photodiode were connected to a printed circuit board (PCB) that, in turn, was connected to a data acquisition card (DAQ) NI USB-6211 (National Instruments, Austin, Texas, USA). The DAQ was responsible for the modulation of the LED and the acquisition and transference of the detected signal to a personal computer (PC). A digital lock-in amplification was used for processing the raw data, increasing the signal-to-noise ratio and permitting the operation of the system in ambient light conditions without requiring any physical amplifier.

The detection system was designed to allow the easy change of both the LED and the photodiode, thus permitting the selection of the appropriate components for each particular application. In this specific case, a 621 nm LED HLMP-EH1A from Avago (Digi-Key Electronics, Thief River Falls, USA) and a Si photodiode S1337-66BR from Hamamatsu Photonics (Hamamatsu, Japan) with an effective area of 33 mm² were

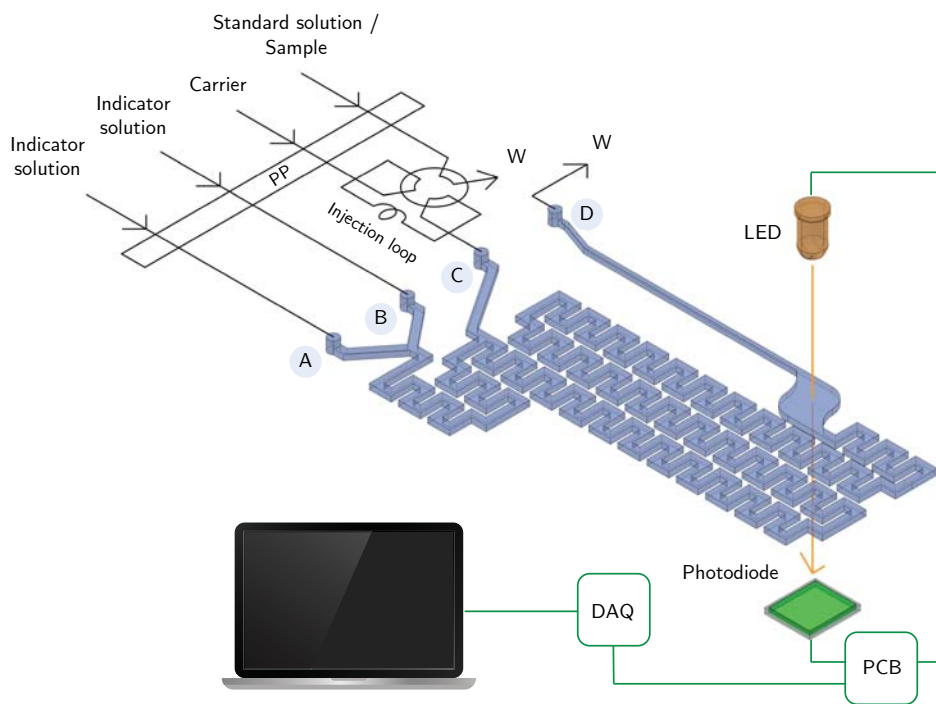


Figure 4.1: Schematic illustration of the experimental setup. PP: peristaltic pump; W: waste.

selected. Two other LEDs, a 621 nm LED HLMP-EH3A from Avago and a 607 nm LED L-53ND from Kingbright (Digi-Key Electronics) were also tested.

The home-made insertion structure was constituted of several 3 mm PMMA layers (see Figure 4.2). The LED and the photodiode were embedded in the external layers (Figure 4.2, a, e), while the central layer (Figure 4.2, c) was used for the insertion of the microanalyser. Two extra PMMA layers (Figure 4.2, b, d) were placed in front of the LED and the photodiode, one to eliminate the non-direct light emitted by the LED and the other to define the desired sensing area of the photodiode.

The design of the insertion structure was based on a lock and key concept for allowing a reproducible positioning of the device with respect to the LED and the photodiode.³⁷ The insertion structure could be adapted to fit a wide variety of micro-analysers differing in size, shape and/or thickness by the modification of the number and/or shape of the PMMA layers.

The possibility of changing the LED and the photodiode as well as of adapting the insertion structure to the dimensions of the microanalyser gave this optical detection system an enormous versatility.

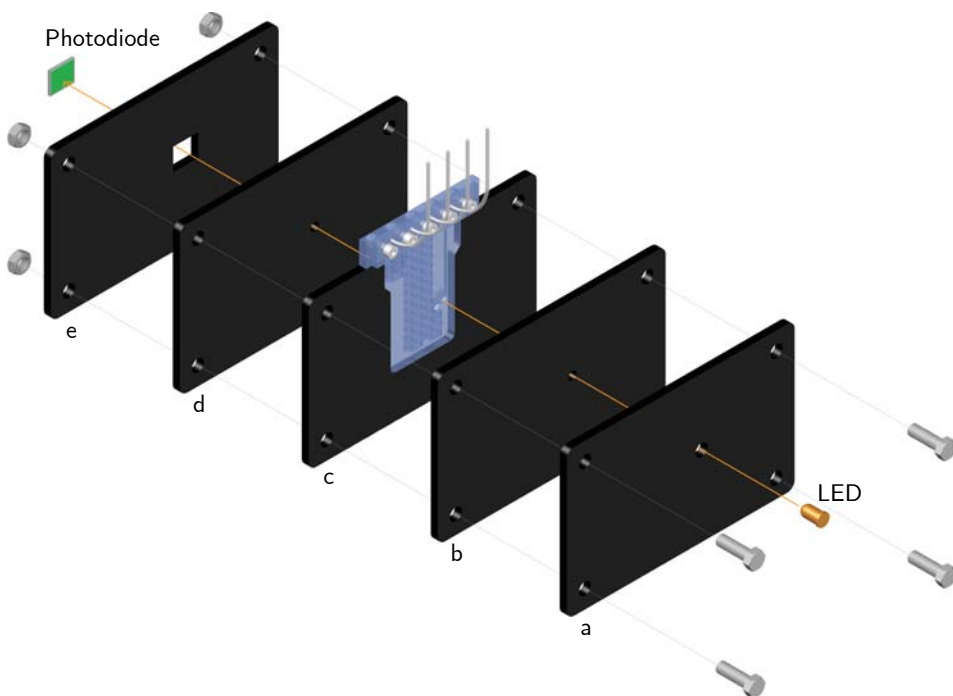


Figure 4.2: Insertion structure of the optical detection system based on a lock and key concept. The several PMMA layers that constitute the structure are used for: fixing the LED (a) and the photodiode (e), eliminating the unwanted light emitted by the LED (b), defining the desired sensing area of the photodiode (d) and inserting the microanalyser (c). Four bolts secure the structure.

4.2.1.4 Flow manifold

The operating procedure of the analysis consisted in the continuous pumping of an acid-base indicator solution (a buffered BTB solution) and a carrier solution (H_2O) into the microanalyser. A fixed volume of sample/standard was then injected into the carrier stream and, when the acidic solution mixed with the BTB solution inside the microanalyser, a colour change was produced. The mixture was directed towards the detection chamber, where the optical detection system measured and monitored the absorbance changes. The microfluidic platform comprised three different channels for the fluid introduction (see § 4.2.1.5 for the complete description of the device). The indicator solution was introduced through the first and the second channels (A and B from Figure 4.1), while the carrier was introduced through the third one (C).

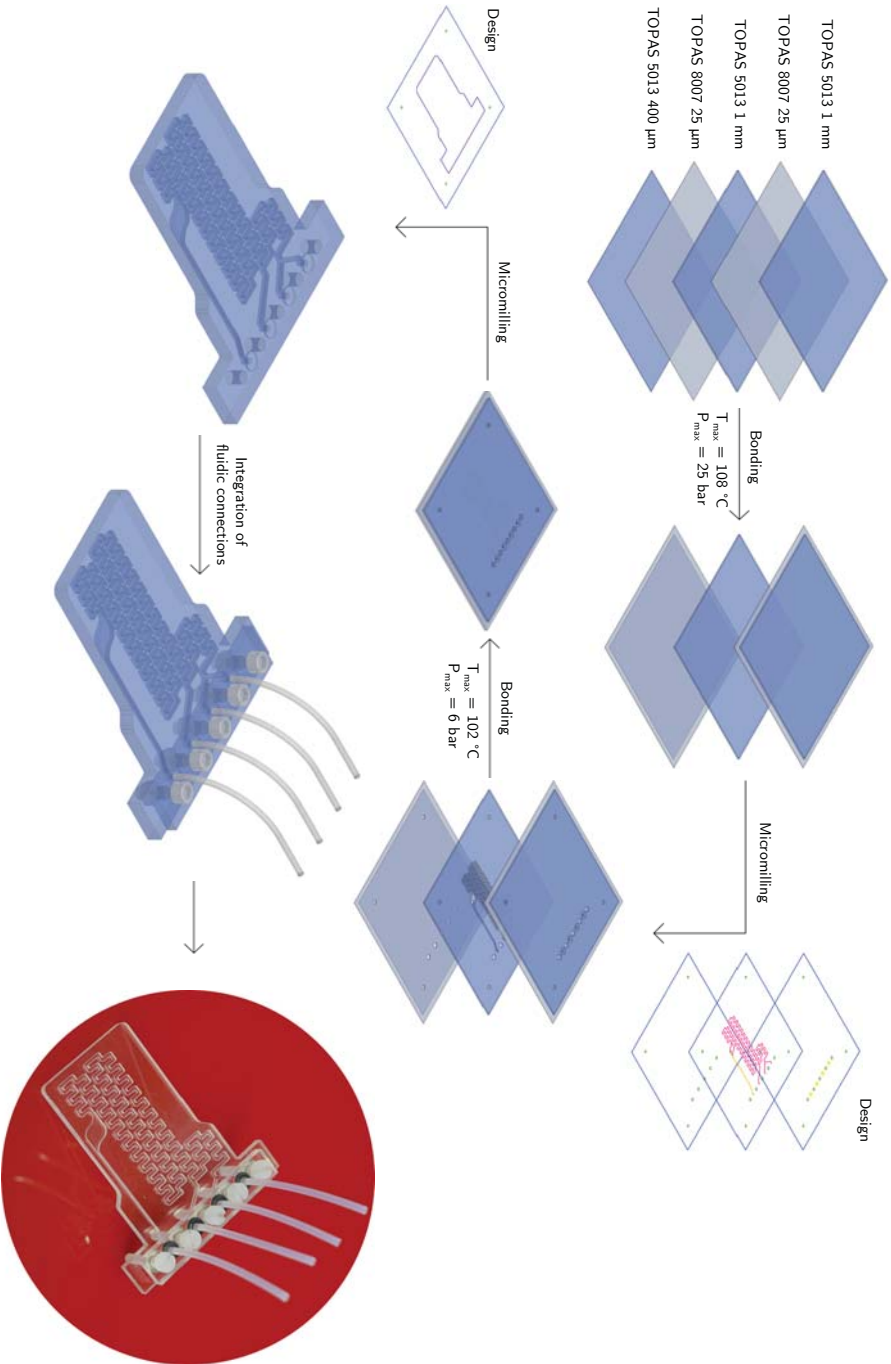


Figure 4.3: Construction scheme of the microanalyser and photograph of the final device including the fluidic connections.

4.2.1.5 Microanalyser design and construction

The construction process of the microanalyser is depicted in [Figure 4.3](#).[†] The platform was constituted by three TOPAS 5013 structural layers, two of 1 mm and one of 400 μm in thickness, and two TOPAS 8007 bonding layers of 25 μm in thickness.

Firstly, the two TOPAS 8007 layers were bonded to two of the structural layers by applying pressure and temperature ($P_{\text{max}} = 25 \text{ bar}$, $T_{\text{max}} = 108 \text{ }^\circ\text{C}$). Next, the motifs were micromilled onto the different layers using 1.0 mm, 0.8 mm and 0.4 mm diameter milling tools. The main fluidic structures were micromilled onto the central layer, while inlet and outlet holes were micromilled onto the top layer; the bottom layer did not contain any fluidic feature. Fiducial holes for the later alignment as well as holes for securing the fluidic connections were micromilled in the three layers. Once the layers were accurately cleaned, dried and aligned, they were irreversibly bonded by applying pressure and temperature ($P_{\text{max}} = 6 \text{ bar}$, $T_{\text{max}} = 102 \text{ }^\circ\text{C}$). Sacrificial Delrin layers were used for preventing the deformation of the structural layers, with special attention to the detection chamber. A last micromilling step was carried out in order to give the microanalyser the desired outer shape, which was designed to fit precisely into the insertion structure of the optical detection system. Fluidic connections were finally integrated.

The final dimensions of the device were 30 mm \times 50 mm \times 2.5 mm, and its final total weight, without the fluidic connections, was approximately 3 g.

The microanalyser was designed to have three different channels for the introduction of fluids. Liquids entering the two first channels merged at a Y-shaped confluence point and were then mixed in a first short serpentine micromixer. A second confluence point connected the third channel with the previous micromixer. This time, a longer serpentine channel ensured the complete mixing of fluids. The length of the micromixers was previously optimised by other members of the group,³⁸ simple verification experiments were performed during this work. All the channels for the liquid introduction as well as the serpentine micromixers were 1.0 mm in height and 0.8 mm in width.

The serpentine micromixer ended into an optical detection chamber of 4.5 mm in diameter and 1 mm in height (i.e. the optical path length). The shape of this chamber (see [Figure 4.4](#)) was designed to minimise the formation of gas bubbles and to prevent their retention inside the chamber.³⁸ Since the formation and accumulation of bubbles is usually favoured by abrupt changes in the geometry of the fluidic features,³⁹ the walls of the chamber were designed to have smooth contours. Besides, an increment in the flow rate at the exit of the chamber was used for favouring the evacuation of bubbles in case they were produced. This flow rate change was achieved by an abrupt decrease in the cross section dimensions of the outlet channel in comparison to the detection chamber. With this particular design, the most common problems related to the presence or the circulation of gas bubbles through the detection chamber, such as

[†]See [§ 3](#) for further information about the construction process of COC devices.

an increase in the noise and the appearance of transitory signals or baseline drifts, were minimised.

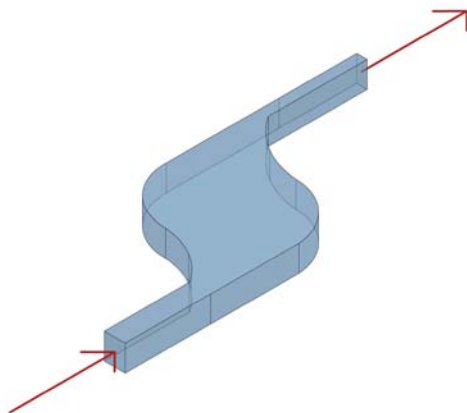


Figure 4.4: Detection chamber design. The arrows indicate the flow direction.

Liquid flowed outside the device through a channel of 1.0 mm in height and 0.4 mm in width. The dimensions of this channel were smaller than those from the inlet and mixing channels in order to produce the aforementioned change in the flow rate at the exit of the detection chamber.

Despite for this application only two channels would have been required for liquid introduction, one for the indicator solution and the other for the carrier solution, the microfluidic platform was designed to have an extra channel in order to increase its versatility. An example can be found in the application of the microanalyser for the continuous monitoring of titratable acidity during wine-making processes, where different solutions were introduced through the three channels.

4.2.2 Results and discussion

4.2.2.1 Optimisation of the hydrodynamic and chemical conditions

The different hydrodynamic and chemical variables that could influence the system were studied for their optimisation. These included, on one hand, the flow rate and the injection volume and, on the other hand, the composition of the acid-base indicator solution and the effect of possible interfering species. Parameters regarding the optical detection system were also adjusted.

Several acid-base indicators have been reported for the determination of titratable acidity in wine samples. However, special attention has been dedicated to phenolphthalein^{24,25,28,35,36} and bromothymol blue³²⁻³⁴, which are the two indicators used in the AOAC¹⁶ and the OIV¹⁷ official methods.

Both white and red wines absorb light at the lower range of the UV-visible spectrum up to 400 nm approximately. Red wines spectra present an absorbance peak from 400 nm to 660 nm with a maximum centred at 520 nm. This peak is mainly due to the presence of anthocyanins and their flavylum combinations, which are the main source of wine's reddish coloration and whose content is minimum in white wines.^{1,4}

The use of phenolphthalein as the acid-base indicator was discarded since the monitoring of the decrease of its pink coloration, with a maximum of absorbance⁴⁰ found at 553 nm, would be challenging as a consequence of the intrinsic coloration of wine. Thus, the use of BTB as indicator was preferred.

BTB has a reported pKa of 7.1 and a reported transition interval from 6.2 to 7.6.⁴⁰ Over this latter value, it is found in its basic form (In^{2-}) (see Figure 4.5) and presents a blue coloration with an absorbance maximum at 616 nm. Below pH 6.2, it is found in its yellow form (HIn^-), presenting an absorbance maximum at 433 nm. Between these two pH values, a green coloration can be observed as a result of the colour contribution of the different species.⁴¹

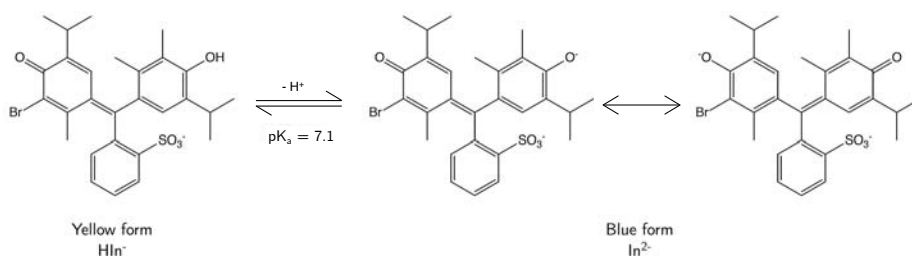


Figure 4.5: Acid-base equilibrium of BTB. Redrawn and adapted from references [41] and [42].

The monitoring of the decrease in the blue coloration of the indicator was preferred over the increase in the absorbance at the yellow range in order to minimise colour interferences from wine samples.

The experimental determination of the linear range for the fading of the blue coloration was carried out. With that purpose, the absorbance spectra of several BTB solutions at different pH values were recorded and the absorbance at 616 nm was plotted against pH. The linear range was established for pH values from 6.9 to 7.8 (see Figure 4.6).

The LED and the photodiode of the detection system were selected for working at the absorbance maximum of the deprotonated specie In^{2-} . A Si photodiode with an appropriate photosensitivity at the working wavelength⁴³ was chosen and three different LEDs (see Table 4.1) were tested by measuring the absorbance of BTB solutions of different concentrations. Despite the fact that all LEDs showed similar performance, HLMP-EH1A was selected due to its lower spectral line half-width in comparison to

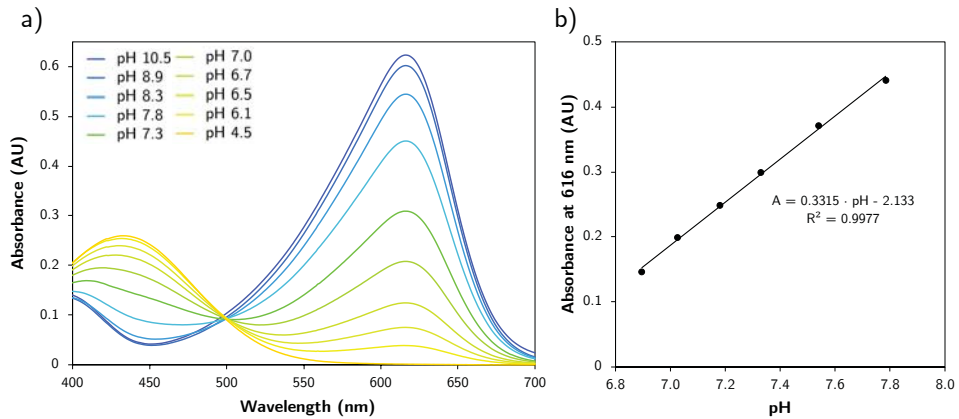


Figure 4.6: a) Absorbance spectra of BTB solutions in the pH range from 4.5 to 10.5. b) Linear range for the monitoring of the blue coloration decrease at 616 nm.

the L-53ND LED and its lower viewing angle and higher luminous intensity regarding both L-53ND and HLMP-EH3A LEDs. The spectral line half-width measures the width of the emitted light peak at 50% relative intensity, thus being a measure of the monochromaticity of the emitted light.⁴⁴

Table 4.2: Main characteristics of the tested LEDs.

LED			L-53ND Kingbright ⁴⁵	HLMP-EH1A Avago ⁴⁶	HLMP-EH3A Avago ⁴⁶
Material			GaAsP/GaP	AllnGaP	AllnGaP
Lens type			Orange diffused	Nondiffused	Nondiffused
Optical characteristics					
Viewing angle	$2\theta_{1/2}$	Deg	60°	15°	30°
Peak wavelength [†]	λ_p	nm	607	621	621
Dominant wavelength [†]	λ_d	nm	610	615	615
Spectral line half-width	$\Delta\lambda_{1/2}$	nm	35	14	14
Luminous intensity at 20 mA	I_v	mcd			
	min		24	12000	5500
	max		60	21000	9300
Electrical characteristics					
Forward voltage (max)	$V_{F,max}$	V	2.5	2.4	2.4
Reverse voltage (min)	$V_{R,min}$	V	5	5	5

†Peak wavelength vs Dominant wavelength^{47,48}

The peak wavelength is defined as the wavelength where the emission spectrum of a light source reaches its maximum, while the dominant wavelength describes the perceived colour of the light source. Normally, these two parameters do not drastically differ. Nonetheless, when the light source is to be used in optical instrumentation, its selection should be based on the peak wavelength rather than on the dominant wavelength.

Once the detection conditions were established, the optimisation of the microsystem parameters was carried out. Tartaric acid was selected as the model acid for preparing the standard solutions since it is the main contributor to titratable acidity in musts and wines. Actually, titratable acidity is generally expressed as g/L of tartaric acid. The targeted working range was established from 0.10 g/L to 0.40 g/L, which corresponded to a titratable acidity from 3 g/L to 10 g/L expressed as tartaric acid for a 25-fold dilution of the samples. This range would cover the most common titratable acidity content in musts and wines (from 6 g/L to 9 g/L and from 4 g/L to 6.5 g/L tartaric acid, respectively).

Arbitrary initial conditions were chosen, some of them based on reference [33]. An 8 mg/L BTB aqueous solution adjusted to pH 8.0 was initially used as the acid-base indicator solution, while deionised water was used as the carrier. The initial injection volume and flow rate were set to 75 μ L and 0.75 mL/min per channel, respectively.[†] Standard solutions of tartaric acid ranging from 0.02 g/L to 0.50 g/L were analysed in triplicate.

With these initial conditions, the absorbance peaks showed no height differences, meaning that all the standard solutions analysed were capable of producing the complete change of the BTB solution from blue to yellow. Hence, several injection volumes were tested, being progressively reduced from 75 μ L to 7.5 μ L, which was the minimum affordable injection volume due to instrumental limitations.

Despite the considerable reduction of the injection volume, low concentrations of tartaric acid were still capable of producing a decrease in the pH to a value where BTB was completely in its yellow acid form (see Figure 4.7).

[†]Flow rates are given per channel unless otherwise specified.

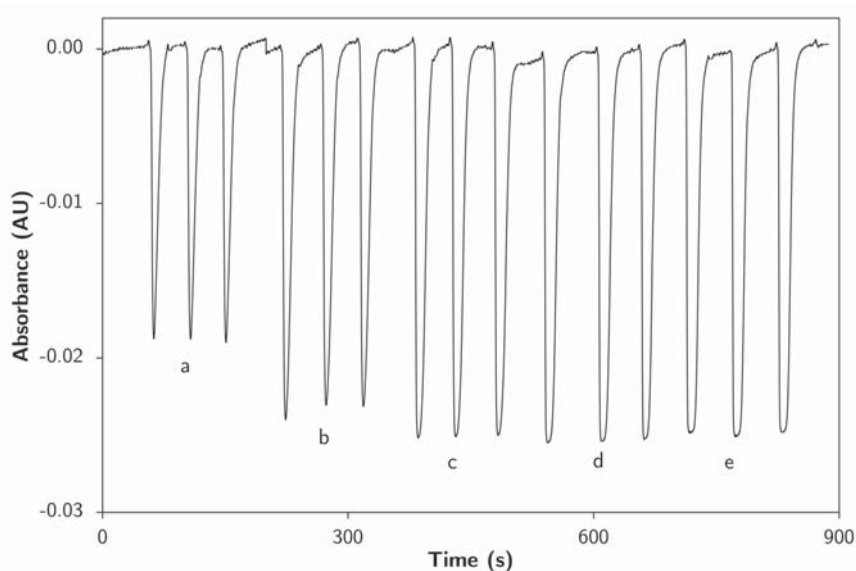


Figure 4.7: Signal record for an injection volume of 7.5 μL of (a) 0.02 g/L, (b) 0.04 g/L, (c) 0.08 g/L, (d) 0.12 g/L and (e) 0.16 g/L tartaric acid standard solutions. No height differences were found for concentrations over 0.08 g/L (c, d, e).

In order to increase the resistance of the indicator solution to change its pH, the introduction of a buffer was proposed based on previous works of our research group.⁴⁹ Indicator solutions containing 8 mg/L BTB and phosphate buffer concentrations ranging from 0.5 mM to 25 mM were prepared and adjusted to pH 8.0. Tartaric acid standard solutions from 0.001 g/L to 1 g/L were analysed in triplicate at a flow rate of 0.75 mL/min and using the minimum injection volume, which was 7.5 μL .

The obtained results are presented in Figure 4.8. Predictably, an increment in the buffer concentration led to a reduction in the sensibility due to an increased buffer capacity of the indicator. A drastic decrease in the sensibility was found for phosphate buffer concentrations over 5 mM, whereas 0.5 mM and 1 mM showed a better compromise between sensibility and linear range. Despite not covering the desired working range, 0.5 mM and 1 mM phosphate buffer indicator solutions were used as starting points for the subsequent experiments, which included the simultaneous optimisation of both BTB and phosphate buffer concentrations.

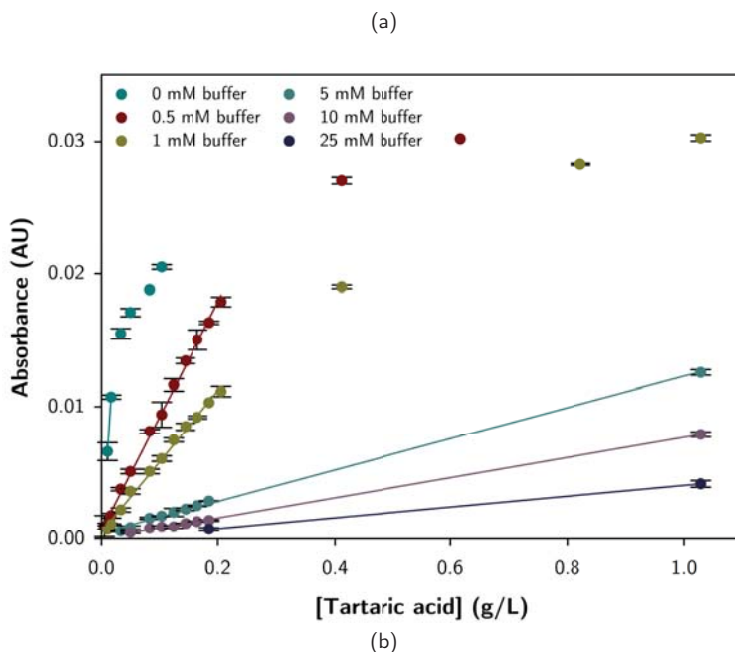


Figure 4.8: Influence of the phosphate buffer concentration in the absorbance peak height. a) Representation of the results. b) Linear regression parameters.

At this point, flow rates from 0.75 mL/min to 1.50 mL/min were examined using an 8 mg/L BTB and 1 mM phosphate buffer solution adjusted to pH 8.0 as the indicator solution. Tartaric acid standard solutions from 0.04 g/L to 0.50 g/L were analysed in triplicate for a 7.5 µL injection volume.

As presented in [Figure 4.9](#), an increment in the flow rate from 0.75 mL/min to 1.00 mL/min entailed a slight decrease in the sensibility but an increase in the linear range, whereas a further increase to 1.50 mL/min did not cause any improvement in the linear range but a slight loss in the sensibility. Hence, 1.00 mL/min was selected as the optimum flow rate. As a result of using a higher flow rate, the injection frequency could be incremented, therefore improving the overall throughput of the system.

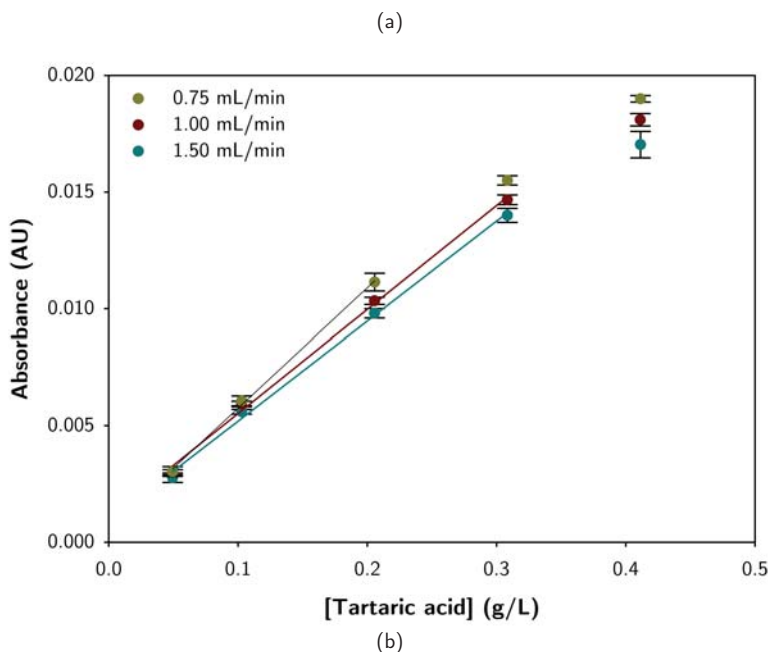


Figure 4.9: Flow rate optimisation. a) Representation of the results. b) Linear regression parameters.

The influence of increasing the pH of the indicator solution was examined by comparing two different experiment runs. Two indicator solutions containing 8 mg/L BTB and 1 mM phosphate buffer were adjusted to pH 8.0 and pH 8.5, respectively. Tartaric acid standard solutions from 0.005 g/L to 0.50 g/L were analysed in triplicate at a flow rate of 1.00 mL/min and using an injection volume of 7.5 μ L.

The shape of the calibration curve is closely connected to pH in analytical methods based on the absorbance change of a colorimetric acid-base indicator. Choosing an initial pH far above the working range of the indicator may difficult the determination of low analyte concentrations, while the selection of low pH values could result in a reduction of the working range.⁵⁰ In this particular case, a pH value of 8.5 appeared to be far away from the working range of BTB, which was previously established from 6.9 to 7.8. However, since the sensibility of the calibration was higher for an initial pH value of 8.5 than it was for pH 8.0 and no loss in sensibility was obtained for low

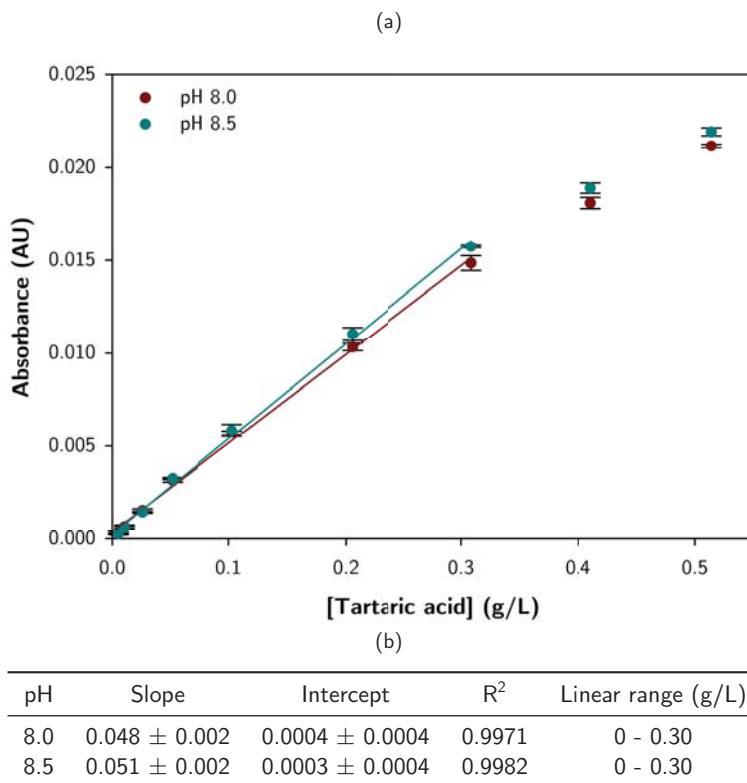


Figure 4.10: Influence of an increment in the indicator solution pH. a) Representation of the results. b) Linear regression parameters.

tartaric acid concentrations (see Figure 4.10), 8.5 was selected as the optimum pH of the indicator solution.

Finally, an optimisation of the BTB and the phosphate buffer concentrations of the indicator solution was carried out. Several solutions containing from 8 mg/L to 40 mg/L BTB and from 0.5 mM to 1.5 mM phosphate buffer, all of them adjusted to pH 8.5, were tested by the analysis in triplicate of tartaric acid standard solutions from 0.005 g/L to 0.50 g/L, using a flow rate of 1.00 mL/min and an injection volume of 7.5 μ L.

The effect of modifying the BTB and the phosphate buffer concentrations is illustrated in Figure 4.11. An increment in the BTB concentration resulted in an improvement in both sensibility and linear range (Figure 4.11.a). On the other hand, an increment in the buffer concentration led to a loss in the sensibility but a wider linear range (Figure 4.11.b). From the tested combinations, 32 mg/L BTB and 1.0 mM phosphate buffer were the lower concentrations which covered the targeted working

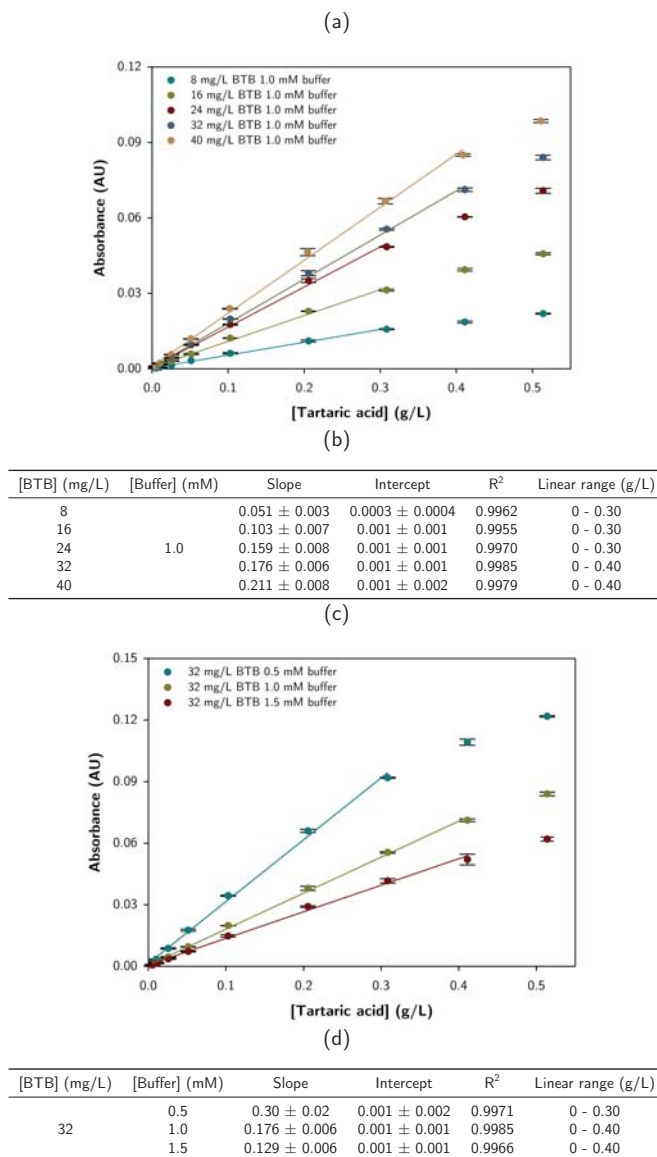


Figure 4.11: Optimisation of the BTB and the phosphate buffer concentrations. Influence of the BTB concentration: a) representation of the results; b) linear regression parameters. Influence of the phosphate buffer concentration: c) representation of the results; d) linear regression parameters.

range to up to 0.40 g/L tartaric acid with an adequate sensibility and repeatability of the peaks.

The evaluated ranges as well as the selected values for the studied parameters are summarised in [Table 4.3](#).

Table 4.3: Optimisation of variables.

	Tested range	Optimum value
Flow rate (mL/min)	0.75 - 1.50	1
Injection volume (μ L)	7.5 - 75	7.5
Indicator solution:		
pH	8.0, 8.5	8.5
[Phosphate buffer] (mM)	0 - 25, 0.5 - 1.5	1
[BTB] (mg/L)	8 - 40	32

4.2.2.2 Wine model solution

The study of the potential interfering species was performed by considering the typical composition of wine. With that purpose, a calibration curve was performed using tartaric acid standard solutions prepared in a 25-fold diluted wine model solution³³ (WMS) containing 3 g/L of sugars (40:60 glucose:fructose), 7 g/L of glycerol, 100 mg/L of Mg^{2+} , 100 mg/L of Ca^{2+} , 50 mg/L of Na^{+} and 10% ethanol. The 25-fold dilution of the WMS corresponded to the required dilution of must and wine samples to fall into the linear range. A calibration procedure was performed using the previously optimised conditions ([Table 4.3](#)) and alternating quintuplicate injections of standard solutions prepared in WMS and standard solutions prepared in deionised water. The two calibration curves obtained are plotted in [Figure 4.12](#).

No statistically significant differences were found between the two calibration curves for a 95% confidence level ($n = 30$), demonstrating no significant interference of the studied species.

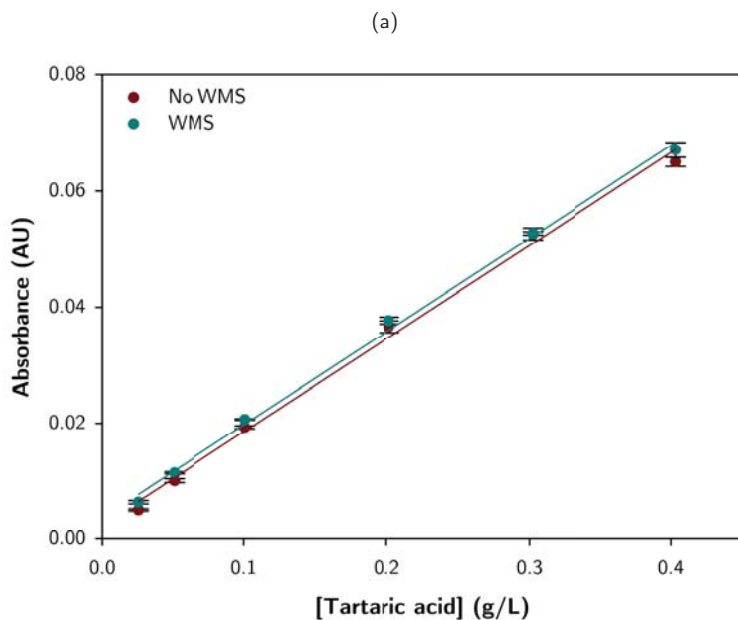


Figure 4.12: Calibration curves for tartaric acid standard solutions prepared in a 25-fold diluted WMS or in deionised water. a) Representation of the results. b) Linear regression parameters.

4.2.2.3 Analytical characterisation of the microsystem

The repeatability of the method was assessed by performing four different calibration procedures in two different working days under identical hydrodynamic and chemical conditions. Tartaric acid standard solutions from 0.005 g/L to 0.400 g/L were analysed in quintuplicate by using the optimal conditions summarised in Table 4.3. Figure 4.13 displays the recorded signal and the calibration curve obtained for one of the experiments (Replicate 1 from Table 4.4). Replicates 2 and 3 from Table 4.4 were carried out during the same day and using the same solutions, while replicate 4 was performed in a different working day and using newly prepared standards.

The within-day repeatability was found to be highly satisfactory, since no statistically significant differences ($n = 40$, 95% confidence level) were found between the calibration curves from replicates 1 to 3. Regarding the between-day repeatability, a

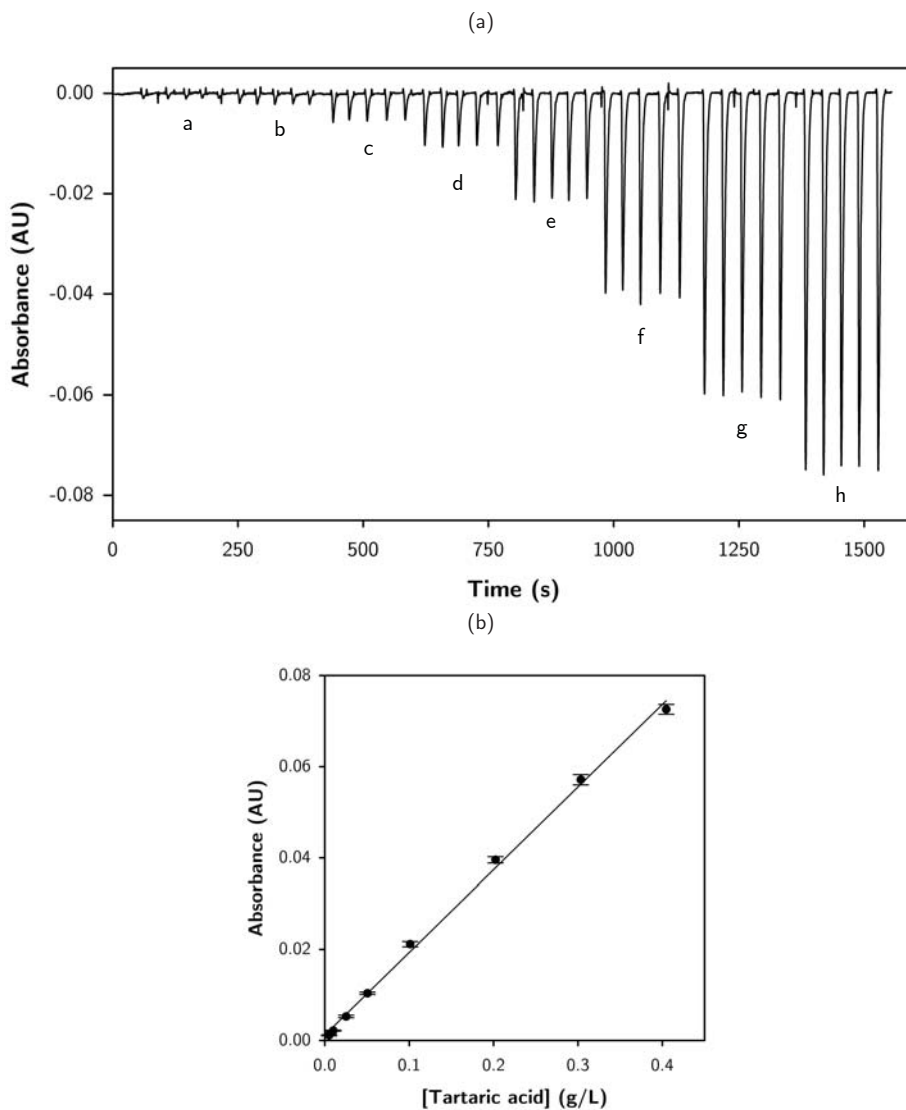


Figure 4.13: Recorded signal (a) and calibration curve (b) for one of the experiments using the optimised conditions. Standard solutions: (a) 0.005 g/L, (b) 0.010 g/L, (c) 0.025 g/L, (d) 0.050 g/L, (e) 0.100 g/L, (f) 0.200 g/L, (g) 0.300 g/L and (h) 0.400 g/L tartaric acid.

significant difference was found between the calibration curves from replicate 4 and the previous calibrations. Nonetheless, this difference would not affect the quality of the

results as long as a calibration of the system was carried out before the analysis of the samples, especially when using newly prepared solutions.

Table 4.4: Analytical characterisation of the microsystem. Linear regression parameters and limits of detection (LOD) and quantification (LOQ) for the four calibration experiments using the optimal conditions. LOD and LOQ were calculated as 3 times and 10 times the standard deviation of the baseline, respectively.

Replicate	Slope	Intercept	R ²	LOD (g/L tartaric acid)	LOQ (g/L tartaric acid)
1	0.181 ± 0.003	0.0012 ± 0.0006	0.9971	0.0009	0.003
2	0.181 ± 0.004	0.0013 ± 0.0008	0.9960	0.0008	0.003
3	0.180 ± 0.004	0.0014 ± 0.0008	0.9958	0.0008	0.003
4	0.164 ± 0.004	0.0017 ± 0.0008	0.9967	0.0009	0.003

With the optimal conditions, a sampling rate of 100 h⁻¹ was achieved, only consuming 7.5 µL of sample, 38.4 µg of BTB and 1.2 µmol of phosphate, and producing 1.8 mL of waste per assay.

4.2.2.4 Real sample analysis

The proper performance of the analytical microsystem was assessed by determining the titratable acidity of eleven Portuguese wine samples, seven white wines and four red wines. Three of the white wine samples were *Vinhos verdes*, slightly sparkling young wines.

In order to select the reference method, the titratable acidity of three wine samples was determined by using the AOAC¹⁶ and the OIV¹⁷ official methods (see § 4.1.1) and the results were compared to the ones obtained by the potentiometric titration of the samples to the equivalence point. The AOAC method, consisting in the potentiometric titration of samples to an endpoint of 8.2, was selected as the reference method since colorimetric titrations with phenolphthalein and BTB as pH indicators were found to be complex due to the intrinsic colour of the samples. Besides, in accordance with previous works^{18,20}, pH 8.2 was found to be closer to the equivalence point than pH 7 for the three samples analysed.

Before being analysed, all samples were thoroughly shaken to remove the CO₂. For the reference method, 5 mL of sample diluted with 100 mL deionised water were titrated to pH 8.2 against a 0.1 M NaOH aqueous solution. The titrant solution was previously standardised using potassium hydrogen phthalate and phenolphthalein as pH indicator.²³ For the developed method, the previously optimised conditions were used (Table 4.3). The linear equation obtained for the calibration was $A = (0.163 \pm 0.003) \cdot [\text{tartaric acid}] \text{ (g/L)} + (0.0013 \pm 0.0007)$, $R^2 = 0.9971$, for $n = 40$ and 95% confidence level. Samples were diluted to 1:25 and were analysed in triplicate.

Table 4.5: Titratable acidity of eleven wine samples determined by the reference method and the developed method.

Sample	Titratable acidity (g/L tartaric acid)		Difference (%)
	Reference method	Developed method	
1 White wine	6.1 ± 0.1	5.9 ± 0.1	-3
2 White wine	8.8 ± 0.1	8.6 ± 0.1	-2
3 White wine	4.8 ± 0.1	4.9 ± 0.2	2
4 White wine	4.8 ± 0.3	5.02 ± 0.07	5
5 Red wine	5.4 ± 0.1	5.6 ± 0.1	4
6 Red wine	5.2 ± 0.1	5.38 ± 0.06	3
7 Red wine	5.0 ± 0.1	5.2 ± 0.1	4
8 Red wine	6.1 ± 0.1	5.8 ± 0.1	-5
9 Vinho verde	5.7 ± 0.1	5.5 ± 0.1	-4
10 Vinho verde	7.0 ± 0.2	6.9 ± 0.1	-1
11 Vinho verde	6.2 ± 0.2	6.3 ± 0.2	2

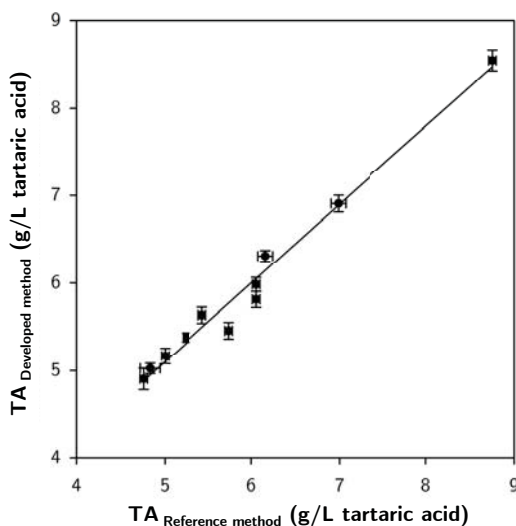


Figure 4.14: Comparison of the titratable acidity (TA) results obtained by the reference and the developed methods. Error bars correspond to the confidence interval of the results.

The results were compared by applying a paired t-test. No statistically significant difference was found between the reference method and the developed method:

$t_{\text{calc}}(0.145) < t_{\text{tab}}(2.2281)$ for $n = 11$ and 95% confidence level. A linear relationship between the two methods could be established, being $\text{TA}_{\text{Developed method}} = (0.9 \pm 0.1) \cdot \text{TA}_{\text{Reference method}} + (0.6 \pm 0.6)$, $R^2 = 0.9784$, for $n = 11$ and 95% confidence level.

4.3 Adaptation of the microsystem for its application to the continuous monitoring of titratable acidity during wine-making processes

Among the large number of parameters to be analysed in wines, only few of them are periodically checked due to the costs and time associated to the commonly used analytical methods. Nonetheless, the higher information of wine is obtained, the better control of the production and storage processes is achieved.⁵¹ An increase in the knowledge of wine would therefore lead to a higher quality of the final product. In this context, the availability of economical automated systems for the continuous monitoring of wine parameters would be extremely advantageous since it would permit a better knowledge and control of the processes yet requiring low economical and time investments.^{6,51}

The purpose of the work described in this second part of the chapter was focused on the adaptation of the previously developed microsystem for its application to the continuous monitoring of titratable acidity during wine-making processes. The same microanalyser and optical detection system as in the previous application were used, whereas flow management peripherals were modified to meet the new requirements. In order to increase the automation of the determination as well as to achieve a further miniaturisation of the system for a higher portability, the 6-port injection valve of the previous system was replaced by several automated solenoid valves which were actuated by a controller. Besides, the composition of the indicator solution was modified for increasing its stability and, therefore, the robustness of the system.

As a consequence of the modifications applied to the fluid management peripherals and the indicator solution, the optimal hydrodynamic and chemical conditions had to be optimised anew.

4.3.1 Methods

4.3.1.1 Reagents and solutions

All used chemicals were of analytical reagent grade and all solutions were prepared in MilliQ water.

BTB (Sigma-Aldrich, Saint Louis, USA) indicator solutions were prepared by accurate weighing and dissolution in phosphate buffer aqueous solutions. Potassium

phosphate monobasic (KH_2PO_4 , Sigma-Aldrich) and potassium phosphate dibasic anhydrous (K_2HPO_4 , Fluka, Buchs, Switzerland) were used for preparing the buffer solutions. Aqueous solutions of 1 M sodium hydroxide (NaOH, Fisher, Pittsburgh, USA) and 1 M hydrochloric acid (HCl, Merk, Darmstadt, Germany) were used for pH adjustment.

Standard solutions of L-(+)-tartaric acid (Sigma-Aldrich) were prepared by dilution of a stock standard solution of 10 g/L.

All tested samples were commercially available. No pretreatment or dilution were required prior to analysis.

4.3.1.2 Materials

The materials involved in the microanalyser construction are equivalent to the ones described in § 4.2.1.2.

4.3.1.3 Experimental setup

As in the previous microsystem, the experimental setup can be divided into three main parts: the fluid management peripherals, the microanalyser and the optical detection system (see Figure 4.15).

The microanalyser and the optical detection system were the same as in the previous experimental setup (see § 4.2.1.3), while the fluid management peripherals were adapted to meet the new requirements, principally aiming to the total automation of the system.

The peripherals consisted in a four channel peristaltic pump Gilson Minipuls 3 (Gilson, Wisconsin, USA) equipped with 0.64 mm internal diameter Tygon tubing (Ismatec, Wertheim, Germany) and three three-way solenoid valves 161T031 from NResearch (West Caldwell, USA). Teflon tubing of 0.80 mm internal diameter (Scharlab SL, Setmenat, Spain) was used for the fluidic connections between the peripherals. An automated controller FlowTest from BioTray (Villeurbanne, France) was used for the actuation of the solenoid valves. Programming of the actuation of the valves was executed in a computer by using the dedicated CosDesigner software.

4.3.1.4 Flow manifold

The operating procedure of the analysis consisted in the continuous pumping of a BTB solution (indicator solution) into the microanalyser through channel A (see Figure 4.15), which was diluted inside the microanalyser by the continuous pumping of H_2O through channel B. Channel C was used for the introduction of the carrier, where fixed volumes of samples and standard solutions were injected and in-line diluted through the actuation of solenoid valves. When the acidic solutions were mixed with the diluted indicator solution inside the microanalyser, a change in the colour of the latter was produced.

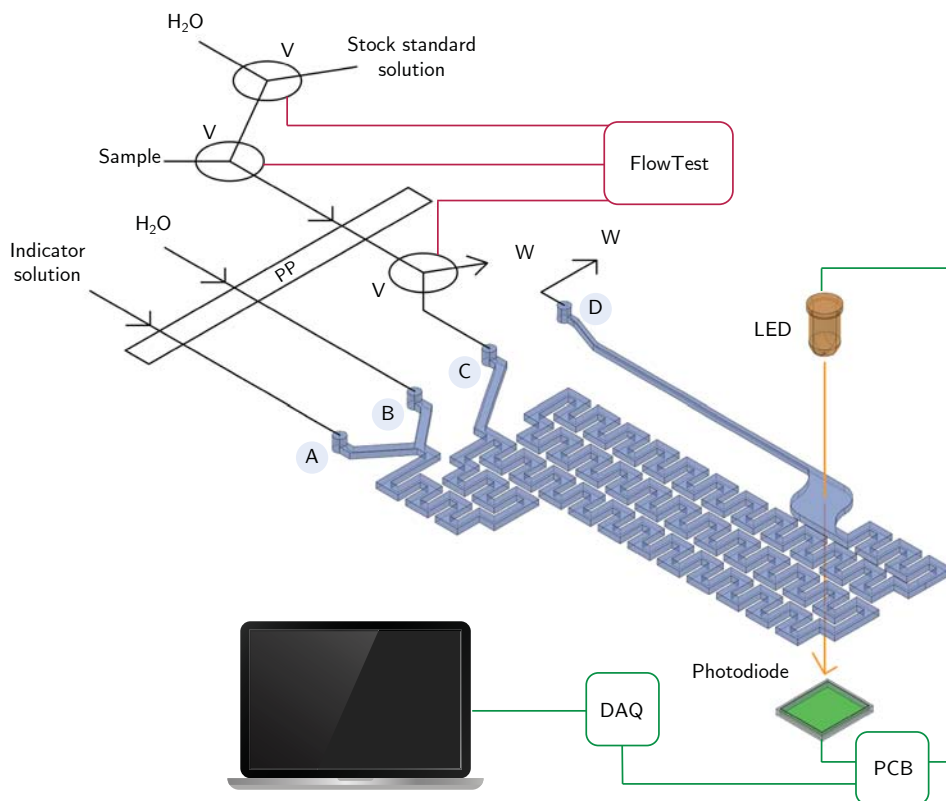


Figure 4.15: Schematic illustration of the experimental setup. PP: peristaltic pump; W: waste; V: valve.

The mixture was directed towards the detection chamber, where the optical detection system measured and monitored the absorbance changes.

4.3.2 Results and discussion

4.3.2.1 Optimisation of the hydrodynamic and chemical conditions

In order to apply the developed microsystem to the continuous monitoring of titratable acidity during wine-making processes, several factors had to be considered concerning, on one hand, the automation of the fluid management and, on the other hand, the stability of the solutions. Changes in the fluid management peripherals as well as a new optimisation of the chemical and hydrodynamic parameters were required for meeting the new requirements.

During the development of the first microsystem, a significant drop in the pH of the indicator solution could be noticed within a few hours. If not controlled, a decrease in the pH could have led to a reduction of the working range of the determination, since part of the working range of the indicator would have been circumvented. Consequently, the pH of the indicator solution was measured before each experiment and readjusted when deemed necessary. Nonetheless, this would not be viable for the new application of the system, where the stability of the reagents would mandatory for obtaining a robust and autonomous analyser.

The stability of several BTB solutions differing on their phosphate buffer content was therefore studied. Solutions containing 32 mg/L BTB and from 2.5 mM to 25 mM phosphate buffer were prepared. Each solution was divided into two different aliquots; one of them was stored in a closed flask, while the other was left open in contact with ambient air. The pH and the absorbance at 621 nm were measured several times during 10 days. The results are depicted in Figure 4.16.

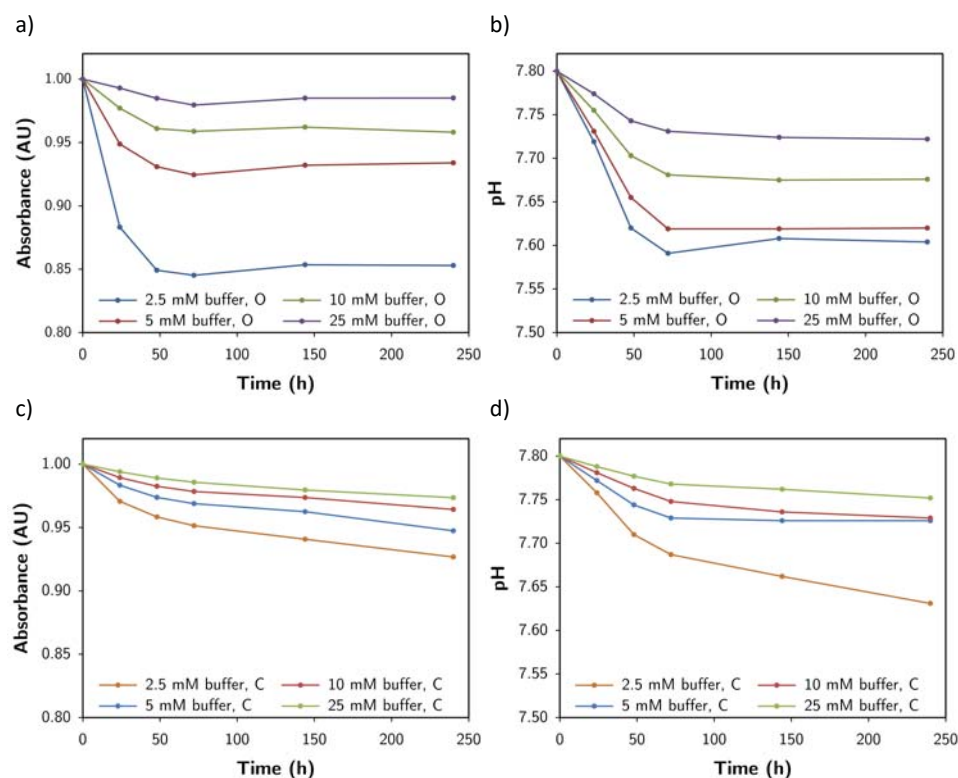


Figure 4.16: Evolution of the absorbance at 621 nm and the pH of several buffered BTB solutions during 10 days when stored open (O) (a, b) or closed (C) (c, d).

As expected, the time evolution of both absorbance and pH presented similar patterns, since the former depends on the latter. When comparing the two groups of aliquots, open (O) and closed (C), different behaviours could be noticed.

The aliquots that were kept open during the experiment experienced a remarkable drop in both absorbance and pH during the first 72 h and, after that period, they remained nearly stable until the end of the experiment. A slight increase in the pH and the absorbance of the 2.5 mM phosphate buffer solution was found between 72 h and 144 h.

On the other hand, the aliquots that were stored closed experienced a decline in both pH and absorbance during the whole experiment, being more pronounced during the first 72 h. While the pH of the 5 mM phosphate buffer solution remained almost stable from the 72nd hour, the 2.5 mM phosphate buffer solution exhibited a remarkable decay up to the end of the experiment.

In general, the group of solutions which were kept open experienced a larger decrease in both pH and absorbance in comparison to the closed ones. The different behaviour between the two groups could be related to the dissolution of atmospheric CO₂ and the achievement of the equilibrium for the solutions stored open but not for the ones which were kept closed. The overall change in the pH values was apparently modest. However, when considering the reduced working range of the BTB solutions (from 7.8 to 6.9), a minor loss in pH could have an important effect on the working range of the determination. This fact can be seen in Table 4.6, which contains the reduction percentage of the working range for each studied solution. For a reduction of less than a 10% in the working range during 10 days, 5 mM phosphate buffer indicator solutions would be needed, while solutions containing more than 25 mM phosphate buffer would be required for less than a 5% loss, in both cases being stored closed.

Table 4.6: Reduction of the working range as a result of a decrease in the pH.

[Phosphate buffer] (mM)	Reduction of the working range (%)	
	Open	Closed
2.5	21.8	18.8
5	20	8.2
10	13.8	7.9
25	8.7	5.3

As described in § 4.2.1.5, the developed microanalyser consisted of three different channels for liquid introduction. In the previous system, two of these channels were used for the continuous introduction of the indicator solution. Alternatively, for the system here presented, it was decided to use one of the channels for the introduction of H₂O, thus in-line diluting the indicator solution to 1:2. Hence, for obtaining the same final concentration of the indicator solution, the introduced solution had to contain twice the quantity of BTB and buffer (see Figure 4.17). With this simple modification

the stability of the indicator solution in terms of pH could be automatically raised as a result of the increase in the initial buffer concentration.

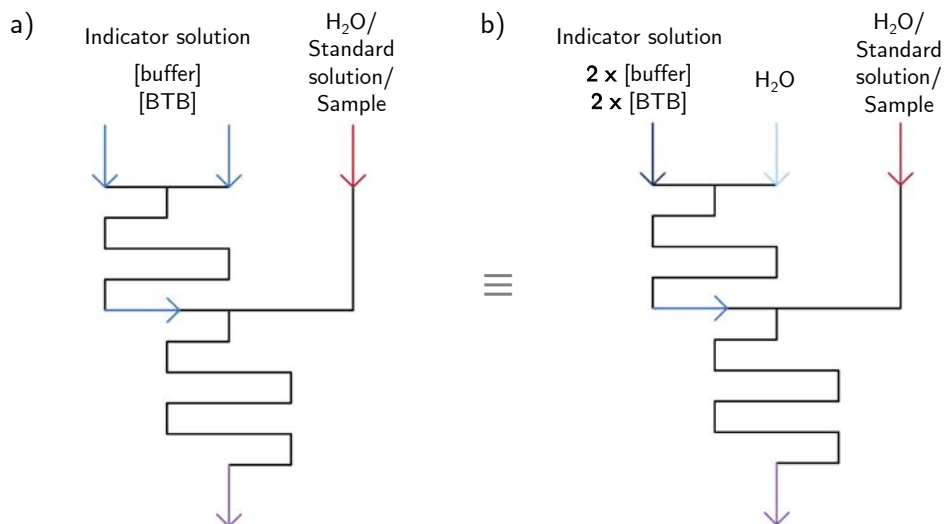
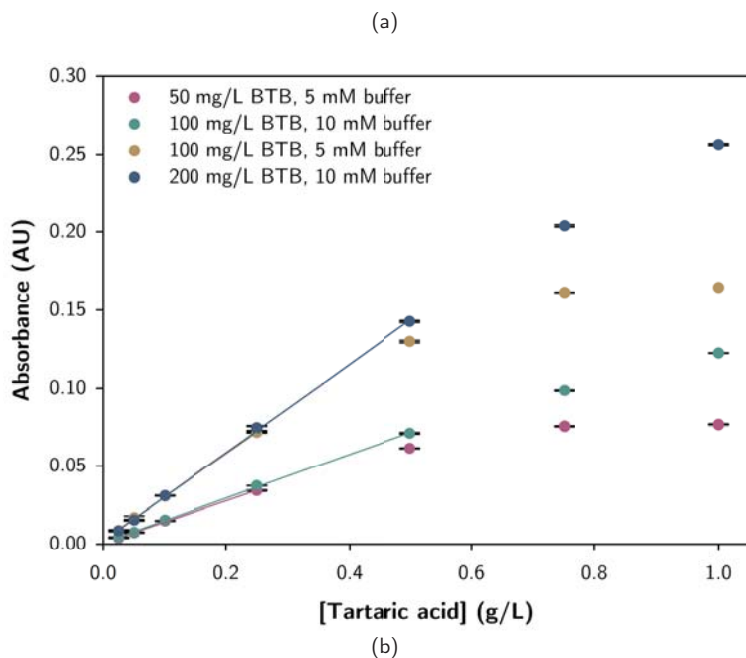


Figure 4.17: The same concentration of the indicator solution is obtained when the solution enters through two of the channels (a) and when it enters through one channel but it has twice the buffer and BTB content (b).

The optimisation of the BTB and the phosphate buffer concentration was then carried out using the manifold shown in [Figure 4.1](#) but with the fluidic configuration of [Figure 4.17.b](#).

As seen during the optimisation of the previous system, an increment in the buffer concentration of the indicator solution led to an increase in the linear range but a reduction of the sensibility, whereas when the BTB concentration was risen, the consequences were the opposite. Therefore, since a higher buffer concentration was needed for this application, an increase in the BTB concentration was also required to compensate the loss in sensibility.

Four different indicator solutions were prepared and adjusted to pH 7.8, containing: 50 mg/L BTB and 5 mM phosphate buffer; 100 mg/L BTB and 5 mM phosphate buffer; 100 mg/L BTB and 10 mM phosphate buffer; and 200 mg/L BTB and 10 mM phosphate buffer. Arbitrary conditions were established for all other hydrodynamic parameters: flow rate and injection volume were set to 500 $\mu\text{L}/\text{min}$ and 50 μL , respectively. Tartaric acid standard solutions from 0.025 g/L to 1 g/L were analysed in triplicate.



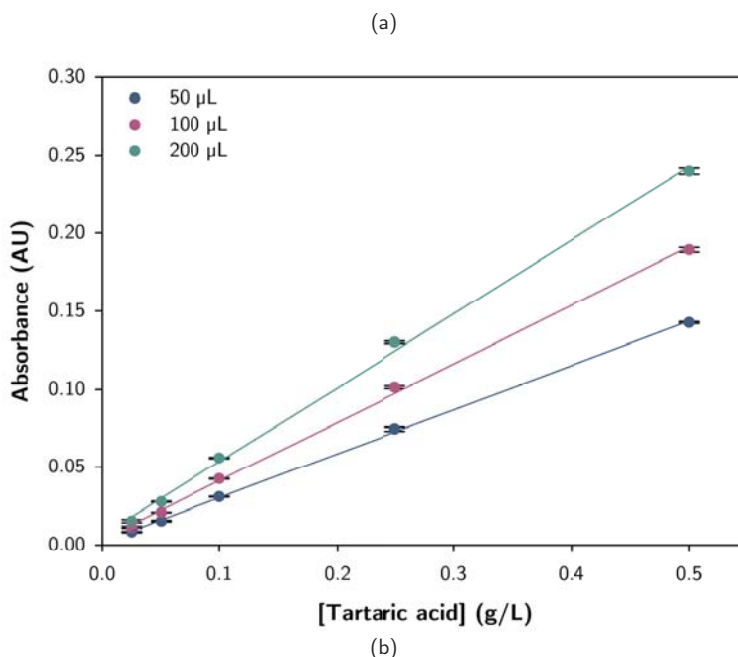
[BTB] (g/L)	[Phosphate buffer] (mM)	Slope	Intercept	R ²	Linear range (g/L)
50	5	0.135 ± 0.004	0.0007 ± 0.0004	0.9986	0 - 0.25
100	10	0.142 ± 0.002	0.0010 ± 0.0004	0.9995	0 - 0.50
100	5	0.279 ± 0.006	0.0024 ± 0.0009	0.9992	0 - 0.25
200	10	0.283 ± 0.004	0.002 ± 0.001	0.9994	0 - 0.50

Figure 4.18: Optimisation of the BTB and the phosphate buffer concentrations of the indicator solution. a) Representation of the results. b) Linear regression parameters.

The opposite consequences of increasing the BTB and the phosphate buffer concentrations are illustrated in Figure 4.18: when both concentrations were doubled, the sensibility remained nearly constant whereas the linear range was doubled. Both 10 mM phosphate buffer solutions presented an appropriate linear range. From these, the solution containing 200 mg/L BTB was selected due to a higher sensibility in comparison to the 100 mg/L one.

Once the composition of the indicator solution was optimised, the injection volume was studied using the same setup and the same conditions as in the previous experiment. Injection volumes of 50 μ L, 100 μ L and 200 μ L were tested by analysing in triplicate standard solutions from 0.025 g/L to 0.50 g/L tartaric acid using a 200 mg/L BTB 10

mM phosphate buffer indicator solution adjusted to pH 7.8.



Injection volume V_i (μL)	Slope	Intercept	R^2	Linear range (g/L)
50	0.283 ± 0.004	0.002 ± 0.001	0.9994	0 - 0.50
100	0.376 ± 0.008	0.004 ± 0.002	0.9987	0 - 0.50
200	0.47 ± 0.01	0.006 ± 0.003	0.9982	0 - 0.50

Figure 4.19: Injection volume optimisation. a) Representation of the results. b) Linear regression parameters.

In spite of an appreciable increase in the sensibility with a raise in the injection volume, the linearity of the results suffered a slight but noticeable decrease (see [Figure 4.19](#)). Thus, injection volumes between 50 μL and 100 μL were considered acceptable yet the use of higher volumes was discarded.

In order to increase the automation of the system, the 6-way injection valve was substituted by three three-way solenoid microvalves operated by a controller. The controller permitted the programming of the actuation of the microvalves by means of very simple and intuitive PC software. Once the actuation program was transferred to the controller, it could be executed with no further need of the controller to be connected to the PC. The actuation of the microvalves was programmed for the automatic calibration of the system as well as for the automatic sampling and in-line sample dilution.

Flow based systems where computer-controlled commutators are used for managing the flow are known as multicommutated flow systems. Multicommutation methods offer several advantages in comparison to the classical FIA systems, including the miniaturisation of the setup due to the reduced dimensions of the commutators, the reduction of sample and reagents consumption due to the precise insertion of volumes, the increase in the reproducibility due to the complete automation of the processes and the minimal operator intervention, and a reduction in the overall costs owing to the previously mentioned advantages. Furthermore, these systems are flexible and versatile, as several hydrodynamic and chemical parameters can be modulated by changing the programmed actuation of the commutators instead of physically modifying the setup.^{52,53}

The autocalibration of the system consisted in the analysis of several standard solutions produced by the in-line dilution of a single stock standard solution. In order to set the dilution sequence for the autocalibration, the limitations of the microvalves had to be considered.

Three-way solenoid valves have two different positions, “on” and “off”, connecting two different fluidic paths. When they receive an electronic pulse, they change their position from “off” to “on” and remain in this position until the pulse is finished. For diluting a solution, several cycles “off” - “on” are performed during a certain period of time, entering the concentrated solution at one position and the diluent at the other. The concentration of the diluted solution is determined by the time that the valve spends on each position.

The precision of the dilution process depends on the precision of the commutation of the microvalves on one hand, and the stability of the flow rate on the other. Despite the technical specifications of the microvalves indicated a response time of less than 20 ms for the “on” position and of less than 30 ms for the “off” one, previous works of our group reported an actual highest commutation speed of 100 ms for an acceptable reproducibility of the dilutions.⁵⁴

In multicommutation methods, the injection volume (V_I) is defined by the time that a valve is being actuated (t_i) and the flow rate (Q) at which the sample/standard is being injected:

$$V_I = t_i \cdot Q \quad (4.1)$$

In order to achieve a proper dilution of the solutions, all mentioned parameters (injection time, flow rate and minimum commutation time of the valves) had to be considered. It is important to highlight that a dilution is only possible when:

$$(t_{on} + t_{off}) \cdot n_{cycles} = t_i \quad (4.2)$$

Where t_{on} and t_{off} are the times that the valve spends on the “on” and the “off” positions, respectively, during one cycle, and n_{cycles} is the number of cycles during the injection of a solution.

As an example, Table 4.7 contains every possible dilution from a 0.40 g/L tartaric acid stock standard solution for an injection time of 10 s. For a flow rate of 500 $\mu\text{L}/\text{min}$, the injection volume would be 83 μL .

Table 4.7: Diluted standard solutions obtained from a stock standard solution (stock ss) of 0.40 g/L tartaric acid for an injection time of 10 s. The actuation of the valve for a 25-fold dilution of the sample is also included.

Injection time (s)	Time "on" (stock ss) (s)	Time "off" (H ₂ O) (s)	Number of cycles	Dilution factor	Stock ss (g/L)	Diluted solution (g/L)
Standard solutions						
10	0.1	9.9	1	100	0.40	0.004
10	0.1	4.9	2	50	0.40	0.008
10	0.1	2.4	4	25	0.40	0.016
10	0.1	1.9	5	20	0.40	0.02
10	0.1	0.9	10	10	0.40	0.04
10	0.1	0.4	20	5	0.40	0.08
10	0.1	0.3	25	4	0.40	0.10
10	0.1	0.1	50	2	0.40	0.20
10	0.3	0.1	25	1.33	0.40	0.30
10	0.4	0.1	20	1.25	0.40	0.32
10	0.9	0.1	10	1.11	0.40	0.36
10	1.9	0.1	5	1.05	0.40	0.38
10	2.4	0.1	4	1.04	0.40	0.384
10	4.9	0.1	2	1.02	0.40	0.392
10	9.9	0.1	1	1.01	0.40	0.396
10	10	0	0	0	0.40	0.40
Sample						
10	0.1	2.4	4	25	-	-

Theoretically, diluted solutions ranging from 0.004 g/L to 0.396 g/L could be obtained in the conditions described above. Nonetheless, when the difference between the time that a valve spends in the "on" and the "off" position is excessively high, the total mixture of the plugs cannot be achieved. This will be discussed later on in this chapter.

As previously mentioned, microvalves were programmed for the automatic calibration of the system as well as for the automatic sampling and in-line sample dilution. An example of a complete operation sequence of the valves for both calibration and sample analysis can be found in Figure 4.20. The sequence starts by filling the system with the respective solutions (a-d): filling with the stock standard solution up to V_1 (a), filling with H₂O up to V_2 (b), filling with the sample up to V_2 (c), and filling with H₂O up to V_3 (d). All excess fluid is conducted to waste through V_3 . Afterwards, this valve is closed, H₂O fills the microanalyser (e) and the baseline is established. The next steps (f-h) are aimed at the autocalibration of the system and exemplify the injection of the stock standard solution being highly diluted (f), diluted to a 1:2 factor (g) and

without dilution (h). Finally, the sample is injected and diluted in-line (i). For changing the sample, V_3 is opened while the new sample fills the system up to V_2 (j). After cleansing the system by the introduction of H_2O up to V_3 (k), this valve is closed and H_2O fills the microanalyser (l). Then, the baseline is recovered and the second sample can be injected (m).

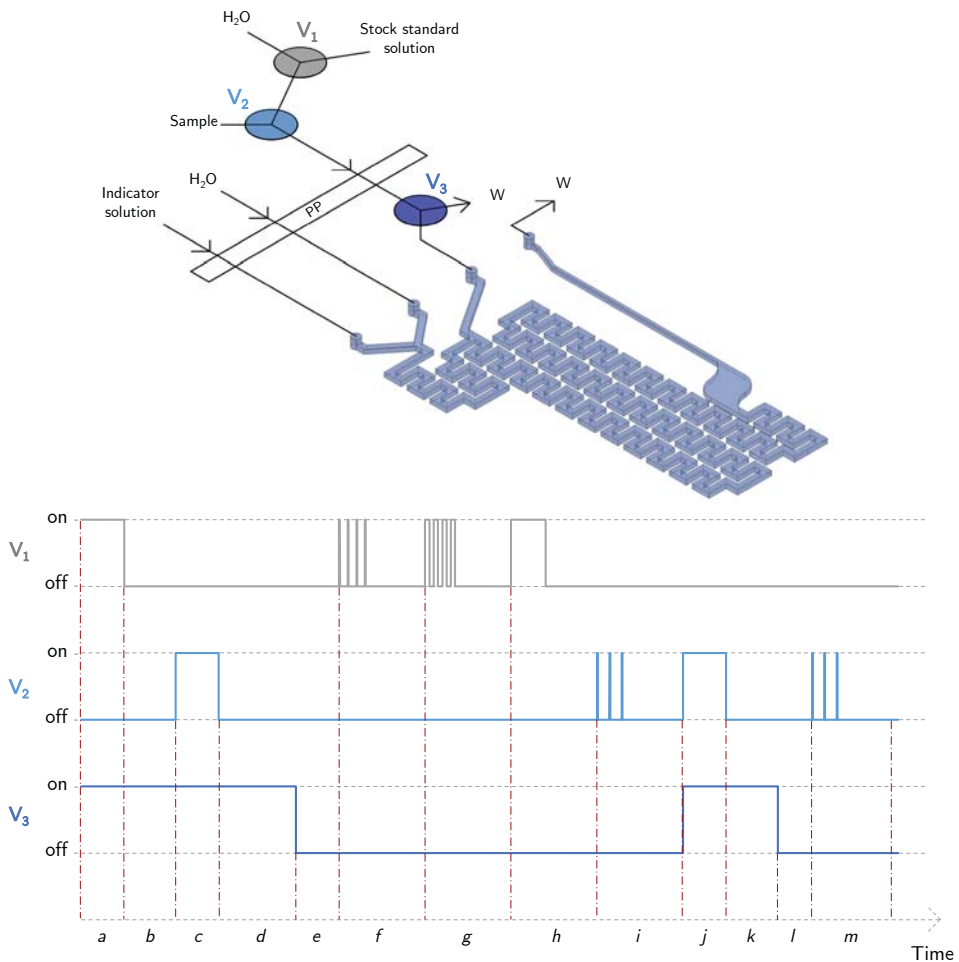


Figure 4.20: Operation sequence of the valves for both calibration and sample analysis. V_1 and V_2 are in charge of the dilution of the stock standard solution and the sample, respectively; V_3 is used for discarding waste solutions before entering the microanalyser. The times here represented for each step are for guidance purposes only.

Once the solenoid valves were implemented, the flow rate at the exit of V_3 (see Figure 4.20) was measured for all possible flow pathways and in combination with the actuation of the valves (no commutation of the valves and commutation cycles of 0.1 s, 1.0 s and 10.0 s). The flow rates of the different pathways showed an overall RSD of 0.55%, while changing the frequency of actuation of the valves led to an overall RSD of 0.76%, demonstrating no influence of the pathway or the actuation cycle in the flow rate.

A first experiment was carried out using the multicommutation manifold (see Figure 4.20) and the conditions previously optimised. A 200 mg/L BTB and 10 mM phosphate buffer indicator solution adjusted to pH 7.8 and a 0.40 g/L tartaric acid stock standard solution were used. The injection time was set to 10 s, corresponding to a volume of 83 μ L at 500 μ L/min. The injection frequency was set to 70 s, based on the previous experiments with the 6-way injection valve. The programmed dilutions from the stock solution are highlighted in grey in Table 4.7. Only one injection per dilution was made.

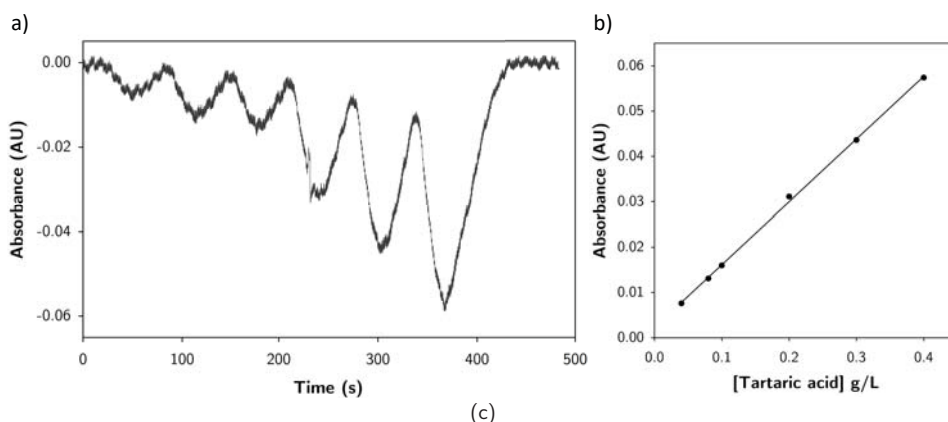


Figure 4.21: First calibration using the multicommutated flow system. a) Recorded signal. b) Representation of the results. c) Linear regression parameters. The height of the peaks was calculated by considering a common constant baseline.

The absorbance record is depicted in Figure 4.21.a. A patent overlapping of the peaks indicating a too high injection frequency was firstly noticed, as well as an increment in the signal-to-noise ratio in comparison to the equivalent manual injection experiment. Although the peaks showed an excellent linearity (see Figure 4.21.b), a considerable loss in sensibility was noticed when compared to similar calibrations using

the previous manifold (a 0.283 slope for 50 μL injection volume and a 0.376 slope for 100 μL).

All these unfavourable changes were thought to be directly related to a higher dispersion of the standard solution plugs inside the system as a consequence of the new configuration of the setup. On one hand, the distance between the injection point of samples and standards and the detection point was notably increased, thus increasing the flow time and, hence, the potential dispersion. Besides, in this configuration, sample and standard plugs had to circulate through the peristaltic pump, which could promote this effect by the movement of the rotating rollers.

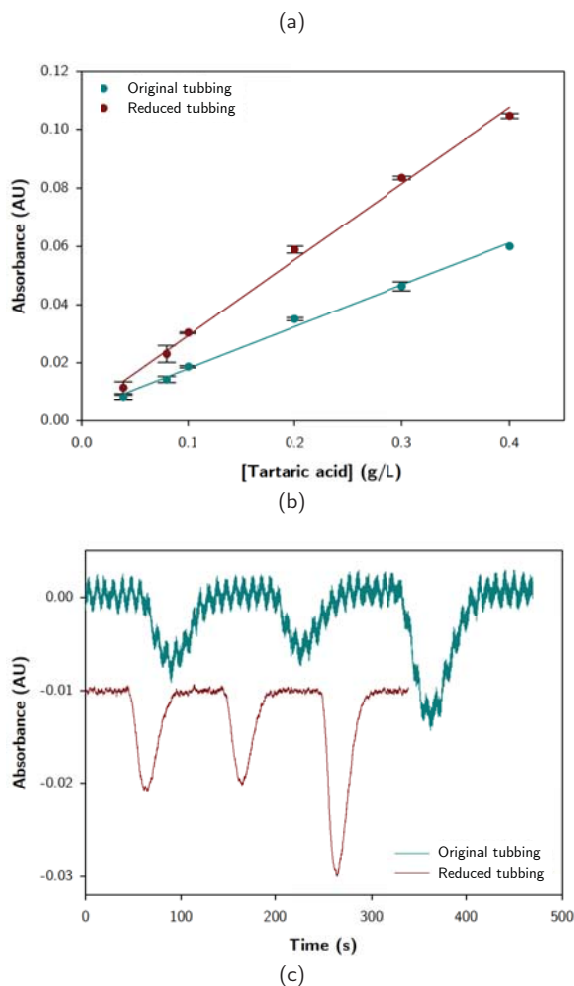
In order to minimise the aforementioned phenomena, all the Teflon tubing connections were shortened and the internal diameter of the Tygon tubing for the peristaltic pump was reduced from 1.02 mm to 0.64 mm.

A calibration using a 200 mg/L BTB and 10 mM phosphate buffer indicator solution adjusted to pH 7.8 and a 0.40 g/L tartaric acid stock standard solution was carried out. The injection time was set to 10 s, corresponding to a volume of 83 μL at 500 $\mu\text{L}/\text{min}$. The injection frequency was increased to 110 s to avoid the overlapping of the peaks. Standard solutions were analysed in triplicate.

The results were compared to those obtained for a calibration using the same conditions but the original Tygon tubing diameter and the Teflon tubing length (see [Figure 4.22](#)).

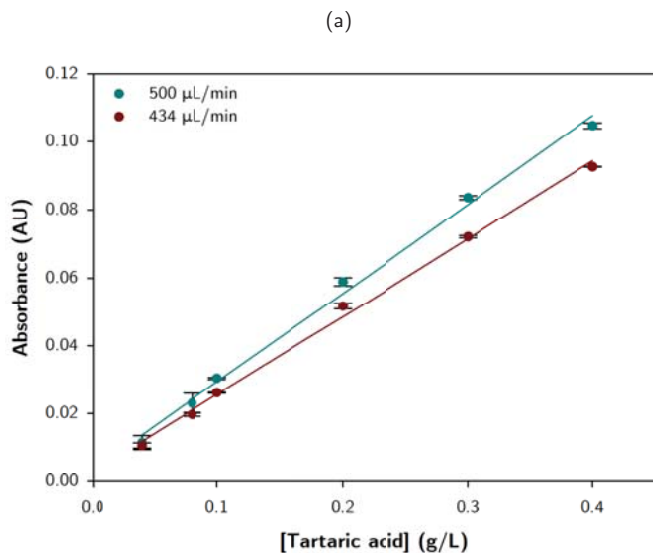
The applied modifications led to a remarkable increase in the sensibility, as well as a drastic increase in the signal-to-noise ratio due a reduction of the baseline noise. When decreasing the diameter of the Tygon tubing, the rotation speed of the peristaltic pump had to be increased for obtaining the same flow rate. This increment caused the reduction of the baseline noise, which, in this particular case, was mainly due to the pulsating flow produced by the peristaltic pump.

The effect of using a lower flow rate in the repeatability of the peaks was then studied (see [Figure 4.23](#)). A new calibration using a flow rate of 434 $\mu\text{L}/\text{min}$ was carried out. It is important to highlight that the actuation program of the valves was not modified for this experiment. As a consequence, the injection volume was reduced from 83 μL to 72 μL , causing a decrease in the sensibility. However, this effect was not taken into account since the injection volumes were studied later.



	Slope	Intercept	R ²	Linear range (g/L)
Original tubing	0.144 ± 0.008	0.004 ± 0.002	0.9920	0 - 0.40
Reduced tubing	0.26 ± 0.01	0.003 ± 0.003	0.9938	0 - 0.40

Figure 4.22: Effect of reducing the length and the diameter of the tubing. a) Representation of the results. b) Comparison of the peak height and the baseline noise of the recorded signal. The plotted peaks correspond to the same standard solution for both cases: two peaks of a 0.04 g/L tartaric acid solution and one peak of a 0.08 g/L tartaric acid solution. An arbitrary intercept has been used for better comprehension of the representation. c) Linear regression parameters.



(b)

Flow rate (μL/min)	Slope	Intercept	R ²	Linear range (g/L)
500	0.26 ± 0.01	0.003 ± 0.003	0.9938	0 - 0.40
434	0.229 ± 0.006	0.003 ± 0.002	0.9960	0 - 0.40

(c)

Tartaric acid standard solution (g/L)	Flow rate (μL/min)		Improvement (%)
	500	434	
	RSD (%)	RSD (%)	
0.04	17.96	6.80	62
0.08	12.58	2.97	76
0.10	0.95	0.59	38
0.20	1.99	1.67	16
0.30	0.66	0.48	27
0.40	0.80	0.12	84

Figure 4.23: Influence of the flow rate in the repeatability of the peaks. a) Representation of the results. b) Linear regression parameters. c) RSD values of the peaks obtained for the two flow rates.

The repeatability of the peaks was noticeably improved with the reduction of the flow rate. However, this improvement was modest for the 0.20 g/L tartaric acid standard solution, being this dilution the one involving the fastest actuation of the valves.

The accuracy of the commutation of the valves was studied in the next series of experiments and the results will be discussed further down in this section.

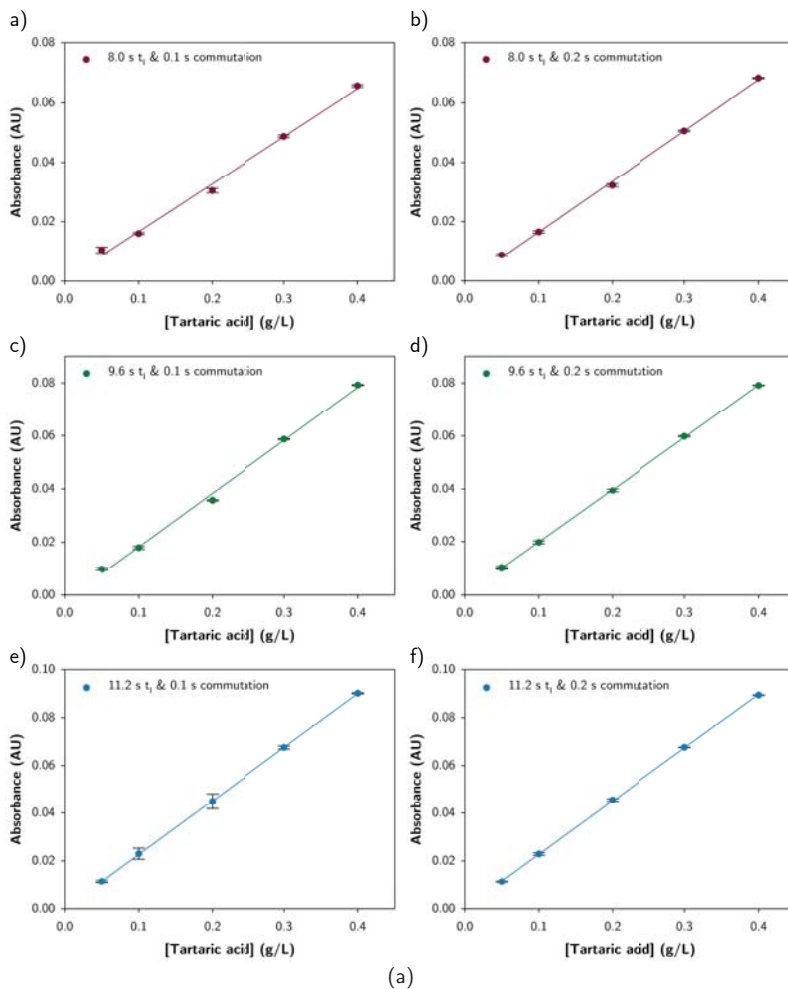
The influence of the injection time (and, therefore, of the injection volume) was studied by performing several calibrations with injection times ranging from 8.0 s to 67.2 s at 434 $\mu\text{L}/\text{min}$. Standard solutions were analysed in triplicate. For injection times of 8.0 s, 9.6 s and 11.2 s two different calibration replicates were carried out, one for a minimum commutation step of 0.1 s and, the other, for 0.2 s. The actuation of the valves for this series of experiments can be found in [Table 4.8](#).

Table 4.8: Actuation of the valves for a minimum commutation speed of 0.1 s and 0.2 s for preparing standard solutions of 0.05 g/L, 0.10 g/L, 0.20 g/L and 0.30 g/L tartaric acid from a 0.40 g/L tartaric acid stock solution.

0.1 s minimum commutation step		0.2 s minimum commutation step		Dilution factor	Stock standard solution (g/L)	Diluted solution (g/L)
t_{on} (s)	t_{off} (s)	t_{on} (s)	t_{off} (s)			
0.1	0.7	0.2	1.4	8	0.40	0.05
0.1	0.3	0.2	0.6	4	0.40	0.10
0.1	0.1	0.2	0.2	2	0.40	0.20
0.3	0.1	0.6	0.2	1.33	0.40	0.30
t_i	0	t_i	0	1	0.40	0.40

As can be seen in [Figure 4.24](#), a clear improvement in both the repeatability of the peaks and the linearity of the calibration curve was achieved by using a minimum commutation speed of 0.2 s instead of 0.1 s. Hence, the actuation of the valves for the subsequent experiments was programmed for minimum commutation steps of 0.2 s.

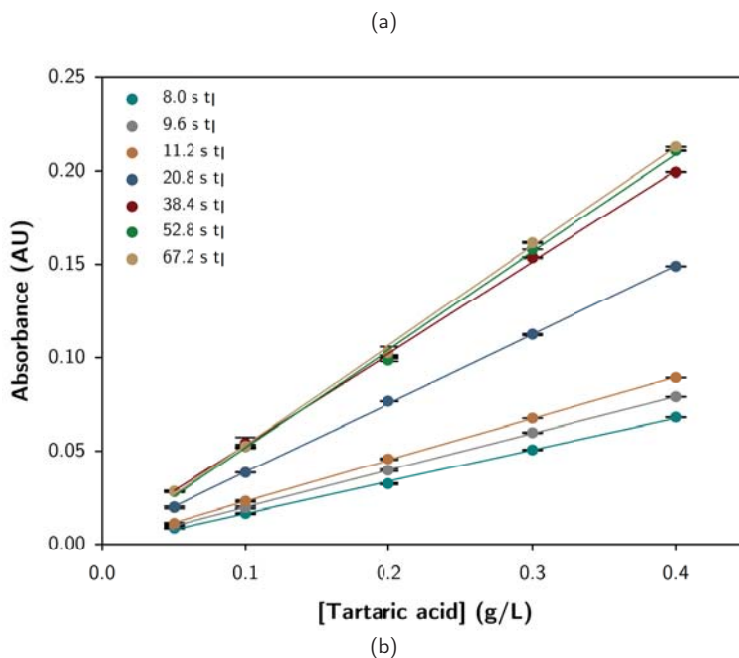
[Figure 4.25](#) displays the calibration curves obtained for all the tested injection times. Adequate linearity and increased sensibility were obtained when increasing the injection time up to 38.4 s, while higher injection times led to no significant increase in the sensibility (see [Figure 4.26](#)) yet no loss in the linear range. Hence, the optimum injection time was set to 38.4 s.



(a)

t_i (s)	V_i (μ L)	Commutation speed (s)	Slope	Intercept	R^2	Linear range (g/L)
8.0	58	0.1	0.160 ± 0.007	0.001 ± 0.002	0.9948	0 - 0.40
		0.2	0.170 ± 0.004	-0.0006 ± 0.0009		
9.6	69	0.1	0.200 ± 0.007	-0.002 ± 0.002	0.9967	0 - 0.40
		0.2	0.198 ± 0.002	0.0000 ± 0.0004		
11.2	81	0.1	0.225 ± 0.007	0.000 ± 0.002	0.9974	0 - 0.40
		0.2	0.223 ± 0.002	0.0005 ± 0.0004		

Figure 4.24: Influence of the minimum commutation speed in the repeatability of the peaks and the linearity of the calibration curve. Representation of the results for injection times of: 8.0 s (a, b), 9.6 s (c, d) and 11.2 s (e,f). g) Linear regression parameters.



t_i (s)	V_i (μL)	Commutation speed (s)	Slope	Intercept	R^2	Linear range (g/L)
8.0	58	0.2	0.170 ± 0.004	-0.0006 ± 0.0009	0.9987	0 - 0.40
9.6	69	0.2	0.198 ± 0.002	0.0000 ± 0.0005	0.9997	0 - 0.40
11.2	81	0.2	0.223 ± 0.002	0.0005 ± 0.0005	0.9998	0 - 0.40
20.8	150	0.2	0.369 ± 0.003	0.0016 ± 0.0008	0.9998	0 - 0.40
38.4	278	0.2	0.491 ± 0.009	0.004 ± 0.002	0.9991	0 - 0.40
52.8	382	0.2	0.52 ± 0.01	-0.001 ± 0.003	0.9980	0 - 0.40
67.2	486	0.2	0.533 ± 0.009	0.000 ± 0.002	0.9992	0 - 0.40

Figure 4.25: Injection time optimisation. a) Representation of the results. b) Linear regression parameters.

A 5 g/L tartaric acid solution was injected in triplicate as a synthetic sample for some of the previous calibration runs using dilution cycles with 0.1 s, 0.2 s and 0.3 s minimum commutation speeds. The results are summarised in [Table 4.9](#).

All the interpolated absorbance values led to sample concentrations far above the expected value, with a slight improvement trend when injection time was increased. Besides, a low repeatability of the peaks was obtained for the majority of the experiments.

Unfortunately, no clear relationship between the calculated concentrations and the

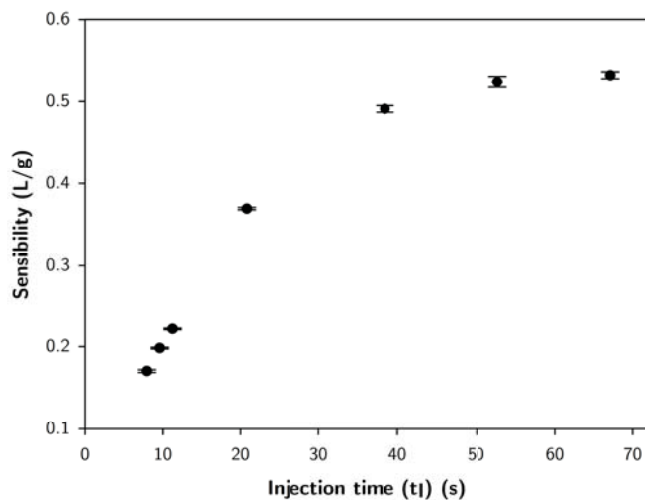


Figure 4.26: Sensibility of the calibration curves against the injection time.

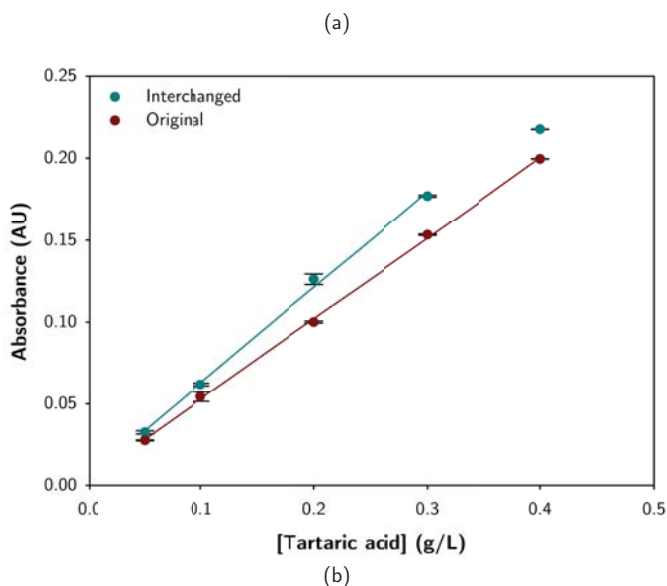
Table 4.9: Interpolated concentration of a synthetic sample of 5 g/L tartaric acid. The sample was injected in triplicate for each experiment.

t _i (s)	V ₁ (mL)	Commutation speed (s)	Cycle (s)	Number of cycles	Dilution factor	[M] _T (g/L)	[M] _{Exp} (g/L)	Error (%)	RSD (%)
8.0	58	0.1	0.1 – 1.9	4	20	5	8.43	69.6	4.0
		0.2	0.2 – 3.8	2			6.33	26.5	8.0
9.6	69	0.1	0.1 – 2.3	4	24	5	8.62	72.5	5.6
		0.2	0.2 – 4.6	2			5.89	17.9	2.0
11.2	81	0.1	0.1 – 2.7	4	28	5	7.22	44.3	6.6
		0.2	0.2 – 5.4	2			6.44	28.9	5.7
20.8	150	0.1	0.1 – 2.5	8	26	5	6.39	27.9	1.9
		0.1	0.1 – 2.3	16			6.85	36.9	9.9
38.4	278	0.2	0.2 – 4.6	8	24	5	6.34	26.9	3.7
		0.3	0.3 – 6.1	6			21.333	5.87	17.4

number of cycles or the minimum commutation speed could be established. The comparison was somehow hindered by the different dilution applied in each specific case since, as mentioned earlier, dilution factor possibilities are limited by the intrinsic characteristics of the system and by the selection of the injection time.

Since a satisfactory repeatability of the peaks was obtained for the dilution of the stock standard solution (carried out by the valve at the position 1, V₁, see Figure 4.20), but not for the dilution of the sample (carried out by the valve at the position 2, V₂), the performance of the valves was examined. The first experiment consisted in interchanging the role of the valves, therefore being V₁ in charge of the sample dilution

and V_2 in charge of the stock standard solution dilution.



	Slope	Intercept	R^2	Linear range (g/L)
Original	0.491 ± 0.009	0.004 ± 0.002	0.9991	0 - 0.40
Interchanged	0.58 ± 0.02	0.005 ± 0.004	0.9970	0 - 0.30

Figure 4.27: Effect of interchanging the roles of V_1 and V_2 valves. a) Representation of the results. b) Linear regression parameters.

Table 4.10: Interpolated concentration of a synthetic sample of 5 g/L tartaric acid. The sample was injected in triplicate for each commutation speed.

t_i (s)	V_1 (mL)	Commutation speed (s)	Cycle (s)	Number of cycles	Dilution factor	$[M]_T$ (g/L)	$[M]_{Exp}$ (g/L)	Error (%)	RSD (%) of the peaks
38,4	278	0.1	0.1 - 2.3	16	24	5	5.05	0.9	13.2
		0.2	0.2 - 4.6	8			4.7	-5.9	5.9
		0.3	0.3 - 6.1	6	21.333		4.51	-9.8	1.6

Unexpectedly, the calibration curve where V_2 executed the dilution of the standards exhibited a higher sensibility but a lower linear range when compared to the equivalent calibration with the original flow manifold (see Figure 4.27). Furthermore, the calculated sample concentrations (see Table 4.10) were found to be noticeably lower for the new configuration than for the previous calibrations, even being below the theoretical

value. On the other hand, the repeatability of the peaks was similar to the previous calibrations.

The differences found when interchanging the actuation of the valves could be mainly related to two different factors: the inherent performance of each valve and/or the differences in the flow pathway for solutions injected at V_1 or V_2 .

The length of the flow path from V_1 to the detector was slightly higher than the one from V_2 . Besides, solutions injected by V_1 had to pass through V_2 (see Figure 4.20). In order to study the effect of these differences, a 0.20 g/L tartaric acid solution was injected ten times by both V_1 and V_2 valves. The injection time was set to 38.4 s.

Table 4.11: Average peak height and RSD for 10 injections of a 0.20 g/L tartaric acid solution carried out by V_1 and V_2 .

	V_1	V_2
Average peak height (AU)	0.123 ± 0.001	0.122 ± 0.001
RSD (%)	0.379	0.515

The results presented a good repeatability of the peaks for both valves and no statistically significant difference between the two sets of results for a 95% confidence level ($n = 10$), demonstrating no significant influence of the flow pathway (see Table 4.11).

Consequently, a thorough study of the actuation of the valves was carried out. Several valves were tested for the automatic dilution of standards and samples using different dilution profiles; the obtained results were compared to the ones obtained by the injection of manually prepared standard solutions. The most relevant conclusions are discussed below.

The actuation of the valves was found to be particular for each valve, thus being difficult to establish a clear behaviour standard. Despite some of them performed an adequate dilution of the stock solution, not all these valves were found to be useful for performing the dilution of the sample, which required a considerably different dilution factor and therefore a remarkably different actuation of the valves. The valves displaying the best results regarding the repeatability of the peaks along with the minimum difference in comparison to the manually prepared solutions were selected.

It is important to note that when a valve suffers from a delay in performing a commutation from "off" to "on" or vice versa, the higher the number of commutation cycles is, the higher the accumulated error will be. This error would translate into a poor linearity of the results due to an inaccurate dilution to an unknown final concentration. Therefore, in order to minimise this effect, all diluted solutions were prepared by using the same number of cycles instead of the same minimum commutation speed. Besides, it was decided to prepare the 0.40 g/L tartaric acid standard solution by dilution (instead of being the stock solution), hence assuming that if there was an error on the dilution of the solutions, the same error would be introduced to the preparation of this one.

Thus, a 0.50 g/L tartaric acid solution was used as the stock standard solution for the following experiments.

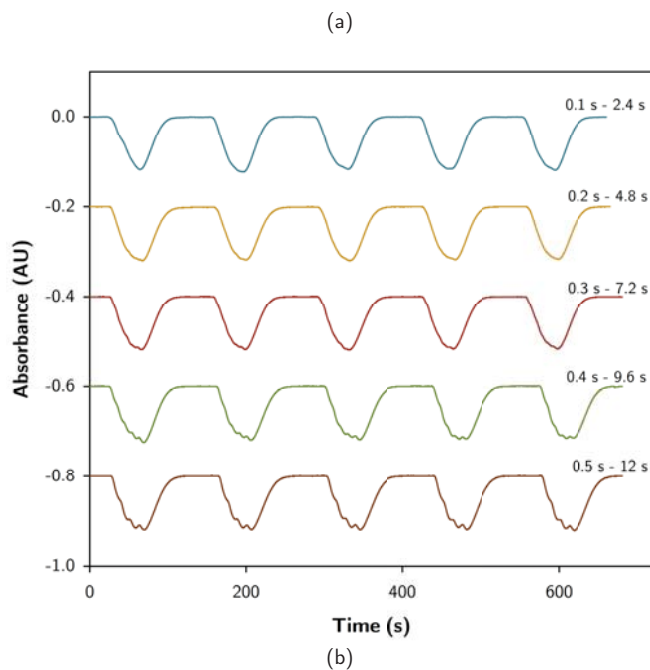
As mentioned before, the number of cycles depends on the injection time, and vice versa. Consequently, in order to apply the aforementioned changes, the injection time was set to 40.0 s (corresponding to 289 μ L injection volume). The number of commutation cycles was set to 20. The actuation of the valves for these new conditions can be found in [Table 4.12](#).

Table 4.12: Programming of the actuation of V_1 for obtaining diluted solutions of 0.05 g/L to 0.40 g/L from a stock solution of 0.50 g/L tartaric acid for 40.0 s injection time and 20 commutation cycles per dilution.

t_l (s)	t_{on} (s)	t_{off} (s)	Number of cycles	Dilution factor	Stock standard solution (g/L)	Diluted solution (g/L)
40.0	0.2	1.8	20	8	0.5	0.05
	0.4	1.6		4		0.1
	0.8	1.2		2		0.2
	1.2	0.8		1.33		0.3
	1.6	0.4		1.25		0.4

Since the dilution required for the sample was significantly higher than the one for the standard solutions, the use of the same number of cycles was not affordable. Thus, a parallel experiment for assessing the optimum actuation of the valve for the dilution of the samples was carried out. Several minimum commutation speeds were evaluated for the 25-fold in-line dilution of a 5 g/L tartaric acid sample solution. The solution was injected in quintuplicate at 434 μ L/min flow rate and using a 200 mg/L BTB and 10 mM phosphate buffer indicator solution adjusted to pH 7.8. The injection times for each cycle were chosen to be as close as possible between them considering the limitations explained earlier. The experiment was repeated twice.

Despite no statistically significant difference for a 95% confidence level ($n = 5$) was found between the average peak height of the two replicates for minimum commutation speeds from 0.1 s to 0.4 s (see [Figure 4.28](#)), the repeatability of the experiment was considerably higher for cycles of minimum commutation speeds of 0.2 s and 0.3 s. On the other hand, when analysing the absorbance peak profiles, an incomplete mixture of the sample - H_2O plugs could be noticed for cycles of 0.3 s – 7.2 s, becoming more evident for cycles with higher minimum commutation times. Therefore, 0.2 s "on" - 4.8 s "off" was selected as the optimum commutation cycle for the sample dilution.



t_i (s)	45.0	45.0	45.0	50.0	50.0
V_i (μL)	326	326	326	362	362
Commutation speed (s)	0.1	0.2	0.3	0.4	0.5
Cycle (s)	0.1 - 2.4	0.2 - 4.8	0.3 - 7.2	0.4 - 9.6	0.5 - 12
Number of cycles	18	9	6	5	4
Dilution factor	25	25	25	25	25
Replicate 1					
Average peak height	0.119 ± 0.007	0.118 ± 0.004	0.118 ± 0.003	0.12 ± 0.01	0.120 ± 0.002
RSD	2.10	1.08	0.89	2.94	0.65
Replicate 2					
Average peak height	0.127 ± 0.005	0.120 ± 0.003	0.120 ± 0.005	0.125 ± 0.004	0.128 ± 0.003
RSD	1.51	0.91	1.45	1.29	0.77
Replicates 1 and 2					
Average peak height	0.12 ± 0.01	0.119 ± 0.003	0.119 ± 0.004	0.122 ± 0.009	0.12 ± 0.01
RSD	3.79	1.15	1.43	3.27	3.6

Figure 4.28: Effect of the minimum commutation speed for a 25-fold dilution of the sample. a) Recorded signal for the different commutation cycles. An arbitrary intercept has been used for clearer illustration. b) Experimental parameters and obtained results.

The conditions being used before the study of the valves were not adequate for a linear range to up to 0.40 g/L tartaric acid, as it could be appreciated in previous experiments (e.g., see [Figure 4.27](#)). The valve that was being used for the optimisation of the injection volume suffered from an inaccurate commutation, leading to an error on the preparation of the diluted standard solutions. Since this error was reproducible it was not easily detected and, by increasing the injection volume, we were simply injecting a higher amount of an incorrectly diluted tartaric acid solution.

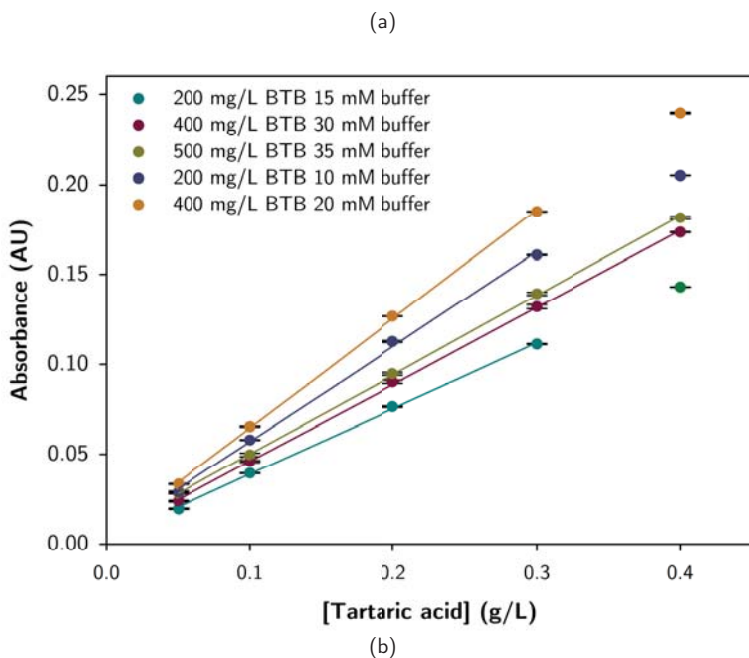
Once the best performing valves were selected, the BTB and the phosphate buffer concentrations of the indicator solution were optimised anew in order to increase the linear range. The alternative of reducing the injection time (and therefore the injection volume) was discarded since the number of cycles for the sample dilution would be affected by this change and could lead to dilution irreproducibility. Furthermore, an increase in the buffer concentration of the indicator solution would add more stability to its pH, which, as mentioned earlier, was crucial for the autonomous operation of the system.

Five different indicator solutions were prepared and adjusted to pH 7.8: 200 mg/L BTB and 10 mM phosphate buffer; 200 mg/L BTB and 15 mM phosphate buffer; 400 mg/L BTB and 20 mM phosphate buffer; 400 mg/L BTB and 30 mM phosphate buffer; and 500 mg/L BTB and 35 mM phosphate buffer. Tartaric acid standard solutions were prepared according to [Table 4.12](#) and were analysed in triplicate at a flow rate of 434 $\mu\text{L}/\text{min}$.

From the several tested combinations, only the two containing the highest buffer concentrations covered the desired linear range (see [Figure 4.29](#)). From these two, 500 mg/L BTB and 35 mM phosphate buffer was preferred over 400 mg/L BTB and 30 mM phosphate buffer due to its higher buffer content, contributing to the stability of the solution, and its slightly higher sensibility.

For the selected indicator solution, a synthetic sample containing 5 g/L tartaric acid was analysed in quintuplicate. The interpolated concentration was 5.0 ± 0.1 ($n = 5$, 95% confidence level) and the RSD of the peaks was 0.77%.

To summarise, the final optimal conditions of the microsystem were: a 500 mg/L BTB and 35 mM phosphate buffer indicator solution adjusted to pH 7.8, an injection time of 40.0 s (corresponding to an injection volume of 289 μL at 434 $\mu\text{L}/\text{min}$), a 0.50 g/L tartaric acid stock standard solution diluted by performing 20 commutation cycles per dilution, and a sample dilution to 1:25 by performing commutation cycles of 0.2 s $t_{\text{on}} - 4.8$ s t_{off} .



[BTB] (g/L)	[Phosphate buffer] (mM)	Slope	Intercept	R ²	Linear range (g/L)
200	15	0.366 ± 0.007	0.002 ± 0.001	0.9994	0 - 0.30
400	30	0.428 ± 0.005	0.003 ± 0.001	0.9996	0 - 0.40
500	35	0.441 ± 0.004	0.006 ± 0.001	0.9997	0 - 0.40
200	10	0.53 ± 0.01	0.004 ± 0.002	0.9984	0 - 0.30
400	20	0.607 ± 0.008	0.004 ± 0.001	0.9997	0 - 0.30

Figure 4.29: BTB and phosphate buffer concentration optimisation. a) Representation of the results. b) Linear regression parameters.

4.3.2.2 Analytical characterisation of the microsystem

The repeatability of the method was assessed by performing three different calibration analyses in three different working days under identical hydrodynamic and chemical conditions using newly prepared solutions. Standards ranging from 0.05 g/L to 0.40 g/L were analysed in triplicate by using the aforementioned optimal conditions. **Figure 4.30** displays the recorded signal and the calibration curve obtained for one of the experiments (Replicate 1 from **Table 4.13**).

No statistically significant differences ($n = 15$, 95% confidence level) were found between the three calibration replicates, demonstrating an excellent between-day repeatability.

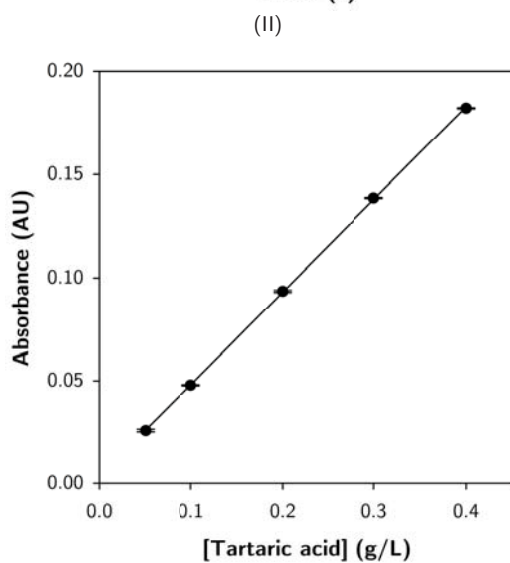
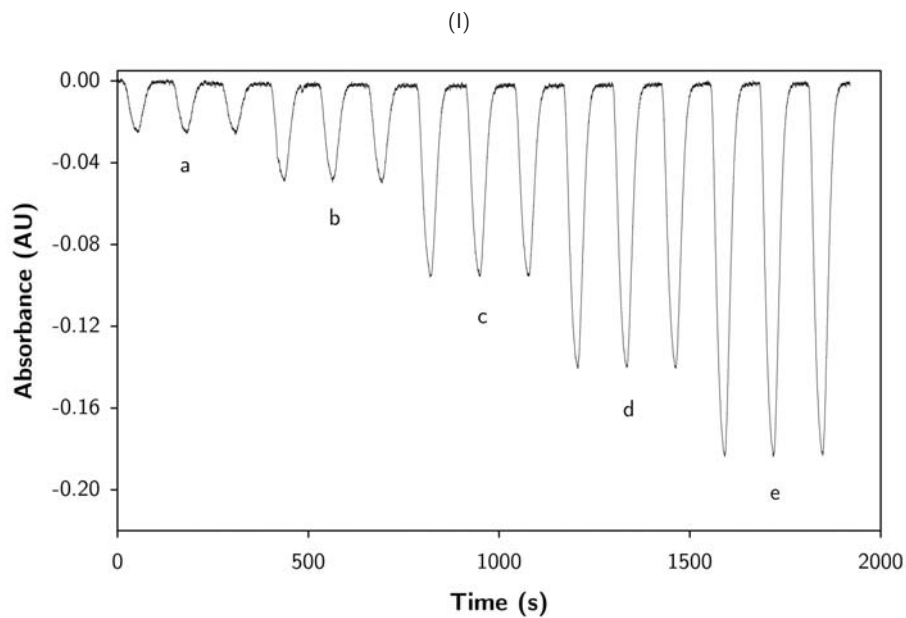


Figure 4.30: Recorded signal (I) and calibration curve (II) for one of the experiments using the optimal conditions. Standard solutions: (a) 0.05 g/L, (b) 0.10 g/L, (c) 0.20 g/L, (d) 0.30 g/L and (e) 0.40 g/L tartaric acid.

Table 4.13: Analytical characterisation of the microsystem. Linear regression parameters, LOD and LOQ for three calibration experiments. LOD and LOQ were calculated as 3 times and 10 times the standard deviation of the baseline, respectively.

Replicate	Slope	Intercept	R ²	LOD (g/L tartaric acid)	LOQ (g/L tartaric acid)
1	0.450 ± 0.002	0.0031 ± 0.0007	0.9999	0.004	0.01
2	0.445 ± 0.004	0.0038 ± 0.0008	0.9998	0.004	0.01
3	0.447 ± 0.006	0.000 ± 0.002	0.9994	0.004	0.01

With the optimal conditions, a sampling rate of 26 h₋₁ was achieved, consuming 289 µL of sample, 500 µg of BTB and 35 µmol of phosphate and producing 3 mL of waste per assay.

4.3.2.3 Real sample analysis

In order to assess the proper performance of the analytical microsystem, the titratable acidity determination of twenty-five wine samples was carried out. The results were compared to those kindly obtained by BioSystems (Barcelona, Spain).

For the developed method, the samples were analysed without any pretreatment or dilution using the previously optimised conditions. The linear equation obtained for the calibration was $A = (0.449 \pm 0.004) \cdot [\text{tartaric acid}] \text{ (g/L)} + (0.003 \pm 0.001)$, $R^2 = 0.9998$, for $n = 15$ and 95% confidence level.

The method used by BioSystems for the titratable acidity determination was based on the same principle as the here proposed method, consisting in the measurement of the absorbance change of a buffered BTB solution when mixed with a sample; the absorbance measurements were carried out at 620 nm using a photometer.⁵⁵ The validation of their method was performed by comparing it to the OIV official method.⁵⁶

An acceptable correlation of the results was obtained for white and rosé wine samples, whereas red wine acidity content was underestimated by the developed microsystem (see Table 4.14).

In order to assess the possible interference of the coloured species of red wine, a blank measurement of the samples 9 to 13 was carried out. With that purpose, the samples were injected in quintuplicate using the same hydrodynamic and chemical conditions but removing the BTB from the indicator solution. The absorbance of the samples was measured and interpolated in the previously obtained calibration curve, and the correction was applied to the titratable acidity content. The results are summarised in Table 4.15.

The correction of the colour for the tested samples led to a drastic decrease in the differences found between the two methods, revealing a clear need to perform a blank measurement for coloured wine samples.

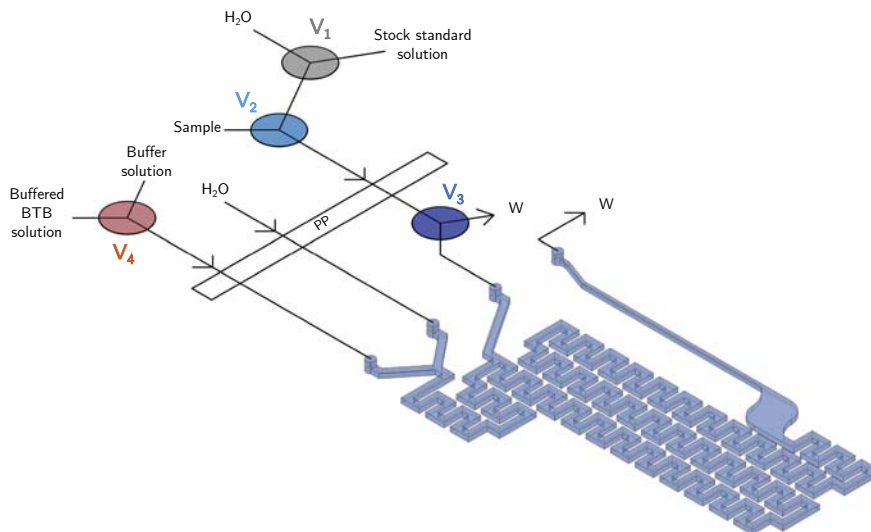
Table 4.14: Results for the titratable acidity determination of twenty-five wine samples obtained by BioSystems and by the system here presented. No confidence interval was given for the BioSystems results.

Sample		BioSystems	Developed method		
		Titratable acidity (g/L tartaric acid)	RSD (%)	Difference (%)	
1	White	5.6	6.05 ± 0.06	1	8
2	White	6.0	5.9 ± 0.1	2	-2
3	White	5.4	5.4 ± 0.1	2	0
4	White	6.2	6.0 ± 0.2	3	-3
5	White	4.3	4.3 ± 0.1	2	0
6	White	5.7	5.6 ± 0.1	1	-2
7	Rosé	4.3	4.3 ± 0.1	2	0
8	Rosé	5.7	5.78 ± 0.09	1	1
9	Red	5.2	4.91 ± 0.04	1	-6
10	Red	5.6	5.4 ± 0.3	4	-4
11	Red	5.3	4.7 ± 0.2	3	-11
12	Red	5.1	4.49 ± 0.06	1	-12
13	Red	5.7	5.3 ± 0.2	3	-7
14	Red	6.2	4.8 ± 0.2	4	-23
15	Red	6.1	5.3 ± 0.1	2	-13
16	Red	6.9	6.2 ± 0.2	2	-10
17	Red	7.7	7.1 ± 0.2	2	-8
18	Red	6.2	5.9 ± 0.1	2	-5
19	Red	7.2	6.4 ± 0.2	2	-11
20	Red	5.2	4.7 ± 0.1	2	-10
21	Red	5.2	4.7 ± 0.2	3	-10
22	Red	5.5	5.02 ± 0.08	1	-9
23	Red	5.4	4.48 ± 0.09	2	-17
24	Red	6.0	5.30 ± 0.06	1	-12
25	Red	5.9	5.2 ± 0.1	2	-12

The measurement of the blank could be easily implemented to the system by the introduction of a fourth three-way solenoid valve (V_4) as shown in [Figure 4.31](#). With this simple modification, which was not carried out during this work, it was expected to achieve an excellent system performance not only for white and rosé wine samples, but also for red wine samples.

Table 4.15: Effect of the colour correction for some of the analysed samples.

Sample	BioSystems Titratable acidity (g/L tartaric acid)	Developed method			
		No colour correction		Colour correction	
		Titratable acidity (g/L tartaric acid)	Difference (%)	Titratable acidity (g/L tartaric acid)	Difference (%)
9	5.2	4.93	-5	5.26	0
10	5.6	5.40	-4	5.60	0
11	5.3	4.70	-11	4.90	-8
12	5.1	4.49	-12	4.79	-6
13	5.7	5.30	-7	5.60	-2

Figure 4.31: Introduction of a fourth valve (V₄) for the measurement of the blank.

4.4 Conclusions & future remarks

In this chapter, two microsystems for the titratable acidity determination of must and wine samples have been proposed, one for its application to the determination of individual samples and the other to the continuous monitoring of this parameter during wine-making processes.

The first microsystem demonstrated an exceptional throughput as well as a wider working range, a reduced sample and reagent consumption and a higher miniaturisation in comparison to other previously reported systems^{31–33,35,36}. The simple and low-cost

system here presented involved minimal pretreatment of the sample (a 25-fold dilution being only required) and produced minimal waste. Its performance was compared to the AOAC official method, proving an adequate accuracy and precision of the measurements. All these advantages make this system a perfect candidate for carrying out routine analyses in wineries.

For the second microsystem, the complete automation of the analytical process, including calibration and sampling, was achieved, therefore eliminating any human intervention. The stability of the reagents and the robustness of the system would permit its application to the on-line continuous monitoring of titratable acidity in wineries, thus improving the control of wine-making processes and contributing to a higher quality of the final product. Several issues are still to be studied, such as the implementation of a blank measurement when titratable acidity of red wines is determined, as well as the complete automation and miniaturisation of the system through the replacement of the peristaltic pump by solenoid micropumps that could be automatedly actuated. Once these final modifications were applied, the microsystem would be ready for its installation, meeting all the requirements for being considered a completely functional micro total analysis system (μ TAS).

References

- (1) Ribéreau-Gayon, P.; Glories, Y.; Maujean, A.; Dubourdieu, D., *Handbook of Enology Volume 2: The Chemistry of Wine Stabilization and Treatments*, 2nd; John Wiley & Sons, Ltd: Chichester, UK, 2006, p 441.
- (2) Moreira, J. L.; Santos, L. Analysis of organic acids in wines by Fourier-transform infrared spectroscopy. *Analytical and Bioanalytical Chemistry* **2005**, *382*, 421–425.
- (3) Drysdale, G. S.; Fleet, G. H. Acetic Acid Bacteria in Winemaking: A Review. *American Journal of Enology and Viticulture* **1988**, *39*, 143–154.
- (4) Jackson, R. S., *Wine Science: Principles and Applications*, 3rd; Academic Press, Elsevier: Burlington, MA, USA, 2008, p 747.
- (5) Jacobson, J. L., *Introduction to Wine Laboratory Practices and Procedures*; Springer: New York, NY, USA, 2006, p 375.
- (6) *Wine Chemistry and Biochemistry*; Moreno-Arribas, M. V., Polo, M. C., Eds.; Springer New York: New York, NY, USA, 2009, p 735.
- (7) Rajković, M. B.; Sredović, I. D. The determination of titratable acidity and total tannins in red wine. *Journal of Agricultural Sciences* **2009**, *54*, 223–246.
- (8) Rajković, M. B.; Novaković, I. D.; Petrović, A. Determination of titratable acidity in white wine. *Journal of Agricultural Sciences* **2007**, *52*, 169–184.
- (9) Boulton, R. The Relationships between Total Acidity, Titratable Acidity and pH in Wine. *Vitis* **1980**, *19*, 113–120.
- (10) Boulton, R. The General Relationship Between Potassium, Sodium and pH in Grape Juice and Wine. *American Journal of Enology and Viticulture* **1980**, *31*, 182–186.
- (11) Ough, C. S.; Amerine, M. A., *Methods for analysis of musts and wines*, 2nd; John Wiley & Sons, Ltd: New York, NY, USA, 1988, p 377.
- (12) Nagel, C. W.; Amistoso, J. L.; Bendel, R. B. The Effect of pH and Titratable Acidity on the Quality of Dry White Wines. *American Journal of Enology and Viticulture* **1982**, *33*, 75–79.
- (13) Plane, R. A.; Mattick, L. R.; Weirs, L. D. An Acidity Index for the Taste of Wines. *American Journal of Enology and Viticulture* **1980**, *31*, 265–268.
- (14) Amerine, M.; Roessler, E. B.; Ough, C. S. Acids and the Acid Taste. I. The Effect of pH and Titratable Acidity. *American Journal Of Enology And Viticulture* **1965**, *16*, 29–37.
- (15) Amerine, M. A., *Uniform Methods of Analyses for Wines and Spirits*; American Society of Enologists: Davis, CA, USA, 1972.

- (16) *Official Methods of Analysis of AOAC INTERNATIONAL*, 18th; Horwitz, W., Latimer, G. W., Eds.; AOAC INTERNATIONAL: Gaithersburg, MD, USA, 2010.
- (17) In *Compendium of International Methods of Wine and Must Analysis*; International Organisation of Vine and Wine: Paris, France, 2018.
- (18) Darias-Martínez, J.; Socas-Hernández, A.; Díaz-Romero, C.; Díaz-Díaz, E. Comparative study of methods for determination of titrable acidity in wine. *Journal of Food Composition and Analysis* **2003**, *16*, 555–562.
- (19) Huerta, M.; Salinas Fernandez, M.; Masoud Musa, T. Titrable acidity of wines at different pH and its relation with the colour. *Journal International des Sciences de la Vigne et du Vin* **1998**, *32*, 163–167.
- (20) Wong, G.; Caputi, A. A New Indicator for Total Acid Determination in Wines. *American Journal of Enology and Viticulture* **1966**, *17*, 174–177.
- (21) Lučan, Ž. D.; Palič, A. Total acids determination in wine with different methods. *Food / Nahrung* **1994**, *38*, 427–433.
- (22) Cardwell, T. J.; Cattrall, R. W.; O'Connell, G. R.; Petty, J. D.; Scollary, G. R. Potentiometric detectors for the determination of acidity by discontinuous flow analysis. *Electroanalysis* **1992**, *4*, 805–810.
- (23) Tyl, C.; Sadler, G. D. In *Food Analysis*, Nielsen, S., Ed., 5th; Springer: Gewerbe-strasse, Switzerland, 2017, pp 389–406.
- (24) Lima, M. J.; Reis, B. F. Fully automated photometric titration procedure employing a multicommuted flow analysis setup for acidity determination in fruit juice, vinegar, and wine. *Microchemical Journal* **2017**, *135*, 207–212.
- (25) Garcia, A. J. C.; Reis, B. F. Instrumentation and Automated Photometric Titration Procedure for Total Acidity Determination in Red Wine Employing a Multicommuted Flow System. *Journal of Automated Methods and Management in Chemistry* **2006**, *2006*, 1–8.
- (26) Honorato, R. S.; Araújo, M. C. U.; Lima, R. A.; Zagatto, E. A.; Lapa, R. A.; Costa Lima, J. L. A flow-batch titrator exploiting a one-dimensional optimisation algorithm for end point search. *Analytica Chimica Acta* **1999**, *396*, 91–97.
- (27) Gaião, E. N.; Honorato, R. S.; Santos, S. R. B.; Araújo, M. C. U. An automated flow-injection titrator for spectrophotometric determinations of total acidity in wines, using a single standard solution and gradient calibration. *The Analyst* **1999**, *124*, 1727–1730.
- (28) Marcos, J.; Íos, A.; Valcárcel, M. Automatic titrations in unsegmented flow systems based on variable flow-rate patterns. *Analytica Chimica Acta* **1992**, *261*, 489–494.

- (29) Cardwell, T. J.; Cattrall, R. W.; Cross, G. J.; O'Connell, G. R.; Petty, J. D.; Scollary, G. R. Determination of titratable acidity of wines and total acidity of vinegars by discontinuous flow analysis using photometric end-point detection. *The Analyst* **1991**, *116*, 1051–1054.
- (30) Tôrres, A. R.; da Silva Lyra, W.; de Andrade, S. I. E.; Andrade, R. A. N.; da Silva, E. C.; Araújo, M. C. U.; da Nóbrega Gaião, E. A digital image-based method for determining of total acidity in red wines using acid–base titration without indicator. *Talanta* **2011**, *84*, 601–606.
- (31) Vahl, K.; Kahlert, H.; von Mühlen, L.; Albrecht, A.; Meyer, G.; Behnert, J. Determination of the titratable acidity and the pH of wine based on potentiometric flow injection analysis. *Talanta* **2013**, *111*, 134–139.
- (32) Vidigal, S. S.; Rangel, A. O. A flow-based platform for measuring the acidity parameters in wine. *Talanta* **2017**, *168*, 313–319.
- (33) Vidigal, S. S.; Ramos, A. T. C.; Rangel, A. O. Flow-Based System for the Determination of Titratable Acidity in Wines. *Food Analytical Methods* **2016**, *9*, 2241–2245.
- (34) Mataix, E.; Luque de Castro, M. Sequential determination of total and volatile acidity in wines based on a flow injection-pervaporation approach. *Analytica Chimica Acta* **1999**, *381*, 23–28.
- (35) Rangel, A. O. S. S.; Tóth, I. V. Sequential determination of titratable acidity and tartaric acid in wines by flow injection spectrophotometry. *The Analyst* **1998**, *123*, 661–664.
- (36) Peris-Tortajada, M.; Maquieira, A.; Puchades, R. Automated Determination of Total Acidity in Wines by Flow Injection Analysis. *American Journal of Enology and Viticulture* **1993**, *44*, 118–120.
- (37) Ymber, O.; Berenguel-Alonso, M.; Calvo-López, A.; Gómez-de Pedro, S.; Izquierdo, D.; Alonso-Chamarro, J. Versatile Lock and Key Assembly for Optical Measurements with Microfluidic Platforms and Cartridges. *Analytical Chemistry* **2015**, *87*, 1503–1508.
- (38) Calvo López, A. Diseño, construcción y evaluación de analizadores miniaturizados para su aplicación aeroespacial, medioambiental, alimentaria, biomédica e industrial., Ph.D. Thesis, Universitat Autònoma de Barcelona, 2017.
- (39) Burger, S; Schulz, M; von Stetten, F; Zengerle, R; Paust, N Rigorous buoyancy driven bubble mixing for centrifugal microfluidics. *Lab on a Chip* **2016**, *16*, 261–268.
- (40) Dean, J. A.; Lange, N. A., *Lange's Handbook of Chemistry*, 15th; McGraw-Hill, Inc.: New York, NY, USA, 1999, p 1424.

- (41) Shimada, T.; Hasegawa, T. Determination of equilibrium structures of bromothymol blue revealed by using quantum chemistry with an aid of multivariate analysis of electronic absorption spectra. *Spectrochimica Acta Part A: Molecular and Biomolecular Spectroscopy* **2017**, *185*, 104–110.
- (42) Klotz, E.; Doyle, R.; Gross, E.; Mattson, B. The Equilibrium Constant for Bromothymol Blue: A General Chemistry Laboratory Experiment Using Spectroscopy. *Journal of Chemical Education* **2011**, *88*, 637–639.
- (43) Si photodiodes - S1337 series Datasheet., Hamamatsu, Japan, 2015.
- (44) Demtröder, W., *Laser Spectroscopy. Volume 1: Basic principles*. 4th; Springer - Verlag Berlin Heidelberg: Heidelberg, Germany, 2008, p 457.
- (45) Kingbright L-53ND Solid State Lamp., Taipei, Taiwan, 2003.
- (46) Avago HLMP-EGxx, HLMP-EHxx, HLMP-ELxx Series Data Sheet., San José, USA, 2014.
- (47) Peak Wavelength vs. Dominant Wavelength in LED selection.
- (48) Arecchi, A. V.; Messadi, T.; Koshel, R. J., *Field Guide to Illumination*, 1st; SPIE Press: Bellingham, WA, USA, 2007, p 152.
- (49) Calvo-López, A.; Ymbern, O.; Izquierdo, D.; Alonso-Chamarro, J. Low cost and compact analytical microsystem for carbon dioxide determination in production processes of wine and beer. *Analytica Chimica Acta* **2016**, *931*, 64–69.
- (50) Ljunggren, E.; Karlberg, B. Determination of total carbon dioxide in beer and soft drinks by gas diffusion and flow injection analysis. *Journal of Automatic Chemistry* **1995**, *17*, 105–108.
- (51) Luque de Castro, M. D.; González-Rodríguez, J.; Pérez-Juan, P. Analytical Methods in Wineries: Is It Time to Change? *Food Reviews International* **2005**, *21*, 231–265.
- (52) Catalá Icardo, M.; García Mateo, J.; Martínez Calatayud, J. Multicommuation as a powerful new analytical tool. *TrAC Trends in Analytical Chemistry* **2002**, *21*, 366–378.
- (53) Rocha, F. R.; Reis, B. F.; Zagatto, E. A.; Lima, J. L.; Lapa, R. A.; Santos, J. L. Multicommuation in flow analysis: concepts, applications and trends. *Analytica Chimica Acta* **2002**, *468*, 119–131.
- (54) Da Rocha, Z. M.; Martínez-Cisneros, C. S.; Seabra, A. C.; Valdés, F.; Gongora-Rubio, M. R.; Alonso-Chamarro, J. Compact and autonomous multiwavelength microanalyzer for in-line and in situ colorimetric determinations. *Lab Chip* **2012**, *12*, 109–117.
- (55) Total Acidity (pH 7) - Instructions of Use., Barcelona, Spain, 2017.
- (56) Total Acidity - Performance Report., Barcelona, Spain, 2017.

Chapter 5

Analytical microsystem for the spectrophotometric determination of Primary Amino Nitrogen in must and wine samples

5.1 Nitrogen compounds in wine

Many nitrogen-containing compounds are found in grape and wine, including inorganic forms such as ammonia and nitrates, and several organic forms such as amines, amides, amino acids, proteins and nucleic acids, among others.^{1,2}

Nitrogen-containing compounds play a major role in wine-making since they are essential for yeast growth and metabolism during alcoholic fermentation. Besides, the composition of the nitrogen fraction and the content of the different species do also have an important effect on other relevant properties of wine such as its acidobasic buffer capacity and its organoleptic characteristics.^{1,2} Special attention has been paid to various nitrogen-containing organic compounds which could have harmful effects on health, including ethyl carbamate³, ochratoxin A⁴ and some biogenic amines⁵ such as histamine, tyramine and putrescine.

Biogenic amines

Biogenic amines are low molecular weight basic nitrogenous compounds, mainly formed by decarboxylation of amino acids and synthesised by microbial, vegetable and animal metabolisms.^{5,6}

Although biogenic amines are essential for many physiological functions, they may become toxic at high concentrations. The consume of significant quantities of these compounds has been related to several pharmacological reactions including headache, hypo- and hypertension, nausea, cardiac palpitation and renal intoxication, among others.^{5,6}

Biogenic amines in wines are predominantly produced by bacteria¹ and their content and distribution is highly variable. The major compounds are commonly histamine, tyramine and putrescine.⁵ However, none of them are usually found in wines at levels capable of producing harmful effects.²

5.1.1 Alcoholic fermentation and Yeast Assimilable Nitrogen

From a biochemical point of view, fermentation is a metabolic process where energy is obtained from organic compounds without involving exogeneous oxidising agents such as oxygen.⁷ During the alcoholic fermentation of wine, yeast and some bacteria transform sugars, mainly fructose and glucose, into ethanol and carbon dioxide in anaerobic conditions producing adenosine triphosphate (ATP).^{2,8} The general reaction can be summarised in:

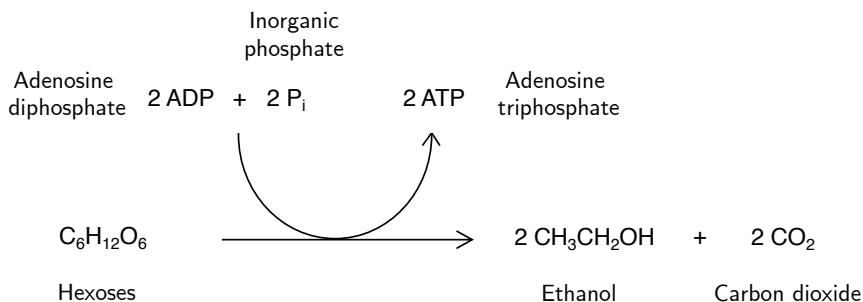


Figure 5.1: Transformation of sugars into ethanol and carbon dioxide during the alcoholic fermentation of wine.

Alcoholic fermentation is a highly complex process. While the reaction in Figure 5.1 occurs, several other biochemical, chemical and physicochemical processes do also take place, involving many different compounds such as numerous nitrogen-containing species.^{8,9}

Apart from sugars, nitrogen compounds are the most important yeast nutrients in wine.² *Saccharomyces cerevisiae*, the principal yeast used for fermentation,⁹ needs nitrogen for its growth and metabolism. However, from the several nitrogen compounds that can be found in wine, only some of them are available for its metabolism. The nitrogen fraction which can be used by yeast during fermentation processes is generally referred to as Yeast Assimilable Nitrogen (YAN) and it mainly comprises ammonium and certain amino acids. The group of amino acids that can be metabolised by yeast conform what is often designated as Primary (alpha-) Amino Nitrogen (PAN) (see Figure 5.2). Both YAN and PAN are usually expressed as mg N/L.

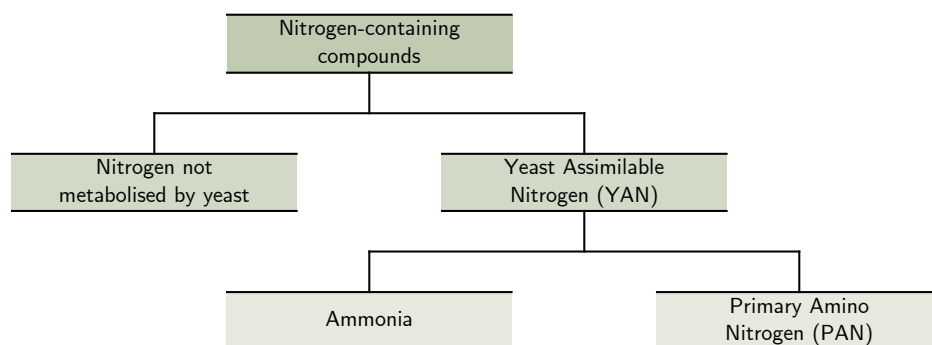


Figure 5.2: Classification of nitrogen-containing compounds in wine.

Secondary amino acids are not included in YAN, since they cannot be used under ordinary conditions. Proline, for example, which is the most abundant amino acid in grape along with arginine, can be assimilated by *Saccharomyces cerevisiae* but only under abnormal aerobic conditions.^{2,8,10} Other compounds such as some low molecular weight peptides can also be used as nitrogen sources, although their contribution is much lower in comparison to ammonia and PAN.¹¹

The YAN content of a must has a significant effect on the success of the alcoholic fermentation and, therefore, on the quality of the final product. Insufficient must YAN is generally related to low yeast population, resulting in poor fermentation vigour and potential risk of sluggish and stuck fermentations.^{11,12} Besides, low must YAN is also associated with the production of undesirable thiols and hydrogen sulfide (H₂S).^{11,13} Ammonium salts such as diammonium hydrogen phosphate (DAP) are commonly added to musts with an excessively low YAN concentration.^{2,11} On the other hand, high must YAN may lead to excessive non-assimilated nitrogen, which can contribute to the microbiological instability of the final product.¹⁴ Furthermore, excessive YAN is

often related to the production of several undesired compounds such as urea, ethyl carbamate and some biogenic amines.^{9,11} YAN has an important impact on the quality of wine since it affects the production of many other compounds during the alcoholic fermentation which have a relevant effect on the stability and organoleptic properties of the final product.^{11,13}

YAN content in musts and wines is highly variable. For example, a survey of 1523 grape juices from California, Oregon and Washington (USA) found YAN concentrations ranging from 40 mg N/L to 559 mg N/L (ammonium: 5 mg N/L to 325 mg N/L; PAN: 29 mg N/L to 370 mg N/L).¹⁵ Similarly, 16 mg N/L and 394 mg N/L were found to be the minimum and maximum YAN contents in 324 grape juice samples from Trentino (Italy).¹⁶ Several studies have been carried out for estimating the nitrogen requirements for achieving a satisfactory fermentation. Some authors have suggested 140 mg N/L to be the minimum YAN concentration.^{17–19} However, significantly different values ranging from 70 mg N/L²⁰ to 267 mg N/L²¹ have been reported due to several factors affecting the nitrogen needs.

5.1.2 YAN measurement in wine

Owing to the extensive influence of nitrogen-containing compounds in the alcoholic fermentation of wine, YAN is routinely measured in grape and must prior to fermentation in order to predict the success of the fermentation process. As mentioned before, nitrogen is frequently supplied to musts containing low YAN concentrations by the addition of DAP. The amount of DAP to be added as well as the timing of the additions is crucial in order to achieve the desired boosting of the fermentation rate yet avoiding unwanted side effects such as an excessive release of H₂S²² or the production of ethyl carbamate²³, among others^{24–26}. Therefore, the availability of rapid analytical methods for measuring and monitoring YAN during the alcoholic fermentation would be highly advantageous for an adequate DAP supplementation.

Most of the developed methods for assessing the nitrogen status of musts have been focused on the quantification of ammonium ions and amino acids, which are the main compounds of YAN. Ammonium is commonly determined using ion selective electrodes (ISE) or commercial enzymatic test kits.^{10,11} Both methods are simple, rapid and provide the necessary accuracy and precision.

Several chromatographic methods have been developed for the identification and quantification of amino acids in wine.²⁷ These methods usually involve pre- or post-column derivatisation of amino acids for their later spectrophotometric or fluorometric detection. The use of different derivatising reagents has been reported, including 6-aminoquinolyl-N-hydroxysuccinimidyl carbamate (AQC),^{28,29} diethyl ethoxymethyl-emalonate (DEEMM),^{30,31} 5-(4,6-dichlorotriazinyl)aminofluorescein (DTAF),³² ninhydrin^{33,34} and *o*-phthaldialdehyde (OPA),^{35–37} among others. Chromatographic methods provide useful and accurate information about the composition of PAN. Nonetheless, these methods are not suitable for routine use, since they are time-consuming and require expensive instrumentation and skilled personnel.

Several alternative methods have been proposed for the quantification of the total concentration of free alpha amino acids. The most common ones are the formol titration method, which includes ammonia and therefore measures the YAN content, and the use of ninhydrin and OPA for the primary amino acid derivatisation and subsequent spectrophotometric determination.

The formol titration method is based on the quantification of the protons which are lost by the amino groups in the reaction between formaldehyde and the free amino acids to produce methylol derivatives.^{38,39} The procedure consists in the neutralisation of a sample to pH 8, followed by the addition of an excess of formaldehyde neutralised to pH 8. Finally, the solution is titrated to pH 8 to quantify the released protons. Using this method, free ammonia is also quantified, whereas proline is only partially titrated.^{39,40}

The use of ninhydrin for the PAN quantification is based on the redox reaction between ninhydrin and the primary amino acids. Ninhydrin oxidises the amino acids producing CO₂, NH₃ and an aldehyde. Then, the reduced ninhydrin reacts with the unreduced ninhydrin and the NH₃ from the previous reaction to form a coloured product which can be determined at 570 nm.^{41,42} With this method, proline is almost not detected, while ammonium ions are partially quantified.⁴⁰

A reagent containing OPA and N-acetyl-L-cysteine (NAC) has been used for the determination of primary amino acids in what is known as the NOPA (standing for Nitrogen by OPA) assay.⁴³ This method is based on the reaction between OPA, NAC and the primary amino group to form isoindole derivatives which absorb at 335 nm. The NOPA assay is quite specific to primary amino acids and it does not quantify either ammonia or proline.^{38,40}

Different studies have been carried out for the comparison of the formol, the ninhydrin and the NOPA methods.^{38,40,44} In these studies, the ammonium fraction was also determined due to the different response of the three methods to ammonium. The results obtained by using the three methods did not show significant differences when a 68% and a 100% of the ammonium nitrogen (determined separately) was added to the values from the ninhydrin and the NOPA assays, respectively.⁴⁰

Although it was demonstrated that all three methods could be used for the evaluation of the nitrogen status of grape juice, their practical applicability widely differs. On one hand, the formol titration method is a manual procedure that requires skilled personnel; it is time-consuming, uses toxic reagents and produces considerable amounts of waste. Furthermore, formaldehyde solutions must be freshly prepared and carefully adjusted to pH 8 before each analysis.^{38,44} On the other hand, the other two methods minimise reagent consumption and produced waste and their precision is less dependent on the executor. However, whereas the reaction of primary amino acids with ninhydrin is carried out at approximately 100 °C⁴², the NOPA assay can be performed at room temperature⁴³.

The underestimation or no response from the three aforementioned methods to proline is considered convenient since this amino acid does not contribute to YAN.⁴³

The existence of rapid and accurate methods for estimating the yeast available nitrogen would constitute a valuable tool for winemakers. Nonetheless, little investigation has been performed for the automation of these analyses and the miniaturisation of the systems. Only two automated (yet not miniaturised) systems for estimating the overall YAN/PAN content have been reported: a flow injection analysis system based on the ninhydrin assay⁴⁵ and a sequential injection analysis system for the NOPA assay automation⁴⁶. Both systems use conventional spectrophotometers equipped with flow cells for the absorbance measurements.

The objective of the work presented in this chapter was the development of a miniaturised flow injection system for the quantification of PAN which could be easily automated, involved minimal reagent consumption and waste, and presented high throughput and wide working ranges. A high degree of miniaturisation and automation would permit the on-line monitoring of PAN during the alcoholic fermentation, enabling a better control of the process and an improved decision-making with respect to the DAP supplementation.

The proposed system was based on the NOPA assay previously described and consisted in the monitoring of absorbance changes at 340 nm when a sample was mixed with a NOPA reagent solution containing OPA and NAC.

In order to demonstrate the versatility of the microsystem presented in the previous chapter, we decided to use the same microfluidic platform and the same miniaturised optical detection system, with minimal modifications applied to the flow management peripherals.

5.2 Development of an analytical microsystem for the spectrophotometric determination of Primary Amino Nitrogen in wine samples

5.2.1 Methods

5.2.1.1 Reagents and solutions

All used chemicals were of analytical reagent grade and all solutions were prepared in MilliQ water.

NOPA reagent solutions were prepared by accurate weighing and dissolution of OPA (Sigma-Aldrich, Saint Louis, USA) and NAC (Merk, Darmstadt, Germany) in borate buffer solutions containing 10% v/v ethanol (Panreac, Castellar del Vallès, Spain). Borate buffer solutions were prepared from boric acid (H_3BO_3 , Fisher, Pittsburgh, USA) and sodium hydroxide (NaOH, Sigma-Aldrich). Hydrochloric acid (HCl, Sigma-Aldrich) and NaOH solutions were used for pH adjustment when required. Blank reagent solutions, which were used for the sample blank measurement, were prepared equivalently but without containing OPA. Both NOPA and blank reagent solutions were prepared at least 90 min before use to minimise self-fluorescence interferences.⁴⁷

Standard solutions for the system calibration were prepared by accurate weighing and dissolution of L-isoleucine (Sigma-Aldrich) in MilliQ water.

All tested samples were commercially available. No pretreatment or dilution were required prior to analysis. Samples were also analysed using a commercial reagent kit Primary Amino Nitrogen (ref. 12807) from BioSystems (Barcelona, Spain) for comparing the obtained results.

5.2.1.2 Materials

The microanalyser was constructed by using COC layers from TOPAS Advanced Polymers (Florence, KY, USA) of diverse thicknesses and grades. Two 1 mm and one 400 μm TOPAS 5013 layers were used as structural layers, while two 25 μm TOPAS 8007 layers were used as bonding layers. MilliQ water and ethanol were used for cleaning all material before the bonding step. Delrin plaques of 2 mm in thickness (DuPont, Wilmington, USA) were used as sacrificial layers for the thermocompression process. Several 3 mm thick PMMA layers (Plásticos Ferplast, Terrassa, Spain) were used for the construction of the detection system support.

5.2.1.3 Experimental setup

The final experimental setup, which is depicted in [Figure 5.3](#), can be divided into three main parts: the fluid management peripherals, the microanalyser and the optical detection system.

The peripherals consisted of a four channel peristaltic pump Gilson Minipuls 3 (Gilson, Wisconsin, USA) equipped with 0.64 mm internal diameter Tygon tubing (Ismatec, Wertheim, Germany), a 6-way injection valve (Hamilton, Bonaduz, Switzerland) and a three-way solenoid valve 161T031 (NResearch West Caldwell, USA) actuated by an HCS-3202 direct current (DC) power supply from Manson Engineering Industrial Ltd (Kwai Chung, China). Teflon tubing of 0.80 mm internal diameter (Scharlab SL, Setmenat, Spain) was used for connecting the peripherals to the microanalyser.

The optical detection system, presented in [§ 4.2.1.3](#), consisted of a light emitting diode (LED) and a photodiode mounted into a compact PMMA structure where the microanalyser was inserted into (see [Figure 4.2](#) from the previous chapter). The LED and the photodiode were connected to a printed circuit board (PCB) that, in turn, was connected to a data acquisition card (DAQ) NI USB-6211 (National Instruments, Austin, Texas, USA). The DAQ was responsible for the modulation of the LED and the acquisition and transference of the detected signal to a personal computer (PC). A digital lock-in amplification was used for processing the raw data, increasing the signal-to-noise ratio and permitting the operation of the system in ambient light conditions without requiring any physical amplifier.

The versatility of the optical detection system permitted its easy adaptation to the new application by changing the LED for measuring absorbance in the near-UV range.

For this particular case, a 340 nm LED MTE340-H32-UV from Marktech Optoelectronics (Latham, USA) was selected. The photodetector was a S1337-66BR photodiode from Hamamatsu Photonics (Hamamatsu, Japan).

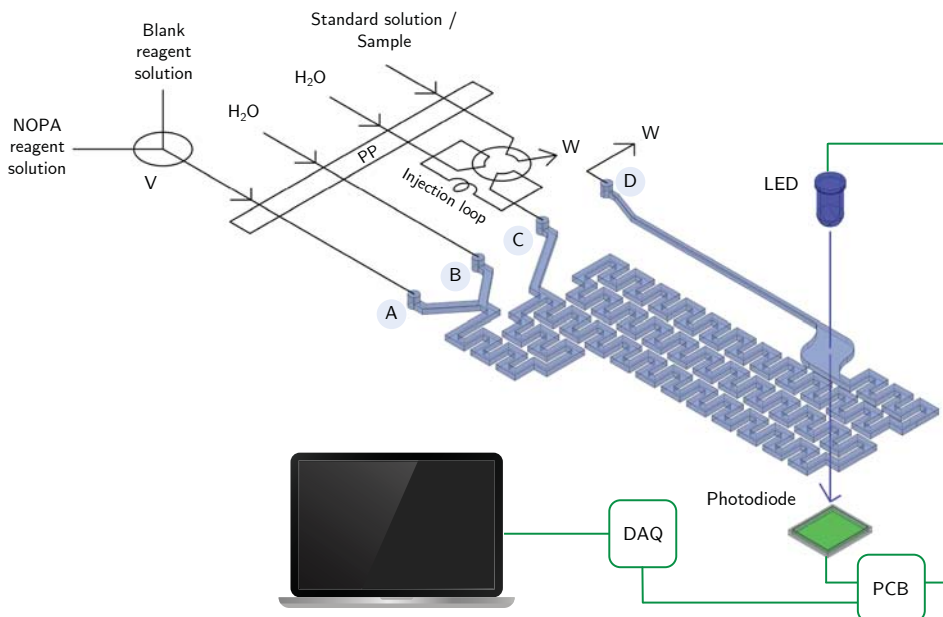


Figure 5.3: Schematic illustration of the experimental setup. PP: peristaltic pump; W: waste; V: solenoid valve.

5.2.1.4 Flow manifold

The operating procedure of the analysis consisted in the continuous pumping of a NOPA reagent solution into the microanalyser through channel A (see Figure 5.3), which was diluted to 1:2 inside the microanalyser by the continuous pumping of H₂O through channel B. Fixed volumes of samples/standards were injected into the carrier stream (H₂O, channel C). When the sample/standard plugs mixed with the diluted NOPA reagent solution inside the microanalyser, the derivatisation reaction took place. The mixture was directed towards the detection chamber, where the optical detection system measured and monitored the absorbance changes at 340 nm produced by the formation of the primary amino acid derivatives.

In order to avoid interference from the sample species absorbing at the same wavelength, a blank was measured for each sample. For the blank preparation, the NOPA

reagent solution was automatically substituted for a blank reagent solution by the actuation of a three-way solenoid valve located at the reagent solution stream. The blank reagent solution, unlike the NOPA reagent solution, did not contain OPA.

5.2.1.5 Microanalyser design and construction

As previously mentioned, in order to demonstrate the high versatility of the microsystem presented in § 4, we decided to use it for the application here proposed by making minimal adjustments. No modification was introduced to the design or the construction process of the microanalyser. For that reason, and in order to reduce the duplicate information, please refer to § 4.2.1.5 for further information.

5.2.2 Results and discussion

5.2.2.1 Optimisation of the hydrodynamic and chemical conditions

The different hydrodynamic and chemical variables that could influence the system were studied for their optimisation. These included, on one hand, the flow rate and the injection volume and, on the other hand, the selection of a reference primary amino acid to be used for the standard solutions, the composition of the NOPA reagent solution and the possibility of preparing the reagent solution in-line. Parameters regarding the optical detection system were also adjusted.

As introduced in the first part of this chapter, the NOPA assay is based on the reaction between OPA, NAC and the primary amino acids to form isoindole derivatives. The general reaction scheme is illustrated in Figure 5.4.

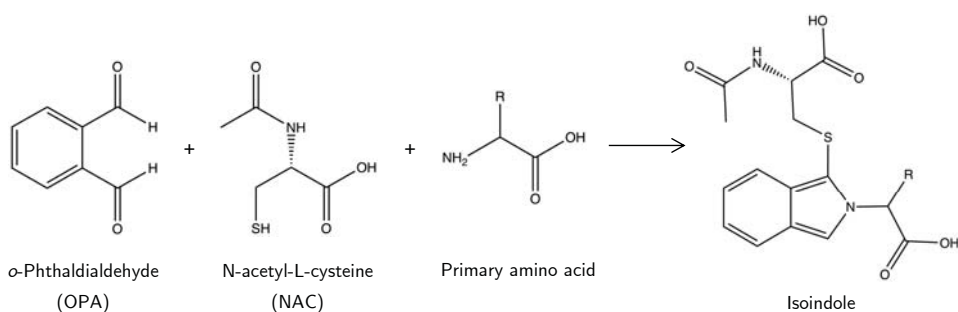


Figure 5.4: NOPA assay reaction.

The resulting isoindole derivatives strongly absorb in the UV-visible spectral region, with an absorbance maximum centred at 335 nm.^{43,48} Thus, in order to perform the absorbance measurements at a wavelength as close as possible to the absorbance maximum, a LED with a peak wavelength centred at 340 ± 5 nm⁴⁹ was selected for the optical detection system. It is worth mentioning that the use of COC as the substrate material for the construction of the devices was appropriate due to its high transmittance in the near UV region of the spectrum^{50,51}. Its optical transparency in the near UV range is, indeed, higher than that of other polymers commonly used in microfluidics, including PMMA, PC and PS.^{51,52}

PAN is composed of several primary amino acids in different proportion and its composition varies (from slightly to considerably) between two musts. Besides, the molar absorptivities of the primary amino acid derivatives⁴³ range from $2700 \text{ M}^{-1} \text{ cm}^{-1}$ to $12660 \text{ M}^{-1} \text{ cm}^{-1}$. Ideally, the reference amino acid to be used for the calibration of the system should present such an absorptivity (ϵ_R) that:

$$\epsilon_R = \sum_{i=1}^n a_i \cdot \epsilon_i \quad (5.1)$$

Where a_i corresponds to the molar fraction of the amino acid i in the sample and ϵ_i represents the molar absorptivity of the corresponding isoindole derivative.⁵³

Considering the different (and in principle unknown) PAN composition of the samples, the selected amino acid should be the one demonstrating the best general fit to this expression. The selection of the reference amino acid was therefore based on previous studies where a linear relationship with a satisfactory correlation was established between the sum of the absorbance of the individual amino acid derivatives and the absorbance of the predicted isoleucine (ILE) equivalent concentration for ten different grape juices.⁴³

The configuration of the flow manifold used during the optimisation of the variables is illustrated in Figure 5.5. The NOPA reagent solution was introduced through the first and the second channels (A and B), while standards were introduced through the third one (C).

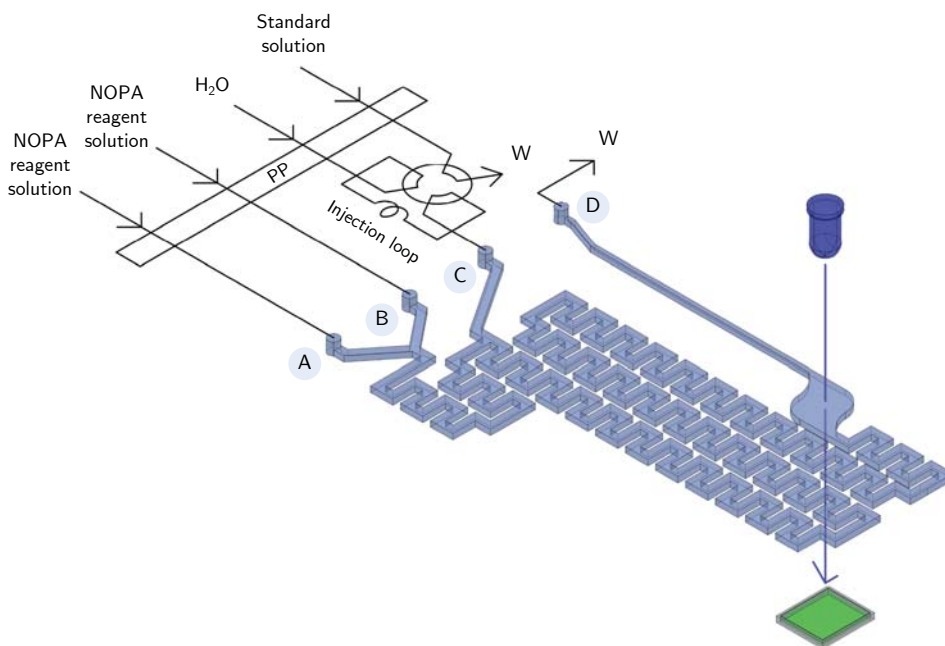


Figure 5.5: Schematic illustration of the flow manifold used during the optimisation of the variables. PP: peristaltic pump; W: waste.

The initial composition of the NOPA reagent solution was based on references [43] and [46], where equimolar amounts of OPA and NAC were used. A 5 mM OPA and 5 mM NAC reagent solution was prepared in borate buffer 0.14 M and was adjusted to pH 9.5. Arbitrary initial hydrodynamic conditions were chosen: the injection volume was set to 7.8 μL , which was the minimum affordable volume due to instrumental limitations, and four different flow rates were tested, from 100 $\mu\text{L}/\text{min}$ to 420 $\mu\text{L}/\text{min}$ [†]. ILE standard solutions ranging from 0.1 mM to 20.0 mM were analysed in triplicate.

As can be seen in Figure 5.6, the sensibility of the calibration using the highest flow rate was slightly lower, whereas for all other tested flow rates no significant differences were found for the linear ranges considered. On the other hand, an increment in the linear range was obtained using the lowest flow rate. However, since 100 $\mu\text{L}/\text{min}$ would entail an excessively low throughput, 207 $\mu\text{L}/\text{min}$ was selected as the optimum flow rate.

[†]Flow rates are given per channel unless otherwise specified.

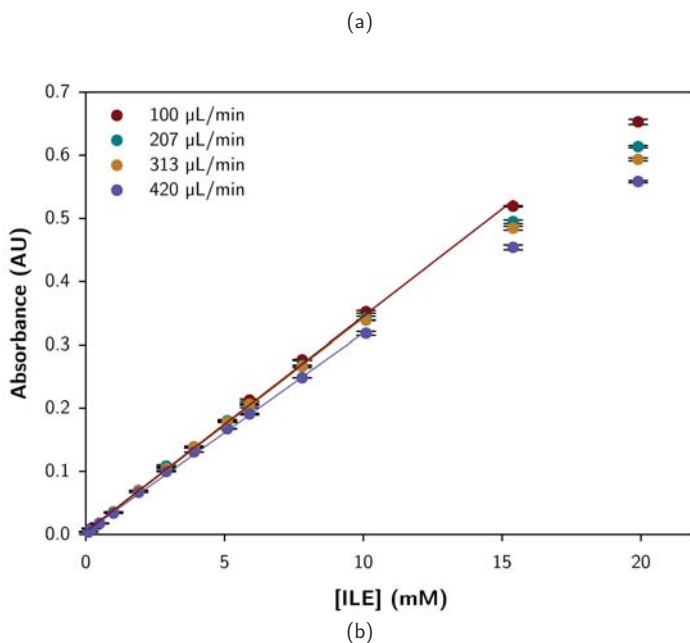
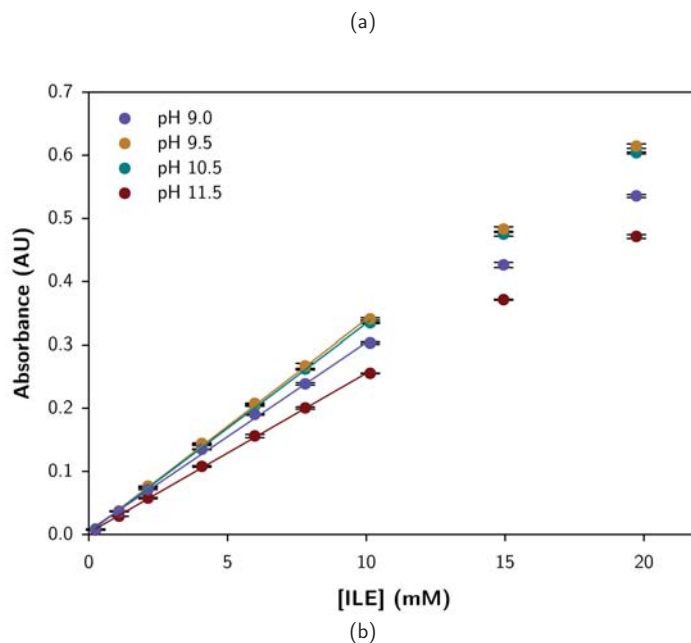


Figure 5.6: Flow rate optimisation. a) Representation of the results. b) Linear regression parameters.

Derivatisation of amines with OPA and NAC is carried out at alkaline pH, generally about 9.5, which corresponds to the pH where the reaction rate and the molar absorptivity and stability of the isoindole derivatives is the highest.⁵⁴⁻⁵⁶ The effect of pH was verified by performing four calibration experiments at different pH of the NOPA reagent solution. Four reagent solutions adjusted to pH 9.0, 9.5, 10.5 and 11.5 were used for the analysis in triplicate of ILE standard solutions ranging from 0.2 mM to 20.0 mM. Flow rate and injection volume were set to 207 μL/min and 7.8 μL, respectively.

As expected, the major sensibility was obtained for the NOPA reagent solution adjusted to pH 9.5 (see Figure 5.7). However, no significant differences were found between pH 9.5 and pH 10.5. Conversely, the sensibilities for the calibrations at pH 9.0 and pH 11.5 were noticeably lower. Hence, suitable pH values were found to be between 9.5 and 10.5, from which pH 9.5 was selected for adjusting the reagent solution for all



pH	Slope	Intercept	R ²	Linear range (mM ILE)
9.0	0.0298 ± 0.0006	0.006 ± 0.004	0.9979	0 - 10
9.5	0.0337 ± 0.0005	0.003 ± 0.003	0.9992	0 - 10
10.5	0.0331 ± 0.0004	0.003 ± 0.002	0.9993	0 - 10
11.5	0.0253 ± 0.0003	0.003 ± 0.002	0.9992	0 - 10

Figure 5.7: NOPA reagent solution pH optimisation. a) Representation of the results. b) Linear regression parameters.

following experiments.

It is important to emphasise the high robustness of the method, where slight variations in the pH of the reagent solution or in the flow rate (see previous set of experiments) did not lead to significant variations of the signal. The robustness of the system will be demonstrated all along this section, where slight variations in some other parameters also had a relatively low effect on the sensibility of the method.

The influence of varying the buffer concentration was also studied. Three different NOPA reagent solutions containing 5 mM OPA and 5 mM NAC were prepared in borate buffer: 1) 0.28 M boric acid, 0.20 M NaOH, 2) 0.14 M boric acid, 0.10 M NaOH and 3) 0.07 M boric acid, 0.05 M NaOH, all of them adjusted to pH 9.5. ILE standard solutions ranging from 0.2 mM to 20.0 mM were analysed in triplicate at 207 $\mu\text{L}/\text{min}$ flow rate and 7.8 μL injection volume.

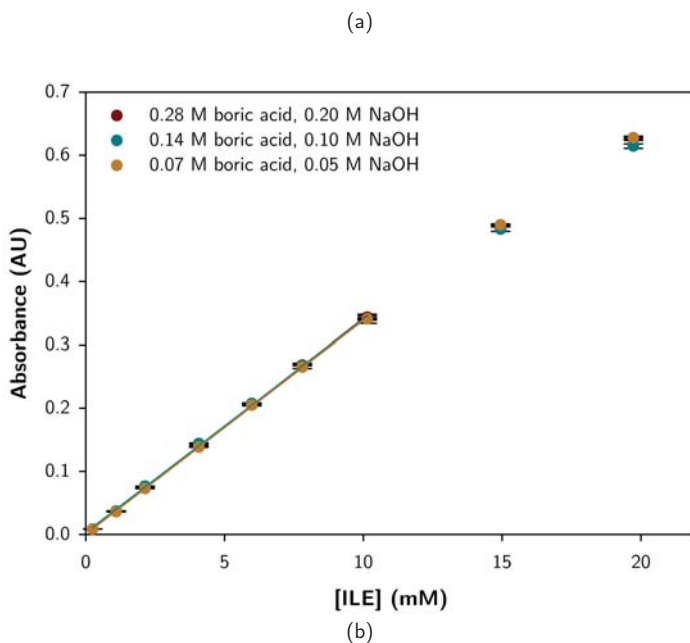


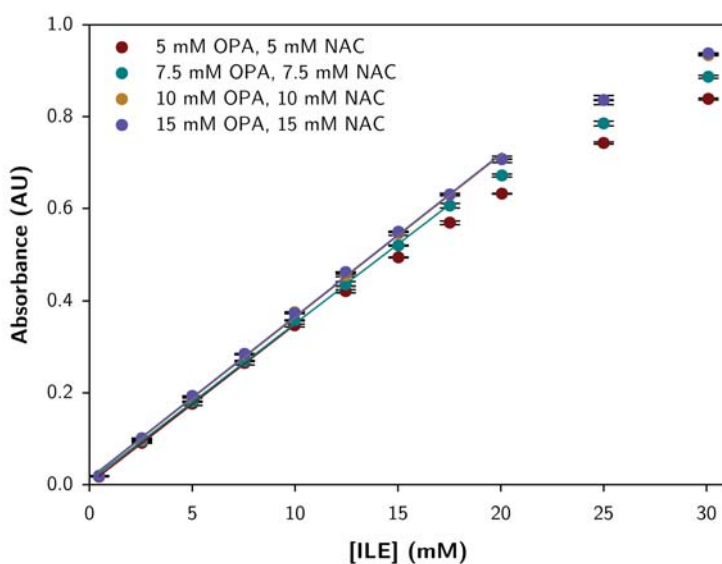
Figure 5.8: Borate buffer optimisation. a) Representation of the results. b) Linear regression parameters.

The three buffer concentrations tested gave similar calibration curves with no significant differences in the sensibility for the considered linear ranges (see Figure 5.8). The obtained results were in concordance with the expected ones, since the formation and stability of the isoindoles is dependent on the pH of the solution yet not on its buffer capacity. The selected buffer concentration was 0.14 mM boric acid and 0.10 mM NaOH, which corresponded to the intermediate composition evaluated.

The buffer capacity of the reagent solution was expected to play a more relevant role when real must and wine samples were being analysed due to their inherent high acidity and buffer capacity. Therefore, the possible need for readjusting the buffer concentration when analysing must and wine samples (in order to keep the pH of the final mixture in the optimum range) was contemplated.

The NAC and OPA concentrations of the reagent solution were studied in two different sets of experiments, a first one where the amounts of the two species were equally varied, and a second one where OPA or NAC were varied whereas the concentration of the other component was kept constant. For the first set of experiments, four different reagent solutions were prepared in 0.14 M borate buffer and adjusted to pH 9.5: 1) 5 mM OPA, 5 mM NAC; b) 7.5 mM OPA, 7.5 mM NAC; 3) 10 mM OPA, 10 mM NAC; and 4) 15 mM OPA, 15 mM NAC. ILE standard solutions ranging from 0.5 mM to 30.0 mM were analysed in triplicate at 207 $\mu\text{L}/\text{min}$ flow rate and 7.8 μL injection volume.

(a)



(b)

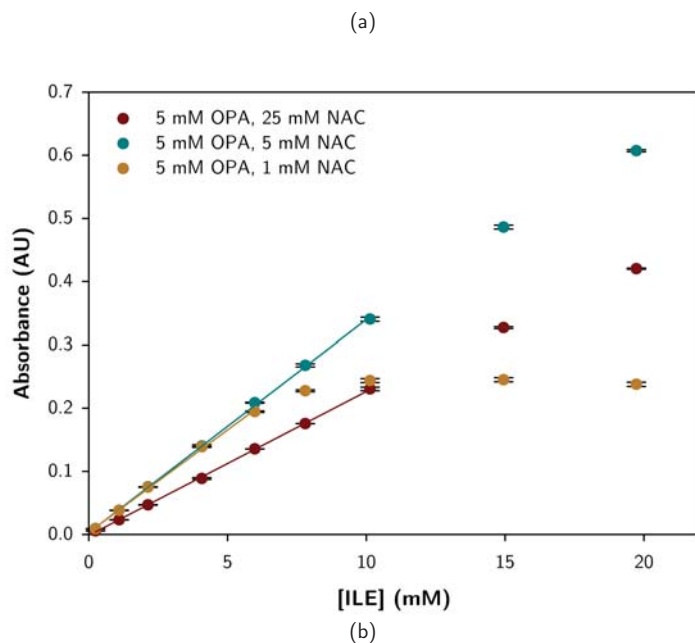
[OPA] (= [NAC]) (mM)	Slope	Intercept	R ²	Linear range (mM ILE)
5	0.0347 ± 0.0004	0.002 ± 0.003	0.9996	0 - 10
7.5	0.0343 ± 0.0004	0.008 ± 0.004	0.9995	0 - 17.5
10	0.0352 ± 0.0005	0.012 ± 0.006	0.9990	0 - 20
15	0.0353 ± 0.0005	0.014 ± 0.006	0.9989	0 - 20

Figure 5.9: Optimisation of the OPA and NAC concentrations of the NOPA reagent solution. a) Representation of the results. b) Linear regression parameters.

As can be seen in [Figure 5.9](#), both sensibility and linear range were slightly improved with the increase in the OPA and NAC concentrations up to 10 mM. However, no further improvement was found when the concentrations were raised to 15 mM. Accordingly, 10 mM was selected as the optimum value for the OPA and NAC concentrations.

The reported methods for the quantification of PAN by the NOPA assay used equimolar concentrations of OPA and NAC, yet the molar relationship between the two species was not studied in either case.^{43,46} Therefore, in order to assess the influence of the OPA:NAC ratio, several reagent solutions were prepared containing: 1) 1 mM OPA, 5 mM NAC (1:5 OPA:NAC); 2) 5 mM OPA, 1 mM NAC (5:1 OPA:NAC); 3) 5 mM OPA, 5 mM NAC (1:1 OPA:NAC); 4) 25 mM OPA, 5 mM NAC (5:1 OPA:NAC); and 5) 5 mM OPA, 25 mM NAC (1:5 OPA:NAC). ILE standard solutions ranging from 0.2 mM to 20.0 mM were analysed in triplicate at 207 $\mu\text{L}/\text{min}$ flow rate and 7.8 μL injection volume.

The obtained calibration curves were compared in two different groups: variable NAC concentrations for a constant OPA concentration ([Figure 5.10](#)) and variable OPA concentrations for a constant NAC concentration ([Figure 5.11](#)).



[OPA] (mM)	[NAC] (mM)	Molar ratio OPA:NAC	Slope	Intercept	R ²	Linear range (mM ILE)
5	25	1:5	0.0228 ± 0.0003	-0.002 ± 0.001	0.9995	0 - 10
5	5	1:1	0.0337 ± 0.0004	0.003 ± 0.002	0.9994	0 - 10
5	1	5:1	0.0325 ± 0.0007	0.003 ± 0.003	0.9986	0 - 6

Figure 5.10: Effect of varying the NAC concentration of the NOPA reagent solution. a) Representation of the results. b) Linear regression parameters.

A decrease in the sensibility was found for a large excess of NAC with respect to OPA (5 mM OPA, 25 mM NAC; 1:5 OPA:NAC) in comparison to the equimolar ratio (see Figure 5.10), probably caused by a reduction in the rate of formation of the isoindoles.^{54,55,57} On the other hand, for a large deficiency of NAC (5 mM OPA, 1 mM NAC; 5:1 OPA:NAC), the sensibility was similar to the equimolar ratio one, whereas the linear range was drastically reduced. In that case, the loss of the linearity was attributed to a lack of NAC, hence impeding the complete derivatisation of the primary amino acid.

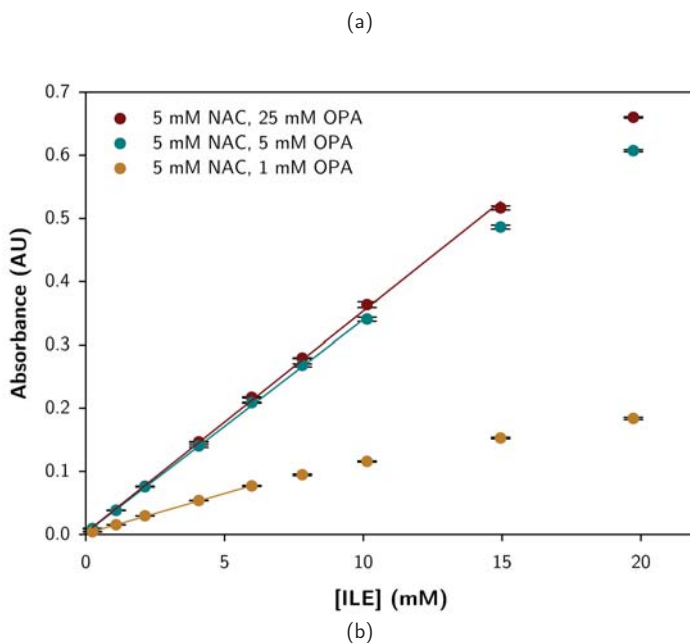


Figure 5.11: Effect of varying the OPA concentration of the NOPA reagent solution. a) Representation of the results. b) Linear regression parameters.

The reduction in the rate of formation of the isoindoles as a consequence of a large excess of NAC with respect to OPA could also be seen for the second set of calibration curves (see Figure 5.11), where the sensibility of the calibration with 1 mM OPA and 5 mM NAC (1:5 OPA:NAC) was noticeably lower than the one of the equimolar relationship. Besides, the linear range was also reduced due to a lack of OPA to proceed with the reaction. On the other hand, an increase in the OPA concentration with respect to the NAC one (25 mM OPA, 5 mM NAC; 5:1 OPA:NAC) entailed a slight rise in both linearity and sensibility, possibly as a result of a slight increase in the reaction rate.

A 1:1 molar ratio of OPA to NAC was selected, since no clear improvement was found for any of the other ratios tested.

Apart from the self-fluorescence of the NOPA reagent solution when freshly prepared, a wide variability regarding its lifetime has been reported, from few days^{46,58} to several weeks^{43,59,60}. A reduction of the ageing effect was described in reference [46] by using separate solutions of OPA and NAC which were in-line mixed, reporting no information about the interference of the NOPA reagent self-fluorescence when used just after being prepared. The possibility of employing separate OPA and NAC solutions, thus producing the NOPA reagent solution in-line, was studied. Taking advantage of the versatility of the microanalyser, a 20 mM OPA solution and a 20 mM NAC solution, both prepared in borate buffer 0.14 M and adjusted to pH 9.5, were introduced through different inlet ports of the microfluidic device and were then mixed inside the microanalyser in a first short micromixer before being merged with the standard/sample (see Figure 5.12.b). The new fluidic configuration was compared to the previous one where the NOPA reagent solution, prepared at least 90 minutes before use[†], was introduced through the two first channels (see Figure 5.12.a). ILE standards ranging from 0.5 mM to 20.0 mM were analysed in triplicate at 207 $\mu\text{L}/\text{min}$ flow rate and 7.8 μL injection volume.

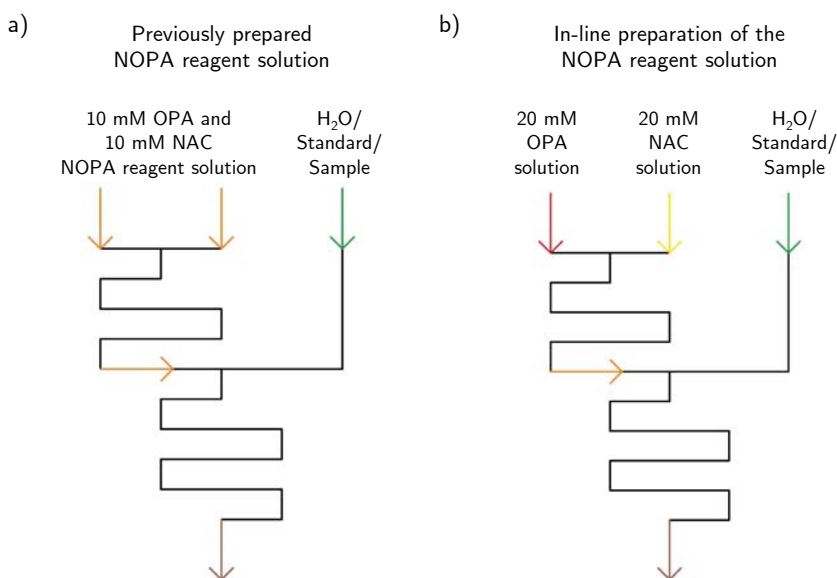


Figure 5.12: Fluidic schemes for: (a) the introduction of a previously prepared NOPA reagent solution and (b) the in-line preparation of the reagent using separate OPA and NAC solutions. OPA and NAC concentrations are equivalent for both configurations (all channel dimensions and flow rates per channel are equal).

[†]As mentioned in § 5.2.1.1, all reagent solutions were prepared at least 90 minutes before use to minimise reagent self-fluorescence interferences.

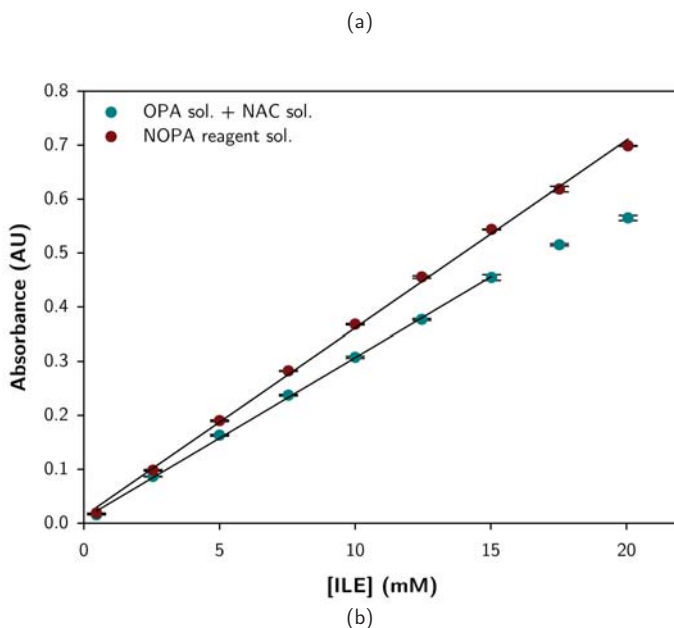


Figure 5.13: Effect of preparing the NOPA reagent solution in-line. a) Representation of the results. b) Linear regression parameters.

As illustrated in [Figure 5.13](#), the in-line preparation of the reagent solution led to a noticeable loss in the sensibility of the calibration curve. Two different factors could be contributing to that event: a decrease in the reaction rate when OPA and NAC are not pre-mixed and/or the self-fluorescence of the NOPA reagent solution, which has been reported to be high for the freshly prepared solutions but to decrease and stabilise after 70-90 minutes.⁴⁷ Self-fluorescence of the reagent solution could be interfering in the absorbance measurements since no light filter was being used between the detection chamber and the photodetector. The in-line preparation of the solution was discarded and neither the reaction rate nor the self-fluorescence of the reagent solution were studied.

Whereas for the analysis of individual must and wine samples the stability of the reagents was not critical, it will become essential for the continuous on-line monitoring of PAN during the alcoholic fermentation process. Once the stability of the reagents is studied, the possibility of preparing the reagent in-line (in spite of the loss in the sensibility) will be considered.

The evaluated ranges as well as the selected values for the studied parameters are summarised in [Table 5.1](#). Higher injection volumes were not tested since the use of the minimum achievable volume was suitable for the purpose of this work.

Table 5.1: Optimisation of variables.

	Tested range	Optimum value
Injection volume (μL)	-	7.8
Flow rate ($\mu\text{L}/\text{min}$)	100 - 420	207
NOPA reagent solution:		
pH	9.0 - 11.5	9.5
[Borate buffer] (M)	0.07 - 0.28	0.14
[OPA] (= [NAC]) (mM)	5 - 15	10
[OPA]:[NAC]	5:1, 1:1, 1:5	1:1
Minimum ageing time (min)	0 (in-line prepared), 90	90

5.2.2.2 Analytical characterisation of the microsystem

The repeatability of the method was assessed by performing three different calibration analyses in three different working days under identical hydrodynamic and chemical conditions and using newly prepared solutions. ILE standard solutions ranging from 0.5 mM to 20.0 mM were analysed in triplicate by using the optimal conditions summarised in [Table 5.2](#). [Figure 5.14](#) displays the recorded signal for one of the replicates (Replicate 1 from [Table 5.2](#)) and the calibration curves obtained for all three experiments.

Table 5.2: Analytical characterisation of the microsystem. Linear regression parameters and limits of detection (LOD) and quantification (LOQ) for three calibration experiments. LOD and LOQ were calculated as 3 times and 10 times the standard deviation of the baseline.

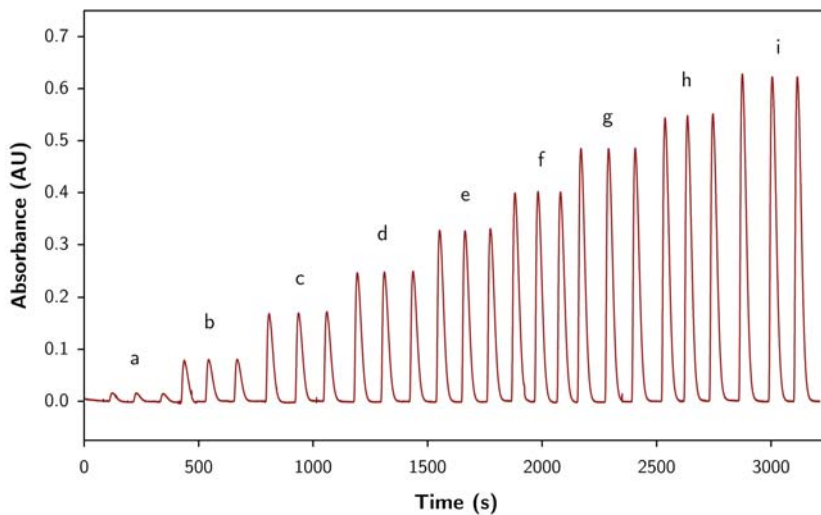
Replicate	Slope	Intercept	R^2	LOD (mM ILE)	LOQ (mM ILE)
1	0.0312 ± 0.0004	0.009 ± 0.004	0.9994	0.03	0.10
2	0.0332 ± 0.0004	0.011 ± 0.005	0.9991	0.02	0.08
3	0.0323 ± 0.0004	0.014 ± 0.005	0.9989	0.03	0.10

A statistically significant difference ($n = 27$, 95% confidence) was found between the sensibility of the calibration curves of the different replicates. Nonetheless, this difference would not affect the quality of the results as long as a calibration of the system was performed before the analysis of the samples, especially when using newly prepared solutions.

With the optimal conditions, a linear range to up to 20 mM ILE, corresponding to 280 mg N/L, and a sampling rate of 30 h^{-1} were achieved, consuming 7.8 μL of sample,

8.3 μmol of OPA, 8.3 μmol of NAC, 115.9 μmol of boric acid and 82.8 μmol of NaOH, and producing 1.2 mL of waste per assay.

(I)



(II)

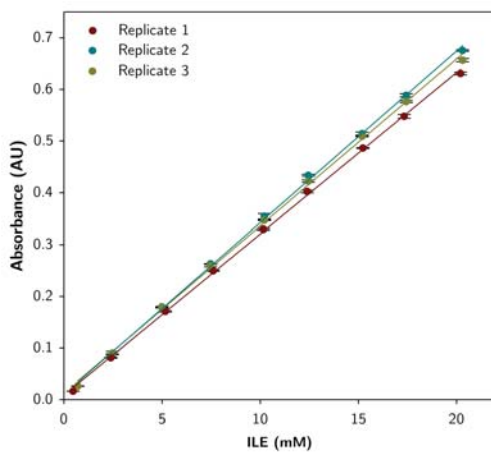


Figure 5.14: Recorded signal (I) for the first replicate from Table 5.2 and calibration curves (II) for all three replicates using the optimal conditions. Standard solutions: (a) 0.5 mM, (b) 2.5 mM, (c) 5.0 mM, (d) 7.5 mM, (e) 10.0 mM, (f) 12.5 mM, (g) 15.0 mM, (h) 17.5 mM and (i) 20.0 mM.

5.2.2.3 Real sample analysis

Musts and wines are composed by a wide variety of compounds, some of them (e.g. phenolic compounds^{61,62}) absorbing in the near-UV spectral range. In order to avoid the possible interference of these species, a blank was carried out for each sample. With that purpose, some modifications were applied to the microsystem, including the implementation of a three-way solenoid valve for the introduction of a blank reagent solution. The blank reagent solution contained the same components and in the same concentration as the NOPA reagent solution but without OPA.

The final flow scheme of the microsystem is depicted in Figure 5.15. In this configuration, the NOPA reagent solution was introduced to the microsystem through channel A (instead of through channels A and B during the previous experiments). Besides, a three-way solenoid valve was implemented into the reagent stream, permitting the automated selection of the NOPA reagent solution or the blank reagent solution.

Since for this configuration the NOPA and the blank reagent solutions were being in-line diluted to 1:2, both solutions were prepared twice as concentrated as the optimised ones. The final composition of the NOPA reagent solution was: 20 mM OPA, 20 mM NAC and 0.28 M borate buffer adjusted to pH 9.5 and containing 20% v/v ethanol; the composition of the blank reagent solution was: 20 mM NAC and 0.28 M borate buffer adjusted to pH 9.5 and containing 20% v/v ethanol.

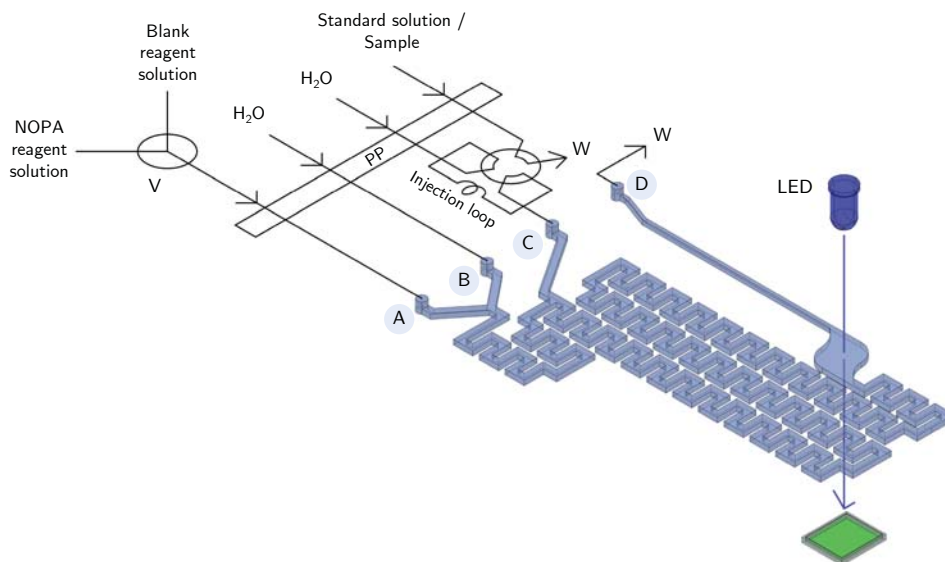


Figure 5.15: Schematic illustration of the flow manifold used for the analysis of real samples. PP: peristaltic pump; W: waste; V: solenoid valve.

The blank absorbance (A_B) corresponded to the absorbance of a mixture composed by the sample and the blank reagent solution. This value was subtracted from the absorbance obtained with the sample plus the NOPA reagent solution (A_S). The absorbance of the NOPA reagent solution and the blank reagent solution were slightly different due to the absence of OPA in the second one. However, this fact did not affect the measurement of the the blank peak height or the sample peak height, since they were measured in relation to their corresponding baselines (the blank reagent solution baseline and the NOPA reagent solution baseline, respectively). Figure 5.16 illustrates a conceptual example of the measurement of a blank peak and a sample peak.

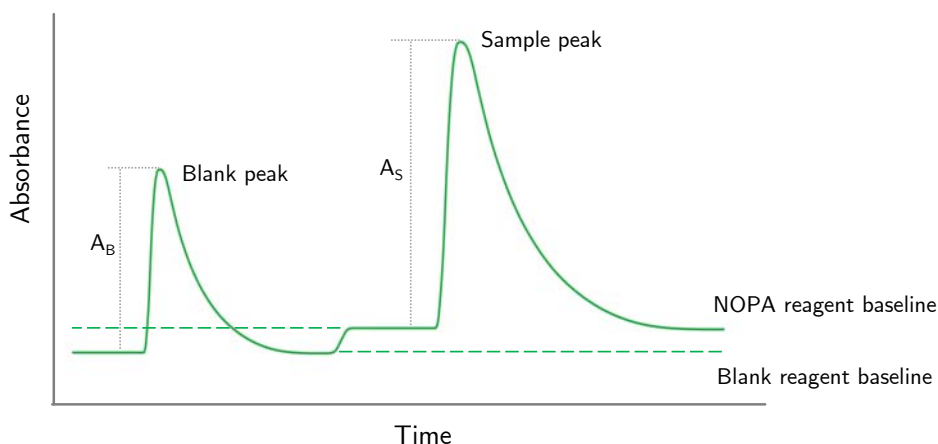


Figure 5.16: Measurement of the absorbance of a sample (A_S) and its corresponding blank (A_B). Firstly, the absorbance of the sample is measured using a blank reagent solution (without OPA). Then, the blank reagent solution is automatically substituted by the NOPA reagent solution. The baseline shifts upwards and, once it stabilises, the sample is injected again. A_B is subtracted from A_S .

The proper performance of the microsystem was assessed by measuring the PAN content of six wine samples. The results were compared to those obtained by using a commercial reagent kit from BioSystems (Barcelona, Spain).

For the developed microsystem, the samples were analysed in triplicate without any pretreatment or dilution. For the calibration of the system, ILE standard solutions ranging from 0.5 mM to 20.0 mM were analysed in triplicate by using the optimal conditions summarised in Table 5.1. As previously mentioned, the concentration of the reagent solutions was adapted to the new flow manifold. The linear equation obtained for the calibration was $A = (0.0335 \pm 0.0004) [\text{ILE}] \text{ (mM)} + (0.010 \pm 0.005)$, $R^2 = 0.9990$, for $n = 27$ and 95% confidence.

The method used by BioSystems for the PAN determination was also based on the NOPA assay. The analysis of the samples was performed by following the procedure

described in the kit brochure⁶³ and the absorbance measurements were carried out at 340 nm using a spectrophotometer equipped with a 1 cm optical path cuvette.

The results obtained by using the developed microsystem and the commercial kit are summarised in Table 5.3. The relationship between the two methods is illustrated in Figure 5.17. The results are expressed as mg N/L.

Table 5.3: Results for the PAN determination of six wine samples obtained by using the BioSystems kit and the microsystem presented in this chapter.

Sample	PAN (mg N/L)		Difference (%)
	BioSystems kit	Developed microsystem	
1 White	26	21 ± 1	-19
2 White	25	24 ± 2	-4
3 Rosé	59	57 ± 1	-3
4 Rosé	94	96 ± 1	2
5 Red	63	64 ± 1	2
6 Red	63	61 ± 2	-3

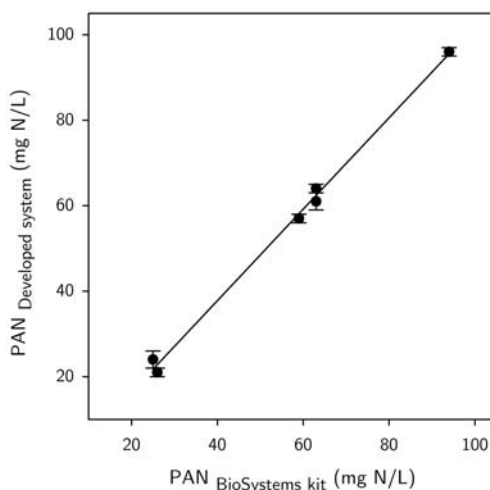


Figure 5.17: Comparison of the PAN content obtained by using the commercial kit and the developed microsystem. Error bars correspond to the confidence interval of the results.

The results were compared by applying a paired t-test. No statistically significant difference was found between the results obtained by using the commercial kit and the ones obtained by using our system; $t_{\text{calc}} (1.15079) < t_{\text{tab}} (2.7765)$ for $n = 6$ and 95%

confidence level. A linear relationship between the two methodologies used could be established, being $\text{PAN}_{\text{Developed system}} = (1.07 \pm 0.09) \cdot \text{PAN}_{\text{Reference method}} - (5 \pm 5)$, $R^2 = 0.9963$, for $n = 6$ and 95% confidence level.

Further comparative studies with a higher number of samples will be performed in the near future.

5.3 Conclusions & future remarks

In this chapter, a microsystem for the quantification of PAN in must and wine samples has been proposed. The developed microsystem involved minimal sample and reagent consumptions and produced waste. Besides, it demonstrated an excellent throughput, a high degree of miniaturisation and a wide working range in comparison to other systems reported.^{43,46}

The analysis of several wine samples was performed and the results were compared to those obtained by using a commercial reagent kit, proving no statistically significant difference between the two procedures. The developed microsystem required no pre-treatment or dilution of the samples. However, due to the high variability in the PAN content of musts and wines (e.g. from 29 mg N/L to 370 mg N/L for 1523 grape juices from USA¹⁵) a 1:2 dilution would be required for samples with higher PAN content.

Several issues are still pendant, such as the study of the stability of the reagents and the complete automation of the system for its application to the on-line continuous monitoring of PAN during alcoholic fermentation. Nonetheless, the automation of the system is expected to be somewhat straightforward in view of the experience acquired during the automation of the microsystem presented in § 4. The automation of the process would also permit the in-line preparation of the standards as well as the in-line dilution of the samples (when required), therefore avoiding any human intervention.

The real-time monitoring of PAN levels during alcoholic fermentation would permit a more precise control of the process and would entail an improved decision-making with respect to the DAP supplementation (when required), contributing to a higher quality of the final product.

The possibility of using an inexpensive, simple, miniaturised and automated system for monitoring several parameters during wine production would be extremely advantageous for wineries. Currently, several systems which permit the measurement of a wide panel of parameters are commercially available. However, most of these systems are expensive and do not allow the continuous monitoring of the parameters. On the contrary, the developed microsystem, which has been used for measuring titratable acidity in § 4 and PAN in this chapter, is considerably economical and would permit the on-line monitoring of two relevant wine parameters (so far) by simply changing the LED and the reagent solutions. It is expected that small wineries, where the continuous monitoring of relevant parameters is sometimes economically not worthy, will benefit from the system here presented.

References

- (1) Ribéreau-Gayon, P.; Glories, Y.; Maujean, A.; Dubourdieu, D., *Handbook of Enology Volume 2: The Chemistry of Wine Stabilization and Treatments*, 2nd; John Wiley & Sons, Ltd: Chichester, UK, 2006, p 441.
- (2) Jackson, R. S., *Wine Science: Principles and Applications*, 3rd; Academic Press, Elsevier: Burlington, MA, USA, 2008, p 747.
- (3) Zimmerli, B.; Schlatter, J. Ethyl carbamate: analytical methodology, occurrence, formation, biological activity and risk assessment. *Mutation Research* **1991**, *259*, 325–350.
- (4) Zimmerli, B.; Dick, R. Ochratoxin A in table wine and grape-juice: Occurrence and risk assessment. *Food Additives and Contaminants* **1996**, *13*, 655–668.
- (5) Anli, R. E.; Bayram, M. Biogenic Amines in Wines. *Food Reviews International* **2009**, *25*, 86–102.
- (6) Stratton, J. E.; Hutkins, R. W.; Taylor, S. L. Biogenic Amines in Cheese and other Fermented Foods: A Review. *Journal of Food Protection* **1991**, *54*, 460–470.
- (7) *Microorganisms and Fermentation of Traditional Foods*; Ray, R. C., Montet, D., Eds.; CRC Press: Boca Raton, FL, USA, 2015.
- (8) *Wine Chemistry and Biochemistry*; Moreno-Arribas, M. V., Polo, M. C., Eds.; Springer New York: New York, NY, USA, 2009, p 735.
- (9) Ribéreau-Gayon, P.; Dubourdieu, D.; Donèche, B.; Lonvaud, A., *Handbook of Enology Volume 1: The Microbiology of Wine and Vinifications*, 2nd; John Wiley & Sons, Ltd: Chichester, UK, 2006, p 497.
- (10) Jacobson, J. L., *Introduction to Wine Laboratory Practices and Procedures*; Springer: New York, NY, USA, 2006, p 375.
- (11) Bell, S. J.; Henschke, P. A. Implications of nitrogen nutrition for grapes, fermentation and wine. *Australian Journal of Grape and Wine Research* **2005**, *11*, 242–295.
- (12) Bisson, L. F. Stuck and sluggish fermentations. *American Journal of Enology and Viticulture* **1999**, *50*, 107–119.
- (13) Mendes-Ferreira, A.; Barbosa, C.; Lage, P.; Mendes-Faia, A. The impact of nitrogen on yeast fermentation and wine quality. *Ciência e Técnica Vitivinícola* **2011**, *26*, 17–32.
- (14) Childs, B. C.; Bohlscheid, J. C.; Edwards, C. G. Impact of available nitrogen and sugar concentration in musts on alcoholic fermentation and subsequent wine spoilage by *Brettanomyces bruxellensis*. *Food Microbiology* **2015**, *46*, 604–609.

- (15) Butzke, C. E. Survey of yeast assimilable nitrogen status in musts from California, Oregon, and Washington. *American Journal of Enology and Viticulture* **1998**, *49*, 220–224.
- (16) Nicolini, G.; Larcher, R.; Versini, G. Status of yeast assimilable nitrogen in Italian grape musts and effects of variety, ripening and vintage. *Vitis - Journal of Grapevine Research* **2004**, *43*, 89–96.
- (17) Martínez-Moreno, R.; Morales, P.; Gonzalez, R.; Mas, A.; Beltran, G. Biomass production and alcoholic fermentation performance of *Saccharomyces cerevisiae* as a function of nitrogen source. *FEMS Yeast Research* **2012**, *12*, 477–485.
- (18) Jiranek, V.; Langridge, P.; Henschke, P. A. Amino Acid and Ammonium Utilization by *Saccharomyces cerevisiae* Wine Yeasts From a Chemically Defined Medium. *American Journal of Enology and Viticulture* **1995**, *46*, 75–83.
- (19) Barre, P.; Bely, M.; Sablayrolles, J. M., *Automatic detection and correction of assimilable nitrogen deficiency during alcoholic fermentation under enological conditions*, Seattle, WA, USA, 1991, pp 211–214.
- (20) Agenbach, W. A., *A study of must nitrogen content in relation to incomplete fermentations, yeast production and fermentation activity*; Sonoma County Wine Library. Cape Town, South Africa, 1977, pp 66–88.
- (21) Mendes-Ferreira, A.; Mendes-Faia, A.; Leao, C. Growth and fermentation patterns of *Saccharomyces cerevisiae* under different ammonium concentrations and its implications in winemaking industry. *Journal of Applied Microbiology* **2004**, *97*, 540–545.
- (22) Mendes-Ferreira, A.; Barbosa, C.; Inˆas, A.; Mendes-Faia, A. The timing of diammonium phosphate supplementation of wine must affects subsequent H₂S release during fermentation. *Journal of Applied Microbiology* **2010**, *108*, 540–549.
- (23) Adams, C.; van Vuuren, H. J. J. Effect of timing of diammonium phosphate addition to fermenting grape must on the production of ethyl carbamate in wine. *American Journal of Enology and Viticulture* **2010**, *61*, 125–129.
- (24) Vilanova, M.; Pretorius, I. S.; Henschke, P. A. In *Processing and Impact on Active Components in Food*; Elsevier: Amsterdam, Netherlands, 2015; Chapter 58, pp 483–491.
- (25) Torrea, D.; Varela, C.; Ugliano, M.; Ancin-Azpilicueta, C.; Leigh Francis, I.; Henschke, P. A. Comparison of inorganic and organic nitrogen supplementation of grape juice – Effect on volatile composition and aroma profile of a Chardonnay wine fermented with *Saccharomyces cerevisiae* yeast. *Food Chemistry* **2011**, *127*, 1072–1083.

- (26) Jin, Q.; Chen, L.; Li, Z.; Li, X.; Li, J. Effect of diammonium phosphate supplementation on the amino acid metabolism during fermentation and sensory properties of fresh spine grape (*Vitis davidii* Foex) wine. *Food Science and Biotechnology* **2015**, *24*, 2051–2057.
- (27) Callejón, R.; Troncoso, A.; Morales, M. Determination of amino acids in grape-derived products: A review. *Talanta* **2010**, *81*, 1143–1152.
- (28) Fiechter, G.; Mayer, H. UPLC analysis of free amino acids in wines: Profiling of on-lees aged wines. *Journal of Chromatography B* **2011**, *879*, 1361–1366.
- (29) Hernández-Orte, P.; Ibarz, M. J.; Cacho, J.; Ferreira, V. Amino Acid Determination in Grape Juices and Wines by HPLC Using a Modification of the 6-Aminoquinolyl-N-Hydroxysuccinimidyl Carbamate (AQC) Method. *Chromatographia* **2003**, *58*, 29–35.
- (30) Wang, Y.-Q.; Ye, D.-Q.; Zhu, B.-Q.; Wu, G.-F.; Duan, C.-Q. Rapid HPLC analysis of amino acids and biogenic amines in wines during fermentation and evaluation of matrix effect. *Food Chemistry* **2014**, *163*, 6–15.
- (31) Gómez-Alonso, S.; Hermosín-Gutiérrez, I.; García-Romero, E. Simultaneous HPLC Analysis of Biogenic Amines, Amino Acids, and Ammonium Ion as Aminoenone Derivatives in Wine and Beer Samples. *Journal of Agricultural and Food Chemistry* **2007**, *55*, 608–613.
- (32) Mandrioli, R.; Morganti, E.; Mercolini, L.; Kenndler, E.; Raggi, M. A. Fast analysis of amino acids in wine by capillary electrophoresis with laser-induced fluorescence detection. *ELECTROPHORESIS* **2011**, *32*, 2809–2815.
- (33) Héberger, K.; Csomós, E.; Simon-Sarkadi, L. Principal Component and Linear Discriminant Analyses of Free Amino Acids and Biogenic Amines in Hungarian Wines. *Journal of Agricultural and Food Chemistry* **2003**, *51*, 8055–8060.
- (34) Huang, Z.; Ough, C. S. Amino Acid Profiles of Commercial Grape Juices and Wines. *American Journal of Enology and Viticulture* **1991**, *42*, 261–267.
- (35) Hu, Z.; Li, L.; Yuan, Y.; Yue, T. Ultrasensitive and simultaneous determination of twenty-one amino acids and amines in culture media, red wine and beer. *Food Chemistry* **2014**, *158*, 56–65.
- (36) Kelly, M. T.; Blaise, A.; Larroque, M. Rapid automated high performance liquid chromatography method for simultaneous determination of amino acids and biogenic amines in wine, fruit and honey. *Journal of Chromatography A* **2010**, *1217*, 7385–7392.
- (37) Pereira, V.; Pontes, M.; Câmara, J.; Marques, J. Simultaneous analysis of free amino acids and biogenic amines in honey and wine samples using in loop orthophthalaldehyde derivatization procedure. *Journal of Chromatography A* **2008**, *1189*, 435–443.

- (38) Gump, B. H.; Zoecklein, B. W.; Fugelsang, K. C.; Whiton, R. S. Comparison of Analytical Methods for Prediction of Prefermentation Nutritional Status of Grape Juice. *American Journal of Enology and Viticulture* **2002**, *53*, 325–329.
- (39) Gump, B. H.; Zoecklein, B. W.; Fugelsang, K. C. In *Food microbiology protocols*; Humana Press: Totowa, NJ, USA, 2001; Chapter 32, pp 283–296.
- (40) Filipe-Ribeiro, L.; Mendes-Faia, A. Validation and comparison of analytical methods used to evaluate the nitrogen status of grape juice. *Food Chemistry* **2007**, *100*, 1272–1277.
- (41) Abernathy, D. G.; Spedding, G.; Starcher, B. Analysis of protein and total usable nitrogen in beer and wine using a microwell ninhydrin assay. *Journal of the Institute of Brewing* **2009**, *115*, 122–127.
- (42) Spedding, G. The World's Most Popular Assay? A Review of the Ninhydrin-Based Free Amino Nitrogen Reaction (FAN Assay) Emphasizing the Development of Newer Methods and Conditions for Testing Alcoholic Beverages. *Journal of the American Society of Brewing Chemists* **2013**, *71*, 83–89.
- (43) Dukes, B. C.; Butzke, C. E. Rapid Determination of Primary Amino Acids in Grape Juice Using an o-Phthaldialdehyde/N-Acetyl-L-Cysteine Spectrophotometric Assay. *American Journal of Enology and Viticulture* **1998**, *49*, 125–134.
- (44) Shively, C. E.; Henick-Kling, T. Comparison of two procedures for assay of free amino nitrogen. *American Journal of Enology and Viticulture* **2001**, *52*, 400–401.
- (45) González-Rodríguez, J.; Pérez-Juan, P.; Luque de Castro, M. D. Flow injection determination of readily assimilable nitrogen compounds during vinification. *The Analyst* **2002**, *127*, 420–423.
- (46) Muik, B.; Edelmann, A.; Lendl, B.; Ayora-Cañada, M. J. Determination of yeast assimilable nitrogen content in wine fermentations by sequential injection analysis with spectrophotometric detection. *Analytical and Bioanalytical Chemistry* **2002**, *374*, 167–172.
- (47) Molnár-Perl, I.; Bozor, I. Comparison of the stability and UV and fluorescence characteristics of the o-phthaldialdehyde/3-mercaptopropionic acid and o-phthaldialdehyde/N-acetyl-L-cysteine reagents and those of their amino acid derivatives. *Journal of Chromatography A* **1998**, *798*, 37–46.
- (48) Hernández, M. J. M.; Camañas, R. M. V.; Cuenca, E. M.; Alvarez-Coque, M. C. G. Determination of the protein and free amino acid content in a sample using o-phthalaldehyde and N-acetyl-L-cysteine. *The Analyst* **1990**, *115*, 1125–1128.
- (49) Ultraviolet Emitter MTE-H32 Series., Latham, NY, USA, 2014.
- (50) TOPAS® COC - Company and Product Brochure., Florence, KY, USA, 2011.

- (51) Khanarian, G. Optical properties of cyclic olefin copolymers. *Optical Engineering* **2001**, *40*, 1024–1029.
- (52) Nunes, P. S.; Ohlsson, P. D.; Ordeig, O.; Kutter, J. P. Cyclic olefin polymers: emerging materials for lab-on-a-chip applications. *Microfluidics and Nanofluidics* **2010**, *9*, 145–161.
- (53) Medina Hernández, M.; Villanueva Camañas, R.; García Álvarez-Coque, M. Determination of total free amino acids with o-phthalaldehyde and N-acetyl-L-cysteine. *Microchemical Journal* **1990**, *42*, 288–293.
- (54) García Álvarez-Coque, M.; Hernández, M.; Villanueva Camañas, R.; Mongay Fernández, C. Studies on the formation and stability of isoindoles derived from amino acids, o-phthalaldehyde and N-acetyl-L-cysteine. *Analytical Biochemistry* **1989**, *180*, 172–176.
- (55) Kutldn, D.; Molndr-Perl, I. Characteristics and Stability of the OPA/ 3-Mercaptopropionic Acid and OPA/N-Acetyl- L-Cysteine Derivatives of Amino Acids. *Chromatographia* **2001**, *53*, 188–198.
- (56) Pastor-Navarro, M. D.; Herráez-Hernández, R. Automated determination of amphetamine enantiomers using a two-dimensional column-switching chromatographic system for derivatization and separation. *The Analyst* **1998**, *123*, 319–324.
- (57) Mengerink, Y; Kutlán, D; Tóth, F; Csámpai, A; Molnár-Perl, I Advances in the evaluation of the stability and characteristics of the amino acid and amine derivatives obtained with the o-phthaldialdehyde/3-mercaptopropionic acid and o-phthaldialdehyde/N-acetyl-l-cysteine reagents. *Journal of Chromatography A* **2002**, *949*, 99–124.
- (58) Buck, R.; Krummen, K High-performance liquid chromatographic determination of enantiomeric amino acids and amino alcohols after derivatization with o-phthaldialdehyde and various chiral mercaptans. *Journal of Chromatography A* **1987**, *387*, 255–265.
- (59) Fujiwara, M.; Ishida, Y.; Nimura, N.; Toyama, A.; Kinoshita, T. Postcolumn fluorometric detection system for liquid chromatographic analysis of amino and imino acids using o-phthalaldehyde/N-acetyl-l-cysteine reagent. *Analytical Biochemistry* **1987**, *166*, 72–78.
- (60) Aswad, D. W. Determination of D- and L-aspartate in amino acid mixtures by high-performance liquid chromatography after derivatization with a chiral adduct of o-phthaldialdehyde. *Analytical Biochemistry* **1984**, *137*, 405–409.
- (61) López-Vélez, M.; Martínez-Martínez, F.; Valle-Ribes, C. D. The Study of Phenolic Compounds as Natural Antioxidants in Wine. *Critical Reviews in Food Science and Nutrition* **2003**, *43*, 233–244.
- (62) Harborne, J. B. In *Phytochemical Methods*; Springer: Dordrecht, Netherlands, 1984; Chapter 2, pp 37–99.

(63) Biosystems Primary Amino Nitrogen., Barcelona, Spain, 2014.

Chapter 6

Novel centrifugo-magnetically actuated valve for centrifugal microfluidic systems

6.1 Valving in centrifugal microfluidic systems

A centrifugal microfluidic platform comprises a set of fluidic unit operations that are combined together to enable its final application. Unit operations are defined as the basic fluidic functionalities¹ and can be seen as the elemental building blocks that constitute the final platform.² The basic fluidic unit operations include sample and reagent supply, reagent pre-storage and release, liquid transport, valving, switching, metering and aliquoting, among others.^{1,2} Out of all these, valving is considered one of the most essential ones, as it allows a precise control of the fluid flow through the fluidic network.³

Valving techniques on centrifugal microfluidic platforms are typically classified into two different categories: passive and active.¹ Passive valves are solely controlled by the inherent forces of a spinning disc, while active valves are totally or, at least, partially controlled by external means and therefore require an external actuation mechanism.

6.1.1 Passive valving

Passive valving relies on the interplay between forces acting on a fluid in a spinning disc and it is directly related to the fluid properties and its interaction with the internal surfaces of the platform. Passive valves are mainly implemented as “normally closed” and are defined by their burst frequency, which is the rotational frequency at which the liquid is released.¹

The most common passive valves are capillary burst valves (Figure 6.1.a). These valves are based on the opposite forces acting on a fluid at a sudden widening of a capillary channel. Liquid is retained at the exit of the channel until the centrifugally

induced pressure resulting from the rotation of the platform overcomes the surface tension of the fluid.⁴ Capillary burst valves have been successfully used in several applications including enzymatic assays^{5,6} and recombinase polymerase amplification (RPA) reactions,⁷ among many others.

Local hydrophobic surface modifications have been applied to capillary burst valves to improve their reproducibility for fluids with high wetting capabilities. These valves, which are commonly referred as hydrophobic valves, are based on the implementation of a hydrophobic barrier that promotes the blocking of the flow at the exit of a channel (Figure 6.1.b). Different approaches have been used for the modification of the surfaces, such as Teflon coatings⁸ or printed toner patches.^{9–11}

Alternatives to the need for local surface modifications have been also proposed. In centrifugo-pneumatic valving, for example, liquid is stopped at the interface between a channel and a dead-end chamber until the centrifugal force overcomes the pneumatic counter pressure (Figure 6.1.d).¹² The opposite concept has also been reported, where liquid is retained at an unvented inlet chamber due to the centrifugo-pneumatic under-pressure generated when liquid is forced radially outwards (Figure 6.1.e).¹³ Auxiliary fluids have been used for controlling both over- and under-pressure centrifugo-pneumatic valves.¹⁴

The integration of dissolvable films in centrifugo-pneumatic valves (Figure 6.1.c) has been demonstrated.^{15–17} In this type of valves, a pocket of trapped air prevents the fluid from wetting the dissolvable film. When the centrifugal force increases, the liquid-gas interface is disrupted and liquid can reach the dissolvable membrane, thus opening the valve.¹⁷

While the previously described valves open with an increase in the centrifugal pressure, in siphon valving a temporary decrease of the rotational speed is required for allowing liquid flow. Siphoning (Figure 6.1.f) is based on the priming of a fluid into a siphon shaped channel as a result of capillary action. The retention of the fluid is achieved at high rotational speeds due to centrifugal forces. When the rotational speed decreases, the capillary pressure exceeds the centrifugal pressure and liquid is pumped over the siphon channel crest towards a radially lower chamber. The fluid is then transferred to this second chamber, aided by an increase in the rotational speed.¹⁸ Since siphoning needs for an hydrophilic siphon channel, most of the reported valves required some sort of surface treatment of an originally hydrophobic surface.^{13,19}

Passive valves arising from the combination of the previously described working principles have been reported. Some examples are pneumatic siphon valves²⁰ and suction-enhanced siphon valves.²¹ Apart from the aforementioned, other passive valves have also been described, including burstable seal valves²² and elastomeric membrane valves,²³ among others. Complex event-triggered valving schemes have been successfully implemented by the combination of several passive valves differing on their burst frequency and/or their principle of operation.^{24,25}

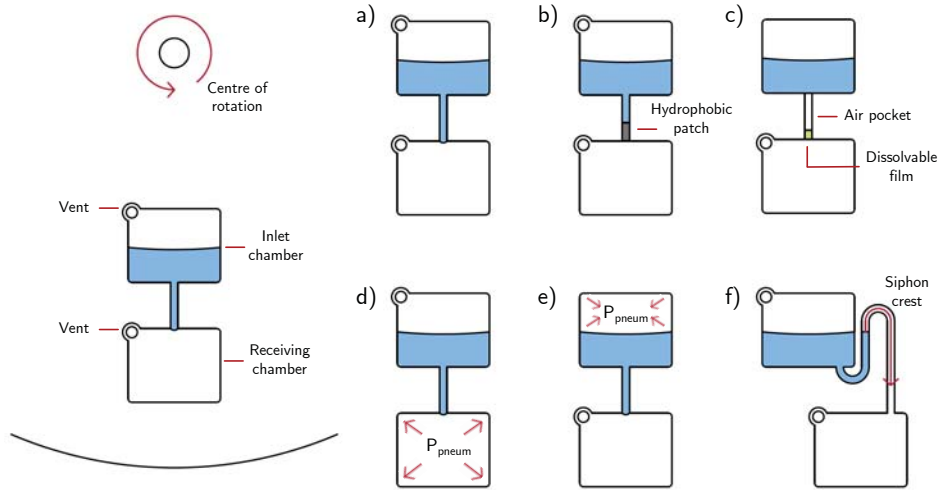


Figure 6.1: Schematic representation of the most commonly used passive valving systems: (a) capillary valving, (b) hydrophobic valving, (c) dissolvable-film valving, (d) centrifugo-pneumatic over-pressure valving, (e) centrifugo-pneumatic under-pressure valving and (f) siphon valving.

Despite passive valving is considered advantageous owing to the reduced need for external actuation,¹ the robustness of these valves is somewhat limited due to reliability issues associated to their burst frequency. Besides, surface modification steps are usually required for increasing the hydrophobicity or hydrophilicity of channels and, apart from adding complexity to the manufacturing process, some of the surface treatments which are commonly applied are reversible and therefore limit the shelf life of the devices.²⁶

6.1.2 Active valving

Active valves are externally controlled and their actuation is totally or, at least, partially independent of the rotation of the disc. These valves can be implemented as either “normally open” or “normally closed” and, in some cases, their state is reversible.

Active valves based on several different principles of actuation have been reported. The most common active valves are based on applying heat to a concrete spot of the rotating platform for melting a sacrificial material thus opening (or closing) the valve. As an example, optofluidic valves based on the piercing of a plastic thin film by a laser beam have been reported.²⁷ Dark spots were laser-printed over a polymeric foil in order to focus the heating energy (Figure 6.2.a).

Paraffin wax valves are the most commonly used active valves and are generally actuated by either infrared lamps²⁸ or heat guns.^{29,30} Laser-irradiated ferrowax microvalves

(LIFM) were introduced as an alternative to paraffin wax valves in order to minimise the energy required for the valve actuation.^{31–33} In that case, low-power lasers were used for melting wax which contained iron oxide nanoparticles (Figure 6.2.b). The opposite concept was applied in ice valving, where liquid plugs were frozen by using thermoelectrics to stop the fluid flow.³⁴ Other temperature actuated valving systems have been demonstrated, including, for example, centrifugo-thermopneumatic valving systems which use temperature-induced partial vapour pressure changes for fluid control.^{35,36}

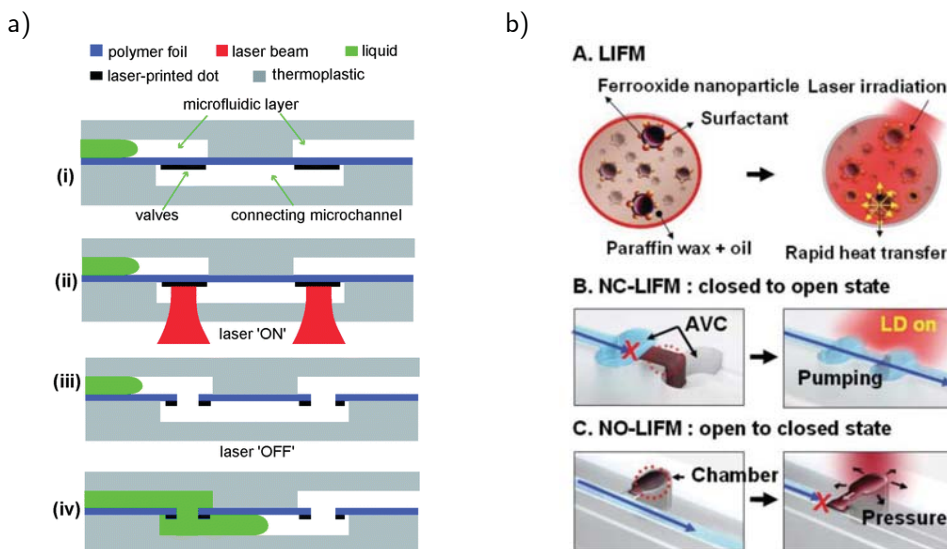


Figure 6.2: Two examples of temperature actuated valving systems. a) Sequential actuation of optofluidic valves based on the piercing of a plastic thin film by a laser beam. Adapted from reference [27]. b) Principle of operation of “normally closed” (NC) and “normally open” (NO) laser-irradiated ferrowax microvalves (LIFM). AVC: Assistant valve chamber; LD: Laser diode. Adapted from reference [33].

Valving systems based on the deformation of a membrane by externally actuated mechanisms have been recently reported. Check valves based on the application of negative or positive air pressures to flexible latex films have been applied to enzyme linked immunosorbent assays (ELISA).³⁷ A similar concept has been demonstrated in reversible thermo-pneumatic valves, where a trapped air volume is heated or cooled for sealing or opening a latex film valve.³⁸ An adhesive tape valve has also been used for effectively creating a barrier between two channels. The configuration in the resting state of this type of valve can be either “normally open” or “normally closed”. In the “normally closed” state, the fluid pressure opens the valve once a critical rotational

speed is achieved, while for the “normally closed” state, a manual pressure is required for sealing the connection between the channels and blocking the fluid flow.³⁹

Membrane deformation has also been achieved by mechanical compression using spring plungers and a flyball governor.^{40–42} At low rotational frequencies, spring plungers are pressed against the membrane thus blocking the liquid transfer. When the spinning frequency is increased, the flyball governor drives the plungers downwards hence opening the valve and allowing liquid to flow. A similar approach using a flyball governor has been applied to magnetically-actuated valves (Figure 6.3).⁴³ At low rotational speeds, two magnets keep the valve closed by pressing a membrane due to magnetic attractive forces. When the rotational speed increases, the bottom-side magnet is driven away by the flyball governor thus releasing the pressure and opening the valve.

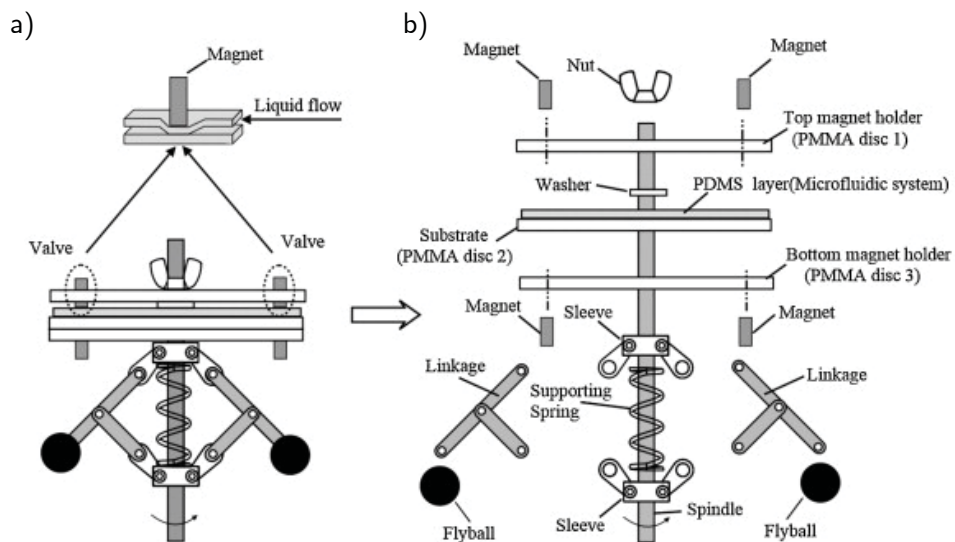


Figure 6.3: Magnetically-actuated valve based on the use of a flyball governor. a) Schematic diagram of the valve system. b) Exploded view of the assembly. Adapted from reference [43].

Magnetic attractive forces have also been used for a reversible valving system consisting on a movable plug that closes a channel at high rotational speeds due to centrifugal forces.⁴⁴ The channel is reopened by lifting off the plug using an external magnet.

Although the need for external actuation is considered disadvantageous since it adds complexity to the system and increases manufacturing costs, active valving is regarded to be more reliable and robust than passive valving.²⁶

6.1.3 The need for new valving systems

As can be deduced by the extensive investigation reported, the integration of simple and robust valving systems in centrifugal microfluidic platforms is still challenging. Despite numerous approaches have been demonstrated, these are usually accompanied by undesired side issues. For instance, passive valves often require deliberate geometric designs or surface modifications, adding complexity to the construction process and sometimes limiting the shelf life of the devices. Another example would be found in dissolvable-film and wax valves, where contamination of fluids could occur since they are usually in direct contact with the sacrificial material. Evidently, the need for external actuation in active valving is a major disadvantage for their actual implementation, increasing the complexity of the system and the manufacturing costs. In addition, even though some reversible valves have been demonstrated, the major part of the valving systems reported do not allow the commutation of the valve to its initial state once it has been actuated.

Owing to the aforementioned rationale, the development of new types of valves with enhanced operational performance is still a target. In this context, the development of a novel reversible centrifugo-magnetically actuated valve is presented in this chapter.

6.1.4 Development of a novel active valving system for centrifugal microfluidic platforms

Magnetism has been extensively used in a wide variety of microfluidic applications. Magnetic forces have been employed for manipulating magnetic objects such as magnetic particles or ferrofluids, as well as for effectively implementing basic fluidic unit operations such as pumping, mixing and valving.⁴⁵

In centrifugal microfluidics, the use of magnets has been mainly focused on the control of magnetic particles,^{10,13,32,46–60} although their use has also been described for other applications such as the development of a magnetically-actuated bead-beating lysis protocol,^{61,62} a centrifugo-magnetically actuated gas micropump^{63,64} and a magnetically actuated solid sample preparation technique.^{65–67} Magnetic forces have been solely employed for two valving applications in centrifugal microfluidics, both of them using mobile magnets.^{43,44} Similarly to references [43] and [44], the valving system here presented combines magnetic and centrifugal forces for the effective actuation of the valve.

The valving principle of the proposed system is based on the strategic positioning of two magnets, one at each side of the valve. These magnets are responsible of the control of the fluid flow. At low rotational speeds, a flexible valving area is pressed by the top magnet due to magnetic attractive forces. When the rotational frequency is raised, the top magnet is displaced outwards as a consequence of an increase in the centrifugal force. Hence, the pressure that kept the valve closed is released and the fluid can flow through the valve. The valving principle is schematically illustrated in [Figure 6.4](#).

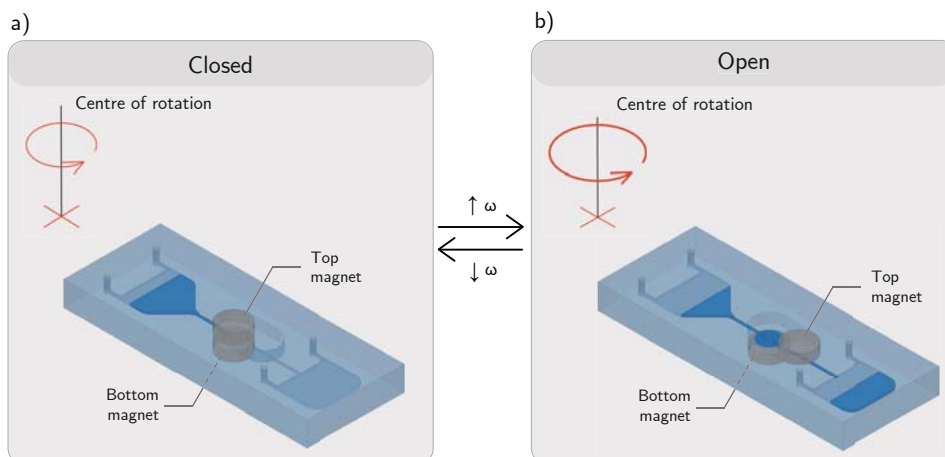


Figure 6.4: Valving principle of the developed valve. Rotational frequency is represented by ω .

The novel valving system here presented is simple, robust and requires minimal external actuation. Besides, it is easy to implement, economical and does not involve complex construction processes.

6.2 Materials & methods

6.2.1 Materials

For the construction of the valves, several COC layers from TOPAS Advanced Polymers (Florence, KY, USA) of diverse thicknesses and grades were used: TOPAS 8007 layers of 25 μm and 50 μm in thickness; TOPAS 5013 layers of 100 μm , 150 μm , 400 μm and 2 mm in thickness; and TOPAS 6015 layers of 100 μm , 150 μm , 400 μm , 500 μm and 2 mm in thickness. Neodymium Iron Boron (NdFeB) disc magnets of 6 mm in diameter and 2 mm in height M1D08-032 were purchased from Chen Yang Technologies GmbH (Finsing, Germany). PDMS discs were prepared from a SYLGARD 184 Silicone Elastomer Kit purchased from Sigma-Aldrich (Saint Louis, USA). Adhesive plate seals AB-0850 Absolute qPCR from ABgene Advanced Biotechnologie (Epsom, UK) were used for the reversible sealing of the prototypes. Delrin plaques of 2 mm in thickness (DuPont, Wilmington, USA) were used as sacrificial layers for the bonding steps. Previous to the bonding steps, COC layers were cleaned using MilliQ water and ethanol (Panreac, Castellar del Vallès, Spain).

The rotating platform was constructed by using PMMA plaques (Plásticos Ferplast, Terrassa, Spain) of 3 mm in thickness.

6.2.2 Experimental setup

The experimental setup for the evaluation of the valve actuation can be divided into two main parts: the support platform and the rotatory actuator (see [Figure 6.5](#)).

A disc shaped support platform was constructed for accommodating four valve prototypes. The platform consisted of four 3 mm thick PMMA layers (see [Figure 6.6](#)). The different layers were individually machined using a CNC micromilling machine and were assembled together by four metallic bolts. An aluminium shaft adapter was employed for anchoring the support platform to the motor axis, securing the platform to the aluminium shaft adapter using four extra bolts.

The rotatory actuator consisted of a motor Maxon EC-i 40 50W, an encoder Maxon MR Type L 256-1024 CPT and a positioning controller (or driver) EPOS 24/5 from Maxon Motor Ibérica S.A. (Torrejón de Ardoz, Spain). The driver controlled and processed the orders from a PC and sent the results to the encoder, which was in charge of the conversion of the digital information to an angular movement of the motor and vice versa. The motor, the encoder and the positioning controller were powered by an HCS-3202 direct current (DC) power supply from Manson Engineering Industrial Ltd (Kwai Chung, China).

A complete user interface was developed for controlling the actuation of the motor. The interface was created using the NI LabVIEW 2012 System design software (National Instruments, Austin, USA) and was designed to permit a wide and user-friendly operational control of the motor including, for example, the automatic sequencing of multiple spinning steps. The rotational speed, the acceleration and deceleration rates and the time of each step could be defined by the user.

6.3 Principle of operation

The developed valve has been constructed by using COC as the substrate material and consists of two channels that are only connected when a PDMS disc, which is placed over them, moves upwards as a result of liquid pressure. The valve is closed by the strategic positioning of two magnets, one on each side of the valve. The position of the bottom magnet is permanent, while the top magnet can move along an expressly machined lane. A thin COC layer allows the upward and downward movement of the PDMS disc.

As previously mentioned, the actuation of the valve relies on the interplay between magnetic and centrifugal forces. At low rotational frequencies (ω), the magnetic force (F_m) is higher than the centrifugal force (F_c) and therefore the two magnets remain in their initial position. Due to magnetic attractive forces, the PDMS disc is compressed against the channel holes, plugging the liquid exit and impeding the liquid flow. When the rotational speed is increased, the centrifugal force becomes higher than the magnetic force and the top magnet is displaced outwards. Consequently, the PDMS disc moves upwards due to hydraulic pressure (P) and liquid can flow from one channel

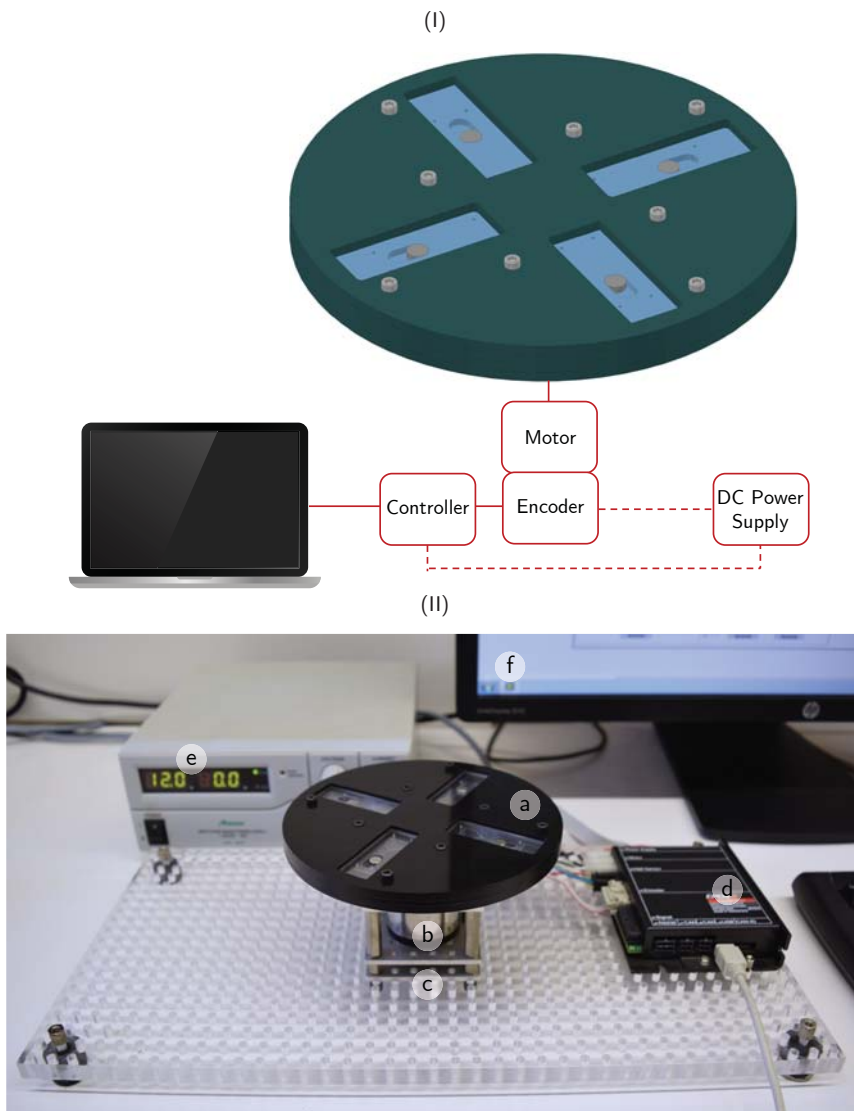


Figure 6.5: Schematic (I) and actual (II) experimental setup for the evaluation of the valve actuation: support platform (a) and rotatory actuator, including a motor (b), an encoder (c), a positioning controller (d), a power supply (e) and a PC (f). The motor, the encoder and the positioning controller were mounted onto a polymeric perforated base.

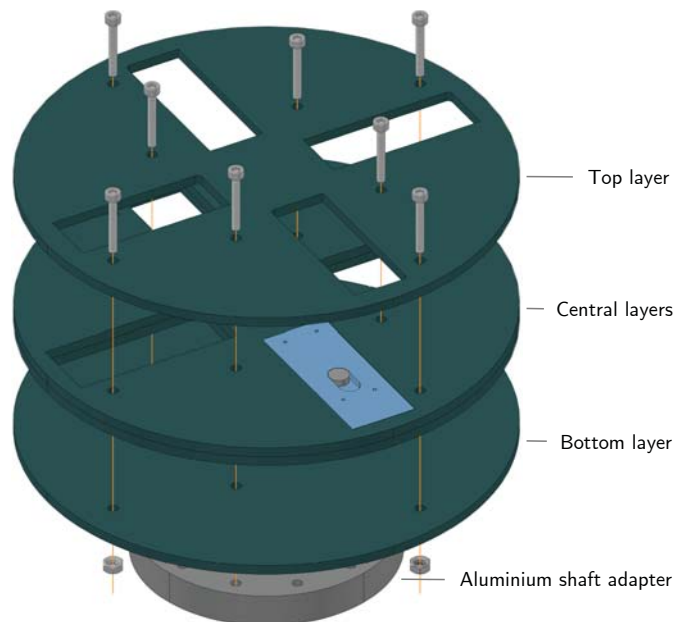


Figure 6.6: Support platform layers. Top and bottom layers impeded the ejection of the devices during the rotation of the platform. The different layers were assembled together by the four outer bolts; the four central ones secured the platform to the aluminium shaft adapter.

to the other. As far as the centrifugal force decreases, the top magnet returns to its initial position, closing the valve and blocking the liquid flow again. The principle of operation of the valve is illustrated in [Figure 6.7](#).

6.4 Optimisation of the valve design

In order to achieve the proper performance of the valve, three main factors had to be considered: 1) the total sealing of the valve during its closed state, 2) the possibility of overcoming the magnetic force through the rotation of the platform; and 3) the ability to generate enough hydraulic pressure to open the valve once the magnets separate.

Basically, the functionality of the valve depended on its design, including the geometry, the materials employed for the construction and the construction process itself. The final structure of the valve was found after an optimisation process which involved the development of several prototypes. The design and construction of these prototypes will be explained and discussed hereafter.

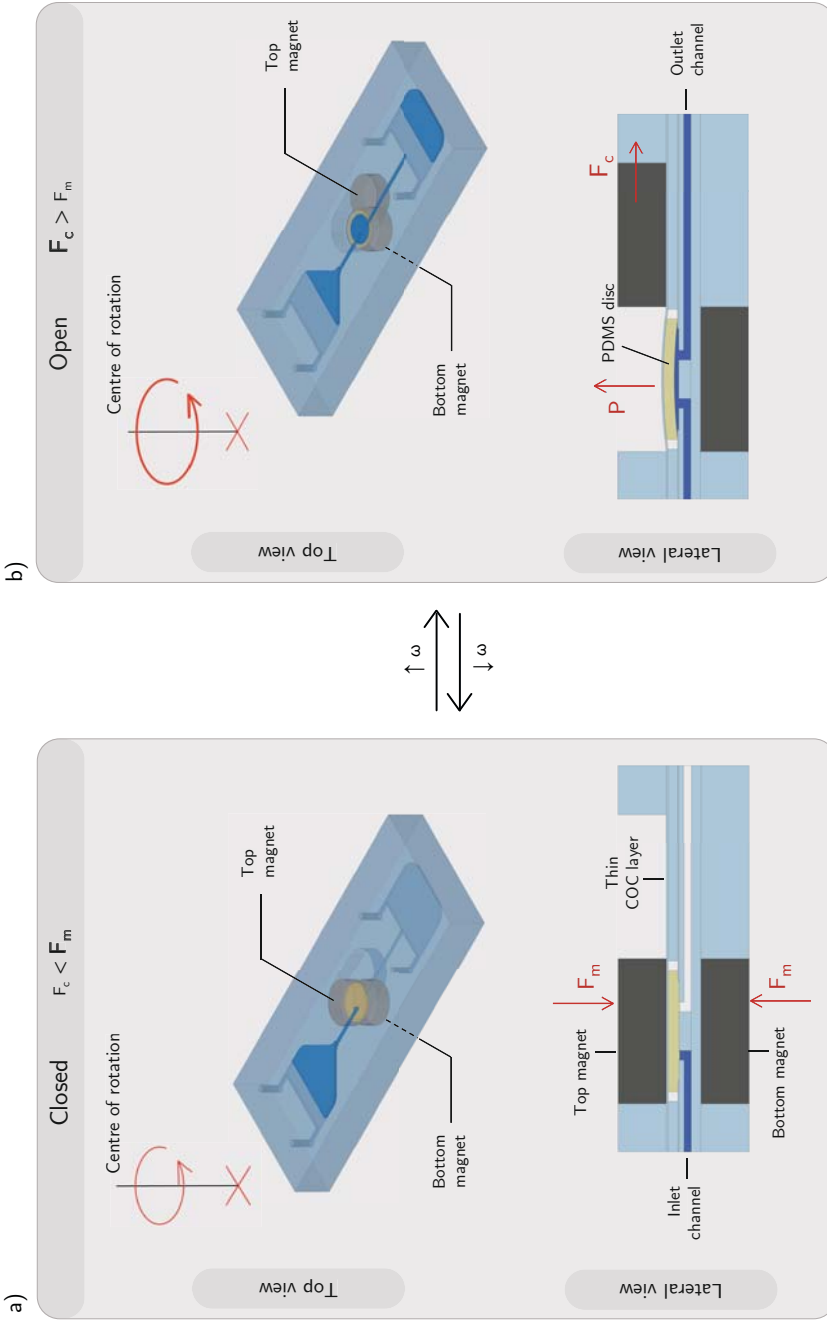


Figure 6.7: Principle of operation of the developed valving system. a) Closed state, where the magnetic force (F_m) is higher than the centrifugal force (F_c). b) Open state, where F_c is higher than F_m . Closed and open states are reversible and can be controlled by changing the rotational frequency (ω) applied to the platform.

All prototypes were based on a common simple design consisting of two chambers at a different distance from the centre of rotation: a radially inward chamber for injecting the liquid (inlet chamber) and a radially outward chamber for receiving the transferred liquid (receiving chamber). Both chambers included two inlets. Two 0.4 mm wide channels connected the chambers and the valve. The centre of the valving area was located at 4 cm distance from the centre of rotation. The two disc-shaped magnets (6 mm in diameter and 2 mm in thickness) were placed over and under the valve, respectively. A lane of 1.2 cm in length was machined onto the devices for the top magnet displacement. Figure 6.8 shows a general scheme of the developed prototypes.

The final dimensions of the prototypes were 5 cm long and 2 cm wide; the thickness was of about 5 mm and depended on the number and the individual thickness of the layers required for each prototype.

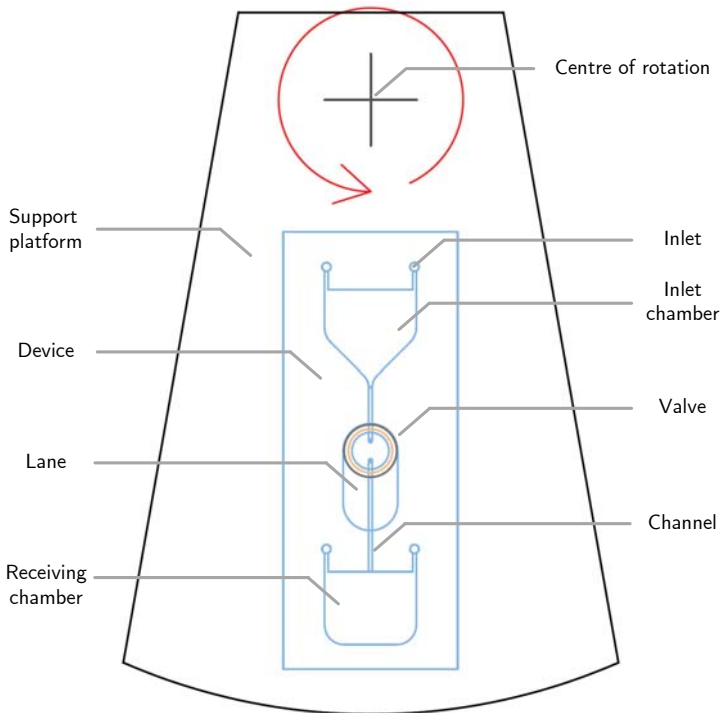


Figure 6.8: Schematic representation of a device placed into the support platform.

6.4.1 All-COC prototypes

Most of the reported works based on the deformation of a membrane for valving^{23,40–43} or pumping^{63,64} purposes in centrifugal microfluidics used PDMS as the substrate material in combination with other polymers. However, the commercial application of PDMS devices is limited owing to their challenging mass manufacturing and their relatively high costs when compared to other polymers.⁶⁸ Besides, PDMS is poorly resistant to bases, organic acids and organic solvents⁶⁹ and its use is commonly associated to water evaporation, gas permeability and absorption of small hydrophobic molecules and biomolecules.^{70–72}

COC offers some advantages with respect to PDMS concerning the costs, the manufacturing processes, the chemical resistance to solvents and the evaporation, permeability and absorption events, among others.^{69,73,74} Thus, the possibility of developing an all-COC valve which avoided the use of PDMS as the substrate material was explored.[†]

The principle of operation of the all-COC magnetically actuated valving system (see Figure 6.9) was similar to the one described in § 6.3. However, in this particular case, the liquid flow was intended to be governed by a thin COC layer. This thin layer was expected to act as a deformable membrane that could seal the valve when magnets were pressed against it and that could permit the liquid flow once the top magnet was displaced.

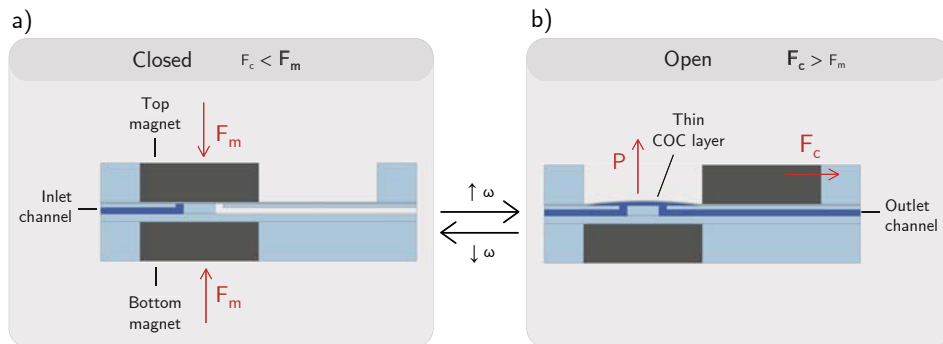


Figure 6.9: Principle of operation of the all-COC valving system. a) Closed state, where the magnetic force (F_m) is higher than the centrifugal force (F_c). b) Open state, where F_c is higher than F_m .

Unfortunately, the construction of a functional valving system could not be achieved by the exclusive use of COC. Two major impediments were found: the irreproducibility of the construction process and the unfeasibility of blocking the fluid flow during the closed state of the valve. These major handicaps are discussed below.

[†]For further information about the properties, advantages and disadvantages of the use of both PDMS and COC, please refer to § 1.3.3.

6.4.1.1 Construction process of all-COC valves

The construction of all the devices presented in this chapter was based on the previously described multilayer approach,[†] where TOPAS structural layers with high T_g (TOPAS 5013 or TOPAS 6015) were bonded together by using thin TOPAS layers showing lower T_g values (TOPAS 8007).

The initially conceived prototypes consisted of five different structural layers (see Figure 6.10). The magnets were placed into the outer layers A and E, while layers B, C and D composed the fluidic system. Layer C contained the main fluidic motifs and layer D was used for sealing the fluidic system. Layer B, with a reduced thickness, was used as the membrane layer.

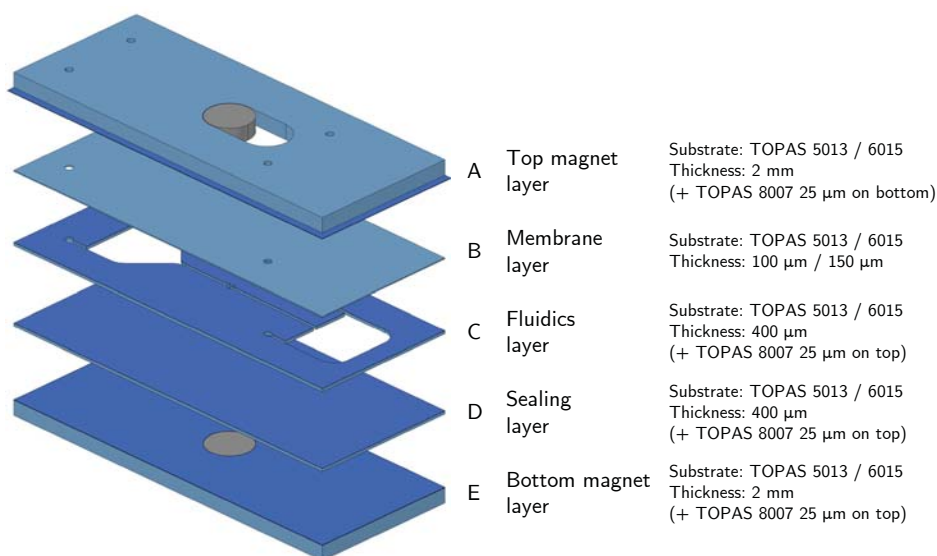


Figure 6.10: Scheme of the first prototypes developed. TOPAS 8007 bonding layers and TOPAS 5013/6015 structural layers are depicted in dark and light blue, respectively.

For the construction of the device, 25 μm thick TOPAS 8007 layers were bonded to layers A, C, D and E at $T_{\text{max}} = 108\text{ }^\circ\text{C}$ and $P_{\text{max}} = 25\text{ bar}$. Afterwards, the motifs were micromilled onto the different layers, from A to E, using 1.0 mm, 0.8 mm and 0.4 mm diameter milling tools. Once the layers were machined, several bonding steps were carried out: a first bonding step for sealing layers C and D, a second bonding step for sealing layer B to the previously obtained block, and a final bonding step for sealing layers A and E to the fluidic system (B+C+D).

[†]See § 3 for further information about the construction process of COC devices.

During the second bonding step, a 5 mm diameter valving area had to be defined by avoiding the sealing of the membrane layer (B) onto the previously obtained block (C+D) in that concrete zone. As explained in § 3.2.3, the bonding of the different COC layers is achieved by applying pressure and temperature. Therefore, in order to avoid the sealing of a layer in a concrete area, pressure and/or temperature had to be suppressed. Since local heating could not be carried out by using the equipment at our disposal, a bonding strategy where no pressure was applied to the valving zone was developed. The strategy consisted in the use of a 2 mm thick Delrin layer as a sacrificial layer during the thermocompression process. A 5 mm diameter circumference was machined onto this layer, corresponding to the desired area to be unsealed. During the bonding process of layer B to layers C and D, the sacrificial layer minimised the applied pressure onto the valving zone (see Figure 6.11). The same approach was applied for the final bonding step, where layers A and E were bonded to the fluidic system. In this particular case, no Delrin layers were required, since the holes for the magnets of layers A and E were larger than the valving area, hence acting themselves as sacrificial layers.

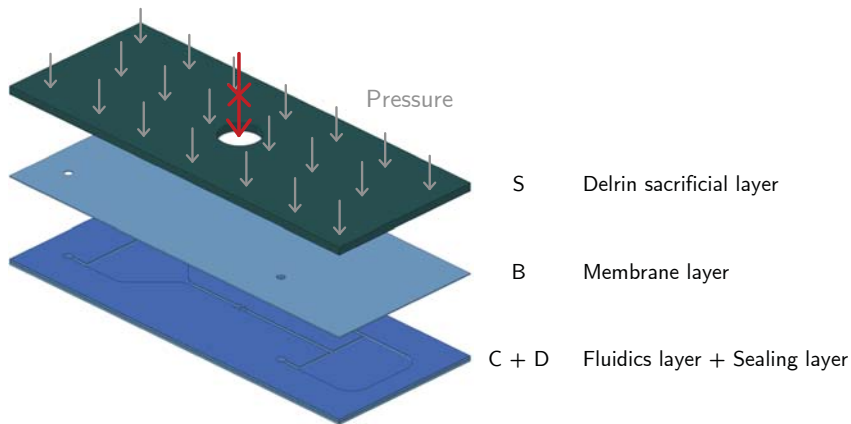


Figure 6.11: Use of a Delrin sacrificial layer for minimising pressure onto the valving area during the bonding of the membrane layer (B) to the previously bonded block (C+D).

As mentioned before, the first obstacle encountered was the reproducible and effective definition of the valving area during the construction of the prototypes. Despite no pressure was applied to the valving zone during the thermocompression processes, the achievement of a totally unbonded membrane was challenging. Several temperature and pressure conditions, TOPAS grades and membrane layer thicknesses were tested (see Table 6.1), obtaining, in most cases, the total or partial sealing of the membrane. Some examples can be found in Figure 6.12.

The optimal conditions were found to be $T_{\max} = 95 \text{ }^{\circ}\text{C}$ and $P_{\max} = 4 \text{ bar}$ for all bonding steps, using TOPAS 6015 as the substrate material and with a membrane layer thickness of $150 \text{ }\mu\text{m}$.

Table 6.1: Optimisation of the construction process for the all-COC valving prototypes.

Variable	Tested range	Optimum value
TOPAS grade	5013 / 6015	6015
Membrane layer thickness (μm)	100 / 150	150
Bonding temperature ($^{\circ}\text{C}$)	85 - 105	95
Bonding pressure (bar)	3 - 8	4

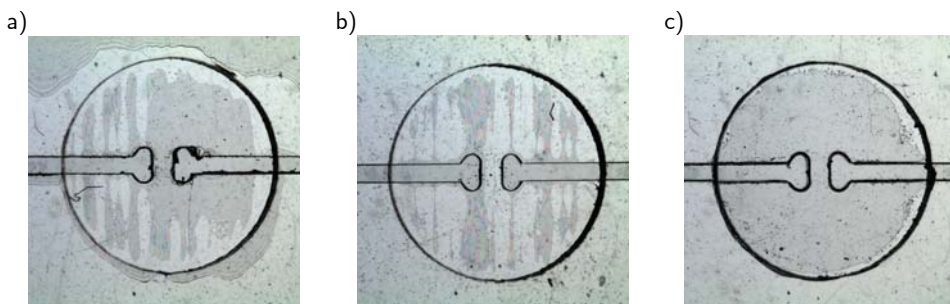


Figure 6.12: Bonding results for some of the tested conditions. a) Poor sealing of the device (see upper part of the image) due to low temperature ($T_{\max} = 85 \text{ }^{\circ}\text{C}$) in spite of high pressure ($P_{\max} = 8 \text{ bar}$), along with a partial bonding of the membrane layer in the valving zone. b) Almost total bonding of the membrane layer as a consequence of high temperature ($T_{\max} = 105 \text{ }^{\circ}\text{C}$) even though low pressure was applied ($P_{\max} = 3 \text{ bar}$). c) Perfectly defined valving area using the optimised conditions ($T_{\max} = 95 \text{ }^{\circ}\text{C}$ and $P_{\max} = 4 \text{ bar}$).

Two extra difficulties were found once the optimal conditions were fixed. The first was related to the low reproducibility of the bonding process: the use of the same conditions led to partially and even completely sealed valving areas in many cases (see Figure 6.13.a,b). The second was related to the need for an extra bonding step after the definition of the valving area, increasing the overall irreproducibility of the construction process (Figure 6.13.c,d). This second issue was easily circumvented by eliminating the final bonding step. The external layers containing the magnets were secured to the rest of the device once they were positioned inside the support platform. Since the devices perfectly fitted into the platform, all layers were precisely placed and immobilised without requiring the final bonding step.

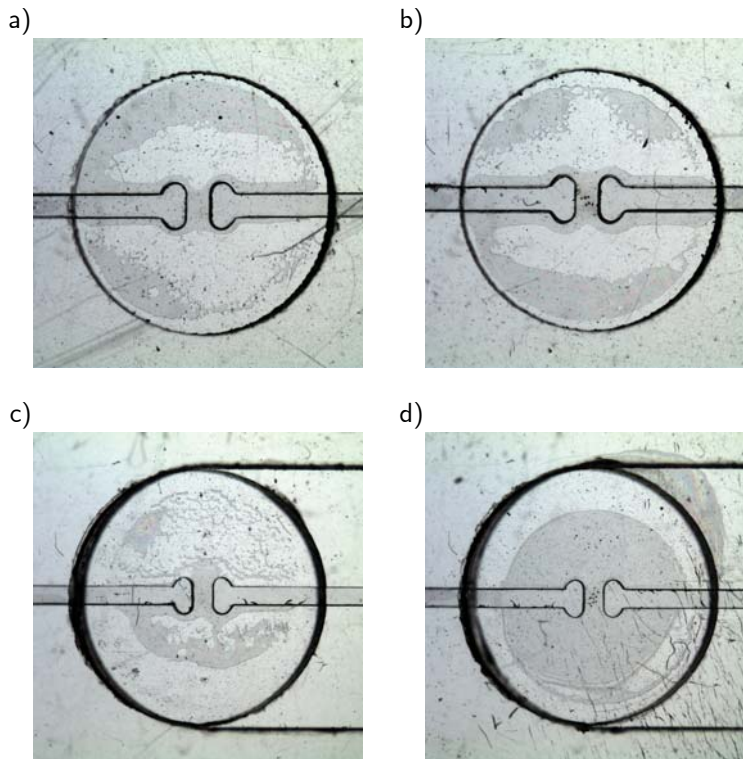


Figure 6.13: Examples of the low reproducibility of the bonding processes: a, b) partial bonding of the membrane layer in the valving area despite using the optimised conditions; c, d) different degrees of the undesired membrane sealing as a result of the final bonding step for the integration of the magnet layers.

6.4.1.2 Performance of the all-COC valves

The properly constructed prototypes were used for assessing the valve performance. The obtained results demonstrated, on one hand, the possibility of overcoming the magnetic force through the rotation of the platform but, on the other hand, the unfeasibility of blocking of the fluid flow during the closed state.

Evaluation of the magnets actuation

The actuation of the magnets was evaluated by progressively increasing and lowering the rotational frequency in 100 rpm increments/decrements during 30 s per step. The process was carried out five times for four different prototypes.

The rotational frequency at which the top magnet was sent outwards was found to be 2600 rpm, while the magnet returned to its initial position when the rotational

frequency was lowered to 1000 rpm. The same frequency values were obtained for all the experiment runs, hence demonstrating a 100% reproducible actuation of the magnets.

It is worth mentioning that these rotational frequencies strictly depended on the magnetic properties of the magnets and the geometric parameters of the devices, the latter including the radial distance of the magnets to the centre of rotation, the distance between the top and the bottom magnets and the length of the lane for the top magnet displacement, among others. All these characteristics defined the magnetic[†] and centrifugal forces at which the magnets were subjected. Other factors such as the frictional force between the top magnet and the surface of the device were also involved in the final force balance. Since a change in the valve design could result in a change in the rotational speed at which magnets were displaced, these values were evaluated for all newly developed prototypes.

Evaluation of the membrane layer actuation

Two different sets of prototypes with different valve designs were analysed: a first set where the zone to be sealed for blocking liquid flow was considerably large (Figure 6.14.a), and a second set where this area was minimised, expecting better gathering results (Figure 6.14.b). In the first design, the area to be sealed comprised part of the channels, whereas on the second design only two 0.4 mm diameter holes gave access to the fluid to reach the valve. Besides, in order to favour the plug of at least one of these holes, the distance between the end of the channels was increased. In both cases, the valving area was designed to be smaller than the magnet in order to ensure that the totality of the unsealed membrane would be pressed.

Minor changes on the design and an extra 400 µm thick TOPAS 6015 layer were required for the construction of the second set of prototypes. The extra layer (C in Figure 6.15) was bonded to layers D and E prior to the bonding of the membrane layer and using the same temperature and pressure conditions.

The actuation of the valve was evaluated by injecting 30 µL of H₂O into the inlet chamber. Rotational frequencies from 100 rpm to 2600 rpm in 100 rpm increments were applied to the platform during 30 s per step. The process was repeated five times for four different prototypes. Changes were examined by visual inspection.

Unfortunately, the proper sealing of the valve during its closed state was not achieved by any of the four tested prototypes, two of them corresponding to the first valve design and the remaining two to the second design. Water started to leak at very variable rotational frequencies ranging from 1300 rpm to 1700 rpm.

The unfeasible sealing of the valve during its closed state was presumably related to two main factors: a heterogeneous pressure being applied to the membrane due to irregularities on the involved surfaces and/or the presence of microapertures due to the lack of elasticity of the membrane layer.

[†]The magnetic forces between cylindrical permanent magnets and their relationship with geometrical and magnetic parameters can be found elsewhere.⁷⁵

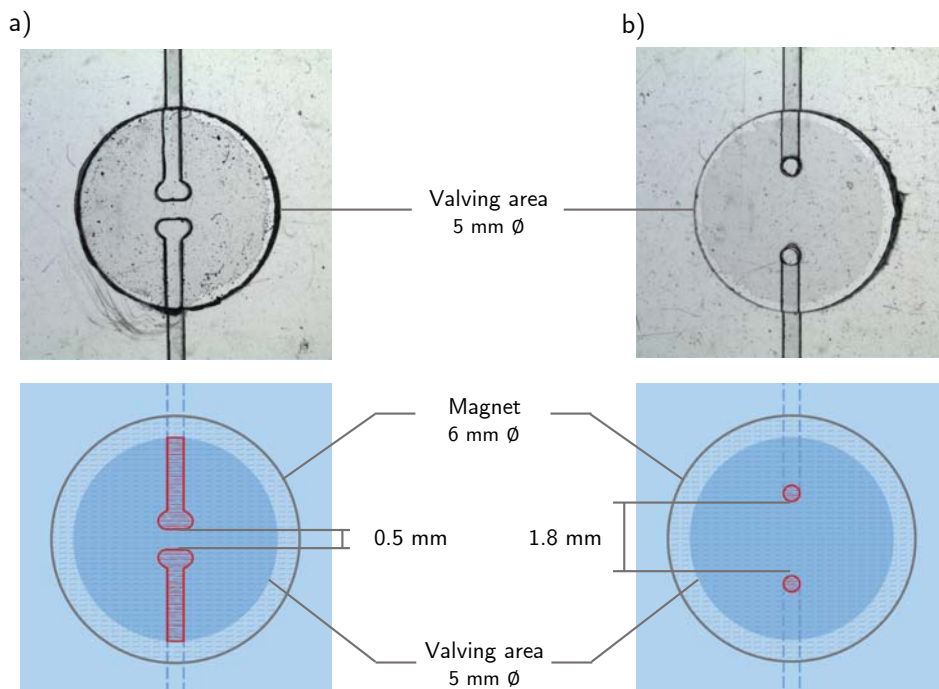


Figure 6.14: Real and schematic top view of the two valve designs: a) with a higher area and b) with a reduced area through which liquid could reach the valve. These areas are highlighted in red in the schematic view. Channel ends were at 0.5 mm and 1.8 mm distance for designs (a) and (b), respectively. For both designs, the 5 mm diameter valving zone was completely covered by the 6 mm diameter magnet.

In order to homogenise the applied pressure, PDMS discs of several thicknesses ranging from 100 μm to 500 μm were placed under the top magnet as depicted in [Figure 6.16](#).

PDMS was prepared from a commercial kit by mixing the curing agent with the PDMS pre-polymer at 1:10 weight ratio. After 10 minutes of vigorous mixing, vacuum was applied to the liquid state polymer to remove all bubbles for 20 minutes. The liquid PDMS was poured into plastic Petri dishes and was cured during 4 hours at 65 $^{\circ}\text{C}$. Discs were die-cut using hollow rivets.

The actuation of the valve was evaluated by following the previously described procedure, obtaining no successful results with the new configuration. However, some differences were found between the performance of the valves with and without using PDMS discs. The first major difference was an increment from 2600 rpm to up to 3400 rpm in the rotational frequency at which the top magnet was displaced. This

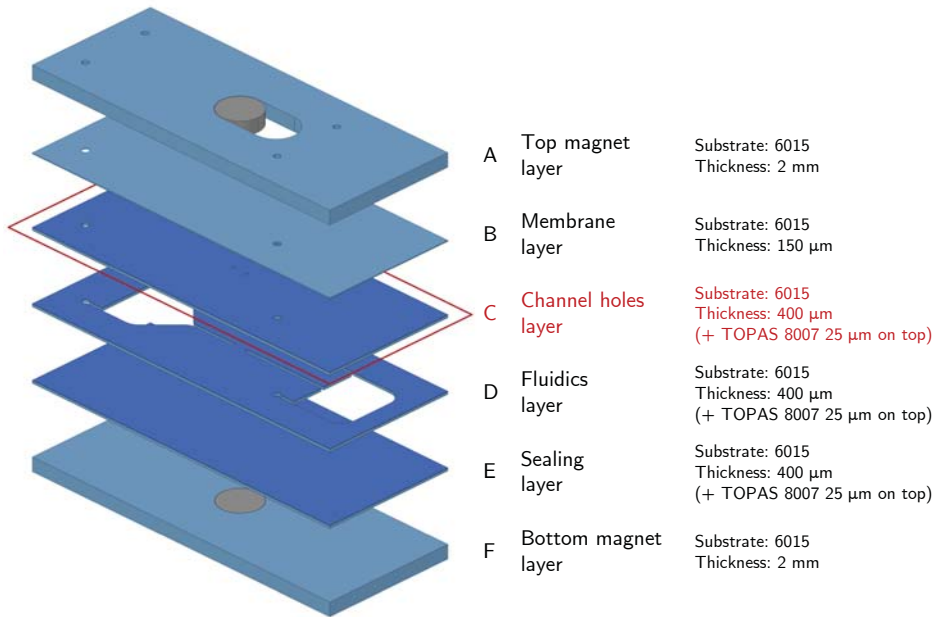


Figure 6.15: Scheme of the second valve design prototypes. The extra 400 μm thick layer required for these prototypes is framed in red.

effect was caused by an increment in the friction force as a result of the adhesion of the magnet to the PDMS. On the other hand, for this valve configuration, water leaks appeared at higher but more disparate rotational frequencies, ranging from 1300 rpm to up to 2700 rpm.

The slightly improved retention of fluids when PDMS discs were being used was considered a consequence of a higher homogeneity in the applied pressure along with the higher elasticity of PDMS in comparison to COC. In spite of the relatively high flexibility of the COC layer, it was concluded that its elasticity was insufficient for an effective sealing of the valve during its closed state.

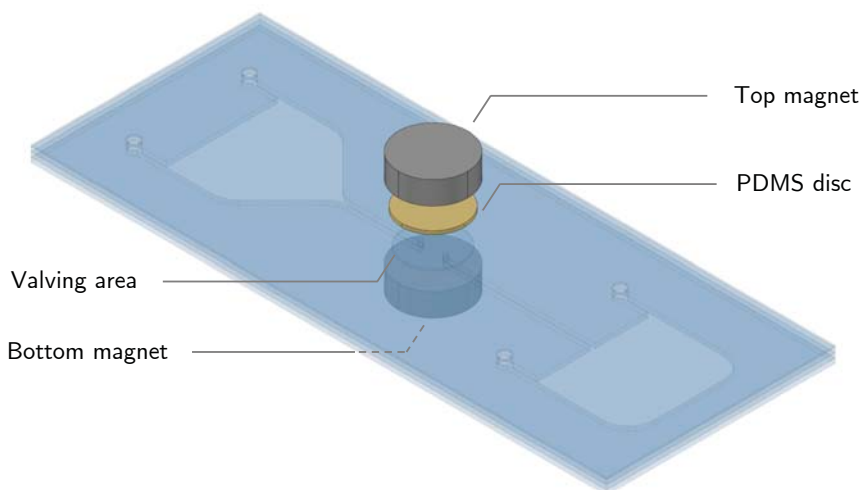


Figure 6.16: Placement of a PDMS disc under the top magnet for achieving a homogeneous pressure onto the valving area.

6.4.2 Prototypes integrating PDMS discs

Owing to the limited elasticity of COC, its use as a membrane for effectively sealing the valve during its closed state was found to be unsatisfactory. The use of a PDMS thin layer as the membrane layer could have been a practical solution. However, as discussed before, it would incur a series of unwanted consequences such the increase of the manufacturing costs or the poorer chemical resistance to solvents, among others. A compromise was found by the integration of a PDMS disc inside the valve, thus conserving the use of COC as the main construction material but adding the necessary elasticity for an effective sealing.

6.4.2.1 Construction process of prototypes integrating PDMS discs

As can be seen in [Figure 6.17](#), the new prototypes consisted of six different layers. The magnets were placed into the outer layers A and F, while layers B to E composed the fluidic system. Layer D contained the main fluidic motifs, layer C was introduced for locating the PDMS disc and layers B and E were used for sealing the fluidic system. For this set of prototypes, an adhesive plate seal (B) was employed for the reversible sealing of the fluidic system in order to easily place and remove the PDMS discs. The dimensions of the used PDMS discs were 4.4 mm in diameter and 500 μm in height.

For the construction of the device, 25 μm thick TOPAS 8007 layers were bonded to layers D and E at $T_{\text{max}} = 108\text{ }^{\circ}\text{C}$ and $P_{\text{max}} = 25\text{ bar}$. Afterwards, the motifs were micromilled onto the different TOPAS layers, A, C, D, E and F, using 1.0 mm, 0.8

mm and 0.4 mm diameter milling tools. Once the layers were machined, layers C to E were bonded in a single thermocompression process at $T_{\max} = 95\text{ }^{\circ}\text{C}$ and $P_{\max} = 4$ bar. Finally, the PDMS disc was inserted and the fluidic system was sealed using an adhesive plate seal. Layers A and F were assembled to the fluidic system by securing the layers inside the support platform.

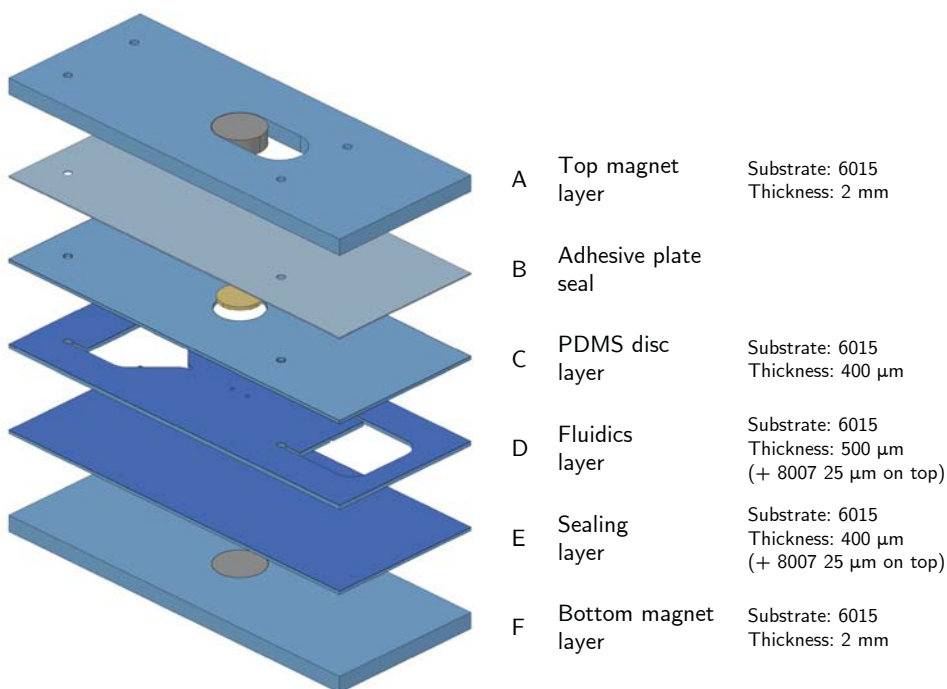


Figure 6.17: Layers of the prototypes integrating a PDMS disc inside the valve.

6.4.2.2 Performance of the valves integrating PDMS discs

The actuation of the magnets was evaluated by progressively increasing and lowering the rotational frequency in 100 rpm increments/decrements during 30 s per step. The process was carried out five times for four different prototypes. For these prototypes, the rotational frequencies at which the top magnet was displaced and returned to its initial position were found to be 2000 rpm and 1000 rpm, respectively, with a 100 % reproducibility.

The actuation of the valves was evaluated by injecting 30 μL of H_2O into the inlet chamber. Rotational frequencies from 100 rpm to 2000 rpm in 100 rpm increments

were applied to the platform during 30 s per step. The process was carried out five times for four different prototypes and changes were examined by visual inspection.

A perfect sealing of the valve was achieved up to the displacement of the top magnet. Liquid flow was successfully stopped with no leaks for any of the process runs. At 2000 rpm, when the top magnet was displaced, the PDMS disc was pushed upwards due to hydraulic pressure and water was completely transferred from the inlet chamber to the receiving chamber.

Since the aim of the project was to achieve a reversible and reusable valving system, the performance of the wet valves was studied. It is worth mentioning that for all the previous experiments, the prototypes were dried in an oven at 40 °C for several hours after being tested. In this case, the evaluation process was carried out five times for four prototypes without letting them dry.

Fluid flow was completely stopped during the closed state. However, a decrease in the reproducibility of the valve opening was obtained as a result of the adhesion of the PDMS disc to the COC surface. At 2000 rpm, when the top magnet moved outwards, liquid pressure could surpass the adhesion forces between the two materials in only 50% of the runs. The adhesion of the PDMS disc to the COC surface was found to be higher for the wet valves than for the completely dry ones.

In order to favour the deadhesion of the PDMS disc from the COC surface, a minor change was introduced to the design, consisting in the machining of a seat for the PDMS disc at a slightly higher height than the central part of the valve. The 25 μm thick TOPAS 8007 layer on top of layer D (see Figure 6.17) was changed for a 50 μm thick TOPAS 8007 layer. Prior to their bonding, a 4.2 mm diameter hole was machined onto the TOPAS 8007 layer, obtaining, as a result, a 1.6 mm wide and 50 μm height ring for the seat of the PDMS disc (see Figure 6.18).

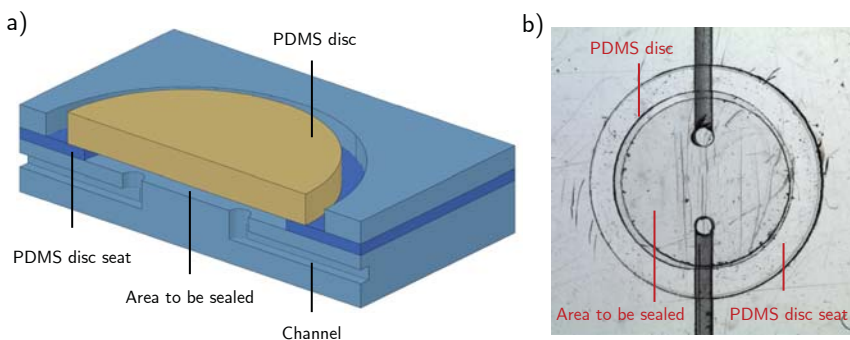


Figure 6.18: Internal structure of the final valve design: (a) schematic view (not at scale) and (b) real microscopic image.

The performance of these prototypes was analysed by following the previously described process, achieving an exceptional reproducibility for both dry and wet situations. The process was carried out fifteen times for four different prototypes, three of the runs with the valves being completely dry and all remaining runs by using the valves still wet. A 100% effectiveness was obtained for the experiments where the valves were dry, and a 92% for the valves being wet.

6.4.3 Final prototype

A final set of prototypes was constructed where the adhesive plate seal was replaced by a thin COC layer in order to demonstrate the possibility of obtaining a completely functional valve entirely constructed in COC and integrating a PDMS disc.

6.4.3.1 Construction process of the final valve prototype

The final design consisted of the same layers as the previous one, only differing in layer B (see [Figure 6.19](#)), which, in this case, was substituted by a 150 μm thick TOPAS 6015 layer.

For the construction of the device, 25 μm thick TOPAS 8007 layers were bonded to layers D and E at $T_{\text{max}} = 108\text{ }^{\circ}\text{C}$ and $P_{\text{max}} = 25\text{ bar}$. Afterwards, the motifs were micromilled onto the different TOPAS layers, from A to F, using 1.0 mm, 0.8 mm and 0.4 mm diameter milling tools. Once the layers were machined, layers C to E were bonded in a single thermocompression process at $T_{\text{max}} = 95\text{ }^{\circ}\text{C}$ and $P_{\text{max}} = 4\text{ bar}$. Next, a PDMS disc was integrated into the structure and layer B was bonded to the previously obtained block (C to E) using the same temperature and pressure conditions. Layers A and F were assembled to the fluidic system by securing all the layers inside the support platform.

6.4.3.2 Performance of the final valve prototype

The actuation of the magnets was evaluated by increasing and decreasing the rotational frequency in 100 rpm increments/decrements during 30 s per step. The process was repeated five times for four different prototypes.

The rotational frequency at which the top magnet was sent outwards was found to be 2000 rpm, while the magnet returned to its initial position when the rotational frequency was lowered to 1100 rpm, with a 100% reproducibility.

The actuation of the valve was evaluated by injecting 30 μL of H_2O into the inlet chamber. Rotational frequencies from 100 rpm to 2000 rpm in 100 rpm increments were applied to the platform during 30 s per step. The process was repeated fifteen times for four different prototypes, three of the runs with the valves being completely dry and all remaining runs by using the valves being wet, simulating the possible sequential gathering of fluids during a single experiment. Changes were examined by visual inspection.

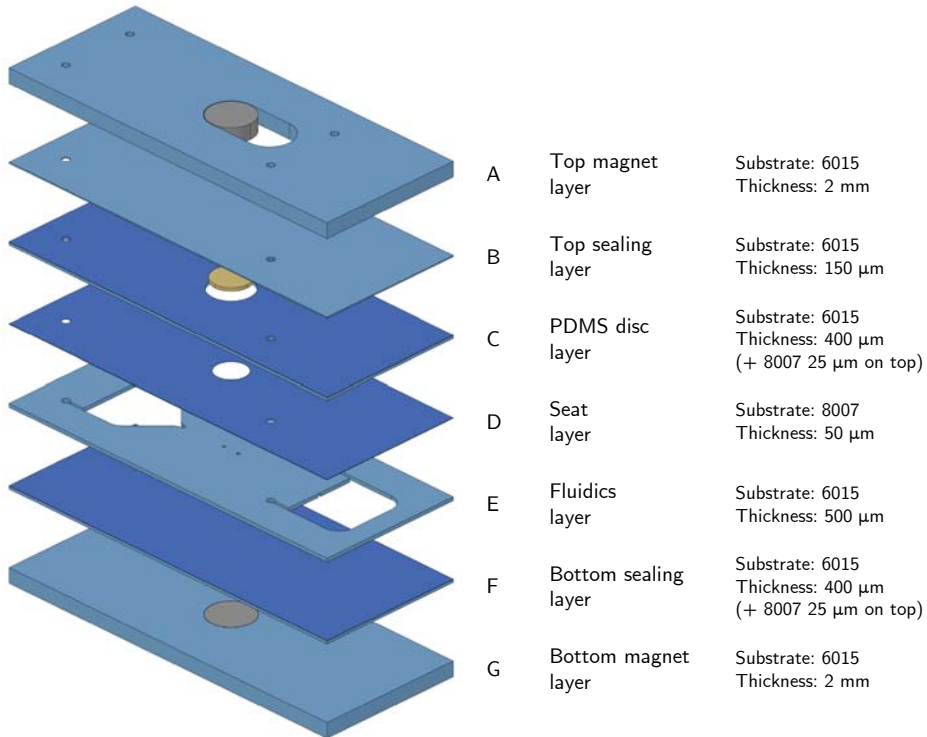


Figure 6.19: Layers of the final prototypes, where the adhesive plate seal was substituted by a 150 µm thick TOPAS 6015 layer.

Three of the prototypes demonstrated a perfect valving actuation, with no water leaks up to 2000 rpm and the total transfer of the liquid once the top magnet was displaced for the 100% of the process runs. For the remaining prototype, discrete water leaks appeared at 1900 rpm, very close to the opening of the valve, for the 66% of the runs as a result of an inaccurate positioning of the PDMS disc inside the structure during the construction process.

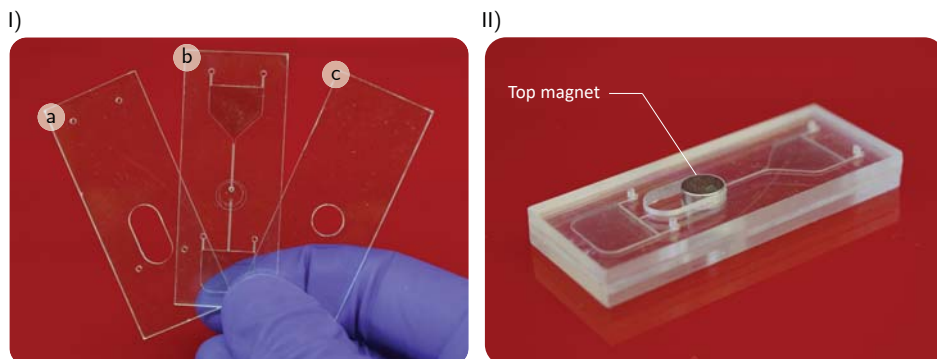


Figure 6.20: Real images of the final prototype. I) The different layers to be assembled inside the support: a) top magnet layer, b) fluidic block and c) bottom magnet layer. II) The assembled valving prototype containing the magnets.

6.5 Conclusions & future remarks

Owing to the importance of fluid flow control in centrifugal microfluidics, the development of robust valving systems is still a milestone. In this context, we have presented a novel reversible centrifugo-magnetically actuated valve displaying a simple and highly reproducible actuation. The new valving system here exposed is simple, robust and requires minimal external actuation. Besides, it is easy to implement, economical and does not involve complex construction processes.

Despite a functional all-COC valving system was not achieved, the perfect performance of a system entirely constructed in COC but integrating a small PDMS disc has been demonstrated. Furthermore, as a consequence of the use of a PDMS disc, the irreproducibility of the construction process was minimised, involving no critical bonding step.

The potential of the valving system relies on its capacity to be sequentially opened and closed, totally preserving its functionality for at least 10 sequential runs when wet and 15 different runs in total. The reversibility of the developed valve enables a highly sophisticated, robust and flexible fluid management.

Its capabilities have not been exploited yet, since several geometric parameters could be modified in order to obtain other valving systems based on the same principle of operation but actuating at different rotational speeds. For instance, by modifying the distance of the valve to the centre of rotation, the rotational frequency at which the top magnet is displaced could be tuned up. Other options could be, for instance, changing the length of the lane for the top magnet displacement or choosing magnets with a different degree of magnetisation.

The importance of valving systems in centrifugal microfluidics relies not only on

the development of new valves but also on the feasibility of combining several valving systems for achieving fluid control at a wide range of rotational frequencies. An example can be found in reference [76], where three different types of valves (siphon valves, centrifugo-pneumatic valves and wax valves) are combined. In that regard, the developed valve would be a perfect candidate to be combined with other types of valves, whether active or passive, due to its simple fabrication, integration and principle of operation. An interesting application could be, for example, its combination with capillary valves, typically working at lower rotational frequencies and being irreversibly opened.^{5,6,25}

References

- (1) Strohmeier, O.; Keller, M.; Schwemmer, F.; Zehnle, S.; Mark, D.; von Stetten, F.; Zengerle, R.; Paust, N. Centrifugal microfluidic platforms: advanced unit operations and applications. *Chemical Society Reviews* **2015**, *44*, 6187–6229.
- (2) Tang, M.; Wang, G.; Kong, S.-K.; Ho, H.-P. A Review of Biomedical Centrifugal Microfluidic Platforms. *Micromachines* **2016**, *7*, 26.
- (3) Gorkin, R.; Park, J.; Siegrist, J.; Amasia, M.; Lee, B. S.; Park, J.-M.; Kim, J.; Kim, H.; Madou, M.; Cho, Y.-K. Centrifugal microfluidics for biomedical applications. *Lab on a Chip* **2010**, *10*, 1758–1773.
- (4) Cho, H.; Kim, H.-Y.; Kang, J. Y.; Kim, T. S. How the capillary burst microvalve works. *Journal of Colloid and Interface Science* **2007**, *306*, 379–385.
- (5) Lai, S.; Wang, S.; Luo, J.; Lee, L. J.; Yang, S.-T.; Madou, M. J. Design of a Compact Disk-like Microfluidic Platform for Enzyme-Linked Immunosorbent Assay. *Analytical Chemistry* **2004**, *76*, 1832–1837.
- (6) Duffy, D. C.; Gillis, H. L.; Lin, J.; Sheppard, N. F.; Kellogg, G. J. Microfabricated Centrifugal Microfluidic Systems: Characterization and Multiple Enzymatic Assays. *Analytical Chemistry* **1999**, *71*, 4669–4678.
- (7) Choi, G.; Jung, J. H.; Park, B. H.; Oh, S. J.; Seo, J. H.; Choi, J. S.; Kim, D. H.; Seo, T. S. A centrifugal direct recombinase polymerase amplification (direct-RPA) microdevice for multiplex and real-time identification of food poisoning bacteria. *Lab on a Chip* **2016**, *16*, 2309–2316.
- (8) Grumann, M.; Steigert, J.; Riegger, L.; Moser, I.; Enderle, B.; Riebeseel, K.; Urban, G.; Zengerle, R.; Ducrée, J. Sensitivity enhancement for colorimetric glucose assays on whole blood by on-chip beam-guidance. *Biomedical Microdevices* **2006**, *8*, 209–214.
- (9) Ouyang, Y.; Wang, S.; Li, J.; Riehl, P. S.; Begley, M.; Landers, J. P. Rapid patterning of 'tunable' hydrophobic valves on disposable microchips by laser printer lithography. *Lab on a Chip* **2013**, *13*, 1762–1771.
- (10) Ouyang, Y.; Li, J.; Haverstick, D. M.; Landers, J. P. Rotation-Driven Microfluidic Disc for White Blood Cell Enumeration Using Magnetic Bead Aggregation. *Analytical Chemistry* **2016**, *88*, 11046–11054.
- (11) Ouyang, Y.; Li, J.; Phaneuf, C.; Riehl, P. S.; Forest, C.; Begley, M.; Haverstick, D. M.; Landers, J. P. Multilevel fluidic flow control in a rotationally-driven polyester film microdevice created using laser print, cut and laminate. *Lab on a chip* **2016**, *16*, 377–387.
- (12) Mark, D.; Metz, T.; Haeberle, S.; Lutz, S.; Ducrée, J.; Zengerle, R.; von Stetten, F. Centrifugo-pneumatic valve for metering of highly wetting liquids on centrifugal microfluidic platforms. *Lab on a Chip* **2009**, *9*, 3599–3603.

- (13) Siegrist, J.; Gorkin, R.; Bastien, M.; Stewart, G.; Peytavi, R.; Kido, H.; Bergeron, M.; Madou, M. Validation of a centrifugal microfluidic sample lysis and homogenization platform for nucleic acid extraction with clinical samples. *Lab on a Chip* **2010**, *10*, 363–371.
- (14) Al-Faqheri, W.; Ibrahim, F.; Thio, T.; Bahari, N.; Arof, H.; Rothan, H.; Yusof, R.; Madou, M. Development of a Passive Liquid Valve (PLV) Utilizing a Pressure Equilibrium Phenomenon on the Centrifugal Microfluidic Platform. *Sensors* **2015**, *15*, 4658–4676.
- (15) Nwankire, C. E.; Czugala, M.; Burger, R.; Fraser, K. J.; O'Connell, T. M.; Glennon, T.; Onwuliri, B. E.; Nduaguibe, I. E.; Diamond, D.; Ducreé, J. A portable centrifugal analyser for liver function screening. *Biosensors and Bioelectronics* **2014**, *56*, 352–358.
- (16) Kinahan, D. J.; Kearney, S. M.; Dimov, N.; Glynn, M. T.; Ducreé, J. Event-triggered logical flow control for comprehensive process integration of multi-step assays on centrifugal microfluidic platforms. *Lab Chip* **2014**, *14*, 2249–2258.
- (17) Gorkin III, R.; Nwankire, C. E.; Gaughran, J.; Zhang, X.; Donohoe, G. G.; Rook, M.; O'Kennedy, R.; Ducreé, J. Centrifugo-pneumatic valving utilizing dissolvable films. *Lab on a Chip* **2012**, *12*, 2894–2902.
- (18) Siegrist, J.; Gorkin, R.; Clime, L.; Roy, E.; Peytavi, R.; Kido, H.; Bergeron, M.; Veres, T.; Madou, M. Serial siphon valving for centrifugal microfluidic platforms. *Microfluidics and Nanofluidics* **2010**, *9*, 55–63.
- (19) Kitsara, M.; Nwankire, C. E.; Walsh, L.; Hughes, G.; Somers, M.; Kurzbuch, D.; Zhang, X.; Donohoe, G. G.; O'Kennedy, R.; Ducreé, J. Spin coating of hydrophilic polymeric films for enhanced centrifugal flow control by serial siphoning. *Microfluidics and Nanofluidics* **2014**, *16*, 691–699.
- (20) Zehnle, S.; Schwemmer, F.; Bergmann, R.; von Stetten, F.; Zengerle, R.; Paust, N. Pneumatic siphon valving and switching in centrifugal microfluidics controlled by rotational frequency or rotational acceleration. *Microfluidics and Nanofluidics* **2015**, *19*, 1259–1269.
- (21) Gorkin, R.; Soroori, S.; Southard, W.; Clime, L.; Veres, T.; Kido, H.; Kulinsky, L.; Madou, M. Suction-enhanced siphon valves for centrifugal microfluidic platforms. *Microfluidics and Nanofluidics* **2012**, *12*, 345–354.
- (22) Hoffmann, J.; Mark, D.; Zengerle, R.; von Stetten, F. In *TRANSDUCERS 2009 - 2009 International Solid-State Sensors, Actuators and Microsystems Conference*, IEEE: 2009, pp 1991–1994.
- (23) Hwang, H.; Kim, H.-H.; Cho, Y.-K. Elastomeric membrane valves in a disc. *Lab on a Chip* **2011**, *11*, 1434–1436.
- (24) Godino, N.; Gorkin III, R.; Linares, A. V.; Burger, R.; Ducreé, J. Comprehensive integration of homogeneous bioassays via centrifugo-pneumatic cascading. *Lab on a Chip* **2013**, *13*, 685–694.

- (25) Madou, M. J.; Lee, L. J.; Daunert, S.; Lai, S.; Shih, C.-H. Design and fabrication of CD-like microfluidic platforms for diagnostics : Microfluidic functions. *Biomedical Microdevices* **2001**, *3*, 245–254.
- (26) Kong, L. X.; Perebikovskiy, A.; Moebius, J.; Kulinsky, L.; Madou, M. Lab-on-a-CD: A Fully Integrated Molecular Diagnostic System. *Journal of Laboratory Automation* **2016**, *21*, 323–355.
- (27) Garcia-Cordero, J. L.; Kurzbuch, D.; Benito-Lopez, F.; Diamond, D.; Lee, L. P.; Ricco, A. J. Optically addressable single-use microfluidic valves by laser printer lithography. *Lab on a Chip* **2010**, *10*, 2680–2687.
- (28) Abi-Samra, K.; Hanson, R.; Madou, M.; Gorkin III, R. A. Infrared controlled waxes for liquid handling and storage on a CD-microfluidic platform. *Lab on a Chip* **2011**, *11*, 723–726.
- (29) Sayad, A. A.; Ibrahim, F.; Uddin, S. M.; Pei, K. X.; Mohktar, M. S.; Madou, M.; Thong, K. L. A microfluidic lab-on-a-disc integrated loop mediated isothermal amplification for foodborne pathogen detection. *Sensors and Actuators B: Chemical* **2016**, *227*, 600–609.
- (30) Al-Faqheri, W.; Ibrahim, F.; Thio, T. H. G.; Moebius, J.; Joseph, K.; Arof, H.; Madou, M. Vacuum/Compression Valving (VCV) Using Paraffin-Wax on a Centrifugal Microfluidic CD Platform. *PLoS ONE* **2013**, *8*, e58523.
- (31) Hwang, H.; Kim, Y.; Cho, J.; Lee, J.-y.; Choi, M.-S.; Cho, Y.-K. Lab-on-a-Disc for Simultaneous Determination of Nutrients in Water. *Analytical Chemistry* **2013**, *85*, 2954–2960.
- (32) Cho, Y.-k.; Lee, J.-G.; Park, J.-M.; Lee, B.-S.; Lee, Y.; Ko, C. One-step pathogen specific DNA extraction from whole blood on a centrifugal microfluidic device. *Lab on a Chip* **2007**, *7*, 565–573.
- (33) Park, J.-M.; Cho, Y.-K.; Lee, B.-S.; Lee, J.-G.; Ko, C. Multifunctional microvalves control by optical illumination on nanoheaters and its application in centrifugal microfluidic devices. *Lab on a Chip* **2007**, *7*, 557.
- (34) Amasia, M.; Cozzens, M.; Madou, M. J. Centrifugal microfluidic platform for rapid PCR amplification using integrated thermoelectric heating and ice-valving. *Sensors and Actuators B: Chemical* **2012**, *161*, 1191–1197.
- (35) Keller, M.; Czilwik, G.; Schott, J.; Schwarz, I.; Dormanns, K.; von Stetten, F.; Zengerle, R.; Paust, N. Robust temperature change rate actuated valving and switching for highly integrated centrifugal microfluidics. *Lab on a Chip* **2017**, *17*, 864–875.
- (36) Keller, M.; Wadle, S.; Paust, N.; Dreesen, L.; Nuese, C.; Strohmeier, O.; Zengerle, R.; von Stetten, F. Centrifugo-thermopneumatic fluid control for valving and aliquoting applied to multiplex real-time PCR on off-the-shelf centrifugal thermocycler. *RSC Advances* **2015**, *5*, 89603–89611.

- (37) Al-Faqheri, W.; Ibrahim, F.; Thio, T. H. G.; Aeinehvand, M. M.; Arof, H.; Madou, M. Development of novel passive check valves for the microfluidic CD platform. *Sensors and Actuators A: Physical* **2015**, *222*, 245–254.
- (38) Aeinehvand, M. M.; Ibrahim, F.; Harun, S. W.; Kazemzadeh, A.; Rothan, H. A.; Yusof, R.; Madou, M. Reversible thermo-pneumatic valves on centrifugal microfluidic platforms. *Lab on a Chip* **2015**, *15*, 3358–3369.
- (39) Jackson, K.; Borba, J.; Meija, M.; Mills, D.; Haverstick, D.; Olson, K.; Aranda, R.; Garner, G.; Carrilho, E.; Landers, J. DNA purification using dynamic solid-phase extraction on a rotationally-driven polyethylene-terephthalate microdevice. *Analytica Chimica Acta* **2016**, *937*, 1–10.
- (40) Cai, Z.; Xiang, J.; Chen, H.; Wang, W. Membrane-based valves and inward-pumping system for centrifugal microfluidic platforms. *Sensors and Actuators B: Chemical* **2016**, *228*, 251–258.
- (41) Cai, Z.; Xiang, J.; Wang, W. A pinch-valve for centrifugal microfluidic platforms and its application in sequential valving operation and plasma extraction. *Sensors and Actuators B: Chemical* **2015**, *221*, 257–264.
- (42) Wang, K.; Liang, R.; Chen, H.; Lu, S.; Jia, S.; Wang, W. A microfluidic immunoassay system on a centrifugal platform. *Sensors and Actuators B: Chemical* **2017**, *251*, 242–249.
- (43) Cai, Z.; Xiang, J.; Zhang, B.; Wang, W. A magnetically actuated valve for centrifugal microfluidic applications. *Sensors and Actuators B: Chemical* **2015**, *206*, 22–29.
- (44) Carpentras, D.; Kulinsky, L.; Madou, M. A Novel Magnetic Active Valve for Lab-on-CD Technology. *Journal of Microelectromechanical Systems* **2015**, *24*, 1322–1330.
- (45) Pamme, N. Magnetism and microfluidics. *Lab on a Chip* **2006**, *6*, 24–38.
- (46) Strohmeier, O.; Emperle, A.; Roth, G.; Mark, D.; Zengerle, R.; von Stetten, F. Centrifugal gas-phase transition magnetophoresis (GTM) – a generic method for automation of magnetic bead based assays on the centrifugal microfluidic platform and application to DNA purification. *Lab Chip* **2013**, *13*, 146–155.
- (47) Kirby, D.; Siegrist, J.; Kijanka, G.; Zavattoni, L.; Sheils, O.; O’Leary, J.; Burger, R.; Ducrée, J. Centrifugo-magnetophoretic particle separation. *Microfluidics and Nanofluidics* **2012**, *13*, 899–908.
- (48) Schaff, U. Y.; Sommer, G. J. Whole blood immunoassay based on centrifugal bead sedimentation. *Clinical Chemistry* **2011**, *57*, 753–761.
- (49) Grumann, M.; Geipel, A.; Riegger, L.; Zengerle, R.; Ducrée, J. Batch-mode mixing on centrifugal microfluidic platforms. *Lab on a Chip* **2005**, *5*, 560–565.
- (50) Siegrist, J.; Zavattoni, L.; Ducree, J. In *2011 IEEE 24th International Conference on Micro Electro Mechanical Systems*, IEEE: 2011, pp 1107–1110.

- (51) Donolato, M.; Antunes, P.; de la Torre, T. Z. G.; Hwu, E.-T.; Chen, C.-H.; Burger, R.; Rizzi, G.; Bosco, F. G.; Strømme, M.; Boisen, A.; Hansen, M. F. Quantification of rolling circle amplified DNA using magnetic nanobeads and a Blu-ray optical pick-up unit. *Biosensors and Bioelectronics* **2015**, *67*, 649–655.
- (52) DuVall, J. A.; Cabaniss, S. T.; Angotti, M. L.; Moore, J. H.; Abhyankar, M.; Shukla, N.; Mills, D. L.; Kessel, B. G.; Garner, G. T.; Swami, N. S.; Landers, J. P. Rapid detection of *Clostridium difficile* via magnetic bead aggregation in cost-effective polyester microdevices with cell phone image analysis. *The Analyst* **2016**, *141*, 5637–5645.
- (53) Godjevargova, T. I.; Ivanov, Y. L.; Dinev, D. D. In *AIP Conference Proceedings*, 2017; Vol. 1809, 020018(1)–020018(16).
- (54) Uddin, R.; Burger, R.; Donolato, M.; Fock, J.; Creagh, M.; Hansen, M. F.; Boisen, A. Lab-on-a-disc agglutination assay for protein detection by optomagnetic readout and optical imaging using nano- and micro-sized magnetic beads. *Biosensors and Bioelectronics* **2016**, *85*, 351–357.
- (55) Strohmeier, O.; Keil, S.; Kanat, B.; Patel, P.; Niedrig, M.; Weidmann, M.; Hufert, F.; Drexler, J.; Zengerle, R.; von Stetten, F. Automated nucleic acid extraction from whole blood, *B. subtilis*, *E. coli*, and Rift Valley fever virus on a centrifugal microfluidic LabDisk. *RSC Adv.* **2015**, *5*, 32144–32150.
- (56) Czilwik, G.; Vashist, S. K.; Klein, V.; Buderer, A.; Roth, G.; von Stetten, F.; Zengerle, R.; Mark, D. Magnetic chemiluminescent immunoassay for human C-reactive protein on the centrifugal microfluidics platform. *RSC Advances* **2015**, *5*, 61906–61912.
- (57) Kirby, D.; Glynn, M.; Kijanka, G.; Ducrée, J. Rapid and cost-efficient enumeration of rare cancer cells from whole blood by low-loss centrifugo-magnetophoretic purification under stopped-flow conditions. *Cytometry Part A* **2015**, *87*, 74–80.
- (58) Shih, C.-H.; Wu, H.-C.; Chang, C.-Y.; Huang, W.-H.; Yang, Y.-F. An enzyme-linked immunosorbent assay on a centrifugal platform using magnetic beads. *Biomicrofluidics* **2014**, *8*, 052110(1)–052110(11).
- (59) Glynn, M.; Kirby, D.; Chung, D.; Kinahan, D. J.; Kijanka, G.; Ducrée, J. Centrifugo-Magnetophoretic Purification of CD4+ Cells from Whole Blood Toward Future HIV/AIDS Point-of-Care Applications. *Journal of Laboratory Automation* **2014**, *19*, 285–296.
- (60) Choi, G.; Song, D.; Shrestha, S.; Miao, J.; Cui, L.; Guan, W. A field-deployable mobile molecular diagnostic system for malaria at the point of need. *Lab on a Chip* **2016**, *16*, 4341–4349.
- (61) Yan, H.; Zhu, Y.; Zhang, Y.; Wang, L.; Chen, J.; Lu, Y.; Xu, Y.; Xing, W. Multiplex detection of bacteria on an integrated centrifugal disk using bead-beating lysis and loop-mediated amplification. *Scientific Reports* **2017**, *7*, 1460.

- (62) Roy, E.; Stewart, G.; Mounier, M.; Malic, L.; Peytavi, R.; Clime, L.; Madou, M.; Bossinot, M.; Bergeron, M. G.; Veres, T. From cellular lysis to microarray detection, an integrated thermoplastic elastomer (TPE) point of care Lab on a Disc. *Lab on a Chip* **2015**, *15*, 406–416.
- (63) Haeberle, S.; Schmitt, N.; Zengerle, R.; Ducreé, J. Centrifugo-magnetic pump for gas-to-liquid sampling. *Sensors and Actuators A: Physical* **2007**, *135*, 28–33.
- (64) Haeberle, S.; Schmitt, N.; Zengerle, R.; Ducreé, J. In *19th IEEE International Conference on Micro Electro Mechanical Systems*, IEEE: 2006, pp 166–169.
- (65) Duford, D. A.; Xi, Y.; Salin, E. D. Enzyme Inhibition-Based Determination of Pesticide Residues in Vegetable and Soil in Centrifugal Microfluidic Devices. *Analytical Chemistry* **2013**, *85*, 7834–7841.
- (66) Xi, Y.; Duford, D. A.; Salin, E. D. Automated liquid–solid extraction of pyrene from soil on centrifugal microfluidic devices. *Talanta* **2010**, *82*, 1072–1076.
- (67) Duford, D. A.; Peng, D. D.; Salin, E. D. Magnetically Driven Solid Sample Preparation for Centrifugal Microfluidic Devices. *Analytical Chemistry* **2009**, *81*, 4581–4584.
- (68) Mohammed, M. I.; Haswell, S.; Gibson, I. Lab-on-a-chip or Chip-in-a-lab: Challenges of Commercialization Lost in Translation. *Procedia Technology* **2015**, *20*, 54–59.
- (69) Waldbaur, A.; Rapp, H.; Länge, K.; Rapp, B. E. Let there be chip—towards rapid prototyping of microfluidic devices: one-step manufacturing processes. *Analytical Methods* **2011**, *3*, 2681–2716.
- (70) Ren, K.; Zhou, J.; Wu, H. Materials for Microfluidic Chip Fabrication. *Accounts of Chemical Research* **2013**, *46*, 2396–2406.
- (71) Mukhopadhyay, R. When PDMS isn't the best. *Analytical Chemistry* **2007**, *79*, 3248–3253.
- (72) Kuncova-Kallio, J.; Kallio, P. J. In *2006 International Conference of the IEEE Engineering in Medicine and Biology Society*, IEEE: 2006, pp 2486–2489.
- (73) Alrifaiy, A.; Lindahl, O. A.; Ramser, K. Polymer-Based Microfluidic Devices for Pharmacy, Biology and Tissue Engineering. *Polymers* **2012**, *4*, 1349–1398.
- (74) Nunes, P. S.; Ohlsson, P. D.; Ordeig, O.; Kutter, J. P. Cyclic olefin polymers: emerging materials for lab-on-a-chip applications. *Microfluidics and Nanofluidics* **2010**, *9*, 145–161.
- (75) Vokoun, D.; Beleggia, M.; Heller, L.; Šittner, P. Magnetostatic interactions and forces between cylindrical permanent magnets. *Journal of Magnetism and Magnetic Materials* **2009**, *321*, 3758–3763.

- (76) Sayad, A.; Ibrahim, F.; Mukim Uddin, S.; Cho, J.; Madou, M.; Thong, K. L. A microdevice for rapid, monoplex and colorimetric detection of foodborne pathogens using a centrifugal microfluidic platform. *Biosensors and Bioelectronics* **2018**, *100*, 96–104.

Chapter 7

Centrifugal microfluiding system for the implementation of enzyme-based analyses in wine with spectrophotometric detection

7.1 Enzyme-based analyses in wine

Among the broad number of parameters that are typically determined in wines, there is a group of compounds that can be analysed by specific enzymatic reactions where nicotine adenine dinucleotide (NADH, see [Figure 7.1](#)) and nicotine adenine dinucleotide phosphate (NADPH) are involved. These analytes include acetaldehyde, acetic acid, ammonia, citric acid, ethanol, D-glucose, D-fructose, D-gluconic acid, glycerol, L- and D-lactic acid, L- and D-malic acid, succinic acid, sucrose and total sulphite.¹⁻⁴

The enzymatic methods for determining the aforementioned analytes are based on the quantification of the increase or the decrease in the NADH or the NADPH concentrations, which can be stoichiometrically related to the analyte concentration in the sample. NADH and NADPH present a maximum absorbance peak at 340 nm, whereas the oxidised form of these two coenzymes does not. Hence, the conversion reaction of one form of the coenzyme to the other can be monitored by measuring absorbance at 340 nm. The principle of these methods is illustrated in [Figure 7.2](#).

Enzymatic methods offer high specificity towards the targeted molecules and, although they are considered expensive in comparison to other classical alternatives,³ the costs are drastically reduced when combined with microfluidic systems since the required sample and reagent volumes are minimised.⁵

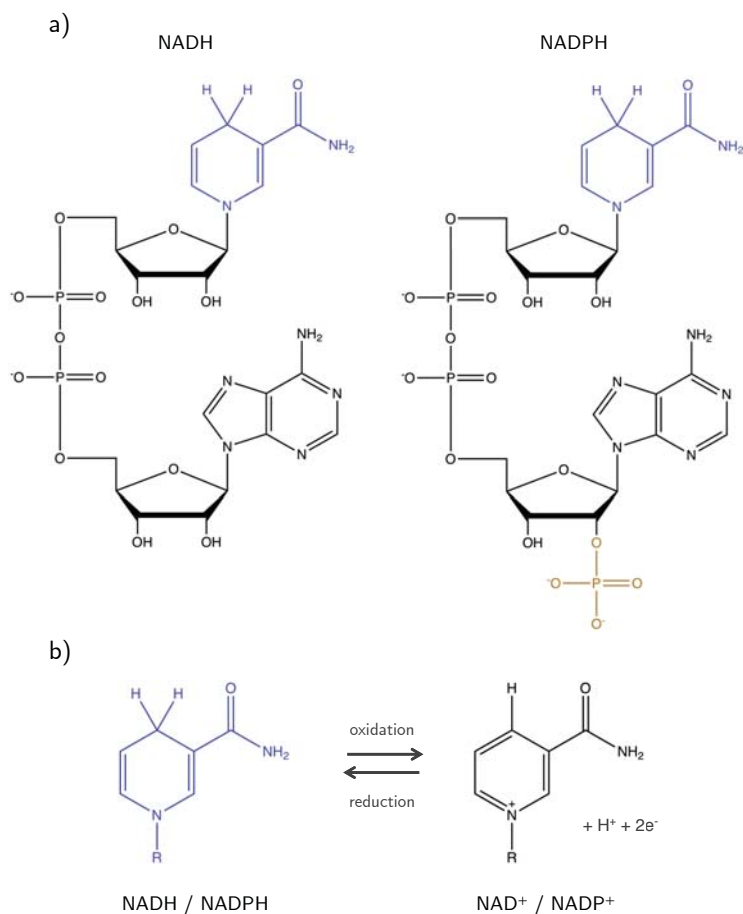


Figure 7.1: a) Reduced structure of NADH and NADPH coenzymes. b) Redox reaction of the coenzymes.

In this context, we aimed to develop a centrifugal microfluidic platform that allowed the parallelisation of several wine analyses based on the same enzymatic method and using UV absorbance detection. The main objective of the work presented in this chapter was the development of a versatile modular centrifugal microfluidic platform where several analytes could be quantified by using a simple miniaturised optical detection system measuring at a fixed wavelength.

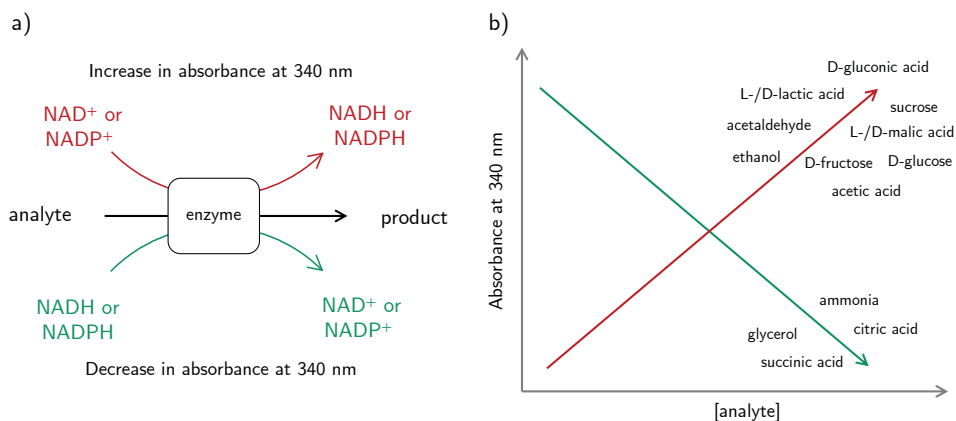


Figure 7.2: Enzymatic methods based on NADH and NADPH coenzymes for the spectrophotometric determination of several wine parameters: (a) reaction schemes and (b) the corresponding calibration curves.

The use of a centrifugal system was preferred over other common microfluidic systems in order to minimise the required external instrumentation, therefore reducing the complexity, size and costs of the system.[†] Furthermore, centrifugal microfluidic platforms permit the easy implementation of modular parallel disposable devices as well as the parallelisation of several analyses in a single device. Parallelisation in centrifugal microfluidics is introduced in the next section of this chapter.

The developed devices integrated two aliquoting structures for the implementation of an automated on-chip standard addition method. Standard addition calibrations are especially useful when analytes in complex matrixes with unknown composition have to be determined,^{6,7} such as in the particular case of wines.

As a proof of concept, the enzymatic determination of L-lactic acid was performed using the developed centrifugal miniaturised system and a commercial reagent kit. Among the several parameters that could be analysed using the same principle, L-lactic acid was selected owing to its relevance not only in wine but also in food industry, clinical diagnosis and sports medicine.⁸ Its importance during wine production as well as its enzymatic determination will be discussed later on this chapter. The enzymatic determination of L-lactic acid was performed using the developed centrifugal miniaturised system and a commercial reagent kit.

[†]See § 1.2.2.2 for further information about the advantages of centrifugal microfluidic platforms in comparison to other common platform types.

7.2 Parallelisation in centrifugal microfluidic platforms

One of the major advantages of centrifugal microfluidic platforms with respect to other microfluidic systems relies on the possibility of integrating multiple parallel analyses in a single device. Parallelisation can be achieved by two different approaches consisting, on one hand, in the integration of several independent systems in a same disc^{9,10} and, on the other hand, in the aliquoting of samples and/or reagents into several sub-volumes.^{11,12} The two principles have been frequently combined, thus further increasing the number of parallel analyses that can be performed in a single platform. Using these strategies, centrifugal microfluidic platforms presenting a high degree of parallelisation have been reported,^{13–17} including, for example, a centrifugal system which is capable of preparing more than one hundred different aliquots in a single platform.¹⁸ Modular systems consisting of independent devices fixed to a common support platform have been also reported.^{19–23} These systems include, in turn, structures that allow the aliquoting of samples and/or reagents within each module (see Figure 7.3).

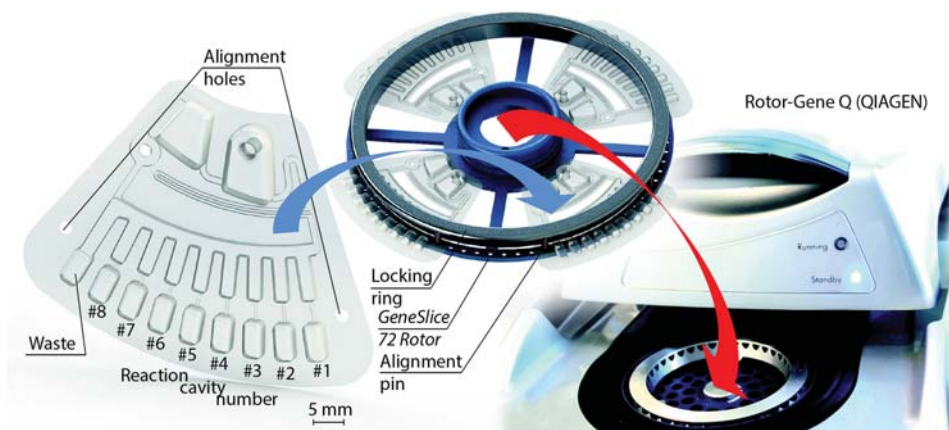


Figure 7.3: Example of a modular centrifugal platform. The platform integrates four different devices, each of them containing an aliquoting structure. Adapted from reference [22].

The reported modules, subsystems and aliquoting structures have been used for different purposes, including the analysis of several parameters in a single sample,^{11,13,14} the analysis of one parameter in several samples^{10,15} and the analysis of several parameters in several samples.^{16,17,19}

Aliquoting consists in splitting an input liquid volume into multiple defined sub-volumes and it commonly involves a first step where liquid is metered into several aliquots and a second step where these aliquots are transferred into independent chambers. Single-step aliquoting processes where liquid is directly transported from an inlet

chamber into multiple receiving chambers are not frequently used since cross contamination could easily occur as a consequence of a liquid thin film interconnecting the adjacent chambers.²⁴ On the contrary, two-stage aliquoting systems avoid any cross-contamination and permit the further processing of the individual aliquots.^{23–25}

During the metering phase of the two-stage aliquoting processes, the multiple sub-volumes are defined. Two main metering structures have been commonly used: a continuous zig-zag shaped metering channel,^{12,14,16,17} where the dimensions of the channel determine the discrete volumes into which the total volume will be split; and a series of metering chambers interconnected by a distribution channel,^{11,13,15,16,18–25} where the volume of the aliquots is defined by the size of the metering chambers. During the transfer phase, the metered volumes are forwarded into separate receiving chambers, where they can be individually processed.

The aforementioned metering strategies are illustrated in **Figure 7.4**. The centrifugal platform in **Figure 7.4.a**, which was designed for the parallel genetic analysis of twenty-five pathogen samples, integrates three different aliquoting structures in each of the five identical subsystems.¹⁷ **Figure 7.4.b** shows one device of a modular centrifugal platform used for the automation of real-time polymerase chain reaction (PCR) amplification of *Escherichia coli* DNA (see **Figure 7.3** for the complete setup).²² Required primers and probes for the PCR amplification were pre-stored in the reaction cavities of the platform. The use of pre-stored reagents, either dried or lyophilised, for the post-processing of the aliquoted volumes has been frequently reported.^{11,15,16,19–22} Reagent pre-storage simplifies both the design of the platforms and the analytical procedures, since it reduces the need for extra liquid handling structures and/or manual injection steps.

The retention and transfer of fluids during the metering and transfer phases, respectively, is achieved by the actuation of several valves which connect the metering structures to the receiving chambers. The integration of diverse valving systems has been demonstrated, being capillary valves^{13,14,16,18} and centrifugo-pneumatic valves^{11,15,19,21,24,25} the most widely used ones.

7.3 Lactic acid as the proof-of-concept analyte

As mentioned before, lactic acid determination is carried out in different fields and for many different purposes. For instance, serum lactate levels in blood are measured for the diagnosis and medical management of several illnesses.⁸ Lactate levels in blood are also used as a fitness indicator and they are frequently measured during performance testing of athletes.²⁶ Lactic acid determination is also relevant in food and beverage industry, where it is used for monitoring fermentation processes as well as for quality control.²⁷ Its importance during wine production and its enzymatic determination are presented hereafter.

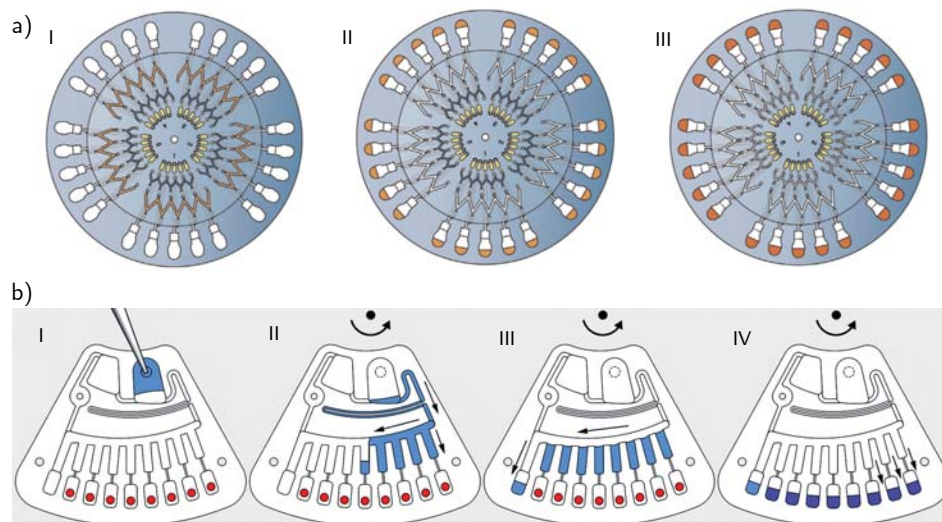


Figure 7.4: Commonly used two-stage aliquoting strategies: a) continuous zig-zag shaped metering channel and b) interconnected metering chambers. In (a): (I) loading of the metering structures and (II, III) sequential transfer of the metered liquids. In (b): (I) injection, (II) distribution, (III) metering and (IV) transfer of the metered sub-volumes. Adapted from references [17] and [22], respectively.

7.3.1 Lactic acid and the malo-lactic fermentation of wine

As introduced in § 4.1, lactic acid is one of the main organic acids of wine and its content can reach up to several grams per litre.²⁸ Although it is not naturally found in grape, it is produced during two different stages of the wine-making process: the alcoholic fermentation and the malolactic fermentation.

During alcoholic fermentation, pyruvic acid can be reduced to lactic acid by the yeast lactate dehydrogenase enzyme, mainly producing the D-lactic acid stereoisomer in low concentrations (under 300 mg/L).²⁹ However, the major part of the lactic acid comes from the malolactic fermentation, where lactic acid bacteria transform L-malic acid to L-lactic acid (see Figure 7.5). This reduction of L-malic acid to L-lactic acid is not a true fermentation but an enzymatic decarboxylation, yet it was given this name due to its similarities with the alcoholic fermentation.³⁰

The major benefit of the malolactic fermentation is the deacidification of highly acidic wines. During this process, a dicarboxylic harsh tasting acid (L-malic acid) is converted to a monocarboxylic smooth tasting acid (L-lactic acid). Malolactic fermentation is carried out in most red wines, especially in those from cool climatic regions,

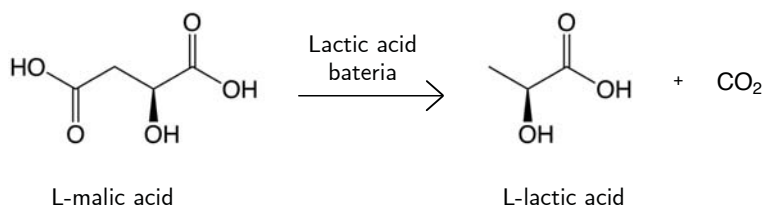


Figure 7.5: General reaction of the transformation of L-malic acid to L-lactic acid during the malolactic fermentation. Adapted from reference [30].

where a reduction in the acidity level leads to an improvement in flavour. On the contrary, fewer white wines undergo malolactic fermentation, since the desired freshness provided by L-malic acid would be substituted by a milder and warmer taste coming from L-lactic acid.^{3,29,31,32} Apart from an improvement in the taste of excessively acidic wines, malolactic fermentation is also considered to increase the microbial stability of wines by the removal of residual fermentable substrates.³²

Malolactic fermentation can be monitored by measuring the concentration of L-malic acid and/or L-lactic acid over time.^{33–35} Actually, one of the classical methods for monitoring this process consisted in performing periodical paper chromatographic analyses, where the vanishing and growth of the spots corresponding to malic acid and lactic acid, respectively, could be observed.⁴

7.3.2 L-lactic acid enzymatic determination

As previously mentioned, L-lactic acid can be determined by using an enzymatic method based on the spectrophotometric quantification of NADH. This enzymatic method is recommended by the OIV and accepted by the AOAC.^{1,36} The analytical procedure as well as the preparation of the reagent solutions are described elsewhere.¹ Besides, several kits containing all necessary enzymes and reagents are commercially available. These reagents are generally ready to use and they usually contain preservatives for increasing their shelf life.³ Since the purpose of this work was not aimed at the study of the involved reactions but at the development of the centrifugal microfluidic system, one of these reagent kits was used for performing the analyses.

The enzymatic reaction for the L-lactic acid determination consists in the oxidation of L-lactic acid (L-lactate) to pyruvic acid (pyruvate) by NAD⁺ in the presence of L-lactate dehydrogenase (L-LDH), where the amount of NADH produced is proportional to the concentration of L-lactic acid in the sample. Since the equilibrium lies strongly in favour of the L-lactic acid, a further reaction for the removal of the pyruvate from the reaction mixture is frequently used. The OIV, for example, proposes the transformation of pyruvate into L-alanine in a reaction catalysed by the L-glutamate pyruvate

transaminase (L-GPT).¹ Alternatively, in the commercial kit used in this work, the reaction consisted in the conversion of the produced pyruvate to the D-alanine stereoisomer (instead of the L- stereoisomer) and 2-oxoglutarate in the presence of an excess of D-glutamate and catalysed by the D-glutamate pyruvate transaminase (D-GPT) enzyme.³⁷ The two enzymatic reactions involved in the quantification of L-lactic acid by using the purchased reagent kit can be found in **Figure 7.6**.

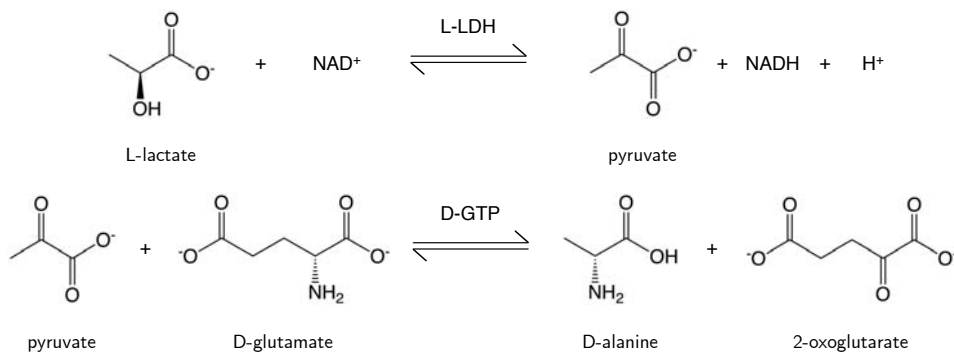


Figure 7.6: Enzymatic reactions involved in the quantification of L-lactic acid.

7.4 Development of a centrifugal microfluidic system for the enzymatic determination of L-lactic acid in wine samples using spectrophotometric detection

7.4.1 Methods

7.4.1.1 Reagents and solutions

All used chemicals were of analytical reagent grade and all solutions were prepared using MilliQ water.

NADH stock solutions were prepared by accurate weighting of NADH dipotassium salt (Sigma-Aldrich, Saint Louis, USA) and dissolution in tris(hydroxymethyl)amino-methane (TRIS, Sigma-Aldrich) buffer aqueous solutions. NADH standard solutions were prepared by dilution of the stock solution in TRIS buffer solutions. Aqueous solutions of 1 M sodium hydroxide (NaOH, Panreac, Castellar del Vallès, Spain) and 1 M hydrochloric acid (HCl, Merk, Darmstadt, Germany) were used for the pH adjustment of the TRIS buffer solution.

Standard solutions of L-(+)-lactic acid (Sigma Aldrich) were prepared by dilution of a 10 mM stock standard solution. The stock solution was prepared by accurate

weighting and dissolution of the solid in MilliQ water. L-lactic acid was analysed by using a commercial reagent kit L-lactic acid (L-lactate) assay kit K-LATE 07/14 from Megazyme International (Wicklow, Ireland). The tested wine sample was commercially available. A 50-fold dilution step was required prior to analysis.

7.4.1.2 Materials

The devices were constructed by using several COC layers from TOPAS Advanced Polymers (Florence, KY, USA) of diverse thicknesses and grades, including 400 µm and 500 µm TOPAS 6013 layers and 25 µm TOPAS 8007 layers. Adhesive plate seals AB-0850 Absolute qPCR from ABgene Advanced Biotechnologie (Epsom, UK) were used for the reversible sealing of the devices. Delrin plaques of 2 mm in thickness (DuPont, Wilmington, USA) were used as sacrificial layers for the bonding steps. MilliQ water and ethanol (Panreac, Castellar del Vallès, Spain) were used for cleaning the COC layers before the bonding steps as well as for cleaning the devices after use. A Low Temperature Cofired Ceramics (LTCC) master was required for the hot embossing processes involved in the construction of the devices. The master was made of eight GreenTape 951 PX LTCC sheets of 254 µm in thickness from DuPont.

Several 2 mm and 3 mm thick PMMA layers (Plásticos Ferplast, Terrassa, Spain) were used for the construction of the rotating platform and the detection system support.

7.4.1.3 Experimental setup

The experimental setup, which is illustrated in [Figure 7.7](#), can be divided into three main parts: a support platform for the placement of the modular devices, a rotatory actuator for the movement of the platform and an optical detection system for performing the absorbance measurements.

The support platform was constructed for accommodating two devices and it was composed of several 3 mm thick PMMA layers (see [Figure 7.8.a](#)) which were individually machined using a CNC micromilling machine. The top and the bottom PMMA layers impeded the ejection of the devices during the rotation of the platform. The top layer was also used as a mask for defining the detection areas. The different layers were assembled together by using several magnets and metallic bolts. An aluminium shaft adapter was employed for anchoring the support platform to the motor axis. The platform was secured to the aluminium shaft adapter by using four bolts.

The rotatory actuator, previously introduced in [§ 6.2.2](#), consisted of a motor Maxon EC-i 40 50W, an encoder Maxon MR Type L 256-1024 CPT and a positioning controller (or driver) EPOS 24/5 from Maxon Motor Ibérica S.A. (Torrejón de Ardoz, Spain). The driver controlled and processed the orders from a PC and sent the results to the encoder, which was in charge of the conversion of the digital information to an angular movement of the motor and vice versa. The motor, the encoder and the positioning

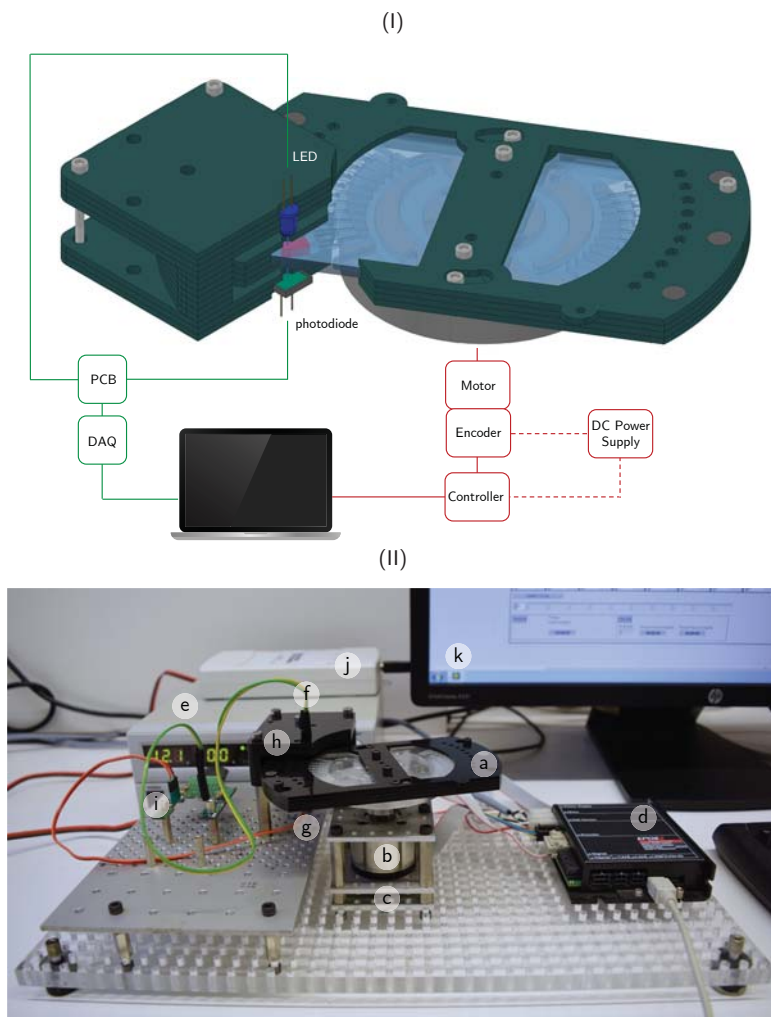


Figure 7.7: Schematic (I) and actual (II) experimental setup for the L-lactic acid determination. In (II): support platform (a); rotatory actuator, including a motor (b), an encoder (c), a positioning controller (d) and a power supply (e); and optical detection system, composed of a LED (f) and a photodiode (g) mounted into a polymeric support (h), a PCB (i) and a DAQ (j). The positioning controller of the rotatory actuator and the DAQ of the optical detection system were connected to a PC (k). The rotatory actuator and the optical detection system (with exception of the power supply and the DAQ, respectively) were fixed onto a polymeric perforated base.

controller were powered by an HCS-3202 direct current (DC) power supply from Manson Engineering Industrial Ltd (Kwai Chung, China).

A complete user interface was developed for controlling the actuation of the motor. The interface was created using the NI LabVIEW 2012 System design software (National Instruments, Austin, USA) and was designed to permit a wide and user-friendly operational control of the motor including, for example, the automated sequencing of multiple spinning steps and the accurate and automated positioning of the detection chambers between the LED and the photodiode for the absorbance measurements. Several parameters, such as the number of detection chambers and their relative position, could be defined by the user.

The optical detection system, presented in § 4.2.1.3, was adapted to the new configuration of the platforms. Similarly to the previously described one, the system consisted of a light emitting diode (LED) and a photodiode mounted into a compact C-shaped PMMA structure. The polymeric structure was designed to allow the free rotation of the platform as well as the accurate alignment of the detection chambers with respect to the LED and the photodiode. The structure was composed of several 2 mm thick PMMA layers (see Figure 7.8.b) machined in a CNC micromilling machine and assembled together by using several bolts. The LED was embedded inside the upper layers of the structure, whereas the photodiode was mounted into the lower layers. Several PMMA pieces were placed between these two groups of layers for creating the C-shaped structure that permitted the free movement of the rotating platform.

The LED and the photodiode were connected to a printed circuit board (PCB) that, in turn, was connected to a data acquisition card (DAQ) NI USB-6211 (National Instruments, Austin, Texas, USA). The DAQ was responsible for the modulation of the LED and the acquisition and transference of the detected signal to a personal computer (PC). A digital lock-in amplification was used for processing the raw data, increasing the signal-to-noise ratio and permitting the operation of the system in ambient light conditions without requiring any physical amplifier.

As explained in § 4.2.1.3, the detection system was designed to permit the easy exchange of both the LED and the photodiode, thus permitting the selection of the appropriate components for each specific application. In this particular case, a 340 nm LED MTE340-H32-UV from Marktech Optoelectronics (Latham, USA) and a Si photodiode S1337-66BR from Hamamatsu Photonics (Hamamatsu, Japan) were selected.

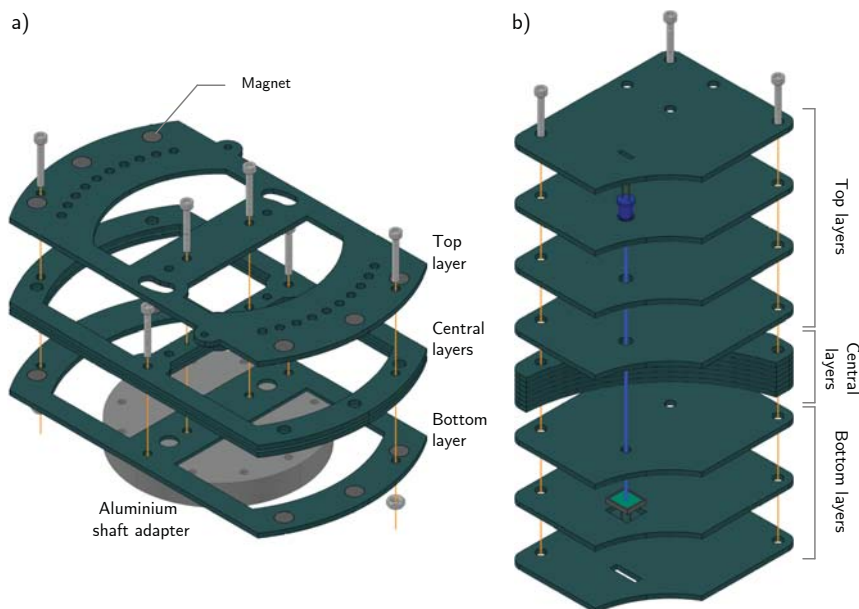


Figure 7.8: a) Support platform layers. The different layers were assembled together using several bolts and magnets; the four internal bolts secured the platform to the aluminium shaft adapter. b) PMMA structure of the optical detection system. The LED was embedded inside the top layers, whereas the photodiode was fixed into the bottom layers. The central layers permitted the free rotation of the support platform between the LED and the photodiode. Several bolts assembled the different layers and secured the structure to the setup.

7.5 Modular centrifugal microfluidic platform

As mentioned before, the purpose of the work presented in this chapter was the development of a modular centrifugal microfluidic system for the implementation of several parallel wine analyses in a single platform.

A centrifugal platform containing two different modules is here described. The modules were designed to perform an automated on-chip standard addition calibration for the enzymatic quantification of the analytes, where variable volumes of a standard solution were added to equal volumes of a sample. With that purpose, two different aliquoting subsystems were integrated in each device, one for splitting a sample volume into equal sub-volumes and the other for producing different volume aliquots from an initial standard solution. One sample aliquot and one standard aliquot were transferred into a common receiving chamber, thus producing a different final analyte concentration depending on the added standard volume.

7.5.1 Design and principle of operation

The design of the modules was based on previous aliquoting prototypes developed in the group. Part of the optimisation of the aliquoting structures was previously carried out in collaboration with other members of the group and it is described in detail in references [38] and [39].

The developed modules, which are schematically illustrated in Figure 7.9, contained two different aliquoting subsystems: a top subsystem for aliquoting variable volumes of standard and a bottom subsystem for aliquoting equal volumes of sample. Each subsystem consisted of an inlet reservoir and a series of metering chambers interconnected by a distribution channel. A common waste chamber was placed at the end of the distribution channels for collecting excess fluid from the metering process. The metering chambers were connected to the receiving chambers through narrow microchannels acting as hydrophobic valves. Each receiving chamber included a window for the addition of liquid or solid reagents (when required). These windows were sealed previous to the analyses by using adhesive plate seals. Each receiving chamber was also connected to an auxiliary inlet reservoir for the addition of liquid reagents once the windows were sealed.

The principle of operation of the aliquoting systems was based on a two-stage process where liquids were initially metered and were then transferred to the receiving chambers. As previously explained, two-stage aliquoting processes enable the aliquoting of liquids into completely independent chambers, thus avoiding any possible cross-contamination.

The two-stage aliquoting process relied on the use of narrow microchannels connecting the metering and the receiving chambers (see Figure 7.10). These microchannels were used as hydrophobic valves, being capable of retaining the fluids in the metering chambers during the metering phase and allowing the transfer of the metered volumes to the receiving chambers during the transfer phase.

The valving principle of hydrophobic valves is based on the retention of fluids at a hydrophobic barrier until the centrifugally-induced pressure (P_ω), resulting from the rotation of the platform, exceeds the capillary pressure (P_C), resulting from the surface tension of the fluid.⁴⁰ The rotational frequency at which these two pressures are balanced is known as the burst frequency (ω_b) and depends on several geometric parameters and on the properties of the involved fluids and surfaces.^{41,42} In the developed hydrophobic valves, the retention of fluids was achieved due to a sudden change in the dimensions of the microstructured features as well as to the hydrophobic nature of COC. Liquids were effectively stopped at the entrance of the microchannels without requiring any local surface modification or special coating.³⁸ For this application, microchannels of 75 μm in width and 30 μm in height were used, displaying a burst frequency of 1300 ± 100 rpm.

The two-stage aliquoting process is depicted in Figure 7.11. During the metering phase, the platform was spun at rotational frequencies below the burst frequency of the hydrophobic valves ($\omega_m < \omega_b$, $P_C > P_\omega$). At this stage, liquid flowed from the inlet

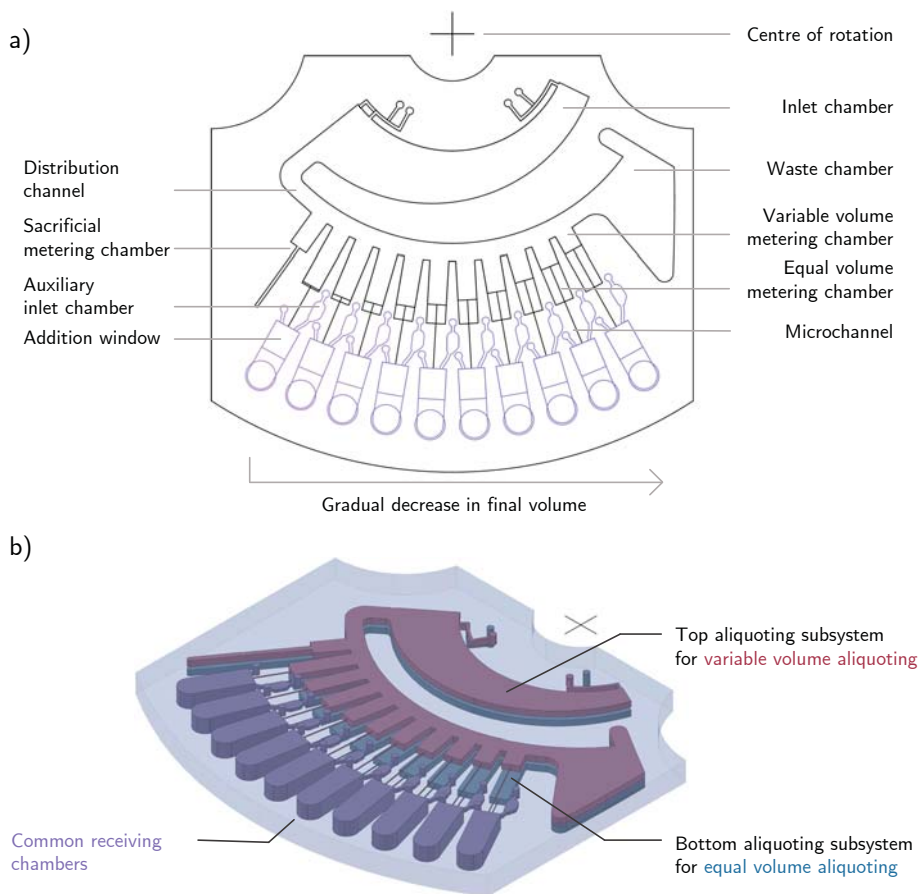


Figure 7.9: Schematic representation of the developed modules: a) 2D view and b) 3D view. To obtain a clear representation, some details of the receiving chambers have been omitted in the 3D view.

chamber to the metering chambers through the distribution channel; the chambers were sequentially filled and excess fluid overflowed into the waste chamber. During the transfer phase, the rotational frequency was increased above the burst frequency of the valves ($\omega_t > \omega_b$, $P_C < P_\omega$), thus allowing the transfer of the metered sub-volumes to the receiving chambers.

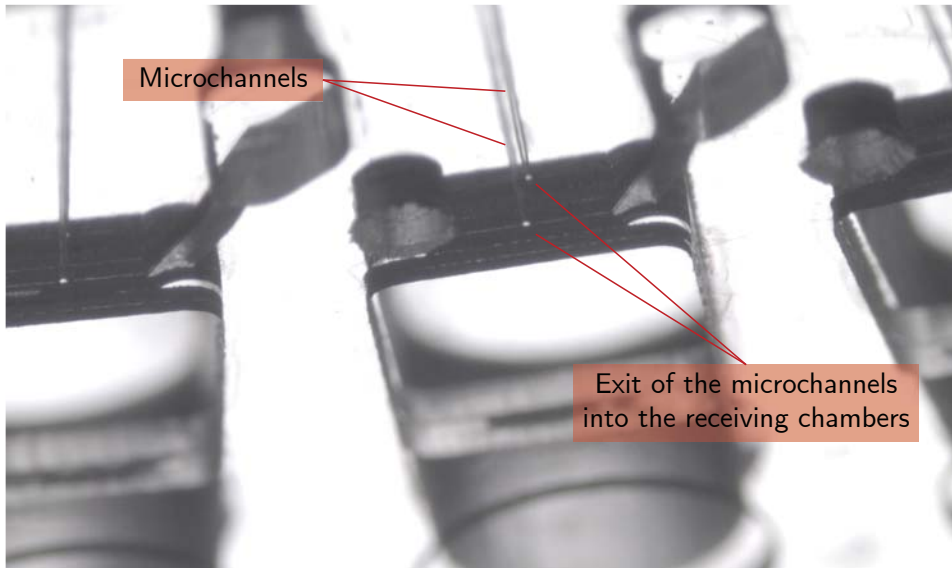


Figure 7.10: Microscopic image of the microchannels being used as hydrophobic valves.

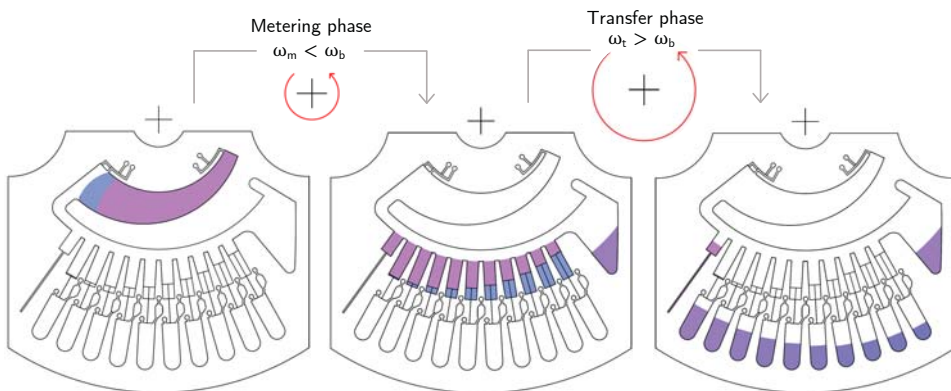


Figure 7.11: Two-stage aliquoting process. A first metering phase is carried out at a rotational frequency ω_m below the burst frequency of the hydrophobic valves (ω_b). The final transfer phase is carried out at a rotational frequency ω_t above ω_b . The different sample (pink) and standard (blue) aliquoted volumes produce a gradual decrease in the analyte concentration at the final volume (purple).

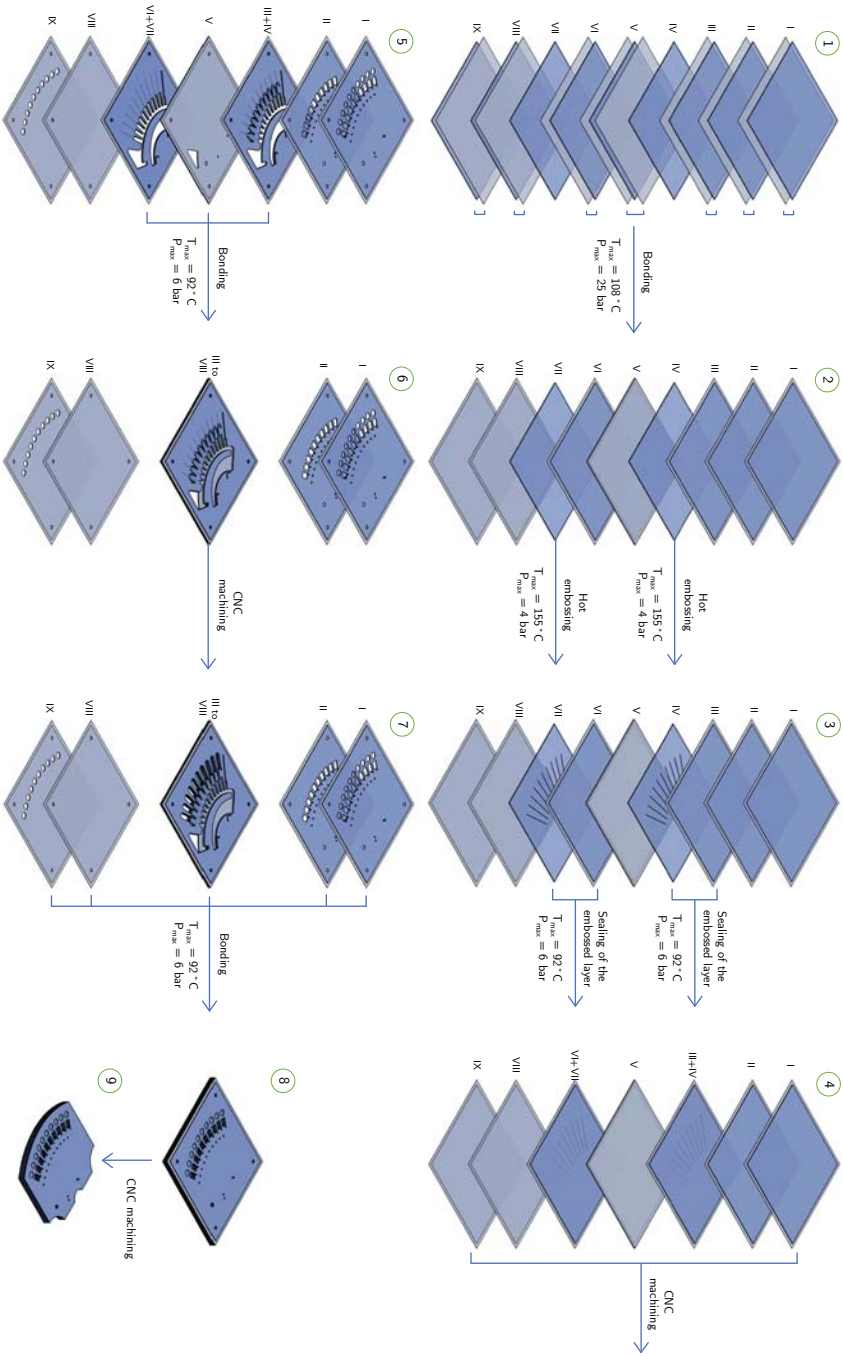


Figure 7.12: Fabrication scheme of the developed devices. TOPAS 8007 bonding layers and TOPAS 6013 structural layers are represented in grey and blue, respectively.

7.5.2 Construction

As explained in the previous section, the developed modules contained several microchannels of 75 μm in width and 30 μm in height. However, the minimum available milling tool for the CNC micromilling machine was 150 μm in diameter (milling tools of lower diameters would easily break). For such cases where the dimensions of the required features were unachievable using the micromilling equipment, we developed a hybrid fabrication method that combined hot embossing for the smallest structures and micromilling for the larger motifs.⁴³ In the proposed method, laser ablated LTCC masters were employed for the hot embossing of the features onto the COC layers. The fabrication of the LTCC masters as well as the hot embossing of the ablated features onto the COC layers are described in § 3.2.2.2.

The fabrication scheme of the devices used in this chapter is presented in [Figure 7.12](#). Each device was composed of eight 25 μm thick TOPAS 8007 bonding layers and nine TOPAS 6013 structural layers, four of them of 400 μm in thickness (I, II, VIII and IX in [Figure 7.12](#)) and five of 500 μm (III-VII).

In the first construction step, the TOPAS 8007 layers were bonded to the TOPAS 6013 layers I, II, III, V, VI, VIII and IX at $T_{\text{max}} = 108\text{ }^{\circ}\text{C}$ and $P_{\text{max}} = 25\text{ bar}$.

Next, ten microchannels arranged in a fan configuration were embossed onto the TOPAS 6013 layers IV and VII at $T_{\text{max}} = 155\text{ }^{\circ}\text{C}$ and $P_{\text{max}} = 4\text{ bar}$. In order to seal the embossed features, layers III and VI were bonded to layers IV and VII, respectively, at $T_{\text{max}} = 92\text{ }^{\circ}\text{C}$ and $P_{\text{max}} = 6\text{ bar}$.

The following step consisted in the individual CNC machining of all the layers using milling tools of 0.4 mm and 0.8 mm in diameter. After that, the central layers (III to VII) were bonded together at $T_{\text{max}} = 92\text{ }^{\circ}\text{C}$ and $P_{\text{max}} = 6\text{ bar}$. The central block was subsequently machined and, finally, all layers were bonded at $T_{\text{max}} = 92\text{ }^{\circ}\text{C}$ and $P_{\text{max}} = 6\text{ bar}$. A further CNC machining step was required to give the device the desired final shape using a milling tool of 2 mm in diameter.

The final dimensions of the device were 66 mm long \times 58 mm wide \times 4.1 mm thick, and its final total weight was of approximately 12 g. The optical path length (i.e. the height of the receiving chambers) was 2.5 mm.

Despite both micromilling and hot embossing are considered fast and simple microstructuring techniques,^{44,45} the construction of the devices here described was somewhat complex and time-consuming, since it involved a considerable number of layers and required several bonding, hot embossing and CNC machining steps. Besides, special attention had to be given to the construction steps involving the layers which contained the embossed microchannels. These steps had to be carefully executed and the conditions had to be precisely controlled in order to prevent the clogging of the channels. The importance of the optimisation of the construction process as well as the careful execution of the different steps for ensuring the proper operation of the final devices is discussed later on in this chapter.

7.6 Implementation of the L-lactic acid enzymatic determination into the developed centrifugal microfluidic platforms

The enzymatic method for the quantification of L-lactic acid involved the monitoring of absorbance at 340 nm for determining the NADH produced in the reactions from [Figure 7.6](#)). The feasibility of measuring these absorbance variations relied on several parameters such as: 1) the COC optical transparency at 340 nm, 2) the suitability of the selected LED and photodiode for the optical detection system and 3) the geometric constraints of both the device and the experimental setup itself.

As demonstrated in Chapter 5, COC allows the absorbance measurement at 340 nm due to its high transmittance in the near UV region of the spectrum.^{46–48} For the optical detection system, the same LED⁴⁹ and photodiode⁵⁰ as in the application presented in Chapter 5 were used. The peak wavelength of the LED was centred at 340 ± 5 nm.

In order to demonstrate the feasibility of using the developed setup for monitoring absorbance changes at 340 nm, the absorbance of several NADH standard solutions ranging from 0.025 mM to 1.0 mM was measured. Standards were prepared in TRIS 0.01 M (pH 8.5) and were directly injected into the receiving chambers through the addition windows. Absorbance was measured by the automatic and sequential positioning of the receiving chambers between the LED and the photodiode. Measurements were carried out in duplicate for each standard solution.

A linear range to up to 0.50 mM NADH was obtained, therefore limiting the analyte concentration at the final volume (i.e. at the receiving chamber) to a maximum of 0.50 mM for a 1:1 stoichiometry and a 100% conversion. For L-lactic acid, the analyte selected as proof-of-concept, the stoichiometry of the reactions was 1:1 (see [Figure 7.6](#)). However, the actual working range for the L-lactic acid determination had to be determined using the reagent kit.

This kit consisted of several reagent solutions (see [Table 7.1](#)), whose components were specified yet their concentration was not. Besides, although the linear range of the analysis was provided by the manufacturer, the conditions used for its determination were a 1 cm optical path cuvette in a spectrophotometer. Since the detection conditions using the developed system differed considerably from the recommended ones, the actual linear range of the analytical procedure had to be established by using our own setup.

All the on-chip analyses were performed by following the recommended procedure³⁷ (see [Table 7.1](#)). Nonetheless, in order to meet the volume requirements for the developed devices but maintaining the relative proportion between the different reagents, the kit solutions had to be occasionally diluted. The procedures followed for the on-chip analyses, including any modification of the recommended one, are specified for all the experiments performed.

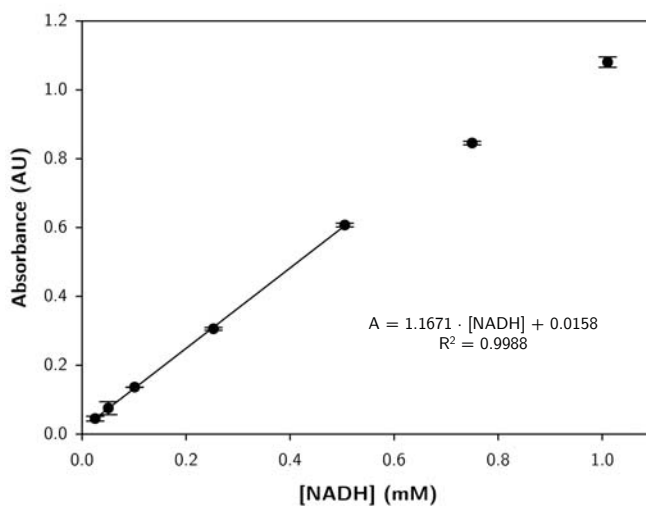


Figure 7.13: Linear working range for the absorbance measurement of NADH solutions at 340 nm using the developed setup. Error bars represent the standard deviation of two replicate measurements.

For the evaluation of the linear range, several L-lactic acid standard solutions from 0.015 mM to 0.763 mM, corresponding to 0.010 mM and 0.500 mM, respectively, at the final volume, were prepared. The solutions were analysed by mixing 1.5 mL of standard, 0.5 mL of Solution 1, 0.1 mL of Solution 2 and 0.02 mL of Suspension 3 in an Eppendorf tube for 3 minutes. Then, 50 μ L of the mixtures were injected into the receiving chambers through the addition windows and absorbance was measured in duplicate. These values corresponded to the absorbance of the blank, since the reaction was started once Suspension 4 was added to the mixture. After the blank measurement, Suspension 4 was diluted to 1:10 and 4 μ L of the dilution were injected into each receiving chamber through the addition windows. The windows were then sealed and the solutions were mixed[†] for 10 minutes. Finally, absorbance was measured in duplicate and the absorbance of the blank was subtracted from the obtained value.

Table 7.1: L-lactic acid (L-lactate) assay kit K-LATE 07/14 (Megazyme) reagents and recommended procedure.

Reagents	
Solution 1	Buffer (pH 10.0) plus D-glutamate and sodium azide (0.02% w/v)
Solution 2	NAD ⁺ and polyvinylpyrrolidone solution
Suspension 3	D-glutamate-pyruvate transaminase suspension
Suspension 4	L-lactate dehydrogenase suspension
Solution 5	L-lactic acid standard solution 0.15 mg/mL in 0.02% w/v sodium azide

Procedure		
Pipette into cuvettes:	Blank	Sample (/standard)
Distilled water (~25 °C)	1.60 mL	0.1 mL to 1.50 mL
Sample	-	1.5 mL to 0.1 mL
Solution 1	0.50 mL	0.50 mL
Solution 2	0.10 mL	0.10 mL
Suspension 3	0.02 mL	0.02 mL
Mix, read the absorbances of the solutions (A_0) after approximately 3 min and start the reactions by addition of:		
Suspension 4	0.02 mL	0.02 mL
Mix and read the absorbances of the solutions (A_1) at the end of the reaction (approx. 10 min). If the reaction has not stopped after 10 min, continue to read the absorbances at 5 min intervals until the absorbances either remain the same, or increase constantly over 5 min. Subtract A_0 from A_1 .		

† Shake mode mixing

One of the simplest methods for the efficient mixing of liquids in centrifugal microfluidic systems consists in the frequent alternation of the sense of rotation of the centrifugal platform in what is commonly known as shake mode mixing.⁵¹ By “shaking” the platform at high rotational frequencies, liquids are rapidly mixed as a result of the inertially induced liquid movement.^{52,53}

A linear range to up to 0.40 mM L-lactic acid at the final volume was established (see Figure 7.14). This information was required to select the appropriate standard concentrations to be used in the standard addition calibration.

Standard addition methods are based on the addition of known quantities of an analyte to a sample containing an unknown quantity of the same analyte. These methods

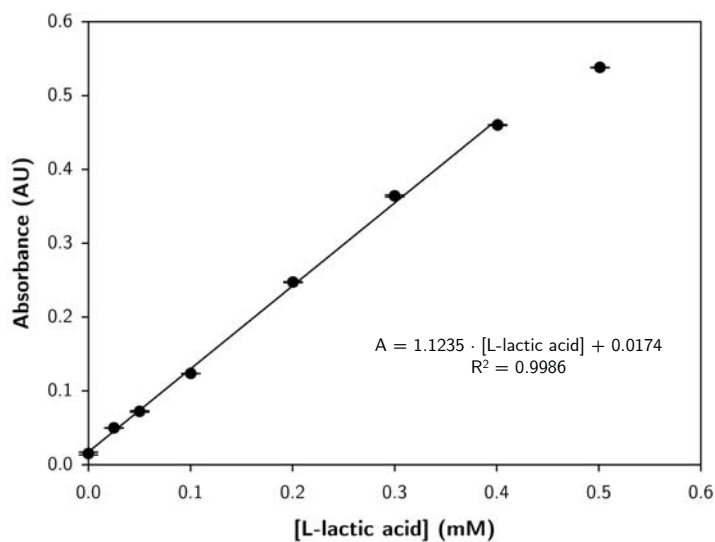


Figure 7.14: Linear working range of the L-lactic acid determination using the kit reagents and the developed setup. The L-lactic acid concentration here represented corresponds to the analyte concentration at the final volume. Error bars represent the standard deviation of two replicate measurements.

usually require a linear response of the signal to the analyte and are especially useful when the sample composition is unknown or complex and could affect the analytical signal.^{6,7}

Batch-mode standard additions are generally carried out by following two different procedures. The first consists in the sequential addition of small volumes of concentrated standard to a single unknown solution, being the signal measured after each of the additions. In the second case, multiple solutions containing increasing volumes of a standard solution and equal volumes of the unknown solution are prepared and diluted to the same final volume.

In the described procedures, the final volume remained constant or practically unaltered. On the other hand, in the developed devices, the procedure consisted in the addition of considerable amounts of standard to equal volumes of sample and reagents. Hence, the final volume at the receiving chambers appreciably differed between the different additions.

For a linear response of the signal to the analyte, where the signal is directly proportional to the analyte concentration, the next relationship can be established when a standard is added to a sample:

$$\frac{\text{Concentration of analyte in initial solution}}{\text{Concentration of analyte in final solution}} = \frac{\text{Signal from initial solution}}{\text{Signal from final solution}} \quad (7.1)$$

For an initial volume V_i with an unknown analyte concentration $[X]_i$ and an initial signal I_x , where a volume of standard V_s with a known analyte concentration $[S]_i$ is added, the previous relationship would be:

$$\frac{[X]_i}{[X]_f + [S]_f} = \frac{I_x}{I_{x+s}} \quad (7.2)$$

Where, for a total final volume of $V_f = V_i + V_s$, $[X]_f$ and $[S]_f$ would correspond to:

$$[X]_f = [X]_i \left(\frac{V_i}{V_f} \right), \quad [S]_f = [S]_i \left(\frac{V_s}{V_f} \right) \quad (7.3)$$

From substituting expressions from Equation 7.3 into Equation 7.2, and rearranging the resulting equation, the following linear relationship can be obtained:

$$I_{x+s} \left(\frac{V_f}{V_i} \right) = I_x + \frac{I_x}{[X]_i} [S]_i \left(\frac{V_s}{V_i} \right) \quad (7.4)$$

Where, when $I_{x+s} \left(\frac{V_f}{V_i} \right)$ is plotted against $[S]_i \left(\frac{V_s}{V_i} \right)$, the x-intercept corresponds to $[X]_i$. However, since the initial solution contains a certain volume of reagents, the analyte concentration in the sample $[X]_0$ is:

$$[X]_0 = [X]_i \left(\frac{V_i}{V_0} \right) \quad (7.5)$$

Where V_i corresponds to the sum of the sample volume V_0 and the reagents volume V_R .

Before performing the on-chip standard addition calibrations, sample and added standard volumes were experimentally calculated by measuring the aliquoted volumes at the receiving chambers. The measurements were carried out by aliquoting an input water volume using the equal volume or the variable volume aliquoting subsystems at a time. Microscopic images of the receiving chambers were taken and volumes were calculated by measuring the area occupied by the liquid and multiplying it by the estimated height of the chamber (2.5 mm). The experiment was carried out in quintuplicate for each aliquoting subsystem. The results of these experiments are summarised in Table 7.2.

Once the experimental aliquoted volumes were measured, several on-chip standard addition calibrations were performed. Based on the previous experiment, where a maximum analyte concentration of 0.40 mM at the final volume was established, a

Table 7.2: Measured volumes for the aliquoting of water by using the equal volume and the variable volume aliquoting subsystems. Volumes correspond to the average value of five experiment replicates.

Equal volume aliquoting subsystem		
	Aliquoted volume (μL)	RSD (%)
	22.2	1.9
Variable volume aliquoting subsystem		
Chamber	Aliquoted volume (μL)	RSD (%)
1	17.2	3.6
2	15.8	4.5
3	14.1	4.5
4	12.8	1.6
5	11.4	3.1
6	10.5	1.4
7	9.3	2.7
8	8.6	2.1
9	7.7	1.4
10	6.3	6.0

0.10 mM L-lactic acid solution was selected as the model sample, whereas 1.00 mM and 0.50 mM L-lactic acid solutions were used as the added standards (the latter was solely used in one of the experiments). The values of the variables from Equation 7.2 to Equation 7.5 are presented in Table 7.3.

The procedure started with the injection of 270 μL of sample solution and 240 μL of standard solution into the inlet reservoirs of the equal volume aliquoting subsystem and the variable volume aliquoting subsystem, respectively. Then, 15.2 μL aliquots of a reagent mixture containing 500 μL of Solution 1, 100 μL of Solution 2 and 20 μL of Suspension 3 were injected into each receiving chamber through the addition windows, which were subsequently sealed using adhesive plate seals. Sample and standard volumes were then metered by rotating the platform at 900 rpm for 30 seconds. Next, the platform was spun at 5000 rpm for 30 seconds to transfer the aliquots to the receiving chambers, where they were mixed for 3 minutes with the reagent mixture previously injected. Absorbance was measured twice for each receiving chamber. The measured values corresponded to the blank of each receiving chamber and were later subtracted from the corresponding final absorbance. Afterwards, 4 μL of Suspension 4 diluted to 1:10 were injected into each receiving chamber through the auxiliary inlet reservoirs. Reagent 4 was sent from the auxiliary inlet chambers to the receiving chambers at 2000 rpm for 10 s and the platform was then shaken for 10 minutes to mix the solutions. Finally, absorbance was measured twice for each receiving chamber and the absorbance of the blank was subtracted from the obtained average value.

Table 7.3: Volumes and concentrations used for the on-chip standard addition calibrations. L-lactic acid concentrations at the final volume are also indicated for the two standard solutions used.

Sample volume V_0 (μL)	22.2										
Analyte conc. at V_0 $[X]_0$ (mM)	0.10										
Reagent volume V_R (μL)	19.2										
Initial volume V_i (μL)	41.4										
Analyte conc. at V_i $[X]_i$ (mM)	0.054										
Chamber	1	2	3	4	5	6	7	8	9	10	
Added standard volume V_S (mL)	17.2	15.8	14.1	12.8	11.4	10.5	9.3	8.6	7.7	6.3	
Final volume V_f (mL)	58.6	57.2	55.5	54.2	52.8	51.9	50.7	50.0	49.1	47.7	
Conc. of the standard (at V_S) $[S]_{i,1}$ (mM)	1.00										
Added analyte conc. (at V_f) $[S]_{f,1}$ (mM)	0.294	0.276	0.254	0.236	0.216	0.202	0.183	0.172	0.157	0.132	
Total analyte conc. (at V_f) $[X]_f + [S]_{f,1}$ (mM)	0.331	0.315	0.294	0.277	0.258	0.245	0.227	0.216	0.202	0.179	
Conc. of the standard (at V_S) $[S]_{i,2}$ (mM)	0.50										
Added analyte conc. (at V_f) $[S]_{f,2}$ (mM)	0.147	0.138	0.127	0.118	0.108	0.101	0.092	0.086	0.078	0.066	
Total analyte conc. (at V_f) $[X]_f + [S]_{f,2}$ (mM)	0.185	0.177	0.167	0.159	0.150	0.144	0.136	0.130	0.124	0.113	

$I_{X+S} \left(\frac{V_f}{V_i} \right)$ was plotted against $[S]_i \left(\frac{V_S}{V_i} \right)$ and the analyte concentration in the sample was calculated. The standard addition calibration plots are shown in [Figure 7.15](#), while the linear regression parameters and the calculated analyte concentrations can be found in [Table 7.4](#).

Table 7.4: Linear regression parameters of the calibration plots from [Figure 7.15](#) and the corresponding extrapolated concentrations of L-lactic acid.

Replicate	Slope	Intercept	R^2	$[X]_{0, \text{calc}}$ (mM)
a	1.7 ± 0.1	0.10 ± 0.03	0.9906	0.11 ± 0.03
b	1.5 ± 0.2	0.10 ± 0.05	0.9747	0.13 ± 0.04
c	1.55 ± 0.06	0.09 ± 0.02	0.9979	0.11 ± 0.01
d	1.5 ± 0.1	0.08 ± 0.04	0.9832	0.10 ± 0.03
e	1.44 ± 0.07	0.07 ± 0.02	0.9949	0.09 ± 0.02
f	1.6 ± 0.1	0.09 ± 0.02	0.9915	0.10 ± 0.02

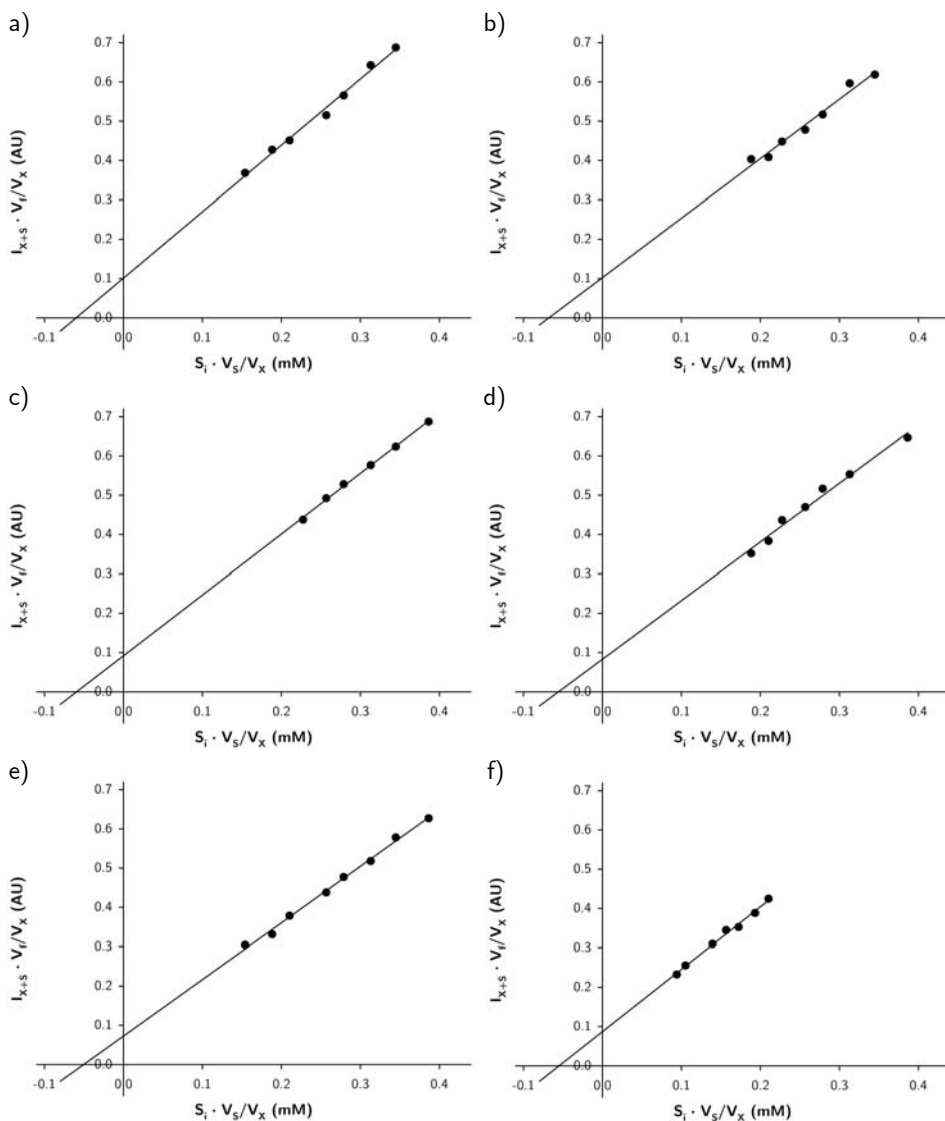


Figure 7.15: Standard addition calibration plots for the six on-chip L-lactic acid enzymatic determinations. The concentration of the standard solution added to the sample was 1.00 mM for replicates (a) to (e) and 0.50 mM for replicate (f).

The precision of the method was significantly poor, as can be noticed by the broad confidence intervals obtained for the slope and the intercept of the regression curves.

Besides, despite the calculated L-lactic acid concentration in the sample did not present a statistically significant difference with respect to the theoretical value (i.e. the concentration of the model sample, which was 0.15 mM) for any of the replicates at 95% confidence level, the confidence limits were considerably wide. Only in one of the six replicates the extrapolated concentration showed a confidence interval under the 10% of the average value.

The obtained results would, therefore, seem to be relatively unsatisfactory. However, they were considered a promising starting point owing to the large number of factors introducing variability to the system. These factors are discussed hereafter.

- Limited reproducibility of the construction process due to the high complexity of the devices

The complexity of a construction process is generally related to the number of layers required, the number of steps to be performed and/or the complexity of the internal structures to be either machined or created by the stacking of the different layers. In this particular case, we were facing a construction process which met all the characteristics to be highly complex: each module was composed by seventeen different COC layers (nine structural layers and eight bonding layers) and its manufacturing process involved two hot embossing steps, seven bonding steps and the CNC machining of eleven different layers/blocks. Additionally, the modules included several narrow microchannels which had to be precisely embedded into the structure and which were susceptible to collapse during the construction process (see [Figure 7.16](#)).

As a consequence, the constructed prototypes occasionally suffered from diverse flaws, which could include:

- Significant variations in the burst frequency of the valves due to differences on the final dimensions of the channels. This size variability could be a consequence of several factors related to the thermocompression conditions during hot embossing and bonding processes. Slight deviations in the applied temperature and/or pressure could lead to an inaccurate embossing of the master features, an incomplete sealing of the microchannels or a partial or total collapse of the embossed channels.
- Possible clogging of the microchannels during the CNC micromilling steps as a result of the introduction of expelled material (chips) inside the channels or the melting of the material due to frictional forces between the tool and the substrate.
- Slight variability of the metered volumes due to minor misalignments of the layers during the micromilling steps or the bending of the structural layers at the metering chambers during the bonding processes.
- Differences in the optical path length (i.e. in the height of the receiving chambers) as a consequence of the deformation of the outer structural layers during the last bonding step.

The complexity of the construction process limited its reproducibility, therefore compromising the quality of the results. Besides, slight variations could not only occur between devices but also in a single prototype containing twenty microchannels, twenty metering chambers and ten receiving chambers.

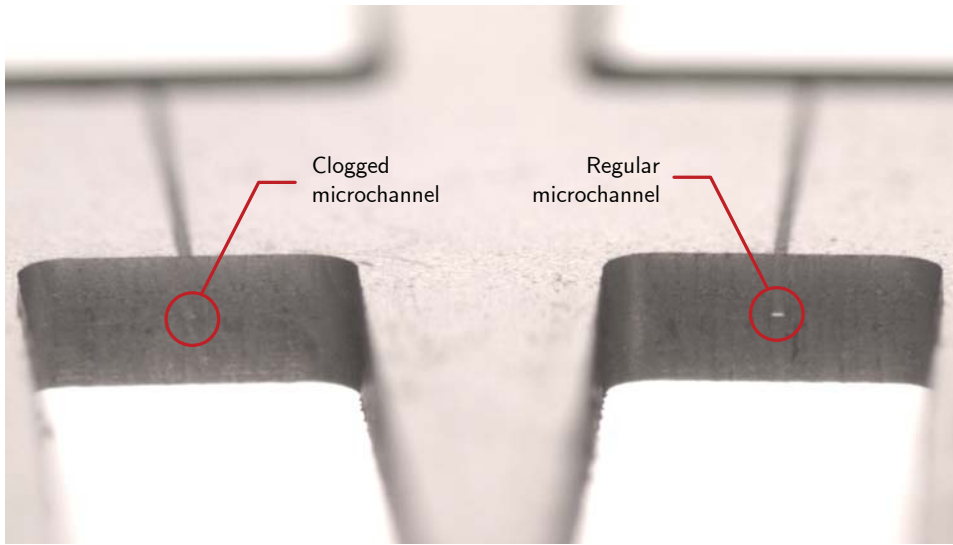


Figure 7.16: Microscopic image of two microchannels. The one in the left is completely clogged, whereas the one in the right is properly sealed.

Some of the aforementioned problems were easily detected and could be efficiently corrected or, at least, minimised. For example, the bending of the outer layers at the receiving chambers was prevented by using micromachined Delrin sacrificial layers (see § 3.2.3). On the other hand, the occurrence of some other construction imperfections depended on the ability and the accuracy of the doer (e.g. the positioning of the layers onto the CNC micromilling machine) or were difficult to further control or predict (e.g. the collapse of the microchannels during the bonding processes).

The different problems occurring during the construction of the modules were mainly related to the high accuracy required for their final proper functioning, which was barely unattainable by using a construction process where human intervention played such an important role. Hence, most of these problems could be easily circumvented by the automation of the construction process and the use of alternative construction techniques (e.g. injection moulding^{54,55}). This way, human intervention would be minimised, thus reducing the complexity and increasing the reproducibility of the process. Besides, the automation of the construction process would lead to a drastic reduction of the manufacturing time

(an additional handicap which is introduced hereafter). Notwithstanding, the automation of the construction processes at the prototyping scale is generally not economically worthy and it is usually restrained to the mass production of the devices once they have been already optimised.

Although its limited reproducibility, the construction process described in this chapter permitted the development of operational prototypes which could be used for the conceptual and functional validation of the new fluidic structures.

- Reuse of the devices

The construction process used for the development of the devices was considerably laborious and time-consuming in comparison to all other devices presented in this dissertation. As a consequence, although the modules were designed to be disposable, they were frequently reused. After each experiment, the devices were thoroughly cleaned using MilliQ water and ethanol and were dried in an oven at 40 °C for approximately 48 h.

As a result of the reuse, the devices progressively showed degradation symptoms. For example, the transparency of the material became gradually compromised, hampering the measurement of the absorbance at the receiving chambers. Besides, the variability between the burst frequency of the valves increased over time, generally being a consequence of the total or partial obturation of the channels.

It is worth mentioning that even though these issues were affecting the study of the system, they were not expected to hinder the final application of the devices which, as previously mentioned, were intended to be disposable.

- Irreproducible transfer of Suspension 4 from the auxiliary inlet chambers to the receiving chambers

One of the main factors affecting the analyses was found to be the low reproducibility of the addition of Suspension 4 to the reaction mixture. The suspension was easily and accurately injected into the auxiliary inlet reservoirs of the receiving chambers. However, when the rotation of the platform decreased after its transfer to the receiving chambers, part of the liquid occasionally returned to the auxiliary inlet reservoir. This effect was probably due to the surface tension of the solution and the resulting capillary forces.^{56,57} Since liquid returned before the solutions had been properly mixed, it was not possible to know the composition of the returned liquid nor predict its effect on the analysis results. A strong relationship could be noticed between the results differing the most from the expected ones and the auxiliary inlet reservoirs where a considerable amount of liquid could be found at the end of the experiment.

- Limited reproducibility of the alignment of the receiving chambers with respect to the LED and the photodiode

The absorbance measurements were affected by several parameters concerning the alignment of the detection areas between the LED and the photodiode. Slight variations on the positioning of the devices inside the modular platform as well as small differences on the collocation of the platform layers led to a slight variability of the measured absorbance. Besides, in spite of the high accuracy of the motor movement, slight variations of the absorbance values could be noticed between different measurement replicates. The parameters which were most significantly affecting the movement of the motor were identified and optimised, including the acceleration and deceleration rates and the rotational speed between steps, among others.

- Intrinsic problems of the standard addition method being applied

Standard addition methods assume that the effect of adding a standard to a sample matrix is not significant and that therefore matrixes can be considered identical.⁵⁸ When several solutions containing the same volume of sample and increasing volumes of standard are prepared and diluted to the same final volume, this assumption is valid. For the addition of small volumes of standard to a sample, the effect of the addition to the sample matrix can be generally neglected. Nonetheless, in the developed devices, the amount of standard being added to the sample was significant and, despite the dilution factor was considered for the calculation of the analyte concentration, the effect of the matrix dilution could have other implications that were not being contemplated.

Standard addition calibrations are considered to degrade the precision when compared to ordinary calibrations since extrapolation methods are estimated to be more affected to variations than interpolation methods.⁵⁹⁻⁶¹ However, it has been demonstrated that the uncertainty in the extrapolated value derives only from the random errors of the regression line itself⁶² and that the precision of the method can be improved by the appropriate selection of the number and concentration of the standard additions^{61,63}. In order to maximise the precision of a standard addition calibration, the concentration of the added analyte is recommended to be as high as it is consistent with the linearity of the method and, ideally, at least five times the original concentration.⁶³ In the developed devices, the highest added concentration led to a final concentration of 0.331 mM, which corresponded to more than six times the initial concentration ($[X]_i = 0.054$ mM.) However, we were not measuring the signal corresponding to this initial concentration but the one after the first standard addition, where the total analyte concentration was 0.179 mM. The ratio between these two added concentrations was far away from the ideal factor ($0.331/0.179 = 1.8 < 5$). All added concentrations were, actually, excessively close (since the added standard volumes were excessively similar) and far away from the extrapolated value, thus compromising the precision of the method. On the other hand, for a certain number of calibration points m , the use of n clusters of data of m/n points each has been demonstrated to yield a

better precision than the use of m data points equally distributed along the calibration line.^{61–63} In our case, not only the data points were gathered in a narrow zone of the linear range but also were equally distributed along this zone with no replicate for any of the added volumes.

Owing to all the potential problems that could occur during the construction process of the devices as well as during the analyses, the results obtained for the quantification of the L-lactic acid content of a model sample were considered not only positive but also a promising initial approach.

A first attempt for the quantification of the L-lactic acid content of a commercial red wine was carried out by using the developed prototypes. The result was compared to the one obtained by using the procedure described in the kit brochure (see Table 7.1) and a spectrophotometer equipped with a 1 cm optical path cuvette. The sample was diluted to 1:50 previous to the analyses.

For the on-chip standard addition method, 270 μL of the sample and 240 μL of a 1.0 mM standard solution were injected into the inlet reservoirs of the equal volume aliquoting subsystem and the variable volume aliquoting subsystem, respectively. Then, 15.2 μL aliquots of a reagent mixture containing 500 μL of Solution 1, 100 μL of Solution 2 and 20 μL of Suspension 3 were injected into each receiving chamber through the addition windows, which were subsequently sealed using adhesive plate seals. Sample and standard volumes were then metered and transferred to the receiving chambers at 900 rpm for 30 seconds and 5000 rpm for 30 seconds, respectively. The solutions were mixed for 3 minutes and absorbance was measured twice for each receiving chamber. These values corresponded to the blank of each receiving chamber and were later subtracted from the final absorbance value. Afterwards, 4 μL of Suspension 4 diluted to 1:10 were injected into the auxiliary inlet reservoirs and were transferred to the receiving chambers at 2000 rpm for 10 s. The solutions were mixed for 10 minutes and absorbance was measured twice for each receiving chamber. The absorbance of the blank was subtracted from the average value obtained, $I_{X+S} \left(\frac{V_f}{V_i} \right)$ was plotted against $[S]_i \left(\frac{V_s}{V_i} \right)$ and the analyte concentration in the sample was calculated by extrapolation.

The calibration curves for the on-chip standard addition as well as for the calibration by using the spectrophotometer can be found in Figure 7.17 and Figure 7.18, respectively. The linear regression parameters and the calculated analyte concentrations are summarised in Table 7.5.

Table 7.5: Linear regression parameters and calculated L-lactic acid concentration for the two different procedures.

Method	Slope	Intercept	R ²	[X] _{0, calc} (mM)
On-chip standard addition	1.17 ± 0.09	0.11 ± 0.02	0.9854	0.17 ± 0.02
Calibration using the recommended procedure	4.4 ± 0.1	0.01 ± 0.02	0.9996	0.157 ± 0.003

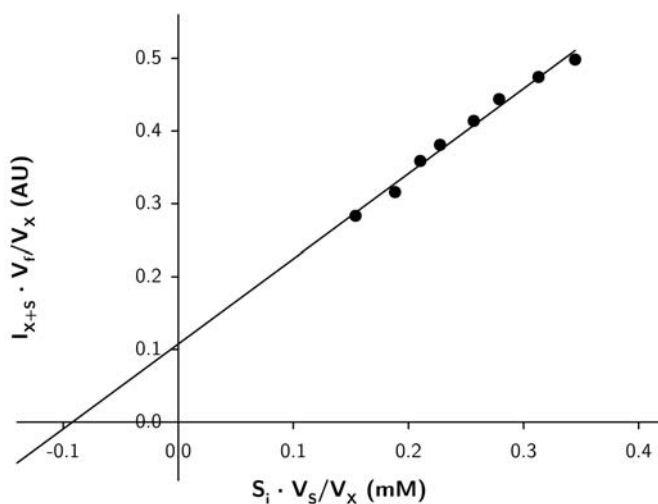


Figure 7.17: On-chip standard addition calibration for the determination of the L-lactic acid content of a commercial wine sample.

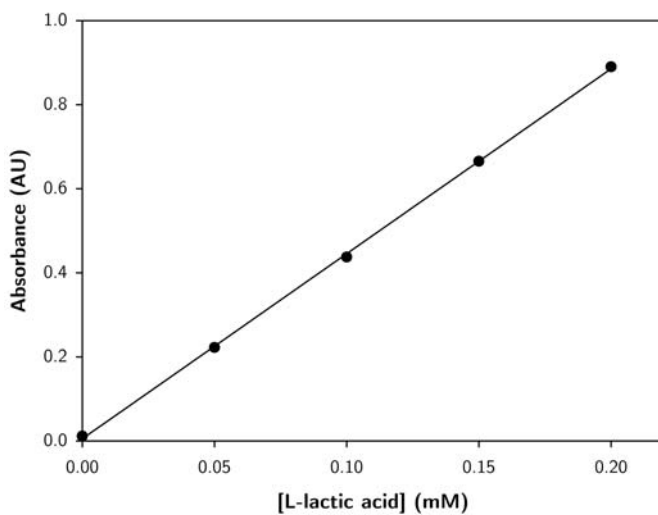


Figure 7.18: Calibration for the determination of the L-lactic acid content of a commercial wine sample using the procedure described by the kit manufacturer.

Although the precision of the on-chip standard addition method was considerably lower than the one of the classic interpolation method, the calculated L-lactic acid concentration in the diluted wine sample did not present a statistically significant difference for a 95% confidence level.

After this promising first result obtained for the determination of the L-lactic acid content of a commercial wine sample, several modifications were introduced to the design of the modules in order to solve some of the issues described before. These changes, which are depicted in Figure 7.19, were mainly applied to the variable volume aliquoting subsystem and were aimed at the improvement of the precision of the method and the minimisation of the possible effect of the matrix dilution.

In order to improve the precision of the method, the size and number of the metering chambers was modified for obtaining three replicates of each added volume (instead of ten different added volumes). Besides, three metering chambers were eliminated for measuring the signal of the initial solution (no standard being added). The relative difference between the added volumes was also increased, being the second addition approximately the double of the first one. Furthermore, the added standard volumes were reduced in order to diminish the dilution of the sample at the final volume and, therefore, minimise the effect of the matrix dilution.

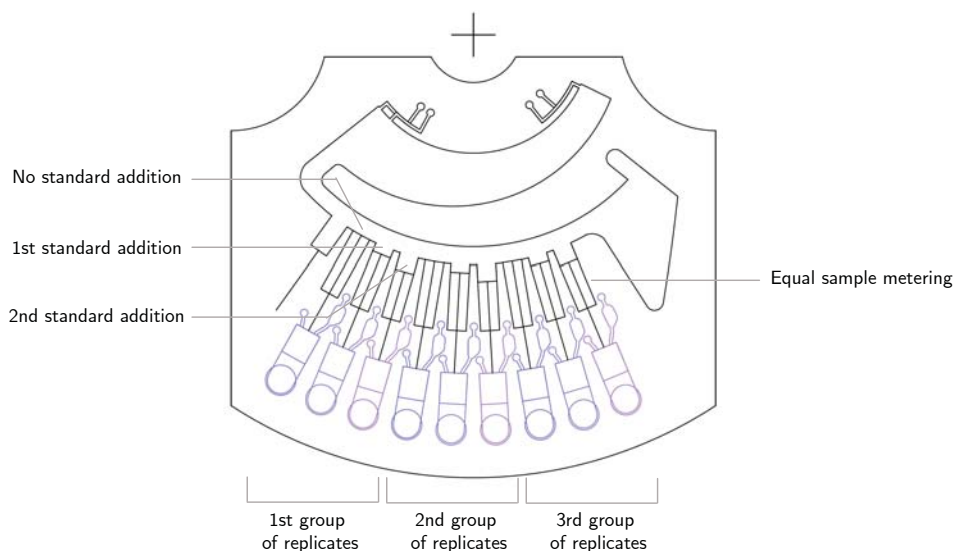


Figure 7.19: New design of the modules for increasing the precision of the method and minimising the effect of the matrix dilution.

The added volumes for the newly constructed prototypes were experimentally calculated by following the previously described method consisting in the determination of the aliquoted volumes at the receiving chambers by using microscopic images. For these

prototypes, aliquoted volumes of both subsystems were measured at the same time; volumes added through the variable aliquoting system were calculated by subtracting the average volume obtained for the "no addition" measurements. The experiment was carried out in triplicate. The obtained results are summarised in [Table 7.6](#).

Table 7.6: Measured volumes for the aliquoting of water by using the equal volume and the variable volume aliquoting subsystems. Volumes correspond to the average value of three experiment replicates.

Chambers	Total volume (μL)	RSD (%)	Added volume (μL)
1, 4, 7	23.4	2.2	0.0
2, 5, 8	26.9	3.1	3.5
3, 6, 9	29.5	3.4	6.1

Several on-chip standard additions were performed using the new prototypes. Based on the linear range of the L-lactic acid determination using the kit reagents and our setup, a 0.15 mM L-lactic acid solution was selected as the model sample, whereas 3.00 mM and 2.00 mM solutions were used as the added standards (the latter was solely used for two of the experiments). The values of the variables from [Equation 7.2](#) to [Equation 7.5](#) are presented in [Table 7.7](#).

Table 7.7: Volumes and concentrations used for the on-chip standard addition calibrations using the new prototypes. L-lactic acid concentrations at the final volume are also indicated for the two standard solutions used.

Sample volume	V_0 (μL)	23.4		
Analyte conc. at V_0	$[X]_0$ (mM)	0.15		
Reagent volume	V_R (μL)	24.5		
Initial volume	V_i (μL)	47.9		
Analyte conc. at V_i	$[X]_i$ (mM)	54		
Chambers		1, 4, 7	2, 5, 8	3, 6, 9
Standard volume	V_S (μL)	0	3.5	6.1
Final volume	V_f (μL)	58.6	57.2	55.5
Conc. of the standard (at V_S)	$[S]_{i,1}$ (mM)		3.00	
Added analyte conc. (at V_f)	$[S]_{f,1}$ (mM)	0	204	339
Total analyte conc. (at V_f)	$[X]_f + [S]_{f,1}$ (mM)	73	273	404
Conc. of the standard (at V_S)	$[S]_{i,2}$ (mM)		2.00	
Added analyte conc. (at V_f)	$[S]_{f,2}$ (mM)	0	136	226
Total analyte conc. (at V_f)	$[X]_f + [S]_{f,2}$ (mM)	73	204	291

The procedure started with the injection of 270 μL of sample solution and 70 μL of standard solution into the inlet reservoirs of the equal volume aliquoting subsystem

and the variable volume aliquoting subsystem, respectively. Then, 20 μL aliquots of a reagent mixture containing 250 μL of Solution 1, 52 μL of Solution 2, 10 μL of Suspension 3 and 188 μL of water were injected into each receiving chamber through the addition windows, which were subsequently sealed. Sample and standard volumes were then metered and transferred to the receiving chambers at 900 rpm for 30 seconds and 5000 rpm for 30 seconds, respectively. The solutions were mixed for 3 minutes and absorbance was measured twice for each receiving chamber. These values corresponded to the blank and were subtracted from the final absorbance. Afterwards, 4.5 μL of Suspension 4 diluted to 1:10 were injected into the auxiliary inlet reservoirs and were transferred to the receiving chambers at 2000 rpm for 10 s. The solutions were mixed for 10 minutes and absorbance was measured twice for each receiving chamber. The absorbance of the blank was subtracted from the average value obtained, $I_{X+S} \left(\frac{V_f}{V_i} \right)$ was plotted against $[S]_i \left(\frac{V_s}{V_i} \right)$ and the analyte concentration in the sample was calculated by extrapolation. Eight standard addition calibrations were performed. The corresponding plots can be found in Figure 7.20. The linear regression parameters and the calculated analyte concentrations are summarised in Table 7.8.

Table 7.8: Linear regression parameters of the calibration plots from Figure 7.20 and the corresponding extrapolated concentrations of L-lactic acid.

Replicate	Slope	Intercept	R ²	[X] _{0, calc} (mM)
a	1.5 ± 0.2	0.18 ± 0.05	0.9773	0.25 ± 0.09
b	1.5 ± 0.2	0.11 ± 0.05	0.9815	0.15 ± 0.08
c	1.1 ± 0.2	0.12 ± 0.05	0.9585	0.2 ± 0.1
d	1.5 ± 0.1	0.16 ± 0.03	0.9925	0.21 ± 0.06
e	1.2 ± 0.1	0.08 ± 0.03	0.9897	0.13 ± 0.05
f	1.2 ± 0.2	0.12 ± 0.04	0.9809	0.21 ± 0.07
g	1.4 ± 0.2	0.13 ± 0.04	0.9775	0.18 ± 0.06
h	1.3 ± 0.4	0.14 ± 0.07	0.9015	0.2 ± 0.1

The obtained results showed an unexpected variability in addition to a noticeable low precision. Despite no statistically significant differences were found between most of the calculated concentrations and the concentration of the model sample solution (0.15 mM), the calculated confidence intervals were considerably wide.

In general, the quality of the results obtained with the new prototypes was lower than the one of the previous ones. This fact seemed to be mainly related to a poorer distribution of the initial standard volume during the metering phase, where excess liquid did not completely overflow to the waste chamber. A thin liquid film connecting all the metering chambers could be usually observed in the distribution channel. This excess liquid strongly affected the metered volumes and their later transfer to the receiving chambers, where higher volumes than the expected ones could be noticed at the end of the experiments, especially in those receiving chambers where no standard

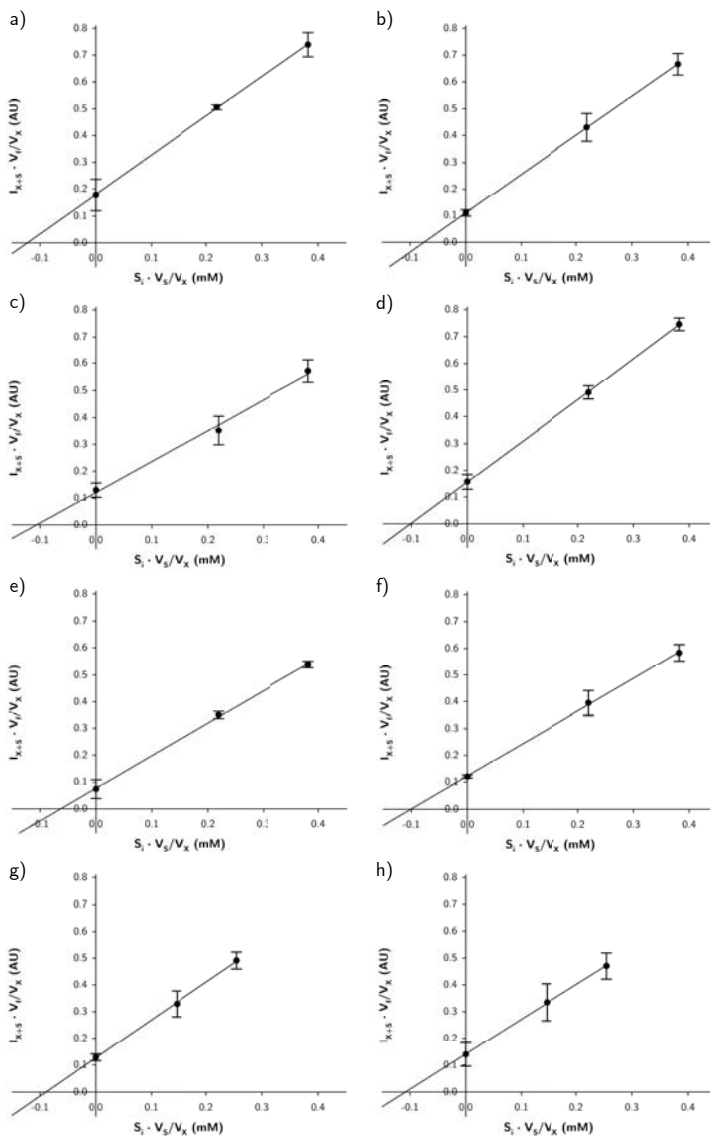


Figure 7.20: Standard addition calibration plots for the eight on-chip L-lactic acid enzymatic determinations using the new prototypes. The concentration of the standard solution added to the sample was 3.00 mM for replicates (a) to (f) and 2.00 mM for replicates (g) and (h). Error bars represent the standard deviation ($n = 3$).

must be added. Although no metering chamber was machined for the "zero addition" of standard, the microchannel that connected the distribution channel to the receiving chamber was still present. As a consequence, excess liquid remaining in the distribution channel after the metering phase could reach all receiving chambers, including the "zero addition" ones, during the transfer phase. Since it was not possible to predict the amount of extra standard added to each receiving chamber, it was difficult to elucidate its effect on the analyte concentration at the final solution.

The poorer distribution of the standard solution using the new prototypes (in comparison to using the previous ones) was thought to be caused by the modifications applied to the design. Unfortunately, the variability of the metered volumes had a stronger impact on these new devices, where the added volumes were considerably lower.

The improper distribution of liquids was not noticed for the experiments where the aliquoted volumes were being measured (see Table 7.6), since those tests were performed using water. Therefore, the properties of the solutions, specially the surface tension, were probably affecting the metering process.

New modular designs introducing some modifications for the distribution of liquids as well as including only one replicate per device (see Figure 7.21) are now under study in order to improve and optimise the aliquoting process. These new modules reduce the construction time and the complexity of the construction process. Aliquoted volumes are now being measured using solutions with different surface tension properties.

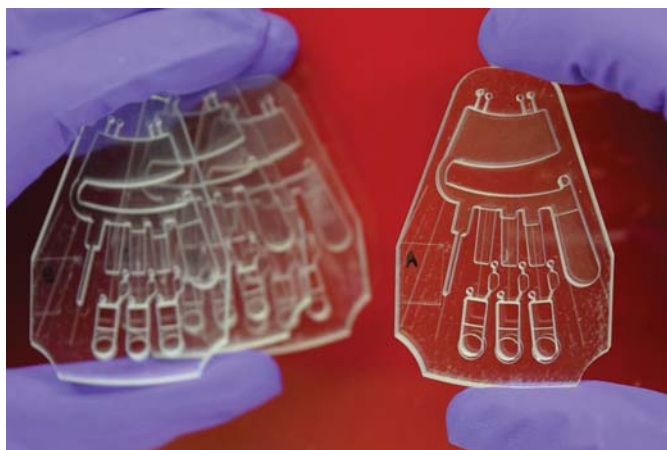


Figure 7.21: Latest developed prototypes for the L-lactic acid enzymatic determination.

7.7 Conclusions & future remarks

In this chapter, the development of a modular centrifugal microfluidic platform for the parallel analysis of several wine parameters has been presented. The centrifugal platform comprised two identical devices which were designed for performing an on-chip standard addition calibration. Each device included two aliquoting subsystems, one for the aliquoting of a sample into equal sub-volumes and the other for the aliquoting of a standard solution into variable sub-volumes.

The developed modules demonstrated an excellent performance on the aliquoting of water. However, the results for the L-lactic acid determination using a standard addition calibration showed low accuracy as well as a considerable irreproducibility. Notwithstanding, these initial results were considered a promising starting point for achieving the main goal of this work.

The different factors which could potentially affect the quality of the results have been successfully identified. At this point, some modifications have been introduced in order to simplify the design and the construction process of the microfluidic platforms. These modifications have not yet produced a substantial improvement of the results, yet it is expected to achieve a completely functional device after the optimisation of the structures. A further study of some variables affecting these devices is still pendant. Improvements in the microfluidic platform design as well as in the analytical procedure are still to be performed, such as the elimination of the microchannel for the "zero addition" or the optimisation of the operational conditions for the addition of the reagents.

Once the platform has been optimised, it will be applied not only for the L-lactic acid quantification in wine samples but for the determination of several other wine parameters which can be quantified by enzymatic methods using spectrophotometric detection.

References

- (1) *Compendium of International Methods of Wine and Must Analysis*; International Organisation of Vine and Wine: Paris, France, 2018.
- (2) *Official Methods of Analysis of AOAC INTERNATIONAL*, 18th; Horwitz, W., Latimer, G. W., Eds.; AOAC INTERNATIONAL: Gaithersburg, MD, USA, 2010.
- (3) Jacobson, J. L., *Introduction to Wine Laboratory Practices and Procedures*; Springer: New York, NY, USA, 2006, p 375.
- (4) Ough, C. S.; Amerine, M. A., *Methods for analysis of musts and wines*, 2nd; John Wiley & Sons, Ltd: New York, NY, USA, 1988, p 377.
- (5) Mross, S.; Pierrat, S.; Zimmermann, T.; Kraft, M. Microfluidic enzymatic biosensing systems: A review. *Biosensors and Bioelectronics* **2015**, *70*, 376–391.
- (6) Kościelniak, P.; Wieczorek, M.; Kozak, J.; Herman, M. Generalized Calibration Strategy in Analytical Chemistry. *Analytical Letters* **2011**, *44*, 411–430.
- (7) Harris, D. C., *Quantitative Chemical Analysis*, 7th; W. H. Freeman and Company: New York, NY, USA, 2007.
- (8) Pundir, C. S.; Narwal, V.; Batra, B. Determination of lactic acid with special emphasis on biosensing methods: A review. *Biosensors and Bioelectronics* **2016**, *86*, 777–790.
- (9) Zhang, L.; Tian, F.; Liu, C.; Feng, Q.; Ma, T.; Zhao, Z.; Li, T.; Jiang, X.; Sun, J. Hand-powered centrifugal microfluidic platform inspired by the spinning top for sample-to-answer diagnostics of nucleic acids. *Lab on a Chip* **2018**, *18*, 610–619.
- (10) Thompson, B. L.; Wyckoff, S. L.; Haverstick, D. M.; Landers, J. P. Simple, Reagentless Quantification of Total Bilirubin in Blood Via Microfluidic Phototreatment and Image Analysis. *Analytical Chemistry* **2017**, *89*, 3228–3234.
- (11) Stumpf, F.; Schwemmer, F.; Hutzenlaub, T.; Baumann, D.; Strohmeier, O.; Dingemanns, G.; Simons, G.; Sager, C.; Plobner, L.; von Stetten, F.; Zengerle, R.; Mark, D. LabDisk with complete reagent prestorage for sample-to-answer nucleic acid based detection of respiratory pathogens verified with influenza A H3N2 virus. *Lab on a Chip* **2016**, *16*, 199–207.
- (12) Park, B. H.; Lee, J. H.; Jung, J. H.; Oh, S. J.; Lee, D. C.; Seo, T. S. A centrifuge-based stepwise chemical loading disc for the production of multiplex anisotropic metallic nanoparticles. *RSC Advances* **2015**, *5*, 1846–1851.
- (13) Sayad, A.; Ibrahim, F.; Mukim Uddin, S.; Cho, J.; Madou, M.; Thong, K. L. A microdevice for rapid, multiplex and colorimetric detection of foodborne pathogens using a centrifugal microfluidic platform. *Biosensors and Bioelectronics* **2018**, *100*, 96–104.

- (14) Phaneuf, C. R.; Mangadu, B.; Tran, H. M.; Light, Y. K.; Sinha, A.; Charbonier, F. W.; Eckles, T. P.; Singh, A. K.; Koh, C.-Y. Integrated LAMP and immunoassay platform for diarrheal disease detection. *Biosensors and Bioelectronics* **2018**, *120*, 93–101.
- (15) Li, H.; Wu, L.; Zhou, W.; Jiang, K.; Fu, W.; Dong, Y.; Chen, S.; Liu, C.; Zhang, T.; Ding, S.; Duan, S.; Li, Y. Microfluidic disk for the determination of human blood types. *Microsystem Technologies* **2017**, *23*, 5645–5651.
- (16) Choi, G.; Jung, J. H.; Park, B. H.; Oh, S. J.; Seo, J. H.; Choi, J. S.; Kim, D. H.; Seo, T. S. A centrifugal direct recombinase polymerase amplification (direct-RPA) microdevice for multiplex and real-time identification of food poisoning bacteria. *Lab on a Chip* **2016**, *16*, 2309–2316.
- (17) Oh, S. J.; Park, B. H.; Jung, J. H.; Choi, G.; Lee, D. C.; Kim, D. H.; Seo, T. S. Centrifugal loop-mediated isothermal amplification microdevice for rapid, multiplex and colorimetric foodborne pathogen detection. *Biosensors and Bioelectronics* **2016**, *75*, 293–300.
- (18) Schwemmer, F.; Blanchet, C. E.; Spilotros, A.; Kosse, D.; Zehnle, S.; Mertens, H. D. T.; Graewert, M. A.; Rössle, M.; Paust, N.; Svergun, D. I.; von Stetten, F.; Zengerle, R.; Mark, D. LabDisk for SAXS: a centrifugal microfluidic sample preparation platform for small-angle X-ray scattering. *Lab on a Chip* **2016**, *16*, 1161–1170.
- (19) Bissonnette, L.; Bergeron, M. The GenePOC Platform, a Rational Solution for Extreme Point-of-Care Testing. *Micromachines* **2016**, *7*, 94.
- (20) Rombach, M.; Keller, M.; Paust, N.; Stetten, F. V.; Mark, D.; Zengerle, R.; Karle, M. In *MicroTAS 2016 - International Conference on Miniaturized Systems for Chemistry and Life Sciences*, 2016, pp 852–854.
- (21) Strohmeier, O.; Laßmann, S.; Riedel, B.; Mark, D.; Roth, G.; Werner, M.; Zengerle, R.; von Stetten, F. Multiplex genotyping of KRAS point mutations in tumor cell DNA by allele-specific real-time PCR on a centrifugal microfluidic disk segment. *Microchimica Acta* **2014**, *181*, 1681–1688.
- (22) Keller, M.; Wadle, S.; Paust, N.; Dreesen, L.; Nuese, C.; Strohmeier, O.; Zengerle, R.; von Stetten, F. Centrifugo-thermopneumatic fluid control for valving and aliquoting applied to multiplex real-time PCR on off-the-shelf centrifugal thermocycler. *RSC Advances* **2015**, *5*, 89603–89611.
- (23) Keller, M.; Naue, J.; Zengerle, R.; von Stetten, F.; Schmidt, U. Automated Forensic Animal Family Identification by Nested PCR and Melt Curve Analysis on an Off-the-Shelf Thermocycler Augmented with a Centrifugal Microfluidic Disk Segment. *PLOS ONE* **2015**, *10*, ed. by Wu, M.-H., e0131845.
- (24) Mark, D.; Weber, P.; Lutz, S.; Focke, M.; Zengerle, R.; von Stetten, F. Aliquoting on the centrifugal microfluidic platform based on centrifugo-pneumatic valves. *Microfluidics and Nanofluidics* **2011**, *10*, 1279–1288.

- 226
- (25) Lutz, S.; Weber, P.; Focke, M.; Faltin, B.; Hoffmann, J.; Müller, C.; Mark, D.; Roth, G.; Munday, P.; Armes, N.; Piepenburg, O.; Zengerle, R.; von Stetten, F. Microfluidic lab-on-a-foil for nucleic acid analysis based on isothermal recombinase polymerase amplification (RPA). *Lab on a Chip* **2010**, *10*, 887–893.
 - (26) Goodwin, M. L.; Harris, J. E.; Hernández, A.; Gladden, L. B. Blood Lactate Measurements and Analysis during Exercise: A Guide for Clinicians. *Journal of Diabetes Science and Technology* **2007**, *1*, 558–569.
 - (27) Vargas, E.; Ruiz, M.; Campuzano, S.; de Rivera, G. G.; López-Colino, F.; Reviejo, A.; Pingarrón, J. Implementation of a new integrated d-lactic acid biosensor in a semiautomatic FIA system for the simultaneous determination of lactic acid enantiomers. Application to the analysis of beer samples. *Talanta* **2016**, *152*, 147–154.
 - (28) Moreira, J. L.; Santos, L. Analysis of organic acids in wines by Fourier-transform infrared spectroscopy. *Analytical and Bioanalytical Chemistry* **2005**, *382*, 421–425.
 - (29) Moreno Vigara, J. J.; Peinado Amores, R. A., *Química Enológica*, 1st; AMV Ediciones and Ediciones Mundi-Prensa: Madrid, Spain, 2010, p 511.
 - (30) Lonvaud-Funel, A. Lactic acid bacteria in the quality improvement and depreciation of wine. *Antonie van Leeuwenhoek* **1999**, *76*, 317–331.
 - (31) *Wine Chemistry and Biochemistry*; Moreno-Arribas, M. V., Polo, M. C., Eds.; Springer New York: New York, NY, USA, 2009, p 735.
 - (32) Jackson, R. S., *Wine Science: Principles and Applications*, 3rd; Academic Press, Elsevier: Burlington, MA, USA, 2008, p 747.
 - (33) Esti, M.; Volpe, G.; Micheli, L.; Delibato, E.; Compagnone, D.; Moscone, D.; Palleschi, G. Electrochemical biosensors for monitoring malolactic fermentation in red wine using two strains of *Oenococcus oeni*. *Analytica Chimica Acta* **2004**, *513*, 357–364.
 - (34) Gamella, M.; Campuzano, S.; Conzuelo, F.; Curiel, J. A.; Muñoz, R.; Reviejo, A. J.; Pingarrón, J. M. Integrated multienzyme electrochemical biosensors for monitoring malolactic fermentation in wines. *Talanta* **2010**, *81*, 925–933.
 - (35) Giménez-Gómez, P.; Gutiérrez-Capitán, M.; Capdevila, F.; Puig-Pujol, A.; Fernández-Sánchez, C.; Jiménez-Jorquera, C. Robust l-malate bienzymatic biosensor to enable the on-site monitoring of malolactic fermentation of red wines. *Analytica Chimica Acta* **2017**, *954*, 105–113.
 - (36) Megazyme Test Kits and Reagents - Wine Product Guide., Wicklow, Ireland, 2018.
 - (37) L-Lactic acid (L-Lactate) Assay Procedure., Wicklow, Ireland, 2018.

- (38) Ymbern Llorens, O. Development of centrifugal microfluidic platforms based on polymer microfabrication technology., PhD thesis, Universitat Autònoma de Barcelona, 2015.
- (39) Sández Fernández, N. Design, construction and evaluation of aliquoting structures for centrifugal microfluidic platforms., Ph.D. Thesis, Universitat Autònoma de Barcelona, 2013.
- (40) Strohmeier, O.; Keller, M.; Schwemmer, F.; Zehnle, S.; Mark, D.; von Stetten, F.; Zengerle, R.; Paust, N. Centrifugal microfluidic platforms: advanced unit operations and applications. *Chemical Society Reviews* **2015**, *44*, 6187–6229.
- (41) Kazemzadeh, A.; Ganesan, P.; Ibrahim, F.; He, S.; Madou, M. J. The Effect of Contact Angles and Capillary Dimensions on the Burst Frequency of Super Hydrophilic and Hydrophilic Centrifugal Microfluidic Platforms, a CFD Study. *PLoS ONE* **2013**, *8*, ed. by Han, A., e73002.
- (42) Zhang, H.; Tran, H. H.; Chung, B. H.; Lee, N. Y. Solid-phase based on-chip DNA purification through a valve-free stepwise injection of multiple reagents employing centrifugal force combined with a hydrophobic capillary barrier pressure. *The Analyst* **2013**, *138*, 1750–1757.
- (43) Berenguel-Alonso, M.; Sabés-Alsina, M.; Morató, R.; Ymbern, O.; Rodríguez-Vázquez, L.; Talló-Parra, O.; Alonso-Chamarro, J.; Puyol, M.; López-Béjar, M. Rapid Prototyping of a Cyclic Olefin Copolymer Microfluidic Device for Automated Oocyte Culturing. *SLAS Technology* **2017**, 1–11.
- (44) Guckenberger, D. J.; de Groot, T. E.; Wan, A. M. D.; Beebe, D. J.; Young, E. W. K. Micromilling: a method for ultra-rapid prototyping of plastic microfluidic devices. *Lab on a Chip* **2015**, *15*, 2364–2378.
- (45) Hecke, M.; Schomburg, W. K. Review on micro molding of thermoplastic polymers. *Journal of Micromechanics and Microengineering* **2004**, *14*, R1–R14.
- (46) TOPAS® COC - Company and Product Brochure., Florence, KY, USA, 2011.
- (47) Khanarian, G. Optical properties of cyclic olefin copolymers. *Optical Engineering* **2001**, *40*, 1024–1029.
- (48) Nunes, P. S.; Ohlsson, P. D.; Ordeig, O.; Kutter, J. P. Cyclic olefin polymers: emerging materials for lab-on-a-chip applications. *Microfluidics and Nanofluidics* **2010**, *9*, 145–161.
- (49) Ultraviolet Emitter MTE-H32 Series., Latham, NY, USA, 2014.
- (50) Si photodiodes - S1337 series Datasheet., Hamamatsu, Japan, 2015.
- (51) Burger, S; Schulz, M; von Stetten, F; Zengerle, R; Paust, N Rigorous buoyancy driven bubble mixing for centrifugal microfluidics. *Lab on a Chip* **2016**, *16*, 261–268.

- 228
- (52) Mortazavi, S. M. A.; Tirandazi, P.; Normandie, M.; Saidi, M. S. Efficient batch-mode mixing and flow patterns in a microfluidic centrifugal platform: a numerical and experimental study. *Microsystem Technologies* **2017**, *23*, 2767–2779.
 - (53) Grumann, M.; Geipel, A.; Riegger, L.; Zengerle, R.; Ducrée, J. Batch-mode mixing on centrifugal microfluidic platforms. *Lab on a Chip* **2005**, *5*, 560–565.
 - (54) Waldbaur, A.; Rapp, H.; Länge, K.; Rapp, B. E. Let there be chip—towards rapid prototyping of microfluidic devices: one-step manufacturing processes. *Analytical Methods* **2011**, *3*, 2681–2716.
 - (55) Fiorini, G. S.; Chiu, D. T. Disposable microfluidic devices: fabrication, function, and application. *BioTechniques* **2005**, *38*, 429–446.
 - (56) Olanrewaju, A.; Beaugrand, M.; Yafia, M.; Juncker, D. Capillary microfluidics in microchannels: from microfluidic networks to capillaric circuits. *Lab on a Chip* **2018**, *18*, 2323–2347.
 - (57) *Microfluidics and Microscale Transport Processes*, 1st; Chakraborty, S., Ed.; CRC Press: Boca Raton, FL, USA, 2013.
 - (58) Cuadros-Rodríguez, L.; Gámiz-Gracia, L.; Almansa-López, E. M.; Laso-Sánchez, J. Calibration in chemical measurement processes. I. A metrological approach. *TrAC Trends in Analytical Chemistry* **2001**, *20*, 195–206.
 - (59) Kościelniak, P. Nonlinear calibration by the standard addition method. *Chemo-metrics and Intelligent Laboratory Systems* **1999**, *47*, 275–287.
 - (60) Danzer, K.; Currie, L. a. Guidelines for calibration in analytical chemistry. Part I. Fundamentals and single component calibration (IUPAC Recommendations 1998). *Pure and Applied Chemistry* **1998**, *70*, 993–1014.
 - (61) Thompson, M.; Ellison, S. L. R. A review of interference effects and their correction in chemical analysis with special reference to uncertainty. *Accreditation and Quality Assurance* **2005**, *10*, 82–97.
 - (62) Miller, J. N. Basic statistical methods for Analytical Chemistry. Part 2. Calibration and regression methods. A review. *The Analyst* **1991**, *116*, 3–14.
 - (63) Ellison, S. L. R.; Thompson, M. Standard additions: myth and reality. *The Analyst* **2008**, *133*, 992–997.

Chapter 8

Concluding remarks & future challenges

This dissertation presents three different applications of LOC systems as well as a novel valving system for centrifugal microfluidic platforms. At the end of each chapter, one can find the specific conclusions and some future remarks on each concrete topic. A more encompassing view is provided hereafter, where the general and most relevant conclusions are outlined.

The use of COC as the substrate material for the construction of LOC devices provides several relevant advantages over the use of other common materials. Some of these advantages have been extensively exploited in this work and include, for example, the possibility of using a multilayer approach as the fabrication methodology. This fact, along with a simple bonding strategy based on the combination of COC layers with different T_g , has enabled the prototyping of complex 3D structures in an easy and rapid fashion. Although in the last chapter a relatively complex construction process has been presented, it is important to emphasize that such intricate structures would have been more difficult, more time-consuming or even impossible to fabricate using other substrate materials.

The selection of the suitable material for the fabrication of a LOC device is fundamental when intended to be scaled up to mass production. The potential of a device to be commercially attractive is directly related to the costs of its mass manufacturing. In this regard, one of the major benefits of using COC as the substrate material is the availability of several economical and well-established techniques for mass production (e.g. injection moulding and hot embossing), thus reducing the gap which is frequently found between industry and academia.

The high optical transparency of COC in the UV-visible range has been crucial to the development of the microsystems presented in this dissertation, all of them based on absorbance measurements for the quantification of the analytes. Titratable acidity in wines was determined at 621 nm, in the visible range, whereas PAN and L-lactic acid were determined at 340 nm, in the near-UV range. Absorbance measurements were performed by using a simple, economical and miniaturised optical detection system.

The microsystems presented in this thesis have benefited from the proprietary fabrication methodology existing in the GSB, which has been developed during the last few years. This technology has permitted the integration of the necessary elements and structures for performing the basic fluidic operations required for each concrete application. These later include, among many others, valving, mixing, metering and aliquoting.

Apart from taking advantage of the available fluidic “toolbox”, this thesis has also contributed to this latter by the development of a novel valving system for centrifugal microfluidic platforms. This novel magnetically actuated valve is simple, robust and easy to implement. Its major strength lies on being reversible (i.e. able to switch between open and closed states). This property, rarely reported in the literature despite being particularly desirable, enables a highly sophisticated and flexible fluid management.

Even though the main objectives have been successfully achieved, some of the microsystems presented in this thesis are still at the prototyping level, requiring further effort to be fully transferable to industry. In the microsystem presented in § 4, for instance, the integration of solenoid micropumps for fluid transport (instead of using a conventional peristaltic pump) would considerably increase the miniaturisation of the system and its potential autonomy.

It is expected to achieve in the near future a completely automated and autonomous microsystem for the continuous monitoring of, at least, titratable acidity and PAN in musts/wines during wine-making processes. “At least” has been deliberately used in order to highlight the enormous versatility of the developed microsystem, which could undoubtedly be applied for the analysis of other parameters of interest whether in wine-making or in other different areas. The high versatility of the system is a result of the high versatility of the involved elements: actuators, microfluidic platform and optical detection system.

The last microsystem presented, a centrifugal microfluidic platform for the parallel enzymatic analysis of several analytes in wine, is still in the development stage. The optimisation of this system will certainly require a thorough study. Nonetheless, the work here presented has paved the way towards the ambitious final objective.